

TECHNISCHE UNIVERSITÄT MÜNCHEN

Department Chemie

Wacker-Lehrstuhl für Makromolekulare Chemie

**FUNCTIONAL POLYMER BRUSHES ON DIAMOND ELECTRODES FOR  
AMPEROMETRIC BIOSENSOR APPLICATIONS**

Aurelia Naima Hutter

Vollständiger Abdruck der von der Fakultät für Chemie der Technischen Universität München zur Erlangung des akademischen Grades eines

**Doktors der Naturwissenschaften**

genehmigten Dissertation.

Vorsitzender: Univ.-Prof. Dr.-Ing K.-O. Hinrichsen

Prüfer der Dissertation: 1. Univ.-Prof. Dr. R. Jordan, Technische Universität Dresden

2. Univ.-Prof. Dr. U. K. Heiz

3. Priv.-Doz. Dr. J. A. Garrido Ariza

Die Dissertation wurde am 14.02.2012 bei der Technischen Universität München eingereicht und durch die Fakultät für Chemie am 28.06.2012 angenommen.



Die vorliegende Arbeit wurde in der Zeit von Juni 2008 bis Oktober 2011 unter der Leitung von Prof. Dr. Rainer Jordan am Wacker-Lehrstuhl für Makromolekulare Chemie von Prof. Dr. Dr. h.c. Bernhard Rieger der Technischen Universität München angefertigt.



**“DIAMONDS ARE A GIRL’S BEST FRIEND”**

lyrics by Marilyn Monroe



# Danksagung

Mein Betreuer Prof. Dr. Rainer Jordan hat es mir ermöglicht an einem äußerst spannenden, fächerübergreifenden Projekt, mit viel experimentellem Freiraum und Platz für Kreativität zu arbeiten, weswegen ihm mein besonderer Dank gilt. Obwohl es sich meistens um „nanokleine“ Experimente und Phänomene handelte, fand ich mein Thema immer großartig. Ich bin sehr erfreut über die Art und Weise, mit der er die nicht ganz einfache Situation einer externen Betreuung gehandhabt hat, nämlich mit viel Vertrauen, Motivation zur Selbstverantwortung, Inspiration und hilfsreichem wissenschaftlichem Input trotz der Distanz Dresden-München. Außerdem bin ich sehr dankbar, dass er mir zahlreiche Möglichkeiten gegeben hat an Konferenzen und Workshops teilzunehmen und mir geholfen hat ein gutes wissenschaftliches Netzwerk aufzubauen, aus dem etliche ergebnisreiche Kooperationen entstanden sind. Seine Idee mich im Zuge eines Forschungsaufenthaltes an die Duke University zu Prof. Dr. Zauscher zu schicken war genau richtig, um dies als Beispiel zu nennen.

Im Laufe der Jahre hat sich Dr. Jose Garrido zu meinem Hauptbetreuer „vor Ort“ entwickelt und ich bin ihm nicht zuletzt wegen seines hilfreichen wissenschaftlichen Knowhows, einer sehr erfreulichen Arbeitsatmosphäre, sowie der Investition seiner wertvollen Zeit zwecks Organisatorischem, Projekttreffen und Diskussionen, zu tiefstem Dank verpflichtet.

Prof. Bernd Rieger danke ich besonders für die Aufnahme, bzw. den Verbleib am Lehrstuhl und die damit verbundenen Möglichkeiten an den interessanten Gruppenseminaren, Lehrstuhlfahrten und Konferenzen teilzunehmen, zudem Einblicke in entferntere fachliche Themengebiete zu erhalten und die Lehrstuhlinfrastruktur mitbenutzen zu können. In dem Zusammenhang möchte ich auch Dr. Carsten Troll meinen Dank aussprechen, der die Nutzung der wissenschaftlichen Geräte und viele organisatorische Details möglich gemacht hat.

Prof. Oskar Nuyken bin ich wegen seines Interesses an meinem Werdegang, aber auch für viele unterhaltsame Geschichten zwischen „Tür und Angel“ dankbar.

Unter den Reihen der Betreuer möchte ich aber auch ganz herzlich Dr. Marin Steenackers (der Mann mit der Pausane) danken, der mir Mentor, Motivator und Freund zugleich war: Vriendelijk bedankt!

Aber ohne die vielen spannenden Kooperationen wäre diese Arbeit gar nicht möglich gewesen. Ganz besonders möchte ich daher meinem IGSSE- und Projektkollegen Andreas

Reitinger danken, der wegen der perfekten Mischung aus seiner fachlicher Kompetenz, Offenheit und Freundschaftlichkeit eine perfekte Teamarbeit ermöglicht hat. In dem Zusammenhang sollten noch die anderen WSI Mitarbeiter Ian Sharp, Peter Weiser, Markus Dankerl, Felix Buth, Moritz Hauf, Franz Fuchs, Roberta Caterino und Susanne Schäfer genannt werden, mit denen man toll zusammenarbeiten oder einfach nur Spaß haben konnte. Weitere Kooperationspartner, denen ich danken möchte, sind Tobias Pirzer für AFM Sessions am IMETUM, Mario Bareis für den spannenden Einblick in Nanoimprinting Technologien, sowie Prof. Dr. Christian Becker, Dr. Martin Haslbeck, Ingrid Span und Anja List aus der Biochemie.

Mein großer Dank gilt Prof. Stefan Zauscher von der Duke University für die tollen drei Monate, die ich in seinen Laboratorien arbeiten durfte, inklusive des typischen US amerikanischen BBQs. Ebenso seinen Mitarbeitern Jeff Coles, Rob Ferris, Eric Zhang und Greg Hardy, die mir mit Rat und Tat offen und hilfsbereit zur Seite standen und den Aufenthalt sehr lebenswert gemacht haben.

Außerdem danke ich allen neuen und alten Mitarbeitern des Makro Lehrstuhls für ein tolles Arbeitsklima. Zuerst einmal Julia Müller, die mich ursprünglich mit Synthesepraktikum und Bachelorarbeit in die Makro gelockt hat. Dann gilt mein Dank dem internen Kreis der „Rainer Jordan Anhänger“ Robert Luxenhofer und Anita Schulz (mein Lieblingshotel in Dresden), Timo Korfmann, Anastasia Golosova, Gerhard Richter, Ning Zhang und Frank Deubel (letzteren beiden wegen Korrekturlesen, aber noch vielem mehr!). Die Arbeit hätte nicht halb so viel Spaß gemacht ohne das Labor 56225 mit Sanna Zimmer, Philipp Zehetmaier, Franziska Graf und Richard Reithmeier, sowie meinem Partnerlook-Labor 56401 mit Max Lehenmeier und Stefan Kissling. Außerdem möchte ich ganz herzlich meinem langjährigen Laborkollegen Stephan Klaus danke sagen, das war eine prima Konstellation. Zudem meinen Knechten, Florian Huber, Roland Weixler und den Makrozugängen Manuela Philipp und Christian Prinz Anger danken, für tolles Engagement, große Motivation und daraus entstandene Freundschaften. Obwohl schon bereits anderweitig erwähnt, danke an meine beiden Uni-BFFs.

# Table of contents

<b>1. INTRODUCTION .....</b>	<b>1</b>
<b>2. THEORETICAL BACKGROUND .....</b>	<b>3</b>
2.1 PRINCIPLES OF A BIOSENSOR.....	3
2.1.1 <i>General function of a biosensor</i> .....	4
2.1.2 <i>Types of biosensors</i> .....	5
2.1.2.1 Electrochemical biosensors.....	5
2.1.2.2 Field-effect transistors.....	9
2.1.2.3 Surface Plasmon Resonance.....	10
2.1.2.4 Quartz Crystal Microbalance .....	12
2.1.2.5 Other techniques.....	14
2.1.3 <i>Detailed insight in glucose biosensors</i> .....	15
2.1.3.1 General detection strategies for glucose .....	16
2.1.3.2 Implantable sensors .....	19
2.2 (BIO)CHEMICAL FUNCTIONALIZATION OF ELECTRODE MATERIALS .....	21
2.2.1 <i>Biofunctionalized self-assembled monolayers</i> .....	21
2.2.1.1 Thiols on gold .....	21
2.2.1.2 Silane functionalization .....	22
2.2.1.3 Diazonium salts .....	23
2.2.1.4 Other monolayer approaches .....	24
2.2.2 <i>Coatings</i> .....	25
2.2.3 <i>Polymer brush - biomolecule conjugates</i> .....	26
2.2.3.1 General remarks on polymer brushes.....	27
2.2.3.2 Polyelectrolytes as matrix for biomolecules .....	29
2.2.3.3 Covalently bonded biomolecules .....	31
2.2.3.4 Biological aspects of poly(2-oxazoline)-based molecular brushes.....	33
2.2.3.5 Preparation of micro- and nanostructured polymer brushes.....	34
2.3 PROPERTIES AND APPLICATION OF DIAMOND ELECTRODES .....	40

2.3.1	<i>Processing of diamond</i>	40
2.3.2	<i>Physicochemical properties of diamond</i>	41
2.3.3	<i>Surface modification of diamond</i>	42
2.3.3.1	Surface termination of synthetic diamond films	42
2.3.3.2	Organic monolayers on diamond – state of the art	43
2.3.3.3	Polymer brushes on diamond - state of the art	44
2.3.4	<i>Biological aspects of diamond</i>	45
<b>3.</b>	<b>PURPOSE AND OBJECTIVES</b>	<b>47</b>
<b>4.</b>	<b>RESULTS AND DISCUSSION</b>	<b>49</b>
4.1	MICRO- AND NANOSTRUCTURED POLYMER BRUSHES ON DIAMOND AND SiO <sub>x</sub> BY SIPGP	49
4.1.1	<i>Reactivity contrast between H- and OH-terminated diamond</i>	49
4.1.1.1	Microstructured polymer brushes on diamond by common photolithography	50
4.1.1.2	Poly(2-oxazoline) bottle-brush brushes on diamond	52
4.1.2	<i>Electron-beam lithography (EBL) on nanocrystalline diamond</i>	55
4.1.2.1	Investigation of different template designs for the EBL on diamond	55
4.1.2.2	EBL with an electron microscope without a lithography tool	61
4.1.3	<i>Electric field-induced lithography on SiO<sub>x</sub></i>	62
4.1.4	<i>Thermal structuring of poly(1-ethoxyethyl methacrylate) brushes</i>	65
4.2	BIOFUNCTIONALIZED POLYMER BRUSHES	67
4.2.1	<i>Background on proteins and enzymes</i>	67
4.2.2	<i>Coupling strategies for biomolecules</i>	70
4.2.2.1	Preparation of biofunctionalized poly(2-oxazoline)e bottle-brush brushes	70
4.2.2.2	Biomolecule coupling to poly(methacrylic acid) brushes	75
4.2.3	<i>Activity and stability of polymer brush protein conjugates</i>	79
4.2.3.1	Detection of the green fluorescent protein in fluorescence microscopy	79
4.2.3.2	Colorimetric essays for the determination of enzymatic reaction kinetics	84
4.3	POLYMER BRUSHES AS POLYMERIC MEDIATORS	92
4.3.1	<i>Theoretical insight into voltammetric and amperometric techniques</i>	92
4.3.2	<i>Carbazole as hole conducting moiety in poly(2-oxazoline) bottle-brush brushes</i>	97
4.3.3	<i>Ferrocene as redox mediator</i>	101
4.3.3.1	Incorporation of ferrocene using vinylferrocene as co-monomer in SIPGP	102

4.3.3.2	Polymer analogue coupling of aminoferrocene to P(MA) brushes.....	105
4.3.3.3	Polymer analogue coupling of aminomethylferrocene in P(MA) brushes.....	107
4.4	ELECTROCHEMICAL ANALYSIS OF BIOFUNCTIONALIZED POLYMER BRUSHES ON DIAMOND ELECTRODES ..	112
4.4.1	<i>Electrochemical enzyme detection without mediator</i> .....	112
4.4.2	<i>Application of free mediator in solution</i> .....	113
4.4.3	<i>Enzymatic reactions in polymeric mediators</i> .....	114
4.4.4	<i>Comparison between monolayer- and polymer brush bound enzymes</i> .....	123
4.4.4.1	Colorimetric assays.....	123
4.4.4.2	Fluorescence bleaching.....	126
4.4.4.3	Amperometric detection of glucose .....	127
<b>5.</b>	<b>SUMMARY</b> .....	<b>129</b>
<b>6.</b>	<b>ZUSAMMENFASSUNG</b> .....	<b>136</b>
<b>7.</b>	<b>EXPERIMENTAL PART</b> .....	<b>144</b>
7.1	INSTRUMENTS AND METHODS .....	144
7.2	SOLVENTS, CHEMICALS, SUBSTRATES .....	147
7.3	SURFACE FUNCTIONALIZATION PROCEDURES .....	148
7.3.1	<i>Treatment of surfaces</i> .....	148
7.3.2	<i>Formation of SAMs and polymer brushes</i> .....	149
7.3.3	<i>Polymer analogue reactions</i> .....	150
7.4	SYNTHESIS OF ORGANIC MOLECULES .....	153
<b>8.</b>	<b>REFERENCES</b> .....	<b>158</b>

## Abbreviations and symbols

ACA	aminocaproic acid
ACN	acetonitrile
AFM	atomic force microscopy
AmFe	aminoferrocene
AmMeFc	aminomethylferrocene
AMP	adenosine monophosphate
APDEMS	aminopropyl-diethoxymethylsilane
APTES	aminopropyltriethoxysilane
ATP	adenosine triphosphate
ATR	attenuated total reflectance
ATRP	atom transfer radical polymerization
BBB	bottle-brush brush
BDD	boron doped diamond
BDE	bond dissociation energy
bpy	bipyridyl
BSA	bovine serum albumin
-c-	-co-
cAMP	cyclic adenosine monophosphate
CarbOx	2-(carbazolyl)ethyl-2-oxazoline
CarboxyOx	2-carboxyethyl-2-oxazoline
cfu	colony forming unit
CHEMFET	chemical field-effect transistor
Cp	cyclopentadienyl
CT	carbon templating/template
CV	cyclic voltammetry
CVD	chemical vapor deposition
DCM	dichloromethane
DPN	dip-pen nanolithography
e <sup>-</sup>	electron
EBL	electron beam lithography
EBCD	electron beam-induced carbon deposition
EDC	1-ethyl-3-(3-dimethylaminopropyl)carbodiimide
EEMA	1-ethoxyethyl methacrylate
EFIL	electric field-induced lithography
EtOx	2-ethyl-2-oxazoline
Fc	ferrocene
FET	field-effect transistor
FM	fluorescence microscope
FMN	flavine mononucleotide
FT-IR	fourier transform infrared spectroscopy

-g-	-graft-
GC(E)	glassy carbon (electrode)
GDP	guanosine diphosphate
GFP	green fluorescent protein
GlucOx	glucose oxidase
GPC	gel permeation chromatography
GTP	guanosine triphosphate
HRP	horseradish peroxidase
HVA	homovanillic acid
ISC	inter system crossing
LCROP	living cationic ring-opening polymerization
MCD	microcrystalline diamond
μCP	microcontact printing
Med	mediator
MeOTf	methyltriflate
MOSFET	metal–oxide–semiconductor field-effect transistor
NAD <sup>+</sup>	nicotinamide adenine dinucleotide
NADH	reduced form of nicotinamide adenine dinucleotide
NCD	nanocrystalline diamond
NEXAFS	near edge X-ray absorption fine structure
NHS	<i>N</i> -hydroxysuccinimide
NIL	Nanoimprinting lithography
NMR	nuclear magnetic resonance
NTA	nitrilotriacetic acid
OTES	octyltriethoxysilane
P(AA)	poly(acrylic acid)
PDMS	poly(dimethylsiloxane)
PEG	poly(ethylene glycol)
PEI	poly(ethyleneimine)
PGM	portable glucose monitor
P(IPOx)	poly(2- <i>isopropenyl</i> -2-oxazoline)
PL	photolithography
P(MA)	poly(methacrylic acid)
P(MAEMA)	poly( <i>N,N</i> -dimethylaminoethyl methacrylate)
PMDETA	pentamethyldiethylenetriamine
P(MMA)	poly(methylmethacrylate)
P(Ox)	poly(2-oxazoline)
PS	poly(styrene)
PSS	sulfonated poly(styrene)
P( <i>t</i> BuMA)	poly( <i>tert</i> butyl-methacrylate)
PVC	poly(vinylchloride)

P4VP	poly(4-vinyl pyridine)
QCM	quartz crystal microbalance
RGD	arginine-glycine-aspartic acid peptide sequence
rms	root mean square
SAM	self-assembled monolayer
SCD	single crystalline diamond
SCE	saturated calomel electrode
SIP	surface-initiated polymerization
SIPGP	self-initiated photografting- photopolymerization
SPL	scanning probe lithography
SPR	surface plasmon resonance
SPW	surface plasmon wave
STM	scanning tunneling microscope
TBAB	tetra- <i>N</i> -butylammonium bromide
tBuMA	<i>tert</i> butyl-methacrylate
THF	tetrahydrofuran
TIRF	total internal reflectance fluorescence
TMB	2,2',5,5'- tetramethylbenzidine
TNT	trinitrotoluene
UNCD	ultrananocrystalline diamond
UV	ultraviolet
VFc	vinylferrocene
XPS	X-ray photoelectron spectroscopy
YAG	yttrium aluminium garnet

A	according to context: area, absorbance or ampere
a	diameter of monomer unit
$\alpha$	extinction coefficient
a.u.	arbitrary units
$^{\circ}\text{C}$	degree Celsius
$c_s$	salt concentration
$D_j$	diffusion coefficient
$\Delta\beta$	propagation constant
$\varepsilon$	dielectric function
$E_{1/2}$	potential taking the mean between $E_a$ and $E_c$
$E_0$	formal potential
$E_a$	anodic potential
$E_c$	cathodic potential
$E_{el}$	elastic free energy
$E_g$	gate potential
$E_{int}$	interaction energy

$E_{SD}$	potential between source and drain
eV	electron volt
F	Faraday constant
f	degree of dissociation
$f_0$	resonance frequency
$h_d$	polymer brush height (dry state)
Hz	hertz
$I_0$	incident light
$I_{DS}$	current between drain and source
$I_T$	transmitted light
$K_M$	Michaelis Menten constant
km	$10^3$ meter
L	height of swollen polymer brushes
n	refractive index
N	number of monomer units
$N_{av}$	Avogadro constant
nA	$10^{-9}$ ampere
ng	$10^{-9}$ gram
nm	$10^{-9}$ meter
m	according to context: mass or meter
mC	$10^{-3}$ coulomb
$\mu\text{g}$	$10^{-6}$ gram
MHz	$10^3$ Hertz
mM	milimolar
$\mu\text{M}$	micromolar
$\mu\text{m}$	$10^{-6}$ meter
mL	$10^{-3}$ liter
$\mu\text{l}$	$10^{-6}$ liter
mV	$10^{-3}$ V
pg	$10^{-12}$ gram
Q	charge
$\rho$	polymer bulk density
Re	real part
$\sigma$	grafting density
$\Theta$	contact angle
$w_{1/2}$	width at half height



# 1. INTRODUCTION

Over 2.5 billion years ago, approximately 140 km deep down the mantle of the earth at pressures over 60,000 bars and temperatures around 1600°C, a mineral was formed which has ever since fascinated and interested mankind: diamond.<sup>[1],[2]</sup> Brought to the surface of the earth through volcanic eruptions, diamond rather served a spiritual and ornamental than a scientific purpose when it was first discovered by human beings. Diamond as jewel is reported to have first appeared in India around 400 BC but the literal hype about the gem has its origin in the 18<sup>th</sup> century when two missionaries first discovered it in Brazil.<sup>[3]</sup> In ancient times, diamond has also been used as a technical tool for coarse applications such as engraving tools or cutting material due to its outstanding hardness. The first users of this unique type of carbon allotrope were probably aware of its irreplaceable functionality but certainly not of the immense application potential which has resulted from the discovery of synthetic routes towards diamond and, more recently, doped diamond. Many centuries later, Nobel Prize winner Henri Moissan paved the way for the first important insights into the artificial preparation of diamond: Analysis of the chemical composition of a piece of meteorite named Canyon Diablo discovered in Arizona revealed diamond crystallites inside an iron shell. Inspired by the natural formation of diamond, Moissan subsequently performed experiments in which a carbon saturated iron melt, prepared in an arc furnace, was abruptly cooled in water or mercury to successfully yield diamond crystallites.<sup>[4]</sup> Nowadays, this carbon material is of great importance in numerous research and commercial fields. Among them are coatings for low friction and wear,<sup>[5]</sup> coatings for implants<sup>[6]</sup> microelectronic devices such as field-effect transistors,<sup>[7],[8],[9]</sup> and electrochemical electrodes<sup>[10],[11],[12],[13]</sup> in e.g. biosensors, to name just some of them. Regarding the latter field, diamond provides material properties which are particularly suitable for life science applications: e.g. high mechanical stability, chemical inertness, formation of strong surface bonds, no degradation of fluorescence and resistance to non-specific binding of proteins.<sup>[14],[15],[16]</sup>

The requirements for the sensing elements in biosensor technology have become more and more challenging, since users expect a high degree of reliability, long-term stability and

biocompatibility. In the very field of glucose detection, there has been an enormous amount of reported innovations and developments based on the constant desire for optimization, specialization and miniaturization. The novel minimally invasive systems include for example reflectance or transmission of infrared radiation through tissue material, the measurement in body fluids other than blood or especially implantable micro devices for continuous glucose monitoring.<sup>[17]</sup>

Despite important research efforts in the area of biosensors, there remains need for some improvements. Amongst others are issues of long-term stability and sensitivity of implantable micro devices as well as the so-called, widely interpretable concept of biocompatibility. According to Williams, a material is biocompatible when during “contact with the tissues of the human body (...) the material shall do no harm to those tissues, achieved through chemical and biological inertness”.<sup>[18]</sup> In other words, it should be able “to perform with an appropriate host response in a specific situation”.<sup>[18]</sup> Diamond, consisting exclusively of carbon and being mechanically and chemically very stable, is a promising candidate for ensuring the least immune reaction possible when applied in biomedicine. Since no material can be regarded as 100% biocompatible, it might be wiser to use instead the term “bioinert” which means that no chemical or biological interactions, such as inflammations, are observed. As provocative example to show how challenging the combination of rigid inorganic electronic materials with sensitive biomolecules in physiological environments can get, one might reflect over these two questions:

What happens when a laptop is dipped into a bucket of diluted blood solution?

What happens if a human being swallows a mobile phone?

Obviously, each action will have hazardous consequences for both the device and the body. It emphasizes the fact that the use of microelectronics in biochemistry and medicine is everything but trivial and that the electronic part needs to be appropriately adapted to its application in physiological environments.

Despite the above mentioned inertness of diamond, which is also reflected in the word's derivation from the Greek adjective “adamas” meaning invincible, research in surface chemistry has managed to introduce functionality to the otherwise inert diamond substrates.<sup>[19]</sup> These achievements allow the current sophisticated applications of diamond and are the basis for further ambitious projects in the interdisciplinary research fields of chemistry, physics and biomedicine.

## 2. THEORETICAL BACKGROUND

### 2.1 Principles of a biosensor

As initial motivation and inspiration for the design of biosensors, we should consider the very powerful and high-performing biosensors which nature has produced, for example the nose. Our olfactory organ can smell and distinguish thousands of different odorants in very high sensitivity and specificity.<sup>[20]</sup> A prominent example for the specificity is the discrimination between two structurally identical, but stereo isomeric different molecules, R-Carvone and S-Carvone, which are responsible for the spearmint and caraway odor respectively.

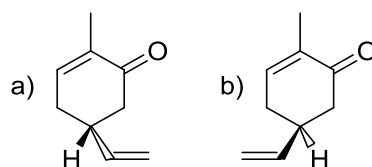


**Figure 1: R- and S-Caravone - responsible for the distinct odor of mint and caraway.**

Between the arrival of a volatile odor molecule and its recognition in the brain a series of complex biochemical processes occur. In the main olfactory epithelium at the top of the nasal cavity the odorant meets a transmembrane 7TM receptor which consists of seven helices and acts as a molecule trap. 7TM receptors play an important role in numerous signaling pathways in the human body and can be activated by e.g. photons, tastants and hormones.<sup>[20]</sup> The interaction of receptor and odorant triggers a series of signalling cascades, which are depicted in Figure 2. The first step involves a GTP-binding protein (G-protein) which releases guanosine diphosphate (GDP) prior to binding guanosine triphosphate (GTP). Subsequently, the GTP-bound form of the G-protein activates the enzyme adenylate cyclase that converts ATP into cyclic AMP (cAMP). The increased cAMP concentration in the cell induces the opening of cAMP-gated channels that allow cations to enter the cell creating an action potential. The sum of action potentials of all concerned neuron cells is carried to the brain and read out as specific scent.<sup>[20]</sup> Although the smelling process seems to be highly complex, it can be reduced to the typical function of a biosensor depicted in Figure 3 and explained in the following chapters.

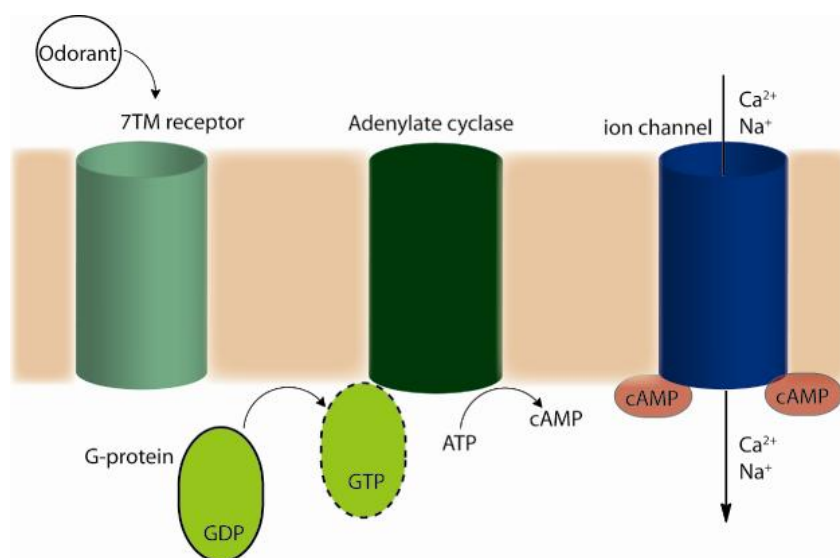


**Figure 2: Sensing principle in the nasal epithelium; enzymatic signal cascade triggered by the binding of an odorant in a 7TM receptor and resulting in an action potential along an ion channel.**

### 2.1.1 General function of a biosensor

Independently of their appearance – be it in environmental analytics, medicine or in the human body – all biosensors generally consist of the same basic elements. As depicted in Figure 3, the basis of biosensing is always given by the interaction of a **substrate** (in a solution or in air), which has to be detected and eventually quantified, and a **bioreceptor** as biological detection element.<sup>[21]</sup> Usually, the bioreceptor is immobilized in a matrix which is embedded in the device. Owing to the precision with which biological reactions are naturally controlled, specific **recognition reactions** between the analyte and the bioreceptor lead to a high selectivity of the biosensor. Biological pairs undergoing such recognition reaction can be for instance substrate/enzymes (e.g. urea/urease<sup>[22]</sup>), antibody/antigens (e.g. mucin/antimucin<sup>[23]</sup>), salts/membranes (e.g. potassium/cell membrane<sup>[24],[25]</sup>). The substrate-bioreceptor interaction can lead to various types of signals, ranging from optical or electric signals to changes in mass or heat. The observed change is converted into a measurable signal by a **transducer** and finally read out in an electronic (software) or physiological (brain) processor.

The performance of a biosensor cannot be reduced to one criterion, but the combination and emphasis of several factors will decide on the respective applicability: sensitivity, selectivity, biocompatibility / bioinertness (in order to avoid intoxication in the human body or e.g. the denaturation of biomolecules within the bioreceptor), interferences by e.g. unwanted oxidation processes and long-term stability / low degradation of the sensor device. Improving these factors has been a major research interest in life science and the health care sector. A

multitude of different approaches and developments have been achieved since the first artificial biosensor has been presented by Clark and coworkers in the 1950's.<sup>[26],[27]</sup>

concept:	general examples:	olfactory system:
analyte / substrate in solution	biomolecules inorganic molecules organic molecules sugars antibodies / antigenes gases ...	odorant
biological detection element	proteins enzymes antibodies / antigenes membranes cell tissues ...	7 TM receptor
change / signal	pH mass light charge ...	change in cAMP concentration
transducer	electrochemical field effect transistor based optical piezoelectric thermal ...	cAMP gated ion channel
readout / signal processor	computer brain ...	neural system/ brain

**Figure 3: Schematic description of the elements of a biosensor (left): specific examples (middle); examples from the nose sensing system (right).**

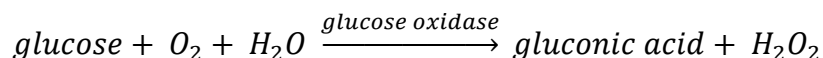
## 2.1.2 Types of biosensors

There are numerous ways of classifying biosensors into different groups. They can be discriminated by their analyte family, by their detection limits, by their industrial relevance, etc. In this chapter, the chosen examples are categorized according to their signal-transducer systems in order to give a rough overview over the most important types of electrochemical, optical and mass biosensors.

### 2.1.2.1 Electrochemical biosensors

Amongst the devices based on electrochemical transducers, the first modern type of sensor is the Clark oxygen electrode for the quantification of glucose.<sup>[26],[27]</sup> The novelty was the design of a so-called enzyme electrode where the bioreceptor (here: glucose oxidase) was immobilized at the electrochemical detector but still shielded from the electrochemical cell

and the surrounding analyte solution through permeable membranes (teflon towards the electrode and cellophane towards the surroundings) and an electrolyte gel.<sup>[21],[28]</sup> The enzymatic reaction is



and at the electrode the oxygen consumption is determined. Figure 4 schematically demonstrates the working mechanism of a Clark-type electrode which has been the basic design for various ensuing electrochemical biosensors.

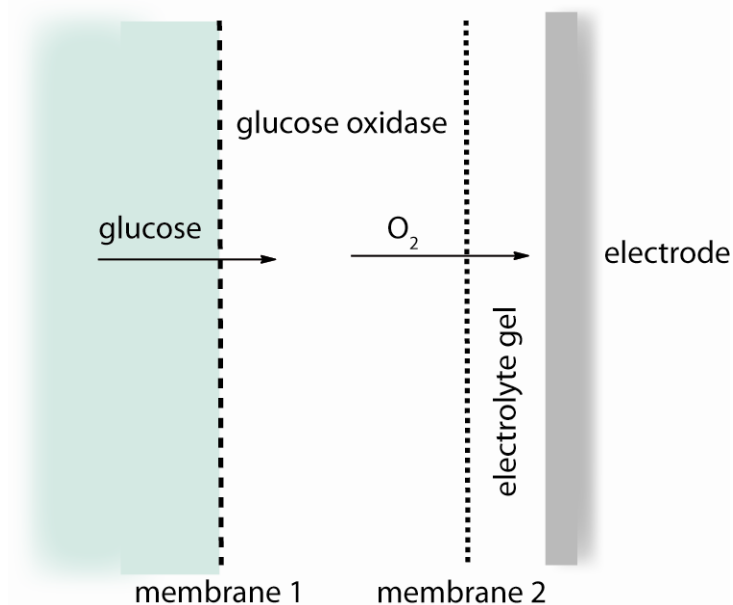


**Figure 4: Structure of a Clark-type oxygen electrode; Glucose is allowed to penetrate the first membrane where it is converted by glucose oxidase into gluconic acid and hydrogen peroxide. The change in oxygen concentration is determined at the electrode which is shielded from the surroundings by a second membrane only permeable for oxygen (adapted from <sup>[21]</sup>).**

Since electrochemical sensors are characterized by a fast response, low costs and relatively simple measuring technique they are the most commonly used biosensor types.<sup>[29]</sup> Depending on the electric variable, electrochemical biosensors can be categorized in conductometric, amperometric and potentiometric biosensors.<sup>[20],[28],[29]</sup>

Conductometric biosensors measure the changes in the conductance between two metal electrodes in bulk solution induced by a biochemical reaction. The conductance (L) is the inverse of the resistance and can be integrated into Ohm's law:  $E = I/L$ . In an electrolyte, L is proportional to the ion concentration. Besides some interesting applications for the identification of alcoholic beverages or urea,<sup>[21],[30]</sup> the detection of creatinine (high blood concentration may indicate kidney deficiency) and desmetryn (herbicide) by measuring the capacitance of an poly(acrylamide) coated gold electrode has been reported.<sup>[31]</sup>

Amperometric (or voltammetric) enzyme electrodes are designed to detect a current while a potential is applied between a working and a reference electrode in an electrochemical cell.<sup>[28]</sup> The current can be recorded versus a sweeping potential (cyclic voltammetry) or versus time at a set potential (chronoamperometry) (see chapter 4.3.1). The reason for the electron flux is a biochemical redox reaction between analyte and bioreceptor and therefore, amperometric techniques possess a linear dependence on the concentration.<sup>[29]</sup> The primarily reported analyte is glucose due to the high research interest in the field of diabetes devices.<sup>[32],[33],[34],[35],[36]</sup> Since the glucose oxidase – glucose couple will play a major role in the course of this PhD project and due to its industrial as well as commercial importance chapter 2.1.3 will exclusively deal with amperometric glucose biosensors. Besides glucose, the detection of hydrogen peroxide using its specific reaction with horseradish peroxidase (HRP) takes up a great part of the scientific literature (Figure 5). Table 1 sums up some of the possible ways of embedding the enzyme in the electrode system and the respective detection performances for H<sub>2</sub>O<sub>2</sub>.

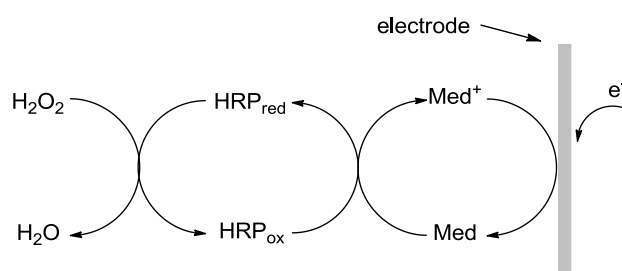


**Figure 5: Reaction cycle at the electrode; the enzymatic reaction of HRP is in most cases supported by a mediator.**

**Table 1: Design of electrochemical biosensors aimed at the detection of hydrogen peroxide by HRP.**

Electrode design – HRP within / on:	Lower detection limit / $\mu\text{M}$ <sup>[37]</sup>
graphite or coal	0.02 <sup>[38]</sup>
tin(IV)oxide	0.01 <sup>[39]</sup>
glassy carbon	0.04 <sup>[40]</sup>
an Os(bpy) <sub>2</sub> <sup>n+</sup> redox polymer	0.01 <sup>[41]</sup>
poly(pyrrole)	0.01 <sup>[42]</sup>
phenylenediamine	1.0 <sup>[43]</sup>
graphite-epoxy composite	0.4 <sup>[44]</sup>
poly(glycidyl methacrylate-co-vinylferrocene)	2.6 <sup>[45]</sup>

Other important analytes for amperometric detection are for instance lactate,<sup>[46]</sup> cholesterol,<sup>[46]</sup> and ethanol<sup>[21]</sup> (see Figure 6). All presented examples have in common that the charge transfer is not measured directly at the electrode but via so-called mediator molecules (see chapter 4.3.1).<sup>[28]</sup> It is an essential requirement for all amperometric biosensors to ensure an electrical connection between the redox center and the transducer.<sup>[47]</sup> The addition of mediators is necessary if the electron transfer is hindered due to e.g. low mobility of the enzyme, a dense protein matrix around the active center or a too large distance between redox center and electrode. The mediator, usually a low molecular weight species, shuttles the generated electrons to / from the destination electrode where it becomes re-oxidized / re-reduced.<sup>[28]</sup>

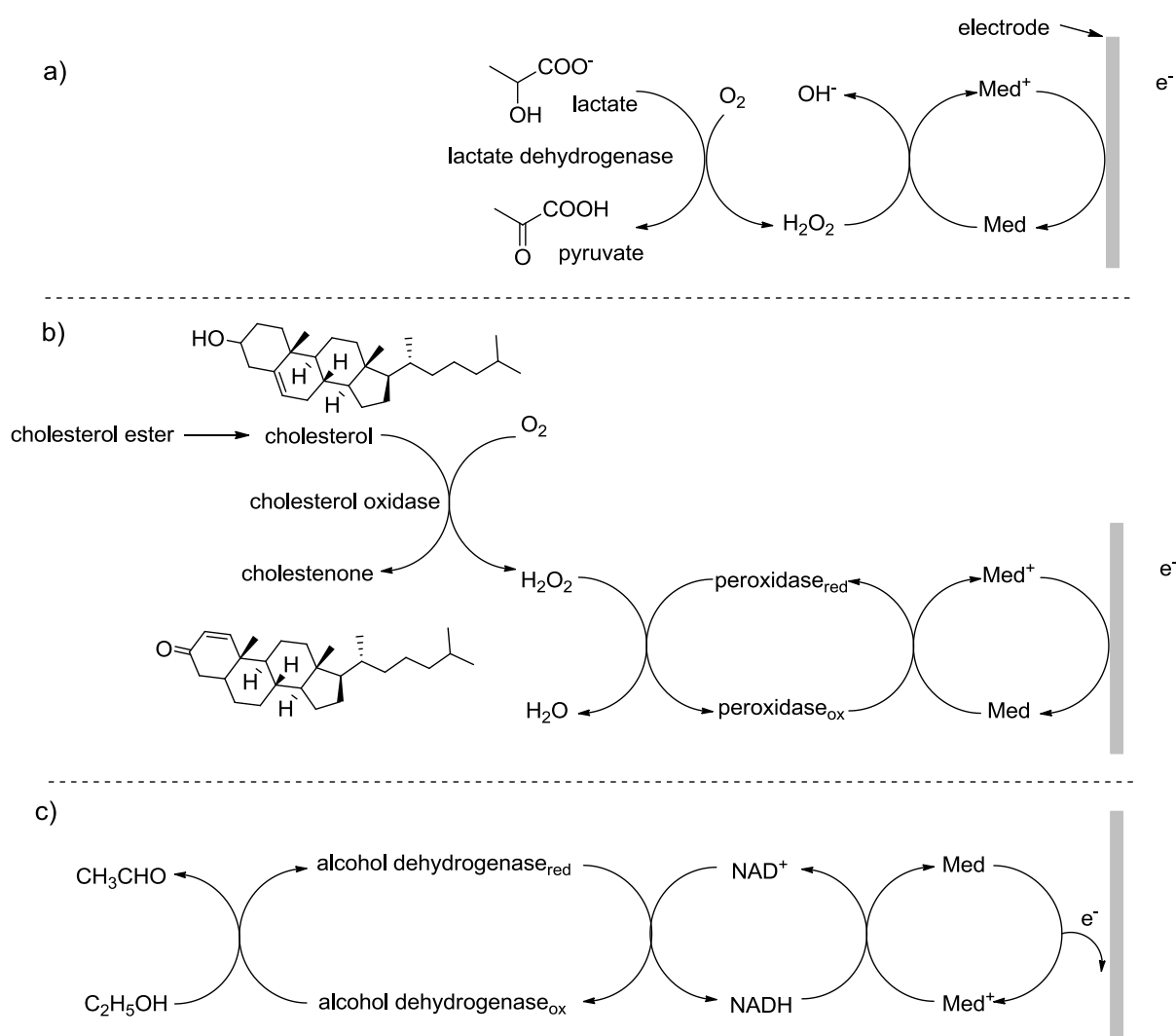
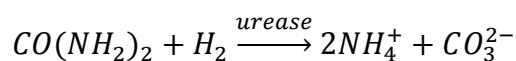


**Figure 6: Electrochemical detection of: a) lactate in the presence of oxygen; b) cholesterol via a peroxidase- and mediator-based pathway; c) ethanol via a coenzyme- and mediator-based pathway.**

Potentiometric biosensors measure the electron pressure induced by selective reactions and accumulation of charge at a working electrode with respect to a reference electrode.<sup>[29]</sup> One of

the most important analytes measured by this method is urea. Urea is hydrolyzed by urease which is attached to a poly(acrylic) gel.



In an alkaline solution, the ammonia generation can be monitored with a low detection limit down to 1  $\mu\text{M}$ . Biosensors with a lifetime of up to four months have been reported.<sup>[21],[48]</sup> Apart from ammonia, other pH-based sensing techniques have been reported for  $\text{Na}^+$ ,  $\text{Ca}^{2+}$ ,  $\text{H}^+$  and  $\text{NH}_4^+$  <sup>[28],[49],[50]</sup> but only very few ion-selective electrodes are actually used in biosensors. A more significant field of potential-dependent measuring techniques is represented by field-effect transistors (FETs).

### 2.1.2.2 Field-effect transistors

Numerous types of field-effect transistors with slightly different formats control processes in computers, cell phones and microelectronics.<sup>[51]</sup> For biosensor applications, it is sufficient to address **metal–oxide–semiconductor field-effect transistors** (MOSFETs) in combination with **chemical field-effect transistors** (CHEMFETs). Figure 7 shows a typical construction of a MOSFET: A **source** region (n-type Silicon) is separated from a **drain** region (also n-type Si) by a p-type Si region and an **insulator** (silicon dioxide). Source and drain are connected via a circuit with an applied potential  $E_{SD}$ . Yet, under starting conditions, electrons cannot flow from source to drain through the p-type Si **body**. On top of the semiconductor-oxide block a metal layer, called **gate**, is charged with a bias potential  $E_G$  and this completes the capacitor-like layer built-up metal-insulator-semiconductor.<sup>[51],[21]</sup>

When  $E_G$  is set to a negative voltage, the electronic arrangement in the p-type body is maintained and no current can flow between source and drain. But in case of a positive  $E_G$  holes from the p-type body are driven away from the body-insulator interface, creating an inversion layer in terms of an n-type channel. Now, current can flow from drain to source because it is no longer hindered by a p-n junction.<sup>[46],[21]</sup> Since changes in  $E_G$  influence the electron flow in the  $E_{SD}$ , the gate can be considered as “potential-driven doorman”. The dependence between applied gate voltage and current flow between source and drain can be seen from an example of Stutzmann *et al.* (Figure 7).<sup>[52]</sup> A CHEMFET operates in an equal manner. Yet, in this case, the gate is not an artificial electrode with a known applied potential, but a potential created by a chemical process. This chemical process can be monitored by the induced current between source and drain.<sup>[53],[21]</sup> The reaction of interest takes place in a

chemically sensitive membrane which mainly consist of hydrophobic polymers (e.g. polyurethanes<sup>[54]</sup>, PVC<sup>[55]</sup>) containing ion-selective or receptor molecules.

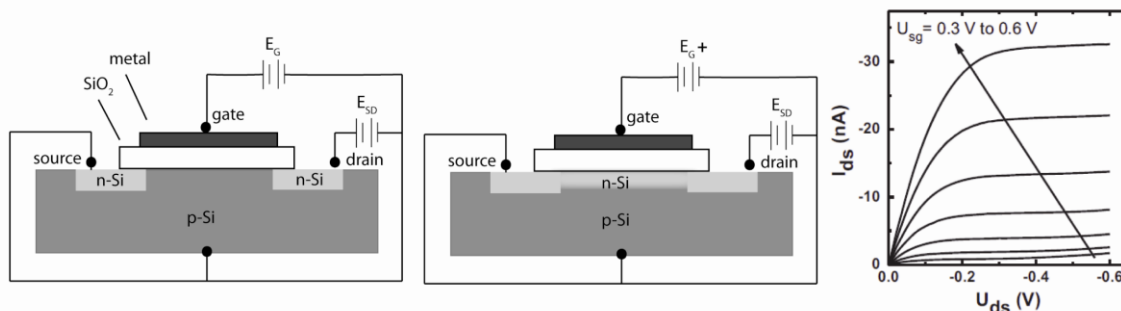


**Figure 7: Mechanism of a FET; left: closed gate at a negative  $E_g$ ; middle: current can flow at open gate conditions for positive  $E_g$  (adapted from<sup>[46]</sup>); right: influence on the applied gate voltage  $E_g$  on the current measured between source and drain (from<sup>[52]</sup>).**

The disadvantage of FETs in applied bioelectronics is mainly their complex fabrication.<sup>[46]</sup> They are considered as promising alternative for other methods, nevertheless, due to a minimized circuit wiring which results in miniaturization, little electronic background noise and electromagnetic disturbances.<sup>[46],[21],[56]</sup>

The application of FETs as biosensors concerns essentially the measurement of cations, such as  $K^+$  and  $NH_4^+$  which could be detected in blood serum by adding a ionophore to the membrane,<sup>[57]</sup> but also larger molecules, such as urea, where urease was immobilized into a poly(acrylate) chemically sensitive membrane.<sup>[54]</sup>

### 2.1.2.3 Surface Plasmon Resonance

Besides electrochemical methods, such as the above named FETs or amperometric devices, optical biosensors represent a likewise powerful tool to follow biochemical reactions, especially for immunoassays.<sup>[23]</sup> Among the optical techniques are attenuated total reflectance (ATR)<sup>[58],[58]</sup>, total internal reflection fluorescence (TIRF)<sup>[59]</sup> and surface plasmon resonance (SPR).<sup>[60],[61]</sup> ATR and SPR use similar experimental configurations, this chapter however, will focus on SPR as it features the major part in scientific literature in terms of biosensing.

Surface plasmons are electromagnetic waves existing at metal or semiconductor boundaries which spread with a certain oscillation parallel to the solid surface.<sup>[60]</sup> The fact that the smallest interferences along their path influence their mode of propagation is used for biosensing. The sensor typically consists of a glass prism and a thin metal layer (e.g. 60 nm silver<sup>[21]</sup> or 200 nm gold<sup>[60]</sup>) onto which the sample dielectric (e.g. air or aqueous solution)

is deposited (see Figure 8). The excitation of a surface plasmon wave (SPW) occurs either by electrons or visible to infrared light, while the latter is mostly used for immunoassays. Due to attenuated total reflection of the incident light beam at the prism, an evanescent wave is created perpendicular to the glass-metal-sample sandwich which propagates into the metal boundaries. There – if the light’s and the SPW’s resonances match - it excites the SPW which, depending on the encountered refractive indices along the spreading axis, alters in the propagation constant  $\Delta\beta$  (real part).<sup>[60]</sup>

Eq. 1 correlates  $\beta$  with the dielectric functions  $\varepsilon$  of the involved parts, a geometric factor  $F$  (considering that only a fraction of the field is probed), and with the refractive indices and their changes ( $\Delta n$ ). This counts for the case that a biomolecular binding event occurs within the whole extent of the SPW field.<sup>[60]</sup>

$$Re[\Delta\beta] \cong \frac{2n_s n_f k^2 d}{\sqrt{Re[\varepsilon]}} \Delta n \cong Fk\Delta n$$

**Eq. 1** with  $n_s$  and  $n_f$ : refractive indices of the background dielectric and the biocomponent;  $k^2$ : constant containing e.g. speed of light in the respective media;  $d$ : distance from the surface, where the affinity reaction occurs,  $\varepsilon$ : dielectric functions of the dielectric and the metal,  $\Delta n$ : change in refractive indices due to affinity reaction

When an affinity reaction occurs on the sample and modifies its chemical environment, it influences the SPW and consequently, the interaction between excitation light wave and SPW changes. This alternation causes the light wave’s characteristics to change, as well, which is expressed in its amplitude, phase or polarization.<sup>[60]</sup>

SPR is a powerful tool to analyze antigene-antibody reactions for environmental protection, health care and food control.<sup>[21],[60]</sup> The lower detection limits of SPR for different analytes with various sizes are summarized in Table 2.

**Table 2: Lower detection limit of different analyte concentrations determined by SPR.**

Detected analyte:	media	detection limit
Simazine herbicide	water	0.16 ng/mL <sup>[62]</sup>
Botulinum toxin	buffer	2.5 µg/mL <sup>[60]</sup>
Staphylococcus	milk	1-10 ng/mL <sup>[60]</sup>
Salmonella	aq. media	10 <sup>7</sup> cfu <sup>1</sup> /mL <sup>[63]</sup>

<sup>1</sup> cfu: colony forming unit – variable to measure bacteria numbers

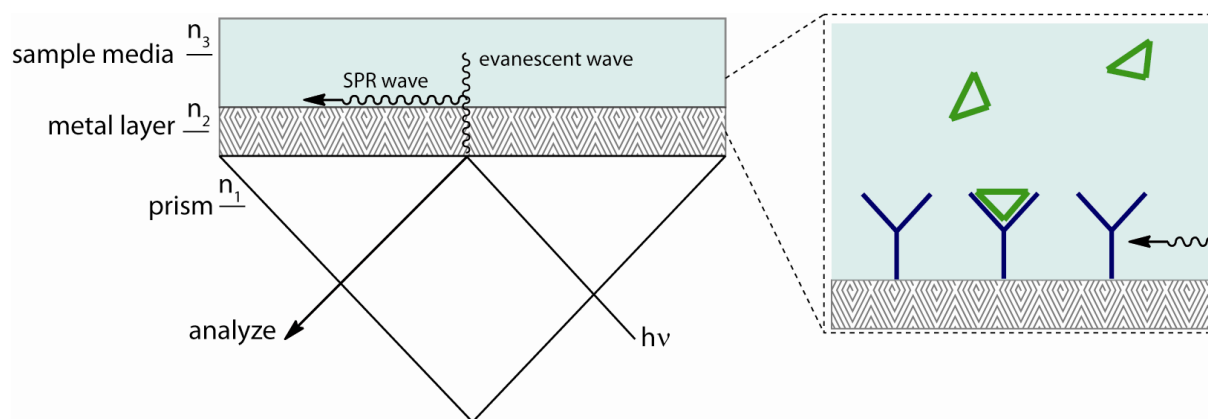


**Figure 8: Schematic sensing principle of a SPR device and zoom into an antibody-modified surface for immunoassay applications.**

SPR biosensors are widely applied on the biotechnological market for e.g. the quantitative detection of vitamins or the detection of process residues in food.<sup>[61]</sup> The two major advantages are that SPR sensors are non-invasive and that no anterior analyte labeling is necessary.<sup>[61]</sup> SPR type biosensors are commercially available on the market under different trade names, such as Biacore™ from GE Healthcare or Spreeta™ from Texas Instruments.<sup>[60]</sup>

#### 2.1.2.4 Quartz Crystal Microbalance

The working principle of a quartz crystal microbalance (QCM) is based on the measurement of a change in mass. The heart of QCM devices is a quartz crystal with piezoelectric properties. Piezoelectricity, disclosed by the Curie brothers 1880<sup>[64]</sup>, denotes the fact that when pressure is applied to certain crystals, they generate electrical voltage. Reciprocally, when placed in an electric field, these same crystals undergo a mechanical deformation. When an alternating current is applied to a quartz crystal, the mechanical conformation will be expressed as oscillation.<sup>[21]</sup> The natural resonance frequency of oscillation of each crystal, typically in the range of 10 MHz, changes during a QCM experiment when surface species absorb, adsorb or desorb. This phenomenon can be mathematically expressed by the Sauerbrey equation<sup>[65]</sup>:

$$\Delta f = -2.3 \cdot 10^6 f_0 \frac{\Delta m}{A}$$

**Eq. 2** with  $f_0$ : resonance frequency of the unperturbed resonator body;  $\Delta m$ : mass difference;  $A$ : sensing area; prefactor: combining the density of the quartz crystal and the shear modulus

An increase of the crystal mass due to the absorption of molecules at its surface results in lower resonance frequencies (and a loss of mass in a frequency increase). QCM devices operate with sensitivities down to 1000 Hz/ $\mu$ g and even 1 pg can be detected.<sup>[21],[65]</sup> They can

be applied for measurements in vacuum, gas as well as in liquid which is especially suitable for the analysis of biomolecules.<sup>[65]</sup> A practical set-up of a piezoelectric bioassay is schematically depicted in Figure 9. Before usage, a pure quartz crystal is coated with a bioactive layer including an analyte-specific receptor. Suitable microfluidic flow channels transport the analyte molecule to the QCM in order to know the exact amount of determined solution.

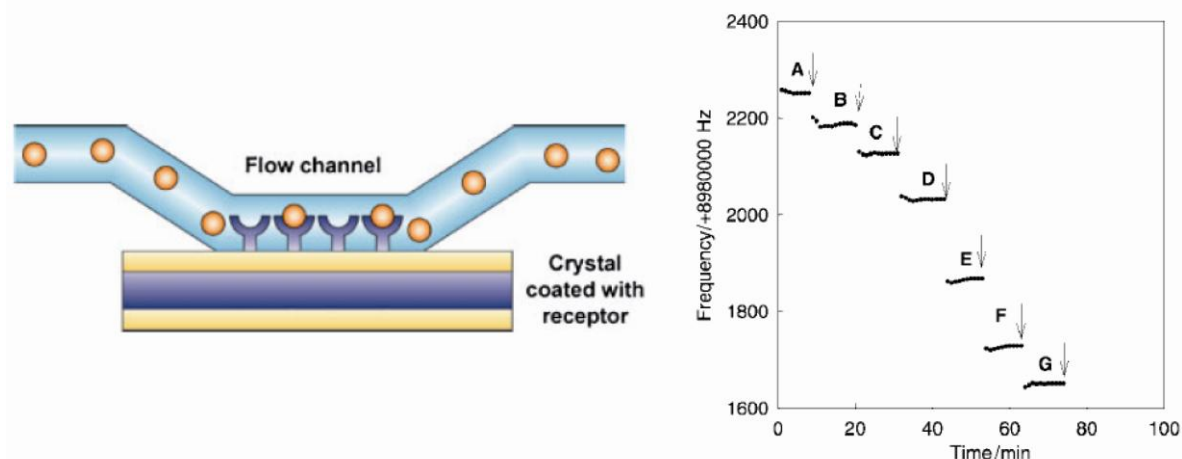


**Figure 9:** left: schematic design of a QCM (from <sup>[66]</sup>); right: observed frequency response over time of a phenytoin QCM sensor at increasing analyte concentrations from A to G. From <sup>[67]</sup>

Most studies are related to protein-protein interactions.<sup>[66]</sup> The first immunosensor was designed to investigate bovine serum albumin (BSA) on an anti-BSA functionalized quartz crystal.<sup>[68]</sup> Later, human serum albumin, an indicator for kidney failure of diabetes patients <sup>[69],[66]</sup>, thrombin, an important enzyme for blood coagulation <sup>[70]</sup>, and cholinesterase <sup>[71]</sup>, an enzyme involved in food metabolism have been successfully determined by QCM just to name a few. Apart from enzymes and proteins, viruses, bacteria, cells, but also small molecules (see Table 3) are the subject of research.<sup>[66]</sup>

**Table 3: Lower detection limit of different analyte concentrations determined by QCM.**

Detected analyte:	detection limit / $\mu$ M
Bisphenol A	0.01 <sup>[72]</sup>
Chloramphenicol (broad spectrum antibiotic)	10 <sup>[73]</sup>
Cocaine	$10^{-5}$ <sup>[74]</sup>
Diazepam (antidepressant) <sup>[66]</sup>	n.d.
Nandrolone (steoroid)	0.18 <sup>[75]</sup>
Niacinamide (vitamine)	$10^{-3}$ <sup>[67]</sup>

### 2.1.2.5 Other techniques

Techniques which are tailored for very specific analyte determinations or which require special sample preparation are briefly discussed to complete the overview of the various biosensor formats.

Optical devices that do not rely on total internal reflectance conditions are based on the direct detection of chemi-/ bioluminescence or fluorescence. One prominent example for bioluminescent assays is the substance group of luciferins, which react with the enzyme luciferase and indirectly provide information on several cofactors, such as ATP, FADH and FMN<sup>[21]</sup> but have also helped to determine small trinitrotoluene (TNT) concentrations.<sup>[76]</sup>

Thermometric sensors measure the heat generated during enzymatic recognition reactions, which are mostly exothermic with enthalpies between -20 and -100 kJ/mol.<sup>[46]</sup> Compared to the previously presented methods, the major disadvantage is their slow response.<sup>[77]</sup> The temperature is monitored by means of a thermistore in combination with a Wheatstone bridge. The resistance of the thermistore (a polymer, ceramic or metal)<sup>[78]</sup> changes strongly upon a temperature variation and is measured in the Wheatstone bridge, designed to determine an unknown resistance in a four-resistance circuit.<sup>[79]</sup> E.g. ethanol (reacting with alcohol oxidase), lactate (with lactate oxidase) and penicillin (with b-lactamase) have been detected biocalorimetrically.<sup>[46]</sup>

Finally, a very special biosensor application is the so-called ion channel switch (see Figure 10).<sup>[80],[24]</sup> On top of a gold electrode, ion channels (= pore forming proteins) are stabilized in a bilayer membrane and an applied flux of ions can be measured. The conductivity of the sensor membrane can be directly related to the surface concentration of conducting, dimeric assemblies of channel proteins. However, the tunnel proteins can be chemically modified with receptor molecules, so that a receptor-analyte interaction may cause the disintegration of a dimeric system and consequently changes the ion path and thereby the current.<sup>[81]</sup> Harding *et al.*<sup>[82]</sup> could for instance detect DNA by streaming single strand DNA molecules through a channel which had been functionalized with the complementary strands, leading thus to a DNA cross-linking and a blocking of the pores. More recently, the same experimental set-up as presented in Figure 10 was successfully applied for the detection of the influenza A virus.<sup>[83]</sup>

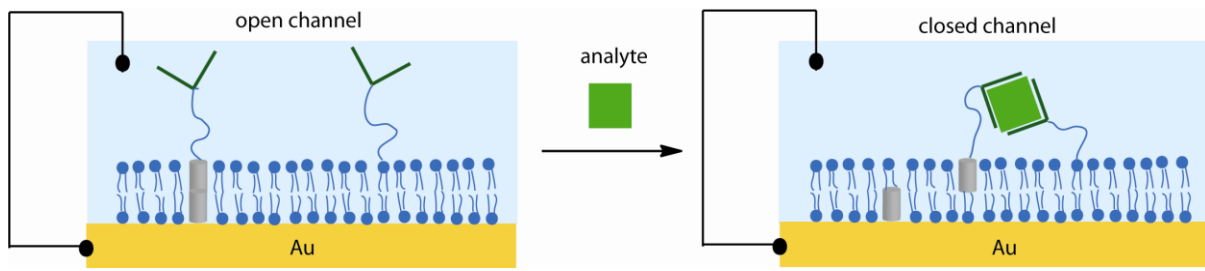


Figure 10: Mechanism of an ion channel switch biosensor; left: open channel allowing an electric circuit; right: closed gates upon addition of a receptor-binding analyte. <sup>[81]</sup>

### 2.1.3 Detailed insight in glucose biosensors

People with diabetes do not produce sufficient amount of insulin which results in a poor metabolism of carbohydrates and an abnormally high level of glucose in the blood. Therefore, patients need to permanently balance the carbon intake and the insulin injection in order to control the blood glucose concentration. Merely a short glance over the world maps <sup>[84]</sup> depicted in Figure 11 stresses the importance of diabetes research and enhancing the development of new treatments, therapeutics and testing devices: In the United States and Germany, the diabetes rate for the ages 20-79 will increase from 8-10% up to 10-14% in the next 14 years. In highly populated Brazil for example, rates from 10-14% will even culminate in estimated rates of 14-20%. Expenditures on diabetes amounts to 11.6% of the total health care investments which represents over three billion dollars spent on treatment and prevention in the year 2010. <sup>[85]</sup> To a certain extent, also the field of biosensor research has thereby gained great interest. With diabetes evolving into a widespread disease the need for modern, efficient and reliable test methods for insulin or blood sugar concentration has increased. In the next section a screening over scientific literature from the early glucose sensor devices to the latest innovations will be presented.

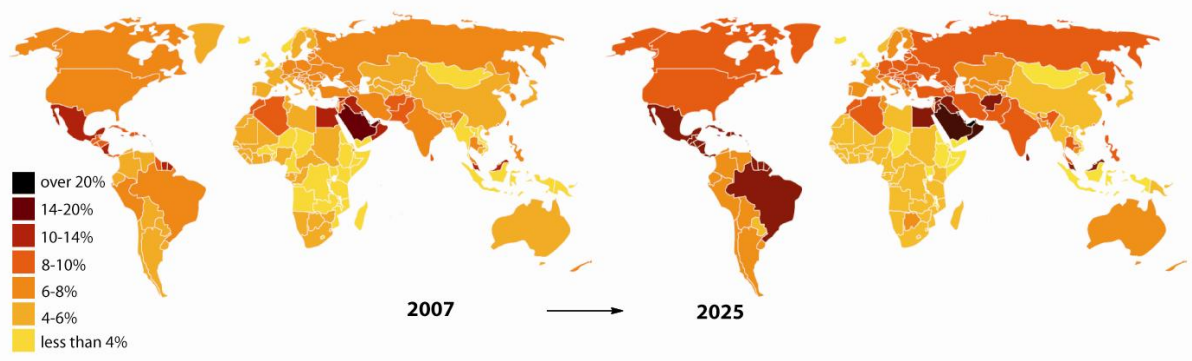


Figure 11: Prevalence estimates of diabetes comparing the proportions of 2007 and 2025. From <sup>[84]</sup>

### 2.1.3.1 General detection strategies for glucose

In the course of the past decades, biosensor design has been adjusted to the complex requirements, leading to the stepwise development of three generations of glucose sensors.

The **1<sup>st</sup> generation** glucose sensor is based on the enzymatically catalyzed reaction, in which molecular oxygen serves as oxidizing agent without the addition of any further reactant. This principle has already been applied in the Clark-type enzyme electrode described in chapter 2.1.2.1.<sup>[21]</sup> The simplicity of these 1<sup>st</sup> generation biosensors is advantageous but the fact that they depend on the bulk oxygen concentration is problematic because controlled and constant oxygen levels can be difficult to control. Furthermore, an increased risk of interferences in the range of the relatively high oxygen reduction potential has been observed.<sup>[28],[21]</sup> In order to overcome these problems, **2<sup>nd</sup> generation** biosensors replace oxygen by synthetic electron transfer molecules whose redox potentials have moderate values compared to oxygen. The most prominent agents are iron ions (free or complexed).<sup>[33],[34]</sup> However, the toxicity of most mediators have prevented this idea to be really turned into *in vivo* products.<sup>[86]</sup> The **3<sup>rd</sup> generation** has therefore been designed in which the enzyme is directly linked to nano-sized electrodes or into electrically conductive coatings.<sup>[86],[87]</sup>

Owing to the fact that uncountable reports on glucose sensing exist, only a few examples and their characteristics will be given for the three sensor generations and some other elected methods.

- 1<sup>st</sup> generation: Modeled on the Clark oxygen electrode, glucose could be quantified in a response time of less than 2 min and a sensor stability of more than 30 days.<sup>[21]</sup> Glucose oxidase is attached to the electrode with an oxygen permeable polypropylene membrane.<sup>[29]</sup>
- 2<sup>nd</sup> generation: Padeste *et al.* <sup>[32]</sup> have presented a method for the functionalizing of gold electrodes with both ferrocene-labeled avidin and biotin-labeled glucose oxidase counterparts. Different glucose concentrations starting from 10 mM could be monitored by chronoamperometry. Stability after storage of several days in buffer was claimed but not further investigated.

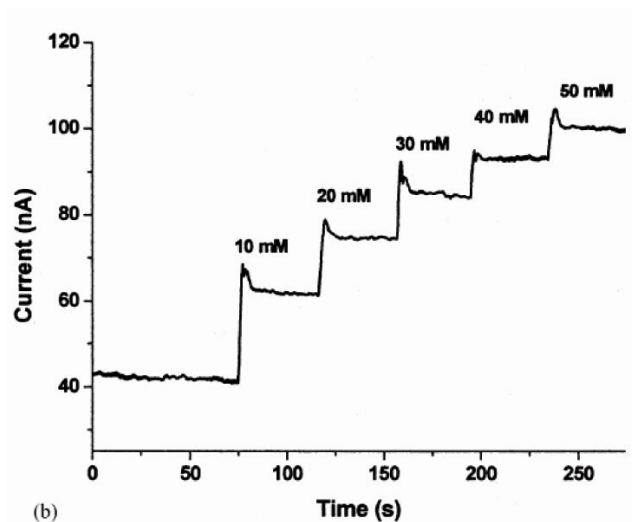
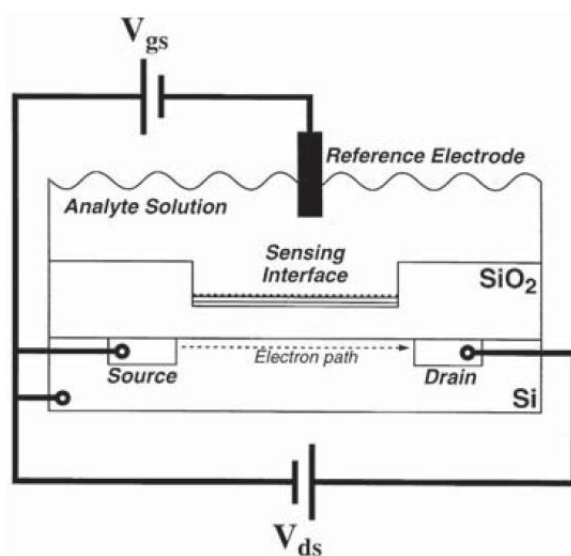


Figure 12: Determination of the cell current at 350 mV upon addition of glucose to glucose oxidase functionalized electrodes by Padeste *et al.* [32]

- 3<sup>rd</sup> generation: Both enzymes and mediators are wired to the electrode surface, for example embedded inside a swollen hydrogel network. [36] Heller *et al.* [35] used redox polyelectrolytes based on poly(4-vinyl pyridine), partially quaternized and coordinated to an osmium mediator complex. The hydrogel is weakly attached to the electrode enabling a high mobility inside the matrix and a good substrate and product diffusion. In order to efficiently determine the current, the rate of electron transfer from enzyme to the mediator has at least to equal the conversion rate for the substrate. Under sufficient enzyme concentrations a current down to  $10^{-13}$  A can be measured with a sensitivity of  $1 \text{ A cm}^{-2} \text{ mol}^{-1}$ . [35]
- Biosensor based on microorganisms: Instead of relatively expensive isolated and purified enzymes, entire microorganism can be immobilized on a transducer and used as bioreceptors. It is a cheaper and often more stable alternative but due to their complex cellular structure, the response time usually increases while selectivity suffers from a multitude of present enzymes. [21] Glucose could be detected electrochemically by the bacteria *pseudomonas fluorescens* which were embedded in a collagen membrane around a platinum electrode. [88]
- Carbon paste electrode: Although their first development by Adams *et al.* [89] dates back more than five decades carbon paste electrodes for glucose sensing are still popular for application and research. Glucose oxidase as bioreceptor is mixed with a paste consisting of a mineral oil, graphite powder, and optionally an additive, such as iron nanoparticles [90], nickel/poly(aminophenol) [91] or nickeloxide nanoparticles [92] in

order to enhance the charge transfer. The paste is filled in a sub-cm sized drill in a glass or plastic rod and contacted with a platinum wire.

- Field-effect transistors: For the detection of glucose with a FET set-up, the sensing interface, i.e. the gate, is functionalized with glucose oxidase. This can for instance be done by an aminopropyltriethoxysilane monolayer which is activated by glutaric dialdehyde for the coupling of biomolecules.<sup>[93]</sup> Reaction with glucose induces a change in charge at the gate surface which consequently affects the drain-source current (compare chapter 2.1.2.2). The detection limits as reported by Willner and Katz<sup>[93]</sup> lie in the range of  $10^{-5}$  M.



**Figure 13: Exemplary set-up for an enzyme-based FET for the detection of glucose with glucose oxidase covalently bond to the sensing interface via silane linker molecules. From<sup>[93]</sup>**

- Optical transducer: Glucose could be quantified on imaging fibers with a detection limit of 0.6 mM. The fibers were coated with glucose oxidase immobilized in poly(hydroxyethyl methacrylate) and the fluorescence was measured at varying oxygen concentrations.<sup>[94]</sup>
- QCM: Glucose binding enzymes were chemisorbed on a gold surface via their cysteine residues.<sup>[95]</sup> Owing to conformational changes in the protein after glucose binding, frequency changes could be detected although glucose single layers alone would have been predicted to be too small for QCM applications.
- Thermal measurement: Glucose oxidase was immobilized in a  $1 \times 3$  mm small porous column and sample volumes of around  $10 \mu\text{l}$  were passed through. Glucose can be measured in concentrations down to  $1 \mu\text{M}$ .<sup>[46]</sup>

Commercially available portable glucose monitors (PGMs) for diabetes patients are usually based on test stripes which are soaked in ca. 1  $\mu\text{L}$  of blood. The main underlying biological recognition reaction is again the oxidation of glucose by glucose oxidase to liberate hydrogen peroxide and can be either read-out colorimetrically or electrochemically.<sup>[17]</sup> A capillary on the test stripe, which contains the enzyme, guarantees constant quantities of analyte solution. A porous membrane prevents larger particles (e.g. blood cells) from entering the analyte cell; only blood plasma passes. The actual measurement is obtained by the generation of a dye on the test stripe by hydrogen peroxide in the colorimetric approach (the intensity of the color represents the glucose concentration). In the electrochemical design, the electrons produced by the reaction generate a current which can be translated into a concentration after calibration.<sup>[17]</sup>

### 2.1.3.2 Implantable sensors

So far, diabetes patients obtain their blood sugar concentration from pricking their fingers for a blood drop which then is to be analyzed externally in a PGM; This procedure is normally carried out three times a day.<sup>[17]</sup> Not only is this a painful procedure, it is also incapable of detecting irregular runaways from normal behavior and of giving an image of the person's blood level over a larger time span in order to derive from it the temporal habits and needs.<sup>[86]</sup> Therefore, it is of great interest to develop an implantable sensor for continuous monitoring.

So far, none of the 2<sup>nd</sup> generation glucose sensors have come to *in vivo* tests because there are concerns about a potential toxicity of the mediator.<sup>[86]</sup> However, there are some commercial products which allow the constant monitoring of glucose by an implantable sensor chip, usually located in the subcutaneous fatty tissue.<sup>[17]</sup> FreeStyle Navigator® from Abbot laboratories, for example, is based on the wired-enzyme system described by Heller *et al.*<sup>[36],[96]</sup> where glucose oxidase is immobilized in an electron-conducting hydrogel. Medtronic Minimed has launched a device under the name Guardian REAL time™ which gives a concentration value taken from the hypodermal fat tissue every five minutes and an alarm if necessary.<sup>[96]</sup> It has to be replaced after approximately six days due to stability issues. Glucose oxidase alone is surprisingly stable and maintains its activity at 0°C for 2 years.<sup>[21]</sup> *In vivo* test showed a sensor performance decrease after three months, only because of polymer membrane degradation rather than enzymatic failure.<sup>[97]</sup> However, when applied in blood serum - instead of in artificial laboratory aqueous solutions - the enzyme tends to interfere

also with compounds other than glucose, such as different sugars, tyrosine and ascorbic acid.<sup>[46]</sup>

The challenge of long-term stability has to be faced by finding the best combination of electrode material, soft interlayer and biomolecule loading. Therefore, efforts have been made in order to give a biological function to semiconductor and metal surfaces by functionalization with monolayers, coatings or polymer brushes.

## 2.2 (Bio)chemical functionalization of electrode materials

In the recent years, a lot of effort has been made in order to investigate suitable techniques for the coupling of biomolecules or DNA on metals or semiconductors. It is a crucial task to find a compromise between a straightforward and simple immobilization method on the one hand, and the guarantee for stability and activity of the biomolecule on the other hand since the adsorption/absorption of proteins is under certain conditions attended by conformational changes and inactivation.<sup>[98]</sup>

### 2.2.1 Biofunctionalized self-assembled monolayers

#### 2.2.1.1 Thiols on gold

Self-assembled monolayers (SAMs) provide a versatile platform in order to attach biomolecules onto metals, metal oxides and semiconductors.<sup>[99]</sup> Organosulfurs on gold definitely belong to the most widely characterized and applied systems since they form highly ordered and relatively stable films in a reproducible manner.<sup>[100],[101]</sup> Organosulfur compounds selectively coordinate to gold (binding energy around 130 kJ/mol<sup>[102]</sup>) which is the most extensively studied substrate, but there have also been reports on other substrates, such as silver<sup>[103]</sup>, copper<sup>[104]</sup>, platinum<sup>[105]</sup>, mercury<sup>[106]</sup> and GaAs.<sup>[107]</sup> Kinetic studies revealed that the SAM formation occurs in two steps: the first one is very fast, depends on the thiol concentration and leads to the formation of a preliminarily packed film, while in the second and slower step, the chains take up an ordered state by a surface crystallization process.<sup>[100]</sup> The choice of possible head groups (terminal functions) is very flexible, so that a great variety of differently tailored surface functionalities, such as hydrophilic, hydrophobic or protein-repellent can be prepared.<sup>[99],[108]</sup> Herein, the focus lies on functional groups which are designed for the coupling of biomolecules or DNA. A suitable spacer is 3-mercaptopropionic acid which represents the role of both the electrode modifier and the bridging molecule.<sup>[109]</sup> By using this approach, amino-termini of enzymes such as cytochrome c could be coupled to the carboxylic acid surface groups.<sup>[110]</sup> Besides amide bond formation, alternative coupling strategies are depicted in Figure 14. An appropriate distance between electrode and biomolecule is essential in order to avoid protein denaturation and to enable direct electron transfer from the bioreceptor to the electronic read-out system. If the transducer is not an electric one but for instance fluorescence-based, also longer spacers can be used. Microarrays

for the detection of lyme borreliosis disease could be designed by linking a respective antigene onto long carboxyl-terminated alkylethiols.<sup>[111]</sup>

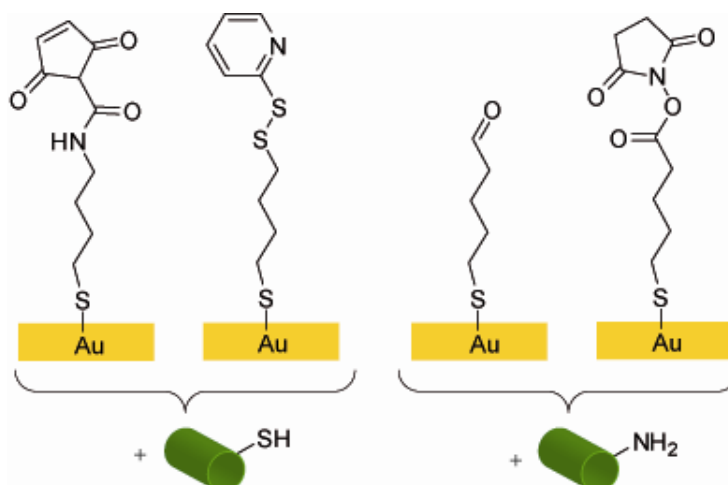


**Figure 14: Coupling of proteins to functional alkyl-thiols on gold via thiol or amine-moieties.**<sup>[109]</sup>

Conveniently, most bioreceptors themselves can be thiol-modified prior to immobilization. In the case of proteins, this can be easily done by chemically modifying lysine groups with thiols.<sup>[47]</sup> Therefore, enzyme or protein derivatives can be directly and selectively coupled to the gold electrode.<sup>[112]</sup> However, it might be necessary to use mixed monolayers in order to avoid sterical repulsion. For example Knoll *et al.*<sup>[113]</sup> have investigated the selective binding of streptavidin onto diluted monolayers of biotin-thiol derivatives by SPR.

### 2.2.1.2 Silane functionalization

Among the most popular surfactant molecules to form silane SAMs are alkoxy-silanes and alkyltrichlorosilanes. Alkylsilane SAMs have been extensively studied on silicon dioxide surfaces in the perspective of applications in the semiconductor technology.<sup>[114]</sup> In principle, this surface coating approach is very straightforward; a high variety of functional silanes is available and if prepared properly, the resulting monolayers are very robust. However, it is challenging to form homogeneous and high quality silane SAMs because a controlled amount of water is needed during the silanization reaction.<sup>[115]</sup> Since a siliconoxide surface is hydrated under standard conditions, the thin water film leads to the hydrolyzation of the trichlorosilanes or the alkoxy-silanes in the very proximity of the surface and subsequently to the coordination of the hydrolyzation product to surface silanols via hydrogen bonds. This step is followed by the elimination of water resulting in a network of cross-linked chains

covalently attached to the surface (Figure 15).<sup>[116]</sup> Yet, if the amount of water during silanization is too high, aggregates will form and hinder a smooth absorption layer.<sup>[117]</sup>

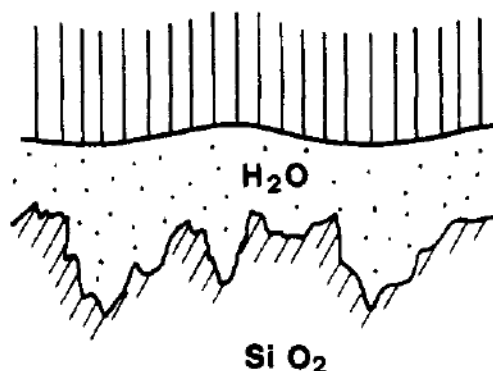


Figure 15: Concept of silane deposition on a silica surface according to Silberzan *et al.* ; formation of an intercalated water film between the silane network and the surface; image from <sup>[116]</sup>.

Silane SAMs are of considerable importance for the development of biofunctionalized glass slides for e.g. biological microarrays in substance screening or diagnostic biomarker discovery.<sup>[114]</sup> A widely used approach is the silanization with amine-terminated chloro- or alkoxy silanes (such as aminopropyltriethoxysilane - APTES) and subsequent coupling of a biomolecule via its carboxy terminus or by means of short linker molecules, such as glutaric dialdehyde or succinic anhydride.<sup>[118],[119]</sup> The successful coupling of enzymes - the criteria being the maintenance of their native activities tested with amperometry or fluorescence - could be shown by different research groups for e.g. glucose oxidase <sup>[120]</sup>, horseradish peroxidase <sup>[119],[121]</sup> and acetylcholine esterase <sup>[122]</sup> to name just some of them. Compared to the “thiols on gold” approach, a clear advantage of “silanes on siliconoxide” is its unlimited use for fluorescence-based transducers because quenching effects are avoided.<sup>[114]</sup>

### 2.2.1.3 Diazonium salts

In first studies, monolayers of phenyl or biphenyl diazonium salts were grafted in an electrochemical process. But in order to overcome unwanted multilayer formation <sup>[123],[124]</sup>, an alternative approach via spontaneous grafting has modernized the electrochemical functionalization. Spontaneous grafting of diazonium salts can be conducted on various substrates such as H-terminated Si, GaAs, Pd <sup>[125]</sup>, diamond <sup>[126]</sup> and Cu <sup>[127]</sup>. The suggested reaction mechanism (Figure 16) is based on a spontaneous electron transfer between the substrate and the diazonium species resulting in an intermediate surface radical which is eventually saturated by the phenyl radical after nitrogen elimination.<sup>[125],[128]</sup>

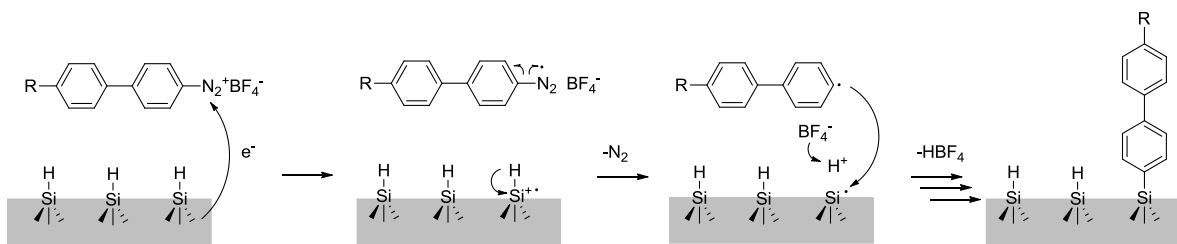


Figure 16: Reaction of (bi)phenyl diazonium salts with H-terminated SiO<sub>x</sub>; adapted from <sup>[125]</sup>

According to results from the work of Gerhard Richter <sup>[129]</sup>, either the organic synthesis of the diazonium species limits the access to certain functional groups or the reactivity of phenyl-bond moieties (such as phenyl-NH<sub>2</sub>) towards further conversion is insufficient. Nevertheless, our group has reported on the successful formation of conjugates of thiolmonophenyls on diamond with both a fluorescent-labeled amino acid and yeast cytochrome c protein via disulfide bridges. <sup>[130]</sup> In order to convert the initially generated phenylsulfonic acid monolayers into a reactive thiol derivative, the surface was irradiated with X-rays or electrons inducing the reduction and a simultaneous cross-linking reaction. Conveniently, this approach involves facile patterning of the biofunctionalized surface. Another way of using the diazonium approach for biofunctionalization has been presented by Limosges *et al.* <sup>[131]</sup> who linked alkyne-labeled biotin to a phenylazide.

#### 2.2.1.4 Other monolayer approaches

Another well-established method for the preparation of functional coatings is the hydrosilylation of alkenes or alkynes onto hydrogen-terminated silicon. <sup>[132],[133],[134],[135]</sup> The proposed mechanism involves the insertion of an unsaturated group into a Si-H bond via radical intermediates which are either created through addition of a radical initiator <sup>[136]</sup>, or thermal <sup>[137],[135]</sup> and photochemical homolytic cleavage of surface Si-H <sup>[138]</sup>. Monolayers in a large variety of functional head groups could be prepared, e.g. nitrile- <sup>[139]</sup>, hydroxyl-, methoxy, and carboxy-alkyls <sup>[134]</sup> or perfluorinated alkyls. <sup>[140]</sup> The groups of Kessler and Stutzmann <sup>[141]</sup> demonstrated the biological functionalization of silicon by thermal hydrosilylation of a vinyl-terminated arginine-glycine-aspartic acid (RGD) peptide. A similar surface functionalization can be achieved with terminal alkenes on diamond; the underlying mechanism however is completely different and will be the subject in chapter 2.3.3.2. <sup>[142],[143],[144]</sup> Stutzmann, Garrido and co-workers <sup>[13]</sup> could thereby demonstrate that enzymes can be coupled to a diamond electrode without losing their native functionality.

Apart from premodifying the surface platform with SAMs, there is also the possibility to directly link enzymes to metals and electrodes. One example is the oxidation of carbon electrodes resulting in a carboxyl-group surface termination which can be converted by carbodiimide activation to a reactive group for protein coupling.<sup>[145]</sup> Direct immobilization of biomolecules on flat and rigid surfaces, however, potentially causes denaturation of proteins. Three-dimensional scaffolds, such as coatings, polymer brushes or other soft interlayers resemble much more the real biological environment and are therefore favorable for applications where reliable enzyme activity and long-term stability are required.<sup>[98],[146]</sup>

### 2.2.2 Coatings

In contrast to coupling biomolecules via short linker molecules which allow electron tunneling to a certain extent, thicker layers require an electrically conductive matrix if the system is applied as an electrochemical biosensor in order to ensure unhindered signal transduction. A synthetically easy technique is the coating of electrodes with a carbon paste containing the redox protein.<sup>[37]</sup> Yoshikawa *et al.*<sup>[147]</sup> have reported on the preparation of a bioactive layer combining horseradish peroxidase (HRP), ferrocene and carbon powder blended in paraffin liquid. Via an enzyme catalytic cycle, they were able to detect glucose and cholesterol (reaction of HRP with in situ generated hydrogen peroxide) by chronoamperometry.

In order to increase the stability of the film, functional polymers can be used instead of pastes. Thiolated gold electrodes modified with a poly(allylamine) redox polymer were used by Calvo *et al.*<sup>[148]</sup> for the immobilization of anti-biotin IgG. After conjugation with HRP their system was analyzed electrochemically and by QCM. The polymer (Figure 17 a) was redox labeled with an Osmium-bipyridyl redox complex (often used as mediator)<sup>[149]</sup>, but the antibody was merely loaded by physisorption. However, using suitable polymers, the enzymes can also be bonded covalently which is claimed to improve the sensor performance.<sup>[45]</sup> Şenel *et al.*<sup>[45]</sup> have demonstrated that on a glassy carbon electrode (GCE) modified with a poly(glycidylmethacrylate-co-vinylferrocene) film (Figure 17 b) in which HRP was coupled via the glycidyl moiety, a clear response to hydrogen peroxide could be shown in chronoamperometry. However, the authors did not provide a reference test for HRP or ferrocene free electrodes in order to exclude non-enzymatic side reaction of hydrogen peroxide with ferrocene.

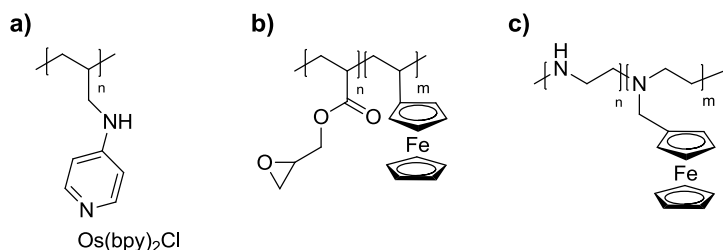


**Figure 17: Examples of polymeric coatings used as interlayer in order to immobilize biomolecules for sensing applications; a) poly(vinylpyridine)-(osmium redox polymer) <sup>[149]</sup>; b) poly(glycidylmethacrylate-co-vinylferrocene) <sup>[45]</sup>; c) ferrocene-modified poly(ethyleneimine). <sup>[150]</sup>**

The last polymer example in Figure 17 c shows a linear ferrocene-modified poly(ethyleneimine) (PEI) coating on a GCE prepared by Schmidtke *et al.* <sup>[151],[150]</sup> Linear PEI was synthesized by the hydrolysis of poly(2-ethyl-2-oxazoline). After acid hydrolysis, the amine functionalities reacted with ferrocenecarboxaldehyde resulting in a ratio of ferrocene to non-ferrocene modified units of around 1:5. <sup>[150]</sup> The activity of the cross-linked glucose oxidase towards glucose conversion was demonstrated by amperometry. Apart from the above named examples, various other polymer coatings have been used in microarray chips, such as porous poly(vinylidene fluoride) <sup>[152]</sup>, nitrocellulose <sup>[153]</sup> or acrylamide. <sup>[154]</sup>

### 2.2.3 Polymer brush - biomolecule conjugates

In recent years, polymer brushes have come into focus for their application in the biomedical sector. Research fields such as protein-resistant and cell-repellant surfaces <sup>[155],[156],[157]</sup>, pH sensitive substrates for reversible protein adsorption chromatography <sup>[158],[159],[160]</sup>, medical implants <sup>[161]</sup> and biosensors <sup>[155],[162],[163],[164],[165],[166]</sup> usually rely on surface functionalization with polymer brushes. Polymer brushes bridge the gap between ultra-thin self-assembled monolayers on the one hand and adsorbed polymer coatings on the other hand. <sup>[167]</sup> Due to the 3D scaffold, swollen polymer brushes allow an access to the binding sites, show a higher loading capacity towards biomolecules and tend to stabilize these delicate compounds better than two dimensional structures. <sup>[98],[168],[162]</sup> Thus, proteins/enzymes can maintain their native conformation, selectivity and enzymatic activity. Moskovitz and Srebnik even state that “*the grafted polymer layer allows for immobilization up to three lattice units closer to the surface, before protein denatures*”. <sup>[98]</sup> The requirements for stabilization effects are considered to be oriented immobilization, hydrophilic groups, protein crowding/embedding in a matrix. <sup>[98]</sup>

Compared to spin-casted systems, polymer brushes can be prepared in a more controlled way, resulting in a defined layer thickness which eases the diffusion of biomolecules towards the inner part of the polymer interlayer. For electrochemical sensing applications, one of the major challenges in case of a three-dimensional polymer brush approach for the incorporation of biomolecules (instead of the attachment to monolayers), is the transduction of an electrochemical signal into the electrode material. Since the distance between bioreceptor and read-out usually exceeds the range of natural tunneling processes, the transduction needs to be supported by charge-transfer agents, also referred to as mediators. Figure 18 provides a schematic illustration comparing monolayer and polymer brush binding approaches for enzymes and takes into account multiple bioreceptor loading and transduction challenges. Although there is no definite limit for a maximum distance between bioreceptor and electrode at which non-mediated electron transfer can still occur, some research groups provide information on the approximate dimensions. Accordingly, distances of 4-5 nm from the electrode still provide a sufficient signal for read-out.<sup>[169],[170]</sup> However, the direct electron transfer slows down with increasing distance between the enzyme and the electrode surface.<sup>[169],[171]</sup> Moreover, electron transfer rates depend strongly on the ionic strength, pH, and temperature of the solution and in case of some proteins, e.g. cytochrome c, on their orientation.<sup>[172],[173]</sup>

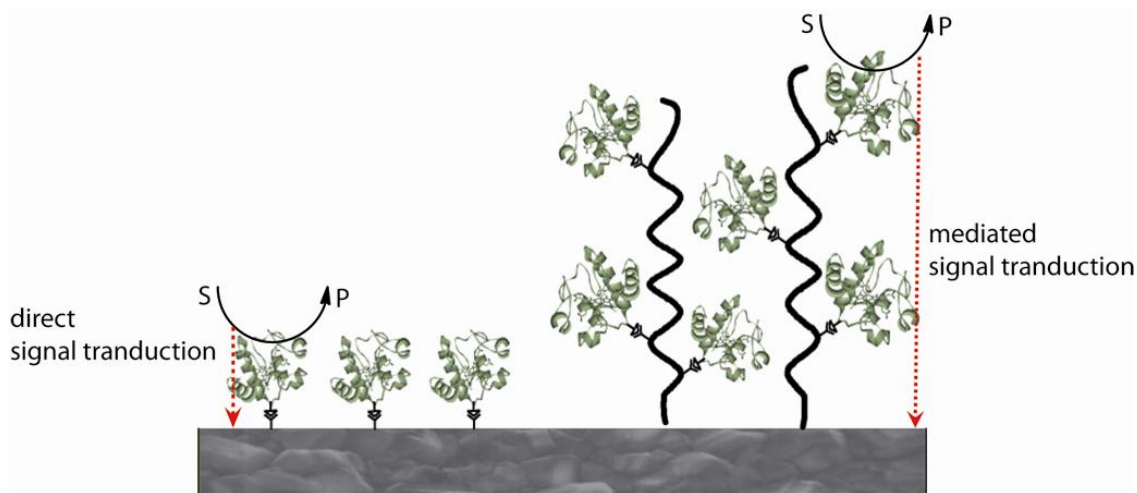


**Figure 18: Scheme of a monolayer or polymer brushes as platform for the immobilization of biomolecules.**

### 2.2.3.1 General remarks on polymer brushes

Before giving an insight in the state of the art of the synthesis of polymer brush-biomolecule conjugates, a short introduction in general polymer brush chemistry and properties will be

provided in this chapter. Although surface coatings in general date back thousands of years and modern coating technologies form part of a highly developed industry, the term “polymer brush” itself, describing “*polymers attached by one end to an interface at relatively high coverage*”<sup>[174]</sup>, is relatively new. It has been subject to publications since the mid 1980’s only.<sup>[175],[176],[177]</sup> In order to avoid repulsive interaction through overlapping, dense polymer brushes stretch away from the surface, unlike so-called polymer “mushrooms” which are present at very low grafting densities and behave similar to free coils in solution.<sup>[175]</sup>

Obviously, the resulting brush conformation depends strongly on the surrounding media. In a good solvent for the polymer, the brush height is related to the chain length and the grafting density according to  $h \approx N\sigma^{1/3}$ , in a bad solvent according to  $h \approx N\sigma$ <sup>[178]</sup> or  $h \approx N\sigma^{1/2}$ .<sup>[175]</sup>

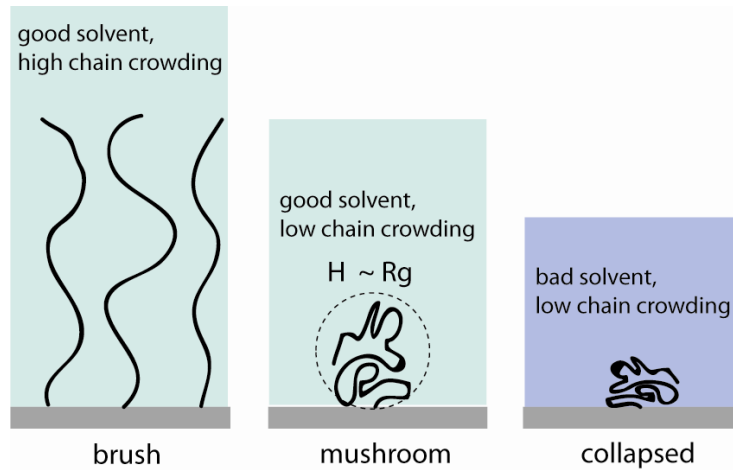


**Figure 19: Polymer brush, mushroom and collapsed coil at different external conditions.**

Another important feature is the height of collapsed polymer brushes without solvent since a lot of analytical methods are operated in dryness (see Eq. 3).<sup>[179]</sup>

$$h_d = \frac{M_n \sigma}{\rho N_{av}}$$

**Eq. 3** with  $M_n$ : average molecular weight;  $\sigma$ : grafting density;  $\rho$ : bulk density of the polymer;  $N_{av}$ : Avogadro constant

From a theoretical point of view, the energetic situation of a polymer chain can be described by the interplay of the interaction energy ( $E_{int}$ , lowered upon chain stretching) and the elastic free energy ( $E_{el}$ , increased upon stretching due to entropy loss) per chain: <sup>[180]</sup>  $E = E_{int} + E_{el}$

Depending on the application area, polymer brushes can be differentiated by various criteria; whether they 1) are physisorbed or chemisorbed onto the surface, 2) attached to a flat surfaces, to micelles or to boundary layers, such as air-liquid interfaces, 3) built up as

homopolymer or copolymer brush, 4) neutral or charged, 5) show rigid, flexible, semiflexible or liquid crystalline behavior, etc.<sup>[180]</sup>

Polymer brushes can be prepared by various synthetic strategies which can generally be classified into “grafting-onto” and “grafting-from” approaches.<sup>[175]</sup> The grafting onto approach is based on polymer chains which are synthesized in bulk and which contain functional end groups for a subsequent grafting. One advantage is that analytical methods for bulk polymers, such as GPC or NMR can be applied prior to use. However, due to chain crowding, the maximum grafting density is limited and results in relatively thin polymer brush layers. In order to overcome this drawback, initiator molecules can be anchored to the surface and the polymer chain is formed by surface-initiated polymerization from the surface. This approach is referred to as “grafting-from”. In contrast to the hindered mobility of entire polymer coils, the diffusion of monomer molecules is facilitated and consequently, the grafting-from methods results in higher grafting densities.<sup>[175]</sup> Among these methods are surface-initiated cationic, anionic, ring-opening, controlled radical and free radical polymerizations. A few examples demonstrating the wide range of possible initiator-SAMs are depicted in Figure 20.

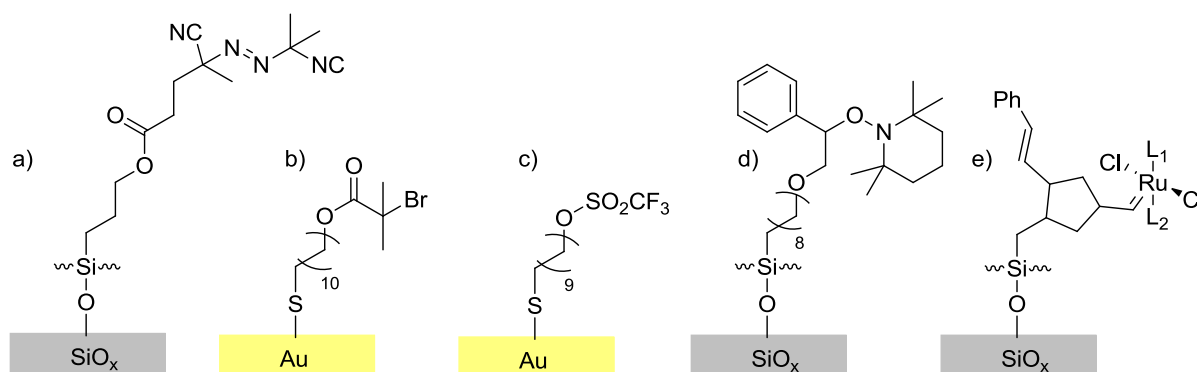


**Figure 20:** Selection of surface-tethered initiators; surface-initiated a) free radical <sup>[181]</sup>, b) atom-transfer radical <sup>[182]</sup>, c) cationic <sup>[183]</sup>, d) nitroxide-mediated radical <sup>[184]</sup> and e) ring-opening metathesis polymerization. <sup>[185]</sup>

### 2.2.3.2 Polyelectrolytes as matrix for biomolecules

Polyelectrolyte brushes are charged polymer chains at a sufficiently high grafting density so that they are stretched away from the surface due to segment-segment and electrostatic repulsion.<sup>[186]</sup> Charged polymer brushes exhibit different behaviors depending on parameters like grafting density, degree of counterion dissociation, size or ionic strength. All together lead to the three defined situations being the osmotic regime, the ‘Pincus’ regime and the salt

brush.<sup>[187]</sup> In the osmotic regime, all counterions are conserved inside the brush which implies a quasi electron neutrality. The osmotic pressure forces the chains to stretch away from the surface, independently on the grafting density (see Eq. 4 a).<sup>[180]</sup> The ‘Pincus’ regime describes the extension of the mobile counterion cloud into a wider proximity around the actual brush length. Here, the brush height does depend on the grafting density according to Eq. 4b.<sup>[187],[188]</sup> When salt is added in a concentration exceeding the concentration of counterions inside the brushes, the osmotic pressure is reduced and the brush height is now affected by both grafting density and salt concentration (Eq. 4 c).<sup>[180],[188]</sup>

As far as the type of polymer is concerned, one has to discriminate between polyanions or polycations, weak or strong polyelectrolytes. In weak electrolytes, an equilibrium exists between undissociated and dissociated counterions, whereas in strong electrolytes the position of the charges on the chain remains unchanged.<sup>[187]</sup>

$$\text{a) } L_{OS} = N \cdot a \cdot f^{1/2} \text{ (osmotic regime)}$$

$$\text{b) } L_P = N^3 \cdot a \cdot f^2 \cdot \sigma \text{ ('Pincus' regime)}$$

$$\text{c) } L_{Salt} = N \cdot f^{2/3} \cdot a \cdot c_s^{-1/3} \cdot \sigma^{1/3} \text{ (salted brush)}$$

**Eq. 4** L: height of the swollen brush; N: chain length / number of monomer units; a: diameter of monomer unit; f: degree of dissociation;  $\sigma$ : grafting density; c: salt concentration

A popular class of polyelectrolyte brushes is ionic poly(acrylic acid) (P(AA)) or methacrylic acid P(MA) which are classified as weak cationic exchangers.<sup>[189],[190],[191]</sup> It was discovered that P(AA) shows exceptional protein affinity at low ionic strength but repellent properties at high molarities. This property can be used for switching the layer properties by the variation of external conditions. Ulbricht *et al.*<sup>[190]</sup> have demonstrated this responsive behavior in a P(AA) column which they alternately loaded and unloaded with lysozyme. An interesting comparison has been drawn by Czelik *et al.*<sup>[189]</sup> in order to show the advantages of polyelectrolyte coupling over direct enzyme immobilization: accordingly, HRP shows an enzymatic activity of more than one order of magnitude higher in the polymer matrix than on a bare silica surface. Other polyelectrolytes which have been applied as biological interlayer are sulfonated poly(styrene) as pH and humidity sensor<sup>[192]</sup> or for the embedding of GFP-type proteins<sup>[193]</sup>, quaternized poly(*N,N*-dimethylaminoethyl methacrylate) joined with lysozyme and pepsin<sup>[194]</sup>, poly(allylamine) with polyphenol oxidase<sup>[195]</sup>, and quaternized poly(4-vinyl pyridine) (P4VP) cross-linked with cholesterol.<sup>[196]</sup> In addition, another very interesting application of quaternized P4VP has been presented by Katz *et al.*<sup>[165]</sup> who induced the switching of an electrode reaction of glucose oxidase with glucose not only by external

changes in ionic strength but also by an in-situ bioelectrocatalytic process. Therefore, the enzymes esterase and urease were added to the electrolytic cell and caused a reaction-induced change in pH leading to the swelling or collapse of P4VP.<sup>[197]</sup>

Closest to biological applications are obviously natural or protein-like polyelectrolytes, as shown in Figure 21.<sup>[198]</sup> Voegel *et al.*<sup>[199]</sup> investigated the adsorption and desorption of human serum albumin onto poly(L-lysine) or poly(glutamic acid) at different pH values. Polyelectrolytes have come into focus for applications such as immunoassays or in so-called tentacle-type ion exchangers for protein purification where switching or loading and unloading are desired processes.<sup>[200],[201]</sup> However, in the perspective of immobilizing biomolecules for long-term biosensor applications, it might be necessary to ensure site-specific binding or the formation of more stable conjugates as in the case of covalent bonds.

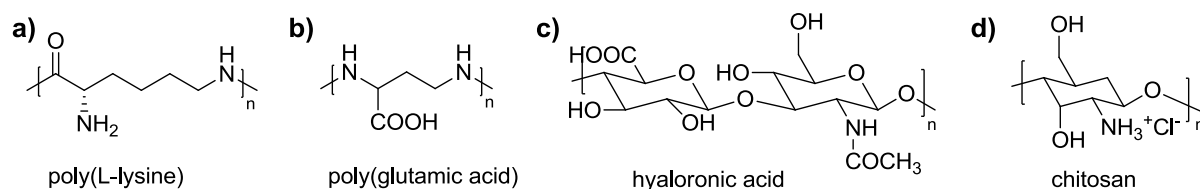


**Figure 21: Natural polyelectrolytes; poly(amino acid)s: a) poly(L-lysine), b) poly(glutamic acid); poly(sugar)s: c) hyaluronic acid, d) chitosan.**<sup>[198]</sup>

### 2.2.3.3 Covalently bonded biomolecules

In recent years, there have been a great number of reports on biomolecules covalently bonded to surface anchored polymers. The following polymer properties are considered to be crucial for the successful interplay between matrix and biomolecule: polymer-protein interactions, stiffness, brush length and grafting density.<sup>[98]</sup> Therefore, controlled radical polymerization techniques, such as atom transfer radical polymerization (ATRP), have gained special interest because they allow a well-defined tailoring of the polymer brushes. Table 4 gives an overview of the most recent strategies for the biofunctionalization of polymer brushes and subsequent characterization.

**Table 4: Synthetic strategies and respective characterization techniques for the covalent coupling of biomolecules to polymer brushes.**

Polymer brush system	coupling strategy	biomolecule	characterization	
Poly(glycidyl methacrylate-co-2-(diethylamino)ethyl methacrylate) via ATRP on Ta <sub>2</sub> O <sub>5</sub>	epoxide opening	bovine serum albumin (BSA)	fluorescence, QCM	[202]
Poly(2-hydroxyethyl methacrylate) via ATRP on glass	<i>p</i> -nitrophenyl chloroformate followed by NTA complexation	acyl carrier protein and others	fluorescence, XPS	[164]
Poly(2-(methacryloyloxy)ethyl succinate) via ATRP on gold	carboxyl activation (NHS/EDC)	BSA	ellipsometry	[203]
Poly(2-vinyl-4,4-dimethyl azlactone) via ATRP on SiO <sub>x</sub>	azolactone ring opening	Glucose oxidase, RNase and others	ellipsometry	[146]
Poly(acrylic acid) via ATRP on SiO <sub>x</sub>	carboxyl activation (NHS/EDC) or NTA-Cu	RNase	ellipsometry, XPS, NEXAFS,	[204]
“_“	“_“	BSA, myoglobin, anti-IgG	ellipsometry, FT-IR, protein assays	[205]
“_“	carboxyl activation (NHS/EDC)	BSA-biotin	fluorescence, XPS	[206]
Poly(acrylic acid) membrane	carboxyl activation (NHS/EDC)	antibodies IgG from rabbit, rat, mouse	fluorescence	[207]
Poly(oligo(ethylene glycol) methacrylate) via ATRP in gold	various hydroxyl group activations	streptavidin	FT-IR, XPS, fluorescence, SPR	[155]

Polymer brushes bearing carboxylic acid or epoxide groups are particularly suitable because they can readily be biofunctionalized.<sup>[162]</sup> Amongst the most common coupling strategies are activation by a carbodiimide in the presence of *N*-hydroxysuccinimide (NHS) to form a reactive NHS-ester intermediate and metal-ion affinity binding, usually with a nitrilotriacetic acid-Cu<sup>2+</sup> complexation agent (NTA) reacting with histidine-tagged proteins.<sup>[162],[198]</sup> For real biotechnological applications the system poly(dimethylsiloxane)-grafted poly(methacrylic acid) (PDMS-g-PMA) has already been proven functional (biosensors and lab on a chip fabrication). Hydrophilic P(MA) compensates for the hydrophobicity of PDMS at still low cost and easy fabrication, durability, low Young's modulus, biocompatibility and optical transparency.<sup>[162]</sup>

#### 2.2.3.4 Biological aspects of poly(2-oxazoline)-based molecular brushes

Poly(2-oxazoline)s (POx) are well-known and thoroughly investigated due to their thermoresponsive behavior at very variably temperatures depending on their composition and chain length.<sup>[208],[209],[210]</sup> Recently, they have come into focus as a potential alternative to the well established PEG systems for the preparation of biocompatible surface coatings.<sup>[211],[212],[213],[214],[215]</sup> Although a significant number of biomedical applications for poly(2-oxazoline)s have been summarized by Adams and Schubert<sup>[211]</sup>, there are very few reports on the use of this polymer class for biosensing in particular. Poly(2-oxazoline)s have predominately covered the fields of biomembrane design<sup>[216],[217],[218],[219]</sup>, antimicrobial surfaces<sup>[220],[221]</sup> and drug-delivery<sup>[212, 214],[222]</sup>. It has been shown that POx is non-toxic and that proteins as well as drugs can be coupled to the polymer without losing their activity.<sup>[211-212, 214, 223],[224]</sup> As depicted in Figure 22a, one exemplary result by our group demonstrates the compatibility of pharmaceuticals encapsulated by micellar poly(2-oxazoline) structures with living organisms.<sup>[222]</sup> POx show great variability due to possible terminal as well as pendant functionalization.<sup>[208],[225],[226],[227],[228]</sup> Recently, we have shown that homogeneous and stable poly(2-isopropenyl-2-oxazoline) (PIPOx) brushes can be prepared by the SIPGP of 2-isopropenyl-2-oxazoline (IPOx) on various substrates, such as diamond, glassy carbon and silicon.<sup>[229]</sup> The pendant oxazoline moieties of the PIPOx brushes were converted to so-called bottle-brush brushes (BBBs) in a consecutive living cationic ring-opening polymerization (LCROP) with different 2-alkyl-2-oxazoline monomers. Such bottle-brush structures have gained interest in the design of functional polymers with tailor-made architectures. As they are related to the structure of glycosylated macromolecules located on nearly every living cell<sup>[230],[231]</sup>, bottle-brush polymers have biocompatible and biomimetical potential. According to results from our group, non-specific protein and cell adsorption could be influenced by the use of different BBB side chain configuration.<sup>[232]</sup> It was found that biological systems show high affinity for *n*-propyl-2-oxazoline side chains whereas 2-methyl- or 2-ethyl-oxazoline has clear anti-fouling properties (see Figure 22 b).

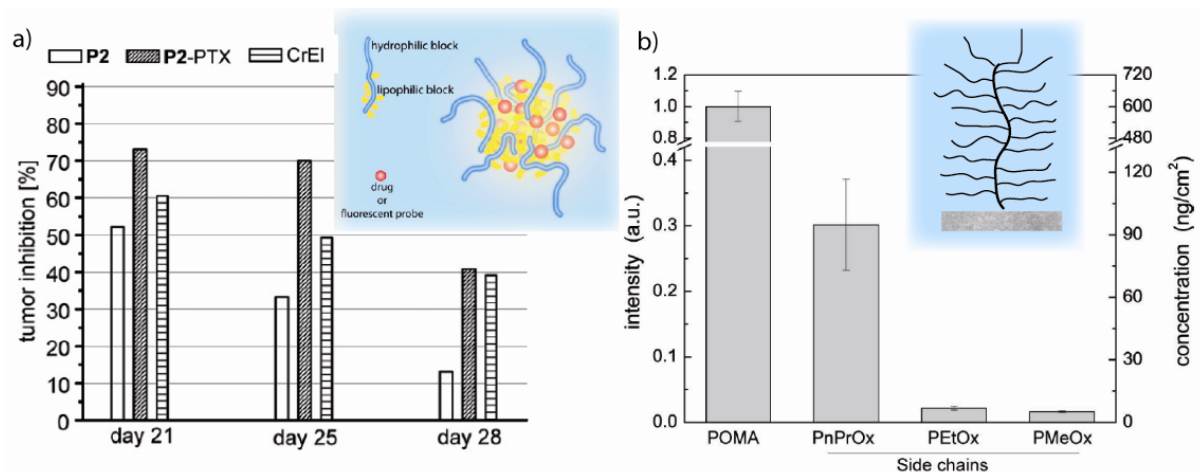


**Figure 22: Examples for POx in biological applications; a) Drug loaded POx-based micelles (P2-PTX) with butyl-oxazoline and methyl-oxazoline building blocks and their calculated tumor inhibition compared to a commercial product (CrEI) and plain POx (P2) <sup>[222]</sup>; b) POx-based bottle-brush brushes with different side chains and their respective behavior for protein adsorption and repellence. <sup>[232]</sup>**

The complex 3D architecture of BBBs qualifies for the application in the biomedical field as responsive polymers in solution,<sup>[233]</sup> or for surface modifications in order to obtain better friction properties, less non-specific binding of proteins and biocompatibility.<sup>[234],[235],[236],[237]</sup> In the literature, one mainly comes across bottle-brushes based on poly(methacrylic acid) and PEG derivatives, whereas only little emanates from 2-oxazolines.<sup>[229, 238]</sup> Furthermore, most reports imply the surface attachment of bottle-brush polymers via electrostatic and ionic adsorption only. However, for tailoring the interface between a semiconductor and a biological environment for biosensor applications, a stable covalent bond between the polymer strand and the surface is desirable.

#### 2.2.3.5 Preparation of micro-and nanostructured polymer brushes

Often, functional polymer interfaces on semiconductors or metals need to be patterned in the micro- or even nanometer scale for specific fields of applications, such as data storage chips, miniaturized transistors, photonic crystals or arrays for diagnostics and substance screening.<sup>[239]</sup> While some of the structuring techniques require a photolithography step along the process (e.g. microcontact printing or nanoshaving), others refrain from that extra step and directly lead to well-defined polymer structures (e.g. nanoshaving or electron-beam lithography). From both categories, the most commonly used methods will be presented in the following.

**Photolithography (PL)** is the most widely used technique for micro- and to some extent nanofabrication and is well-adapted for microelectronic processing.<sup>[51]</sup> Typically, a positive or

negative photoresist coated surface is partially exposed to UV light through a mask which results, after a development step in a suitable solvent, in either positive or negative surface patterns.<sup>[240]</sup> By common PL, feature sizes in the sub-50 nm range can be achieved in highly-advanced industrial processes.<sup>[240]</sup> However, due to light diffraction, the spatial resolution of the structures is limited to half the wavelength of the applied light.<sup>[241]</sup> Better resolution can be achieved by irradiation at short wavelength (157 nm).<sup>[242],[243]</sup> Structured polymer brushes have been generated by functionalizing photoresist-free areas after the first development step with initiators for surface-initiated polymerization (SIP).<sup>[241]</sup> For initiator-free polymerization approaches, PL can simply help selectively terminating e.g. silicon or diamond surfaces in oxygen- or hydrogen plasma. This has been successfully shown by our group who generated structured poly(styrene) grafts by SIPGP selectively on oxidized diamond, while the hydrogenated areas remained polymer-free.<sup>[244]</sup>

**Microcontact printing** ( $\mu$ CP) belongs to the so-called “soft lithography” techniques introduced by Whitesides *et al.*<sup>[245]</sup> This technique also involves PL for the preparation of the polymeric micro-stamps (compare Figure 23). These stamps, usually consisting of poly(dimethylsiloxane) (PDMS = the “soft material”)<sup>[240]</sup>, are subsequently coated with an “ink” which is transferred to the surface by brief stamping. The species then undergo a self-assembly process on the patterned areas predetermined by the stamp design.<sup>[246]</sup> The printed chemical species can for example be a silane for the functionalization of  $\text{SiO}_x$ <sup>[247]</sup> or a thiol for the functionalization of gold<sup>[248]</sup>. Subsequent amplification by SI polymerization leads to complex polymer graft architectures in the micrometer scale.<sup>[249],[250],[251]</sup> Microcontact printing has evolved into a popular techniques since a large parallel printing capacity up to several square centimeters consisting of sub-micrometer sized features can be realized at once.<sup>[246]</sup>

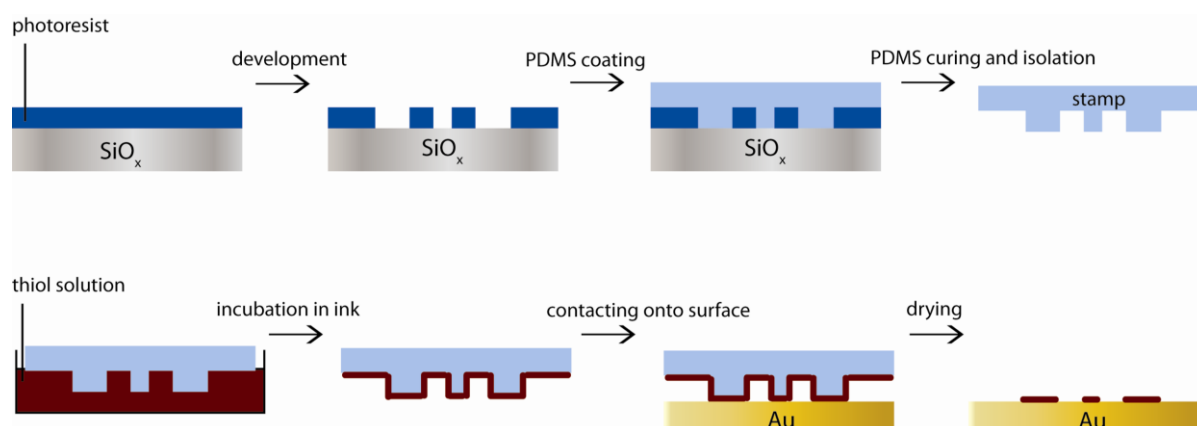


**Figure 23: Schematic representation of microcontact printing; above: preparation of the stamp; below: transferring the ink onto a surface.**

Similarly to  $\mu$ CP, **Nanoimprinting lithography** (NIL) is based on a pressure-induced transfer of patterns by a prefabricated stamp.<sup>[240]</sup> Yet, instead of transferring molecules for SAM formation, the stamp (here: a rigid material, such as silicon or silicon carbide) only serves as mechanical press into a softer thermoplastic polymer film. The polymer is treated at temperatures considerably above its glass transition temperature in the viscous liquid flow state where modulus and viscosity permit an easy and irreversible deformation, and is subsequently allowed to cool down.<sup>[252]</sup> Chou *et al.* have thereby created 100 nm deep and sub-25 nm wide structures of PMMA. In this example, as well as in many other reports, NIL is rather applied to coated polymer layers than to polymer brushes.<sup>[252],[253],[254]</sup> However, some groups use NIL patterned surfaces to combine it with a subsequent SI-polymerization.<sup>[255],[256]</sup>

**Dip-pen nanolithography** (DPN) and the other two following examples represent AFM-based lithography (= scanning probe lithography, SPL) for the structured deposition of SAMs and are schematically depicted in Figure 24. The sharp tip allows the formation of structures down to around 10 nm by “direct writing”. During DPN the AFM tip is covered with an ink layer from which molecules are transferred via capillary forces through a water meniscus onto the surface in precise patterns and velocities.<sup>[246]</sup> The resulting SAMs can further be converted into surface-initiators for ATRP<sup>[257]</sup>, ring-opening metathesis polymerization<sup>[258]</sup> or photoinitiated polymerization.<sup>[259]</sup> Since the deposition of silanes to silicon surfaces via DPN is very delicate due to the sensitivity to water<sup>[260]</sup>, mostly thiols are used for the transfer on gold.<sup>[261]</sup> For a long time, DPN was considered as an inefficient method due to slow processing and low throughput<sup>[241]</sup> until Mirkin *et al.*<sup>[262]</sup> presented large cantilever system (32 silicon nitride cantilevers with 100  $\mu$ m spacing) for parallel writing. Furthermore, they could demonstrate that DPN allows “overwriting” of a first pattern with a second type of ink and, thus enhancing the variability of subsequent surface modifications.<sup>[263]</sup>

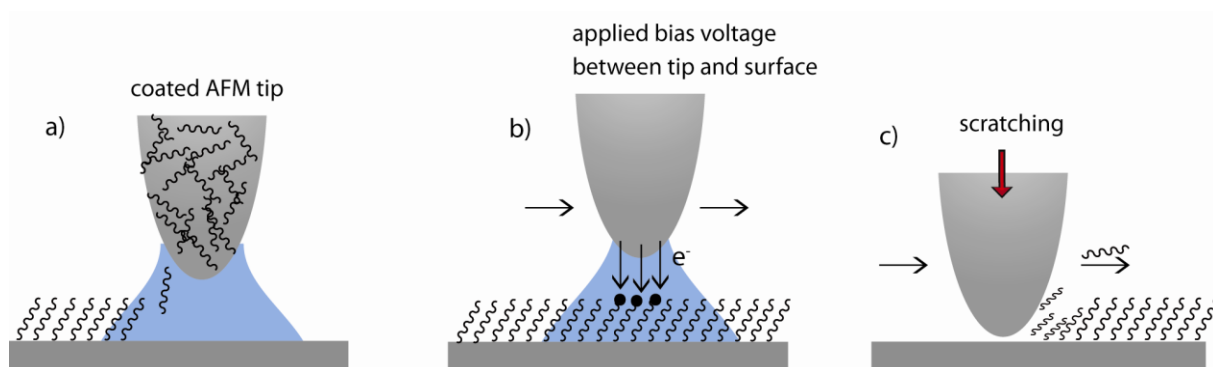


**Figure 24: Scheme of different scanning-probe lithography methods; a) dip-pen nanolithography; b) electric field induced lithography; c) nanoshaving.**

**Electric field induced lithography** (EFIL) - or anodization lithography - is typically used on passivated silicon <sup>[264]</sup> or titanium <sup>[265],[266]</sup> surfaces as presented for the first time by Sugimura *et al.* and can be performed with an AFM or an STM. A potential is applied between the tip and the conductive surface inducing a tip- and a surface-electrochemical reaction (here exemplary for silicon) <sup>[267]</sup>:

Tip reaction in a natural water meniscus:  $4\text{H}_2\text{O} + 4\text{e}^- \rightarrow 2\text{H}_2 + 4\text{OH}^-$

Substrate reaction:  $\text{Si} + 2\text{H}_2\text{O} \rightarrow \text{SiO}_2 + 4\text{H}^+ + 4\text{e}^-$

The silicon oxide layer formed during EFIL gives a chemical contrast to the otherwise H-terminated <sup>[268]</sup> or silane-passivated <sup>[185],[269]</sup> silicon areas and can be further functionalized with other silanes. The preparation of structured polymer brushes by EFIL is rarely reported. This might be due to its limited throughput when larger polymer areas are required. However, EFIL allows the fabrication of well-defined patterns in the sub-100 nm range which was reported by Zauscher *et al.* <sup>[185]</sup> Moreover, a special form of chemical patterning can be exclusively applied in tip anodization: in an appropriate voltage range, the silane-passivation layer is not entirely lifted off and oxidized to SiO<sub>x</sub> but instead, the terminal methyl groups can be locally converted into carboxylic acid functions. <sup>[270]</sup> Besides the scan velocity and the tip voltage, humidity plays a key role for the structure resolution since the electrochemical reaction takes places in the water meniscus surrounding the tip. <sup>[271],[272]</sup>

**Nanoshaving** does not require any special treatment of the AFM tip because it is merely based on the mechanical removal of chemisorbed molecules through sufficiently high shear forces between the tip set to contact mode and the surface. <sup>[240],[241]</sup> The blank areas remaining after scratching can be subsequently backfilled with another SAM or even in-situ by operating the nanoshaving process in a solution containing the desired molecules different from the original SAM. <sup>[273]</sup> SIP resulting in stimuli-responsive P(NiPAAm) brushes on patterned SAMs was demonstrated by Zauscher *et al.*: <sup>[257]</sup> gold surfaces were therefore preliminarily coated with a passivating thiol which was removed by nanoshaving and replaced by a thiol-ATRP initiator. Nanoshaving is not only useful for patterning itself, but is also a powerful analytical tool in order to measure the thickness of ultrathin layers, as has been used in our group for biphenyl SAMs on diamond. <sup>[126]</sup>

**Electron-beam lithography** (EBL) can be used for the exposure of photoresists or as a resist-free method to prepare micro-and nanopatterned surfaces upon irradiation with an electron beam. The lateral resolution of EBL is higher than photolithography because the electron

beam can be focused down to 1 nm and electrons are less susceptible to optical interferences.<sup>[274]</sup> With EBL photoresist coatings can be locally developed <sup>[239]</sup> or precursor molecules can be deposited to surfaces <sup>[275]</sup>, but it has also been used by several groups for the regioselective chemical conversion of SAMs. Some of us locally reduced nitro-biphenyl thiols on gold into stable, cross-linked amino-biphenyls which were further converted into free radical surface initiators for the SIP of poly(styrene).<sup>[276],[277]</sup>

Recently, we have developed a straightforward procedure which allows the synthesis of well-defined micro- and nanostructured polymer brushes with near-molecular precision without the need of precedent monolayer formation: carbon templating (CT).<sup>[278],[279]</sup> Residual precursor molecules present in the vacuum chamber decompose under e-beam and form a stable carbon deposit containing diverse functionalities (including hydroxyl and aliphatic C-H groups) at the point of impact of the beam.<sup>[280],[274]</sup> The resulting so-called electron beam-induced carbon deposition (EBCD) is reactive towards direct photografting of vinyl monomers and can be amplified by the formation of polymer brush layers. In contrast to all existing methods, “carbon templating” (CT) is a SAM-, initiator- as well as photoresist-free process which avoids complex and tedious multi-step reactions and minimizes surface contamination. Another exceptional advantage of EBL in combination with SIP is that two-dimensional as well as 3D patterns can be defined with a high degree of complexity and variability which has been demonstrated by our group.<sup>[281]</sup> The respective strategy for the preparation of e.g. a polymer a brush gradient by CT is presented in Figure 25.

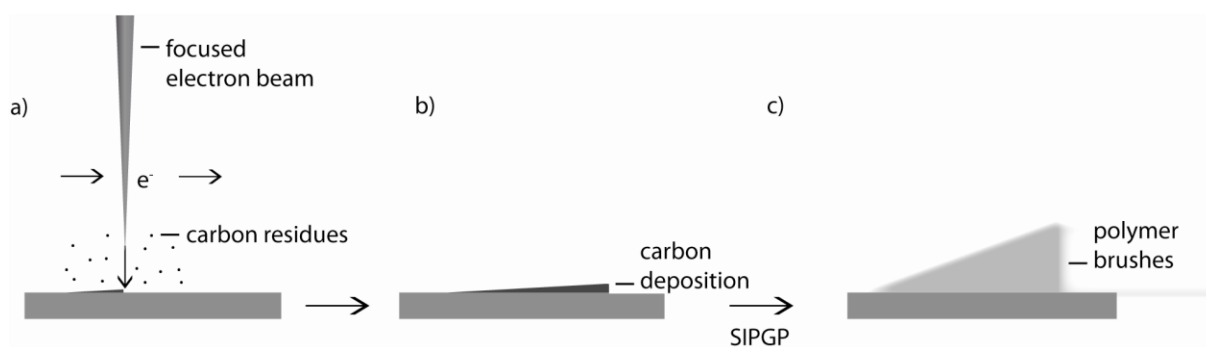


**Figure 25: Preparation of a polymer brush gradient by CT; a) local irradiation of the surface with a focused electron beam in the presence of carbon residues; b) local formation of electron beam carbon depositions (EBCDs); c) selective formation of polymer brushes on the EBCDs during SIPGP.**

## 2.2.4 Comparative study of different surface functionalization techniques and their performance for biosensor applications

In Table 5, the most important features of bioconjugates with monolayers, coatings and polymer brushes are summarized along with the pros and cons of the presented methods. In this PhD thesis, the principle criteria why polymer brushes have been chosen are enhanced biomolecule stability and a higher surface loading which potentially results in increased signal intensity.

**Table 5: Comparison of different coupling strategies for biomolecules, with respect to potential applications as biosensors.**

<b>Binding platform</b>	<b>advantages</b>	<b>disadvantages</b>
thiol monolayer	<ul style="list-style-type: none"> <li>• best studied system</li> <li>• gold does not oxidize easily under standard conditions</li> </ul>	<ul style="list-style-type: none"> <li>• quenching in fluorescent studies</li> </ul>
silane monolayer	<ul style="list-style-type: none"> <li>• thermally more stable than thiols</li> </ul>	<ul style="list-style-type: none"> <li>• limited choice of functional head group</li> <li>• complete OH-termination necessary</li> <li>• hydrolysis</li> </ul>
(bi)phenyl monolayer	<ul style="list-style-type: none"> <li>• thermally stable C-C bond</li> <li>• conjugated <math>\pi</math>-system</li> </ul>	<ul style="list-style-type: none"> <li>• limited choice of functional head group</li> <li>• starting material fragile to light, temperature and air</li> </ul>
monolayers in general	<ul style="list-style-type: none"> <li>• ultrathin</li> <li>• highly ordered</li> </ul>	<ul style="list-style-type: none"> <li>• proximity to surface might lead to loss in activity</li> </ul>
bulk polymer coatings	<ul style="list-style-type: none"> <li>• tailored polymers</li> </ul>	<ul style="list-style-type: none"> <li>• merely physisorbed interlayer</li> </ul>
polymer brushes	<ul style="list-style-type: none"> <li>• membrane-like microenvironment</li> <li>• high binding capacity</li> <li>• enhanced biomolecule stabilization</li> </ul>	<ul style="list-style-type: none"> <li>• often implies multistep procedures</li> </ul>
3 D in general	<ul style="list-style-type: none"> <li>• soft environment for biomolecules</li> </ul>	<ul style="list-style-type: none"> <li>• limited electron transfer through the interlayer</li> </ul>

## 2.3 Properties and application of diamond electrodes

Due to the poor biocompatibility and chemical instability of silicon, alternative semiconductor materials have been investigated for bioelectronic applications over the last decades. Boron-doped diamond (BDD) is a promising candidate to replace previous electronic materials owing to its outstanding chemical and physical properties. Accessibility of synthetic diamond and the reduction of production costs have been achieved by recent developments in diamond growth by chemical vapor deposition (CVD) and have thus opened the way to investigations and experiments with large-area diamond surfaces and their resulting applications.<sup>[282]</sup>

### 2.3.1 Processing of diamond

The fabrication of synthetic thin diamond films has been facilitated since the development of chemical vapor deposition (CVD) in the 1980's.<sup>[283]</sup> During CVD, a gas mixture consisting of hydrogen, a carbon containing precursor gas (mostly methane) and in some cases argon is activated leading to the generation of  $\text{CH}_3\cdot$  radicals which adsorb on nucleation seeds or on the readily growing diamond layer at temperature of usually  $800^\circ\text{C}$ .<sup>[282]</sup> Since nucleation of diamond on non-treated platforms is very low, the carrier substrate is either seeded with diamond or carbide particles, which, depending on their original grain sizes, will naturally affect the resulting minimum diamond crystallites' sizes. If small grains are desired, techniques such as nano-seeding, bias-enhanced seeding and mechanical scratching enhance the nucleation density.<sup>[284]</sup>

The activation of the gas mixture can be performed (a) thermally by a hot filament ( $2200\text{--}2800^\circ\text{C}$  <sup>[285]</sup>), (b) by using a combustion flame of e.g. oxyacetylene or (c) a plasma mostly created by microwave power.<sup>[286]</sup> Since graphite is the thermodynamically stable form of carbon, it is essential to enhance the formation of  $\text{sp}^3$ -bonded carbon and simultaneously suppress  $\text{sp}^2$ -bond formation.<sup>[285]</sup> This is achieved under high hydrogen gas pressures and therefore, the gas mixture is typically composed of 99%  $\text{H}_2$  and merely 1%  $\text{CH}_4$ .<sup>[282]</sup> Although it is known that hydrogen etches diamond in the harsh CVD environment, the growth rate dominates the etch rate upon application of higher microwave power ( $1000\text{--}2500\text{ W}$ ).<sup>[286],[287]</sup> Generally, the interaction of all deposition parameters will influence the later properties of the diamond film, such as its film morphology and thickness and the phase purity (fraction of non-diamond  $\text{sp}^2$  phases in the pure  $\text{sp}^3$  film).<sup>[282]</sup> For example, argon-rich gas plasma with low methane pressure lead to the formation of ultrananocrystalline diamond (UNCD) with

crystallite grain sizes of 3-5 nm.<sup>[286]</sup> Other forms of synthetic diamond are microcrystalline (MCD, highly varying grain sizes up to hundreds of micrometers), nanocrystalline (NCD, 30-100 nm grains) and even single crystalline diamond (SCD).<sup>[288]</sup>

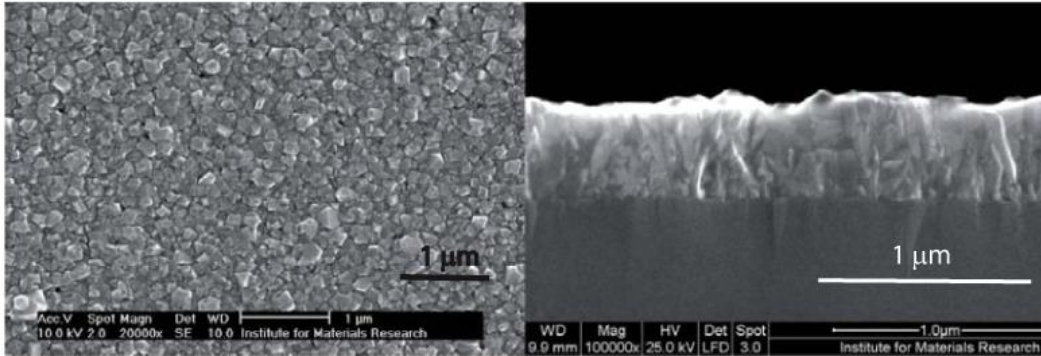


Figure 26: Top and cross-sectional SEM view of a ~400 nm thin NCD film grown by CVD on silicon.<sup>[287]</sup>

### 2.3.2 Physicochemical properties of diamond

Undoped diamond is known to be an insulator with a band gap of 5.5 eV. For (bio)electronic applications however, boron-doped diamond is fabricated by adding diborane impurities during CVD which create an acceptor energy level of only 0.37 eV above the valence band.<sup>[286],[287]</sup> The resistance can thereby be drastically decreased from originally  $10^8 \Omega\text{cm}$  to  $10^4\text{-}10^2 \Omega\text{cm}$ .<sup>[286],[285]</sup>

Conductive diamond films are known to combine exceptional properties such as chemical inertness, unique stability, a large electrochemical potential window ( $\sim 3\text{-}3.5 \text{ V}$ <sup>[285]</sup>), and small background current as electrode material in aqueous media.<sup>[13],[282],[289],[290]</sup>

Table 6: Physicochemical properties of diamond and boron-doped diamond.

Property <sup>[288]</sup>	Diamond	BDD
Thermal expansion / $\cdot 10^{-6}/\text{K}$	1.1	
Electron mobility / $\text{cm}^2/\text{Vs}$	2200	
Hole mobility / $\text{cm}^2/\text{Vs}$	1600	$0.5 - 2$ <sup>[287]</sup>
Breakdown voltage of an insulator / $\cdot 10^5 \text{ V}/\text{cm}$	100	
Hardness / $\text{kg}/\text{mm}^2$	8000	
Young's modulus / GPa	820 - 900	
Density / $\text{g}/\text{cm}^3$	2.8 - 3.5	

The outstanding material properties of diamond summarized in Table 6 have led to numerous applications of diamond films, such as coatings, <sup>[5],[6]</sup> microelectrochemical systems <sup>[10],[7]</sup> and electrochemical electrodes. <sup>[11],[291]</sup>

### 2.3.3 Surface modification of diamond

For a long time, chemical modification of diamond surface was considered difficult due to its chemical inertness. By now however, there exist several techniques to activate the diamond boundaries for subsequent functionalization reactions. In order to classify the different reactions it is important to have a closer look to the diamond surface termination first.

#### 2.3.3.1 Surface termination of synthetic diamond films

In bulk, CVD-grown diamond ideally consists of  $sp^3$  carbon only. But at the grain boundaries,  $sp^2$ -impurities and amorphous carbon domains can be found which strongly influence the chemical reactivity of the diamond surface. <sup>[285]</sup> For most diamond functionalizations, the surface is either pretreated by hydrogen or oxygen termination, but there are also reports on fluor- or amine termination. <sup>[286],[292],[293]</sup>

H-termination can be performed in a hydrogen plasma at elevated temperatures. Unlike hydrogenated silicon, the H-termination of diamond is relatively stable at room temperature because the small sticking coefficient of atomic oxygen reduces the surface oxidation speed. <sup>[294]</sup>

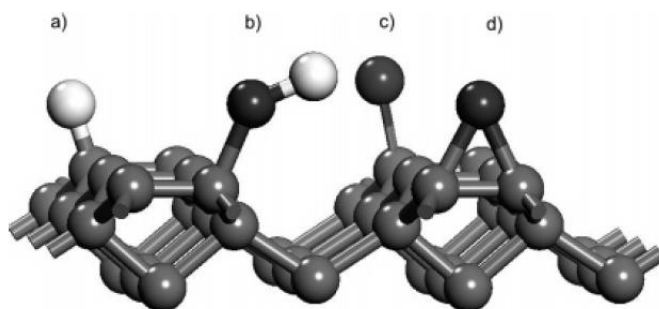


**Figure 27: Possible surface terminal groups of diamond; a) C-H; b) hydroxyl (-OH); c) carbonyl (=O); d) ether (-O-).** <sup>[294]</sup>

In order to oxidize the surface, diverse procedures have been reported, such as thermal, plasma or electrochemical treatment as well as singlet oxygen irradiation and ozone treatment. <sup>[286]</sup> The resulting terminating species are hydroxyl, ether or carbonyl groups (see

Figure 27) and their respective proportion at the surface is determined by the extent of surface coverage (low coverage favors -OH and =O, high coverage -O-)<sup>[294]</sup> and the ratio of  $sp^3$  and  $sp^2$  facets ( $sp^3$  is rather terminated by -OH,  $sp^2$  by =O and -O-).<sup>[286]</sup> The type of diamond surface termination has been shown to affect a large number of material properties, such as surface conductivity, electron affinity and wetting behavior.<sup>[294]</sup> In recent years, many research groups have investigated different chemical functionalization strategies for different terminating species.

### 2.3.3.2 Organic monolayers on diamond – state of the art

**H-terminated diamond:** Figure 28 depicts the two most important functionalization techniques for H-terminated diamond. The first one is a photochemical reaction at 254 nm with a terminal alkene and is widely used for introducing amine functionalities for example, although the exact mechanism is not fully clarified yet.<sup>[142],[143-144]</sup> It certainly plays a role that H-terminated diamond is able to emit an electron from the valence band into vacuum at such excitation wavelength.<sup>[286]</sup> We reported on the second alternative: spontaneous grafting of aromatic diazonium salts on hydrogenated UNCD resulting in densely packed and homogeneous self-assembled monolayers<sup>[126]</sup>

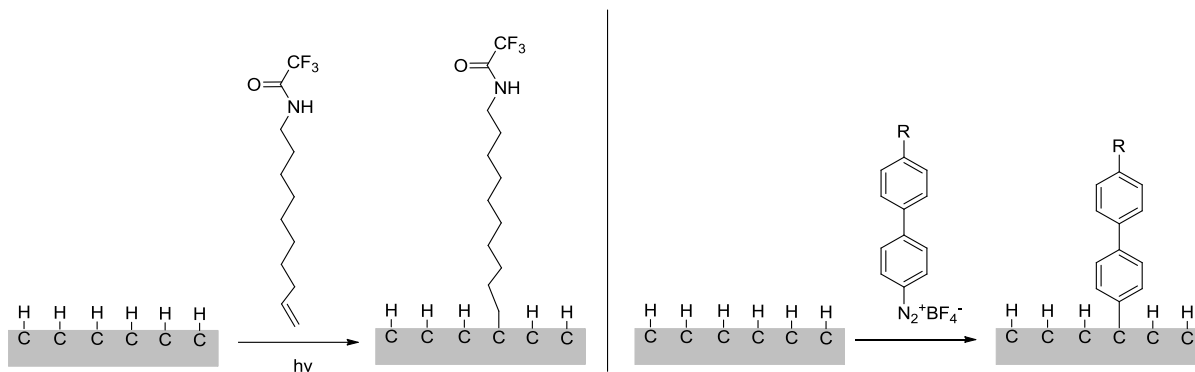


**Figure 28: Surface chemical modification of hydrogenated diamond by terminal alkenes (left) or by aromatic diazonium salts (right).**

**O-terminated diamond:** Organosilanes can be coupled onto hydroxyl-terminated diamond surfaces in a condensation reaction.<sup>[295]</sup> Since the silane monolayer is understood to form a cross-linked, randomly connected net on top of the surface, the bondings are just carefully indicated in Figure 29. Boukherroub *et al.*<sup>[296]</sup> reported on the esterification of an oxidized diamond surface using benzoylbenzoic acid by activating the carboxylic acid moieties with a carbodiimide reagent.

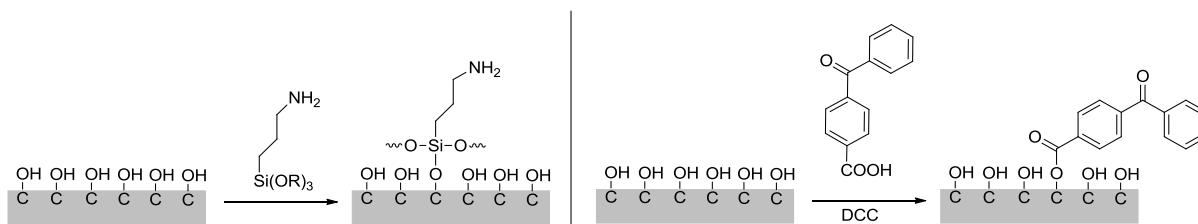


**Figure 29: Surface chemical modification of hydroxyl-terminated diamond by silanization (left) or by esterification (right).**

### 2.3.3.3 Polymer brushes on diamond - state of the art

The preparation of polymer brushes on diamond surfaces has been the subject of only few studies.<sup>[166],[297],[298]</sup> Existing approaches are based on the pre-modification of the diamond substrate with an organic monolayer, followed by surface-initiated polymerization. Chehimi *et al.*<sup>[166]</sup> have reported on an atom-transfer radical polymerization (ATRP) of styrene and MMA on UNCD which had been functionalized with bromo-monophenyl diazonium salts as a first step. In another very recent approach reported by Liu *et al.*<sup>[299]</sup> nano-diamond particles with carboxylic acid surface functionalities were generated by oxidation with sulfuric and nitric acid. After subsequent conversion into bromo-*isobutyryl* bromide moieties, known to act as ATRP initiators, they could graft poly(dimethylaminoethyl methacrylate) brushes. Although controlled radical polymerization techniques lead to well-defined and homogeneous surface chains, their major draw-back is the relatively complex procedure combining several reaction steps. Recently, we have shown that polystyrene (PS) brushes could be prepared directly on OH-terminated diamond by the self-initiated photografting and photopolymerization (SIPGP) of styrene.<sup>[300]</sup> The selective formation of polymer brushes on the OH-terminated areas can be explained by the difference in bond dissociation energy (BDE) of C-H (401.5 kJ/mol)<sup>[244]</sup> and O-H bonds (71 kJ/mol)<sup>[300]</sup> on diamond.

These possible surface modifications are all characterized by a high stability which represents one of the major advantages of diamond as functionalized semiconductor material in (bio)electronic systems, compared to e.g. silicon, glassy carbon or gold whose surface functional groups are susceptible to hydrolysis, surface fouling or decomposition. Therefore, numerous reports deal with the functionalization of diamond films with biomolecules (see chapter 2.3.4).

### 2.3.4 Biological aspects of diamond

Besides its chemical stability, diamond films have repeatedly been reported to be bioinert which renders them additionally advantageous for biological or medical applications.<sup>[301]</sup> It is chemically extremely stable, so that apart from the desired surface functionalization, basically no unwanted side-reactions are expected. For instance, diamond does not degrade upon electrochemical experiments in aqueous solution<sup>[288]</sup> and involves minimal non-specific protein adsorption.<sup>[302]</sup> Preliminary studies have shown that diamond-like materials do not cause inflammatory host reactions or other cellular damage and have the best biocompatibility of all carbon materials.<sup>[6]</sup> Furthermore, due to its exceptional mechanical stability, chances are low that the material is worn off and that small particle splinters break off.

In the perspective of using diamond for biomedical applications, efforts have been made in the past for the direct immobilization of biomolecules on NCD electrodes.<sup>[303],[15],[295]</sup> Boukherroub *et al.*<sup>[292]</sup> investigated the direct peptide immobilization onto amine-terminated BDD prepared in a NH<sub>3</sub> plasma. A semicarbazide group was used as short linker between the surface and the peptide chain. However, this study was merely a proof of principle and no further activity tests have been carried out. Using the photochemical alkene functionalization depicted in Figure 30 (and previously presented in Figure 28), some of us demonstrated that proteins can be covalently immobilized on NCD surfaces without losing their biological functionality.<sup>[13],[289]</sup> The same approach has been successfully demonstrated for the attachment of DNA.<sup>[303],[304],[14]</sup>

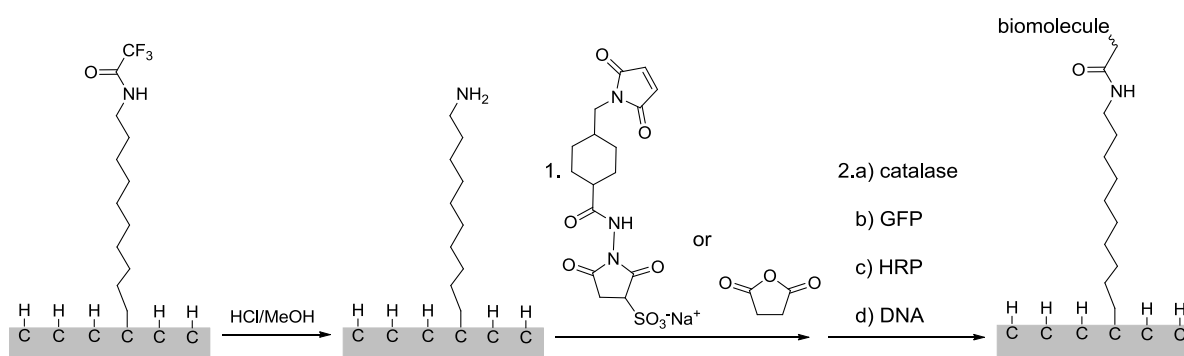


**Figure 30: Preparation of biofunctionalized diamond electrodes; UV-induced coupling of decyltrifluoroacetamide, deprotection to the free amine and subsequent coupling of various proteins and DNA.**

Other methods were based on the functionalization of oxidized diamond with aminopropyltriethoxysilane (APTES) or aminopropyl-diethoxymethylsilane (APDEMS) and subsequent protein or enzyme coupling.<sup>[295]</sup> Stutzmann *et al.*<sup>[290]</sup> could thereby demonstrate the activity

of horseradish peroxidase (HRP) in its recognition reaction with hydrogen peroxide without the addition of a mediator. In Figure 31 the current induced by the stepwise addition of hydrogen peroxide is monitored per time in a chronoamperometric experiment.

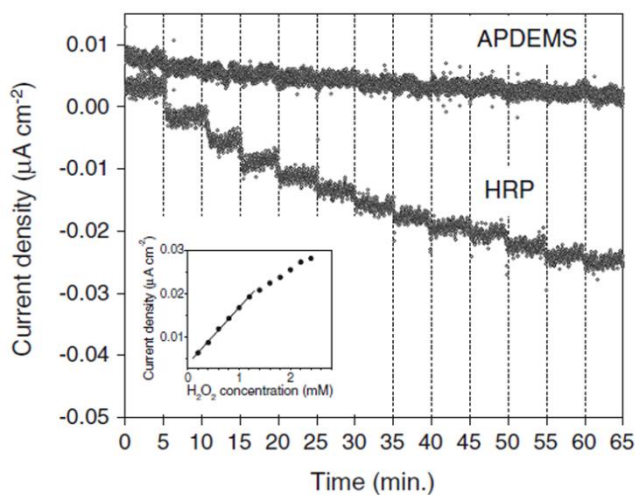


**Figure 31: Monitoring of the reaction of APDEMS-bound HRP with hydrogen peroxide in chronoamperometry. From <sup>[290]</sup>**

While all previous studies on the biofunctionalization of diamond were based on monolayer approaches, it has been shown that thin biocompatible polymer brushes can behave as ideal soft interfaces between biochemical systems and rigid substrates such as semiconductors.<sup>[166],[146],[305]</sup> But so far, very little has been reported on the use of polymer brushes as matrix for biomolecule immobilization. The only results are based on polymer brushes prepared by ATRP on diamond nanoparticles which have been modified with DNA<sup>[299]</sup> and bovine serum albumin (BSA)<sup>[306]</sup>, respectively. In the latter report, only IR spectroscopy was used to show the presence of BSA, but activity test are missing. This shows that there is urgent need for the investigation of diamond-based polymer brush-biomolecule conjugates and that it is interesting to gain a closer insight in the replacement of the monolayer approaches with macromolecular interlayers, i.e. to progress from SAMs to polymer brushes.

### 3. PURPOSE AND OBJECTIVES

The modification of semiconductor surfaces with stable functional organic or polymeric layers has gained an increasing research interest in the past decades. Especially for applications in the field of biomedical micro devices, it is important to create soft biocompatible interlayers between the electrode material and the biological surrounding. Therefore, the motivation of this project was the conceptual design of a novel prototype for an amperometric biosensor, combining diamond as transducer element and functional polymer brushes functionalized with biomolecules as selective sensing sites. The main features of the modified diamond electrode are presented in Figure 32. In order to realize such a bio-sensitive electrode system the objective was divided into the following three main research stages:

(a) Diamond modification with polymer brushes and biofunctionalization with special focus on the compatibility of the semiconductor-polymer system with sensitive proteins and enzymes.

(b) Structuring of the functional polymer brushes by means of lithography techniques. Regarding this aspect, the two main goals were to get a better understanding of the protein absorption into the polymer brushes and to determine strategies for patterning methods for microarray applications.

(c) Amperometric detection of the immobilized biomolecules and their reaction upon a substrate in electrochemical experiments. In respect to voltammetric methods, the challenge to ensure a charge transfer through the polymer brushes to the NCD electrode needed to be addressed by the introduction of a mediator into the polymer brush - electrode system.

In contrast to former studies on biofunctionalized self-assembled monolayers (SAMs), the major part of the research here was dedicated to the surface coupling of redox active moieties, biomolecules or recognition sites into polymer brushes bearing multiple functions and providing a soft three-dimensional scaffold. Therefore, an important aspect of this work was to evaluate whether the polymer brush approach is a versatile alternative to the SAM-based systems. In order to accomplish such scientific challenge in the thematic junction between polymer chemistry, physics and biochemistry, the project was scheduled as close interdisciplinary cooperation between the *Walter Schottky Institute*, the *Wacker Lehrstuhl für*

*Makromolekulare Chemie* (TU Munich) and the *Professur für Makromolekulare Chemie* (TU Dresden).

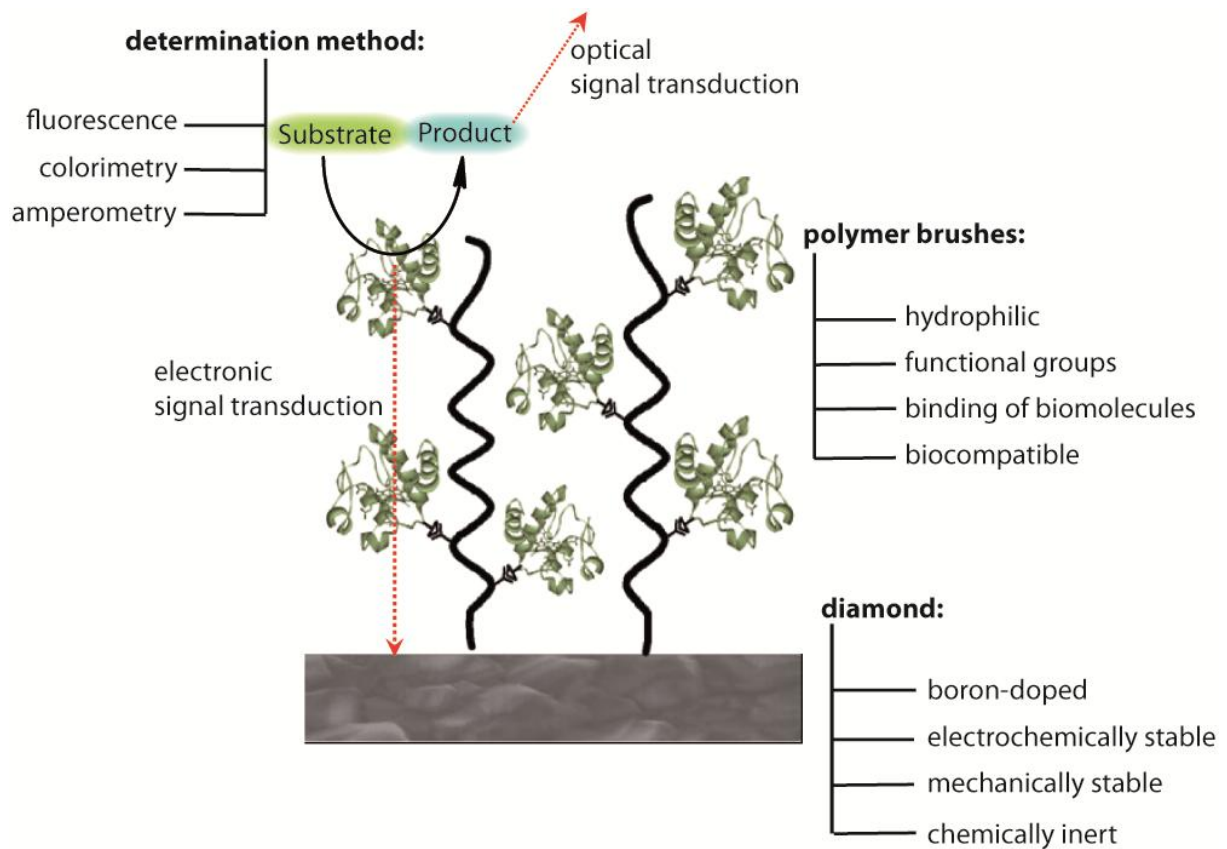


**Figure 32: Conceptual design of an amperometric biosensor based on polymer brush-modified diamond electrodes; presentation of the main features of the three involved parts recognition reaction, polymer brushes and diamond electrode.**

## 4. RESULTS AND DISCUSSION

### 4.1 Micro- and nanostructured polymer brushes on diamond and SiO<sub>x</sub> by SIPGP

The development of diamond-based biosensors for high-throughput and parallel screening, e.g. in microarray applications, requires selective structuring of the sensor surface area resulting in well-defined features down to the nanometer scale. The following chapter addresses various types of patterning methods for the preparation of micro- and nanostructured polymer brushes on semiconductor surfaces. Since nanocrystalline diamond (NCD) samples were not always accessible, SiO<sub>x</sub> and glassy carbon (GC) samples were used on occasion in order to investigate novel structuring techniques or to prove a concept in general. If so, it is explicitly indicated.

#### 4.1.1 Reactivity contrast between H- and OH-terminated diamond

Although surface-initiated controlled radical polymerization techniques enable the preparation of well-defined, tailor-made polymer brushes and represent the major part of respective scientific literature, the self-initiated photografting and photopolymerization (SIPGP) has been primarily used in this PhD project. This is mainly due to the fact that it is a very reliable, straightforward and single-step method which makes it thus suitable for potential industrial applications. Originally, Rånby *et al.* <sup>[307]</sup> have discovered that styrene can graft on poly(ethylene) under UV irradiation in the absence of a sensitizer. Lately, this auto-initiation has been used by our group for the preparation of stable polymer brushes.<sup>[308],[300]</sup> Figure 33 depicts the proposed mechanism for the SIPGP: Upon irradiation with UV light, the double bond of the monomer absorbs energy and is lifted into an excited singlet state S. The more stable triplet state T, being in equilibrium with the biradical form, is reached through inter system crossing (ISC) and probably attacks a surface abstractable atom I, e.g. hydrogen.<sup>[307]</sup> The generated surface radical can initiate the free radical polymerization resulting in polymer brushes.

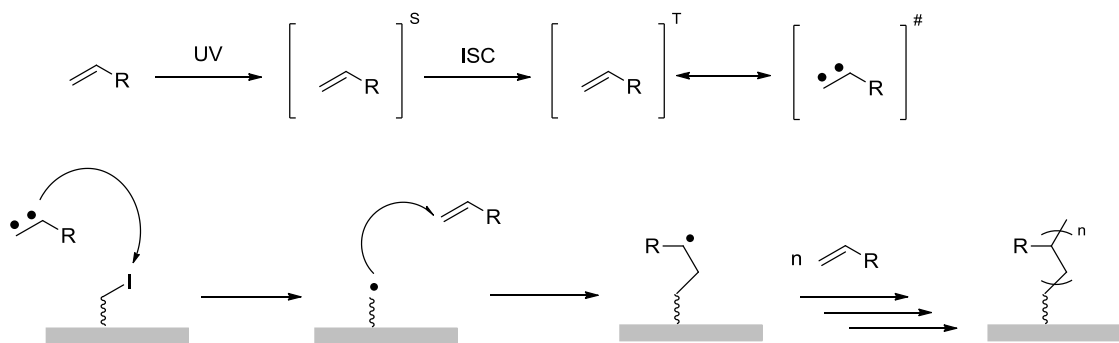


**Figure 33: Proposed mechanism for the self-initiated photografting and photopolymerization (SIPGP) according to Rånby *et al.*<sup>[269]</sup>**

#### 4.1.1.1 Microstructured polymer brushes on diamond by common photolithography

Throughout the experiments, nanocrystalline diamond films (NCD) evaporated on silicon were used. AFM measurements revealed a native roughness of NCD of 9.1-10.7 nm root-mean-square (rms) depending on the charge of the wafer (Figure 34). The reason for the use of NCD instead of UNCD, SCD or PCD lies in its relatively facile and well-established doping, good characterization in doped and undoped state and its accessibility.

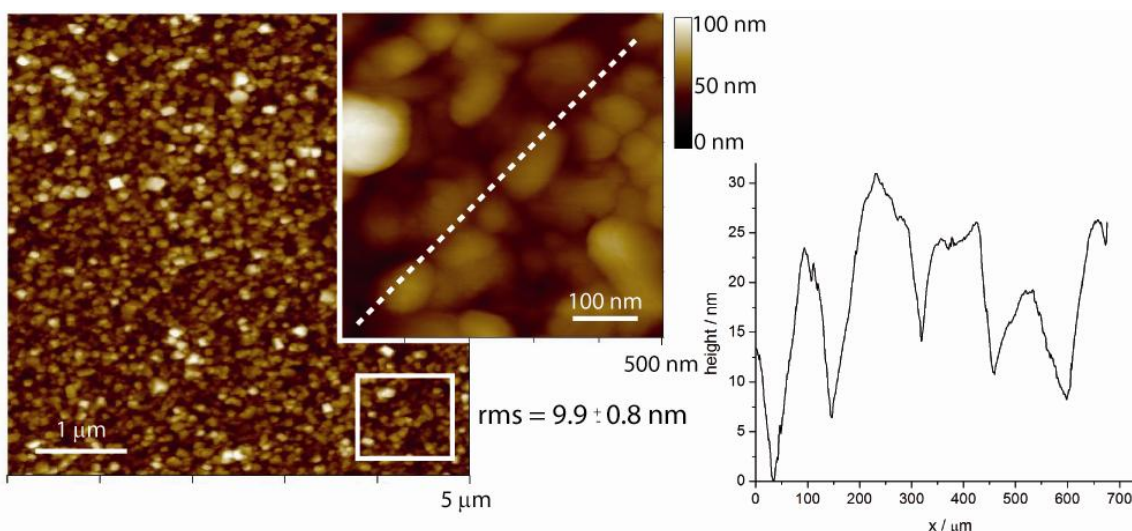


**Figure 34:  $5 \times 5 \mu\text{m}^2$  AFM scan of a freshly oxidized NCD surface with a rms of  $9.9 \pm 0.8 \text{ nm}$  according to roughness analysis; magnification into  $500 \times 500 \text{ nm}^2$ .**

Native NCD substrates were patterned by conventional photolithography using a Novolak (S1818 microposit) type photoresist. The exposed areas were oxidized in an oxygen plasma. After removal of the photoresist and thorough cleaning, the partial oxidized NCD substrate was submerged in bulk monomer and irradiated under UV light ( $\lambda_{\text{max}} = 350 \text{ nm}$ ) for the SIPGP until the solution became strongly viscous. The samples were thoroughly cleaned by

ultrasonication in solvents with varying polarities, in order to remove physisorbed polymer from the surface.

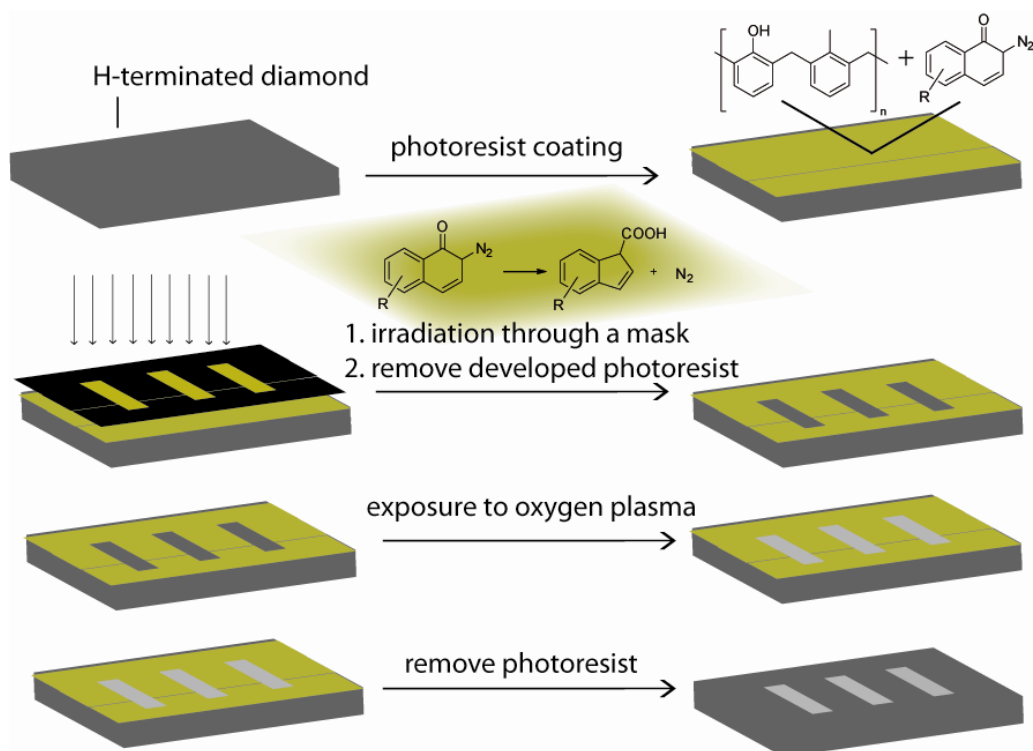


**Figure 35: Preparation of OH- and H-patterns on NCD with common photolithography using a S1818 photoresist. After irradiation through a mask, the developed photoresist areas are removed in an appropriate solvent. The free surface areas are oxidized in an oxygen plasma.**

AFM measurements of PS and PMAEMA brushes revealed that polymer brush layers with thicknesses of  $200 \pm 10$  and  $150 \pm 20$  nm were selectively formed on the oxidized NCD areas after 24 h and 2 h of irradiation time (Figure 36 a), b)). However, since the resolution of the structures depends on the integrity of the photomask which showed signs of frequent usage, new templates with  $10 \times 10 \mu\text{m}^2$  squares and  $10 \mu\text{m}$  thick lines were designed (Figure 36 c)). Polyelectrolyte brushes, such as sulfonated poly(styrene), are of crucial interest for immunoassays where charged polymer interfaces interact with proteins.<sup>[187]</sup> Previously, sulfonated poly(styrene) (PSS) polyelectrolyte brushes were generated starting from PS grafts by sulfonation reaction with concentrated sulfuric acid.<sup>[300]</sup> In order to circumvent a polymer analogue reaction under such harsh conditions PSS brushes were directly prepared by the SIPGP of sulfonated styrene for 2 h in water, resulting in  $100 \pm 15$  nm thick layers patterned with the new PL mask. Data analysis of the AFM scans revealed that the surface roughness of polymer coated regions was, with an rms of around  $3.4 \pm 0.4$  nm, lower as compared to the bare NCD surface region. The reactivity contrast between the H- and OH-terminated surface areas during the SIPGP process is in agreement with our recent account on the SIPGP of

styrene on UNCD.<sup>[300]</sup> The selective formation of polymer brushes on the OH-terminated areas can be explained by the difference in bond dissociation energy (BDE) of C-H (401.5 kJ/mol)<sup>[244]</sup> and O-H bonds (71 kJ/mol)<sup>[300]</sup> on diamond.

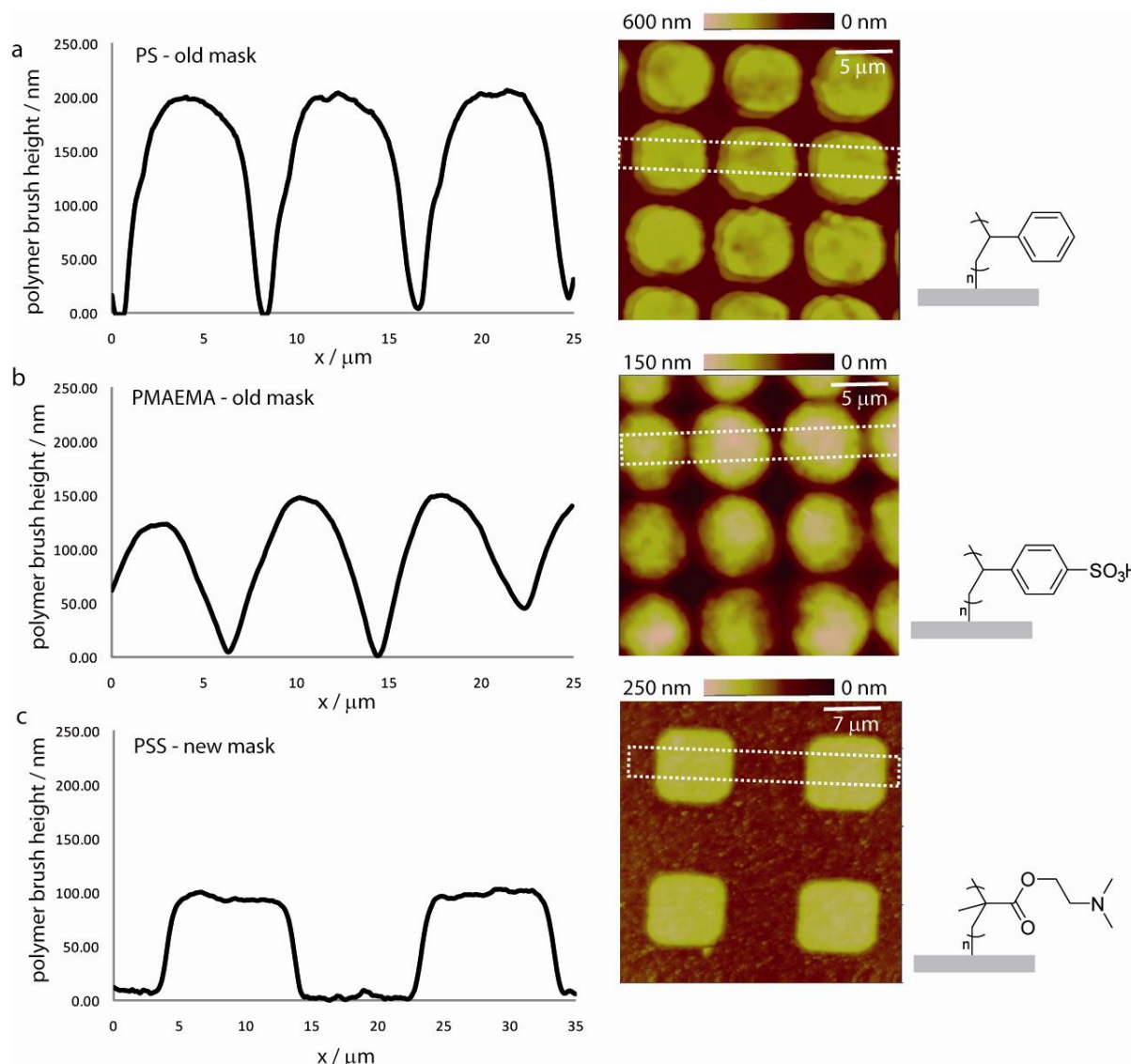


**Figure 36:** AFM section analysis and image of structured a) PS, b) P(MAEMA) and c) PSS brushes on NCD after a) 24 h, b) 2 h and c) 3 h of SIPGP.

#### 4.1.1.2 Poly(2-oxazoline) bottle-brush brushes on diamond

Due to their biocompatibility and broad range of possible polymer analogue functionalization reactions, poly(2-oxazoline) (POx) brushes are good candidates for biomolecule conjugation. They show a great variability due to possible modification in the 2-R position, by the choice of terminating agent, or by controlled copolymerization (see chapter 2.2.3.4). According to the work of Dr. Ning Zhang, functional polymer brushes with outstanding variability can be

prepared based on poly(2-oxazoline) (POx) chemistry. He demonstrated the synthesis of well-defined poly(2-oxazoline) bottle brushes both in bulk and grafted onto glassy carbon and APTES-modified silicon dioxide surfaces. The starting point was the preparation of poly(2-isopropenyl-2-oxazoline) (PIPOx) brushes by the SIPGP of 2-isopropenyl-2-oxazoline (IPOx). IPOx has two orthogonal polymerizable groups, namely the vinyl group used for the SIPGP and the 2-oxazoline ring for the living cationic ring-opening polymerization (LCROP). This dual-functionality of IPOx has been used to prepare defined bottle brushes by the polymerization of IPOx by living anionic or free radical polymerization with consecutive LCROP.<sup>[309]</sup> Furthermore, brushes of bottle brushes on polished glassy carbon (GC) were successfully synthesized and characterized.<sup>[308]</sup> In this work, a similar strategy has been applied for the functionalization of diamond: the SIPGP was performed for 20 h in bulk 2-isopropenyl-2-oxazoline (IPOx). After cleaning, the resulting poly(2-isopropenyl-2-oxazoline) (PIPOx) brushes were characterized by AFM revealing a polymer brush layer with a thickness of  $79 \pm 8$  nm selectively formed on the oxidized NCD areas (Figure 38). A roughness of 9.6 nm rms was found for the native NCD regions, compared to 5.4 nm rms on the PIPOx coated regions. In Figure 37, the mechanism for the preparation of the so-called PIPOx-based bottle-brush brushes (BBBs) is presented:

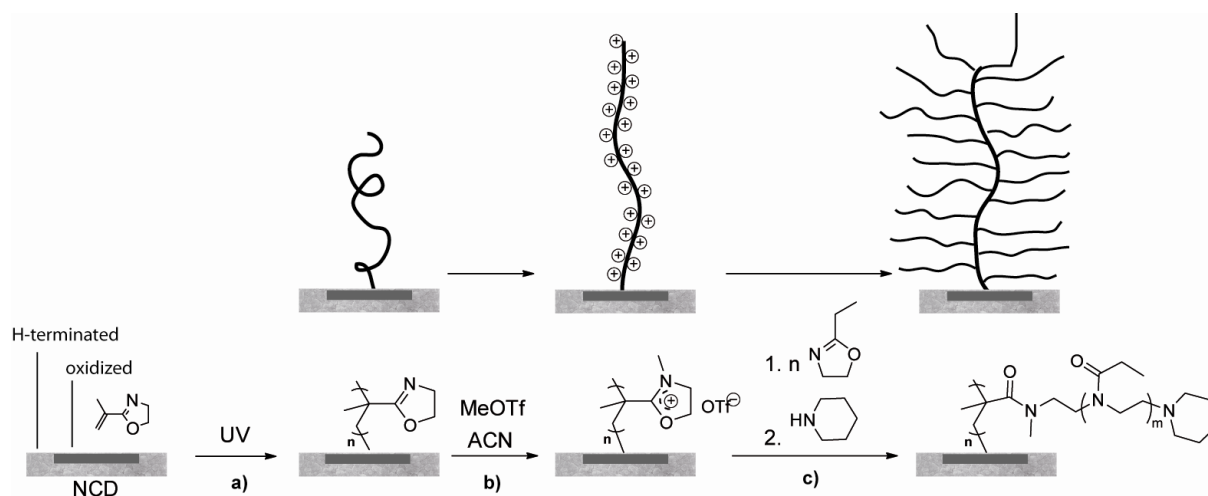


**Figure 37: Preparation of structured poly(2-oxazoline) bottle-brush brushes (BBBs) on NCD - scheme and chemical reaction. a) Selective formation of PIPOx brushes on the oxidized NCD surface regions by UV-induced SIPGP of IPOx. b) Conversion of the PIPOx brush backbone to the macroinitiator salt P(IPOx<sup>+</sup>OTf) by methyl triflate in acetonitrile. c) Surface initiated LCROP of EtOx from the PIPOx<sup>+</sup>OTf macroinitiator salt and termination of the side chain polymerization with piperidine.**

First, the PIPOx brushes were converted into a polycationic macroinitiator followed by the side chain cationic polymerization of 2-substituted-2-oxazolines. Successively, the side chain LCROP was performed over night at 80°C with the P(IPOx<sup>+</sup>OTf) macroinitiator brush and 2-ethyl-2-oxazoline (EtOx) as a second monomer to obtain BBBs. After completion of the

LCROP grafting and selective termination of the side chain polymerization with piperidine the substrate was again intensively cleaned by ultrasonication in different solvents to ensure that only chemically grafted polymer remains on the substrate before further analysis. FT-IR measurements are provided in a complete overview in chapter 4.3.2.

The transformation of the PIPOx brushes into BBBs was investigated by AFM (Figure 38). A significant increase of the polymer brush thickness from  $79 \pm 8$  nm to  $385 \pm 40$  nm for the P(IPOx-g-EtOx) BBBs was found. The almost fivefold increase in brush thickness indicates a very high if not quantitative conversion of the pendant 2-oxazoline rings to BBBs. This is in good agreement with previous studies on glassy carbon and can be explained by the strong stretching of the bottle-brush backbone by the side chain and the overall crowding of grafted polymer at the interface.<sup>[308]</sup> Furthermore, AFM measurements reveal an increase of the lateral structure width of around  $0.5 \mu\text{m}$ . The widening of nano- and microstructured polymer brushes has been the subject of theoretical and experimental studies by Patra, Linse and Zauscher.<sup>[310]</sup> The extension of grafted chains toward polymer-free surface regions was found to be proportional to the polymer chain molecular weight. The chemical conversion into BBBs was further analyzed by contact angle measurements resulting in decreasing contact angles from  $60^\circ \pm 4^\circ$  for PIPOx to  $42^\circ \pm 2^\circ$  for P(IPOx-g-EtOx).

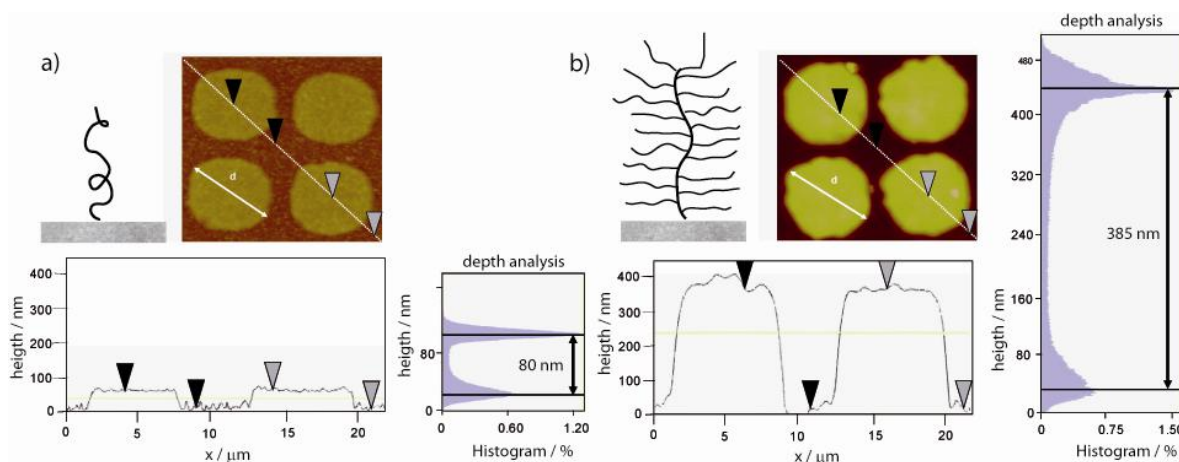


**Figure 38:** AFM scans ( $20 \times 20 \mu\text{m}^2$ ), section analysis and depth analysis of the patterned polymer brush structures on NCD; a)  $79 \pm 8$  nm thick PIPOx brushes selectively formed on the OH-terminated NCD regions; b) The side chain LCROP using EtOx results in  $385 \pm 40$  nm thick P(IPOx-g-EtOx) BBBs.

The properties of P(IPOx) BBBs varied strongly with the choice of the side chain polymer and length.<sup>[232, 308]</sup> Here however, the formation of BBBs on diamond was studied in order to introduce functional end groups for the subsequent coupling of biomolecules, which will be more closely addressed in chapter 4.2.

#### 4.1.2 Electron-beam lithography (EBL) on nanocrystalline diamond

For the first time, micro- and nanostructured polymer brushes on diamond were prepared by carbon templating (CT) which was recently developed in our group.<sup>[278]</sup> This structuring technique allows a significantly better resolution as compared to common PL and avoids multi-step procedures causing surface contamination due to photoresist residues.

##### 4.1.2.1 Investigation of different template designs for the EBL on diamond

For the preparation of structured polymer brushes on conductive boron doped NCD, a clean and freshly hydrogenated NCD surface was locally irradiated with a focused electron beam in an E-Line scanning electron microscope (Figure 39).

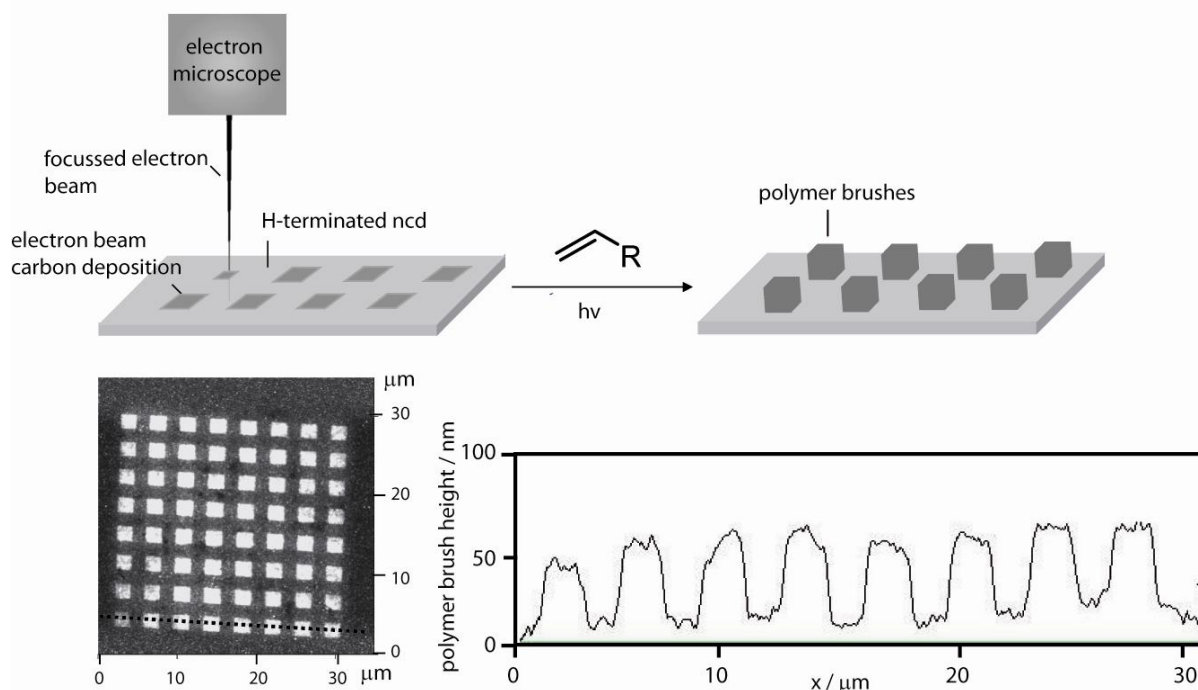


**Figure 39:** Preparation of structured polymer brushes on hydrogenated NCD by carbon templating.  $2 \times 2 \mu\text{m}^2$  squares of electron beam-induced carbon depositions were created with a focused electron beam with an electron dose of  $45 \text{ mC/cm}^2$ . The carbon templates were amplified by SIPGP of vinyl monomers resulting in micro- and nanostructured polymer brushes; below: AFM scan and section analysis over the indicated area of poly(*tert*butyl methacrylate) brushes after CT and SIPGP of *tert*butyl methacrylate for  $t_p = 6 \text{ h}$ .

Carbon templates with different shapes were generated at a pressure of  $10^{-5}$  mbar and electron energies of 20 keV. It is noteworthy that, since the thickness of the carbon deposits (approx. 1 nm<sup>[311]</sup>) lies far beyond the roughness of native NCD (approx. 10 nm rms), it was impossible to visualize the carbon templates by AFM measurements before the photopolymerization. In order to avoid surface oxidation and contamination of the freshly

processed NCDs, the structured samples were immediately emerged in bulk vinyl monomer and exposed to UV light for the SIPGP. In case of a proper hydrogen termination, polymer brushes were exclusively formed on the CTs. The composition of such electron beam induced carbon deposits (EBCD) has been reported to be a mixture of predominately aromatics and aliphatics accompanied by alcoholic and carboxylic groups.<sup>[312],[278]</sup> The chemical contrast for the selective formation of polymer brushes is due to the different bond dissociation energies of diamond-H (401.5 kJ/mol)<sup>[313]</sup> and EBCD-H (between 84 and 301 kJ/mol).<sup>[278],[314]</sup> With EBL probe sizes in lateral resolutions down to 1 nm can be achieved.<sup>[274]</sup> While in principle, any imaginable 2D structure can be written,<sup>[281]</sup> the scan time has to be considered. For example, a CT plane of  $20 \times 20 \mu\text{m}^2$  takes 15 min of exposure time under an electron dose of  $30 \text{ mC/cm}^2$ , 64 dots with the size of  $2 \times 2 \mu\text{m}^2$  take 4 min at  $30 \text{ mC/cm}^2$  and 6 min at  $45 \text{ mC/cm}^2$ . Such a square matrix is depicted in Figure 39. Subsequent amplification of the CTs by SIPGP of *tert*butyl-methacrylate (tBuMA) for 6 h yielded in  $60 \pm 12 \text{ nm}$  thick poly(*tert*butyl-methacrylate) (P(tBuMA)) brushes. The polymer brush height was determined by software-assisted analysis of the depth between bare NCD areas and P(tBuMA) functionalized areas averaged for different spots. P(tBuMA) brushes were chosen because they represent a perfect platform for a polymer analogue reaction on the carboxyl groups after the hydrolysis of the *tert*-butyl moieties. This procedure will be addressed in chapter 4.2.2.2.

The CT-approach provides a direct tool to control not only the 2D locus of the grafting points for the SIPGP reaction but also, by varying the locally applied electron dose, the grafting density of the structured polymer brushes.<sup>[315]</sup> A  $10 \mu\text{m}$  CT gradient on NCD was written by linearly increasing the electron dose to  $100 \text{ mC/cm}^2$  over a range of  $50 \mu\text{m}$  (Figure 40). The required exposure time during CT was 20 minutes. SIPGP of tBuMA resulted in a gradient shaped polymer brush feature with a height plateau reached at approx.  $40 \text{ mC/cm}^2$ . The correlation between polymer thickness and electron dose used for the templating step can be explained by an increase of the polymer grafting density at higher e-beam doses forcing the chains to stretch away from the surface. Presumably, at high electron doses, the polymer height presumably attains the height of the corresponding polymer brush in bulk, according to Zauscher *et al.*<sup>[310]</sup>

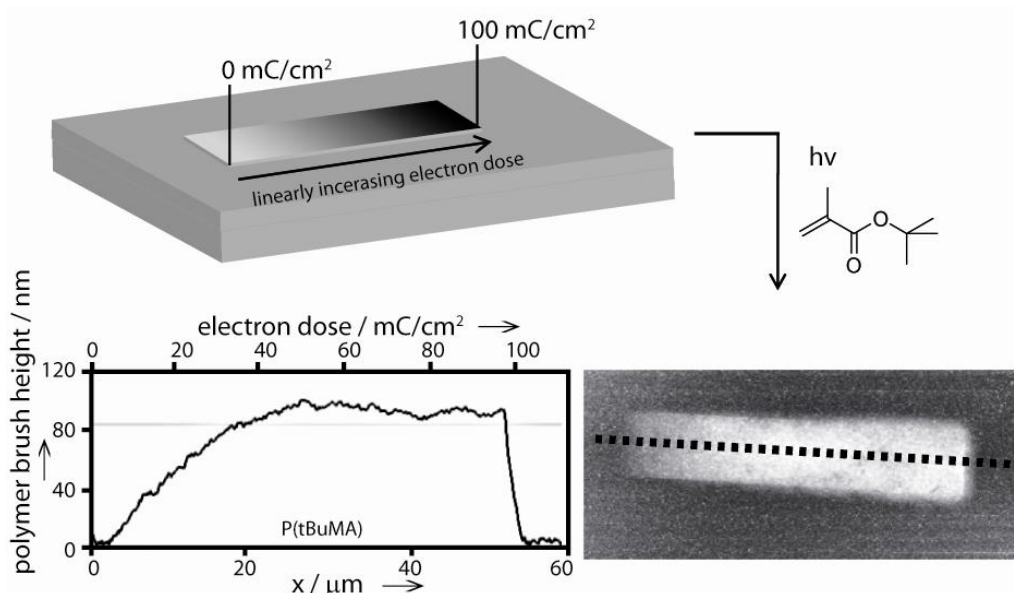


**Figure 40:** Preparation of a  $10 \times 50 \mu\text{m}^2$  sized CT gradient on hydrogenated NCD by linearly increasing the electron dose from 0 to  $100 \text{ mC/cm}^2$ ; SIPGP of tBuMA results in a P(tBuMA) brush gradient selectively on the CT area.

In similar experiments styrene, 2-*iso*-propenyl-2-oxazoline (IPOx), 4-vinyl pyridine, methylmethacrylate (MMA) and *N,N*-dimethyl-aminoethyl methacrylate (MAEMA) were successfully grafted onto gradient carbon templates by means of SIPGP. This shows the large variety of chemical functionalities that can be obtained on NCD surfaces by the combination of CT and SIPGP. It was observed that the profile of all gradients reaches a maximum level at approx.  $40 \text{ mC/cm}^2$  independently on the type of polymer. Table 7 summarizes the polymer thicknesses for different monomers which are reached in the plateau area after the indicated polymerization time. The resulting respective polymer brush gradients including their section analysis are presented in Figure 41.

**Table 7:** Maximal polymer brush height at  $100 \text{ mC/cm}^2$  obtained after SIPGP of various vinyl monomers on a CT gradient.

Monomer	Polymer brush height at $100 \text{ mC/cm}^2$	polymerization time
styrene	$105 \pm 15 \text{ nm}$	24 h
methyl methacrylate	$110 \pm 10 \text{ nm}$	6 h
<i>tert</i> -butyl methacrylate	$90 \pm 5 \text{ nm}$	8 h
dimethyl-aminoethyl methacrylate	$45 \pm 8 \text{ nm}$	2 h
4-vinyl pyridine	$20 \pm 5 \text{ nm}$	24 h
2- <i>iso</i> -propenyl-2-oxazoline	$25 \pm 2 \text{ nm}$	20 h

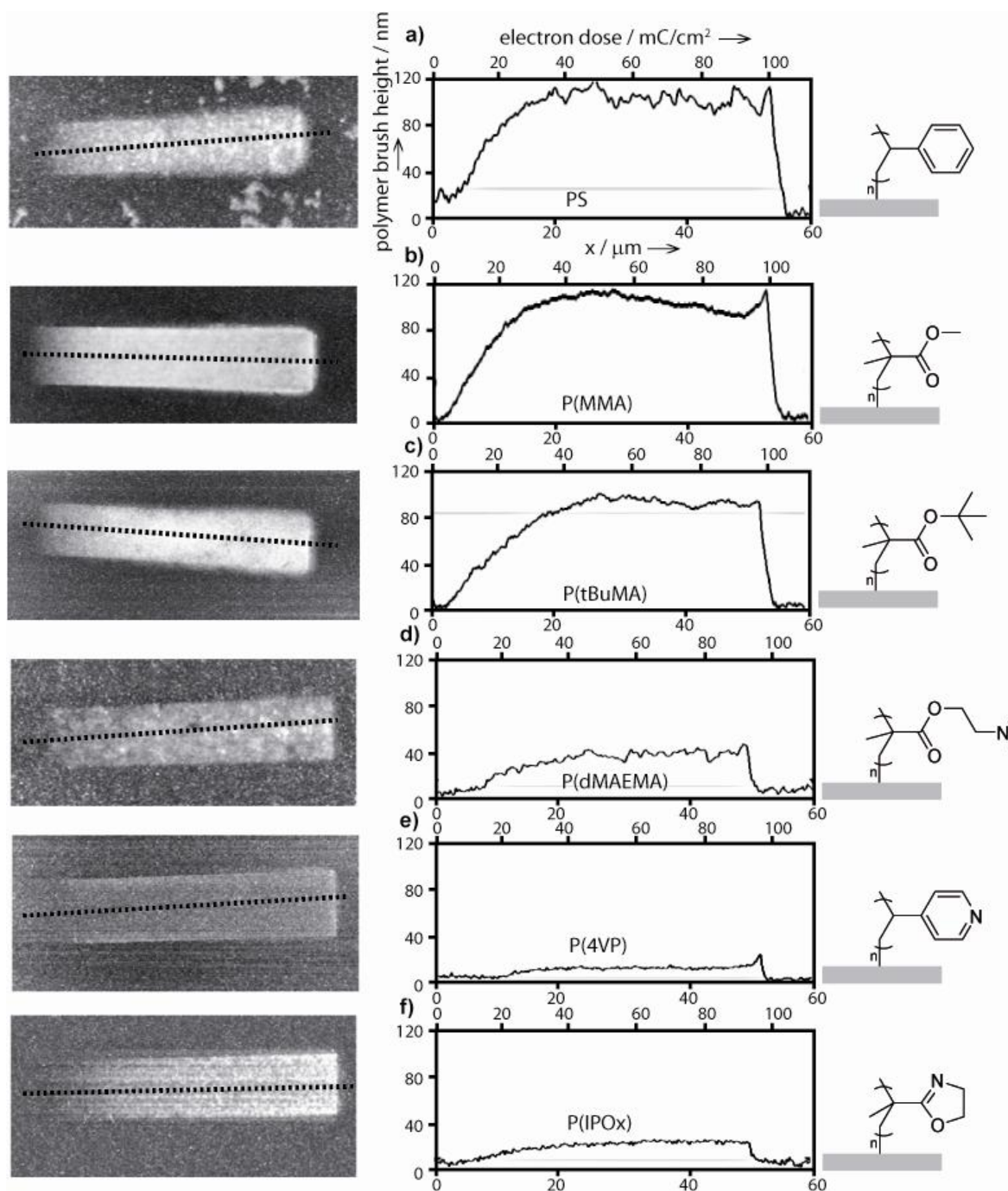


**Figure 41:** left: AFM images of a) PS, b) P(MMA), c) P(tBuMA), d) P(dMAEMA), e) P(4VP), f) P(IPOx), gradients on NCD prepared by CT and SIPGP; right: AFM section analysis along the indicated areas.

In order to investigate the minimal structure size which can be resolved by the CT-technique on NCD, 10  $\mu\text{m}$  long carbon template lines with widths varying from 2  $\mu\text{m}$  down to 5 nm were created on a freshly hydrogenated NCD substrate. Figure 42 shows the AFM scan of the resulting polymer brush structures after SIPGP of IPOx. The amplification of the carbon template structures could be detected by AFM for carbon templates with a line width down to 50 nm, whereas thinner lines (line width of 5 and 10 nm) could not be observed because of the surface roughness. It has been shown recently by theoretical <sup>[316]</sup> as well as

experimental<sup>[317],[310],[276]</sup> studies that the thickness of nanostructured polymer brushes correlates with the footprint structure size. This is due to the overlap of the grafted chains over the grafting regions into the polymer-free surface regions in order to minimize entropic energy which also results in a broadening of the polymer structures.<sup>[318]</sup> On this account, the impossibility to visualize the polymer brush structures on the AFM height section analysis in Figure 2 for the 10 and 5 nm wide lines does not necessarily prove the absence of grafted polymer chains, but is most probably due to the poor signal-to-noise ratio of the very thin polymer brushes on the rough NCD substrate.

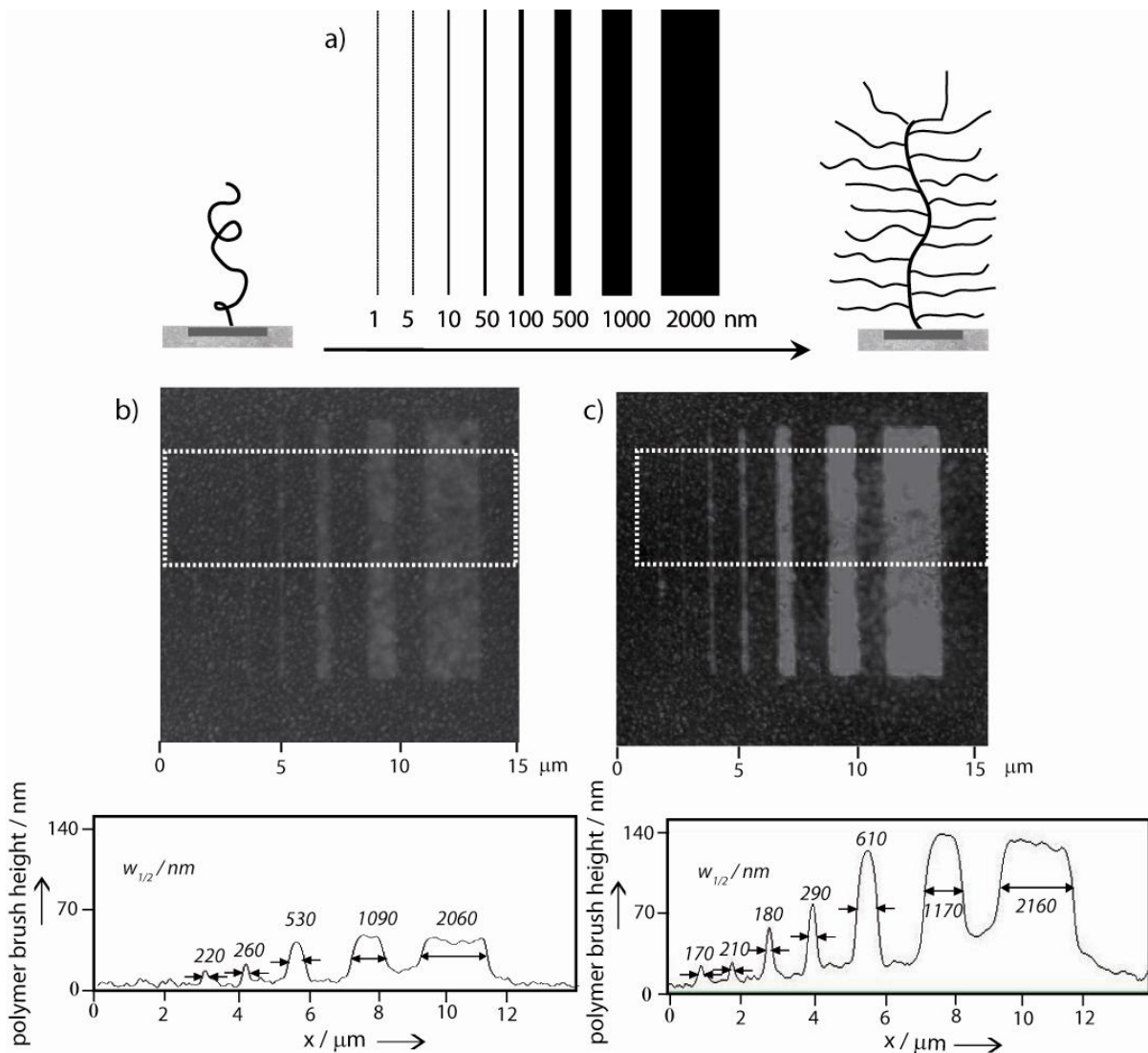


**Figure 42:** a) Template structure design for the preparation of structured P(IPOx) polymer brushes and P(IPOx-g-EtOx) bottle-brush brushes on NCD by carbon templating; b) AFM scan and section analysis of structured P(IPOx) brushes on NCD prepared by the SIPGP of 2-iso-propenyl-2-oxazoline; c) AFM scan and section analysis of structured P(IPOx-g-EtOx) BBBs after LCROP with 2-ethyl-2-oxazoline initiating from the pendant oxazoline moieties of the structured P(IPOx) brushes. The section analysis are averaged at the indicated areas and the structure line widths are indicated for half height ( $w_{1/2}$ ).

To investigate the presence of polymer brushes on the 10 and 5 nm wide carbon templates, the P(IPOx) brush structures were further amplified by an additional polymerization step. The pendant oxazoline rings of the P(IPOx) brushes were converted to P(IPOx-g-EtOx) BBBs by living cationic ring-opening polymerization (LCROP). In Figure 42, the height profile of the polymer structures is depicted for P(IPOx) as well as for the resulting P(IPOx-g-EtOx) BBBs. In agreement with previous studies and the results presented in chapter 4.1.1.2,<sup>[308]</sup> a thickness increase of approximately 200% was found after the side chain LCROP. Notably, carbon templates with line width of 10 as well as 5 nm could be detected after the second polymerization step, unambiguously proving the previous presence of a very thin but still chemically active P(IPOx) brush layer. These experiments could show that the CT-technique can be applied to create a chemical contrast on hydrogenated diamond surfaces with sub-10 nm resolution. Figure 43 additionally demonstrates the influence of the lateral feature size on the polymer brush height. It is in good agreement with studies from Zauscher *et al.*<sup>[310]</sup> who found a strong increase of the polymer brush height with increasing feature width for small footprint sizes and eventually a leveling off for larger pattern widths.

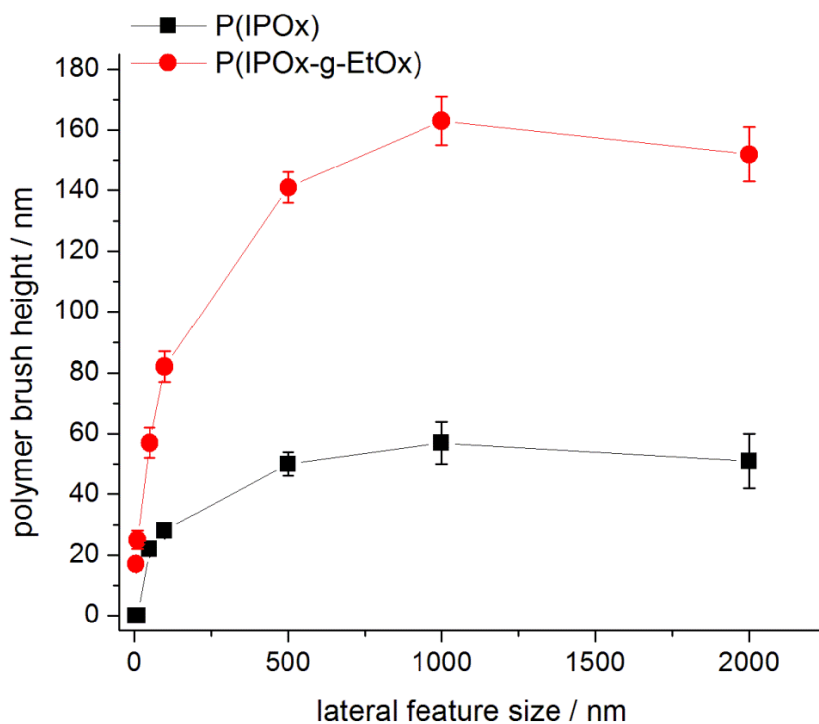


**Figure 43: Dependence of the polymer brush height on the lateral feature widths of the carbon template structures.**

#### 4.1.2.2 EBL with an electron microscope without a lithography tool

With the perspective of applying EBL to larger diamond surface areas the general feasibility of carbon templating in a common electron microscope (EM) was demonstrated. Since this technique lacks a lithography program, CTs were generated by screening the electron beam over  $100 \mu\text{m}^2$  of the freshly hydrogenated NCD. Although the external control over the process is more difficult than in an E-Line very homogeneous and well-defined P(tBuMA) structures could be generated by the amplification of the CTs by the SIPGP ( $t_p = 6 \text{ h}$ ) of tBuMA (Figure 44). Since exposure to the electron beam was achieved through a preset aperture size, the resulting polymer features show a dot shape. The value of the exact applied electron dose is higher but not exactly determinable when using a common electron microscope. However, the comparison of the polymer brush height of  $240 \pm 10 \text{ nm}$  compared to results from E-Line fabricated patterns with a height of  $60 \pm 12 \text{ nm}$  (compare Figure 39 from chapter 4.1.2.1) suggests an electron dose of largely above  $50 \text{ mC/cm}^2$ . This is corroborated by the fact that the brush thickness is even higher at the  $1 \mu\text{m}$  sized features by common EM compared to the  $2 \mu\text{m}$  sized features from Figure 39. According to the brush height - footprint size relation described by Patra, Linse and Zauscher,<sup>[310]</sup> this observation can thus only be attributed to an increased grafting density under a higher electron dose.

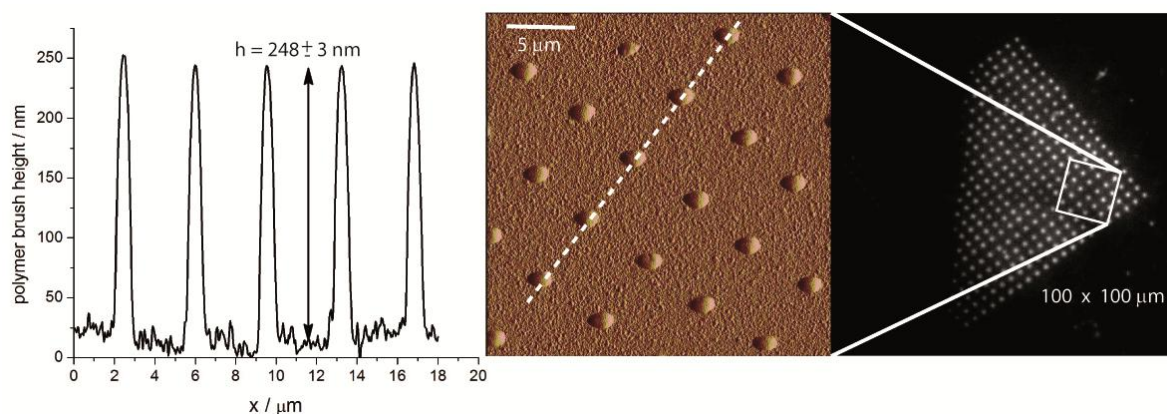


**Figure 44: P(tBuMA) brushes on NCD structured by the CT technique in a common electron microscope. AFM section analysis along the indicated area of the AFM scan image; right: overview over the entire structured area by fluorescence microscopy; the fluorescence was obtained by coupling of the green fluorescent protein into poly(methacrylic acid) brushes after hydrolysis of P(tBuMA). The chemical procedure will be disclosed in chapter 4.2.**

### 4.1.3 Electric field-induced lithography on $\text{SiO}_x$

In the course of a research stay at the Duke University in Durham, North Carolina, in the research laboratories of Prof. Zauscher, electric field-induced lithography (EFIL) technique for patterning of silane-modified semiconductor or metal surfaces was investigated. This method offers the prospect of fabricating polymer brushes with different functionalities on one surface. As introduced in chapter 2.2.3.5, EFIL is based on the local formation of an oxide layer under an applied potential between the AFM tip and a conducting surface. For the first time, EFIL on  $\text{SiO}_x$  surfaces was combined with the preparation of structured polymer brushes by atom transfer radical polymerization (ATRP). The procedure is outlined in Figure 45.

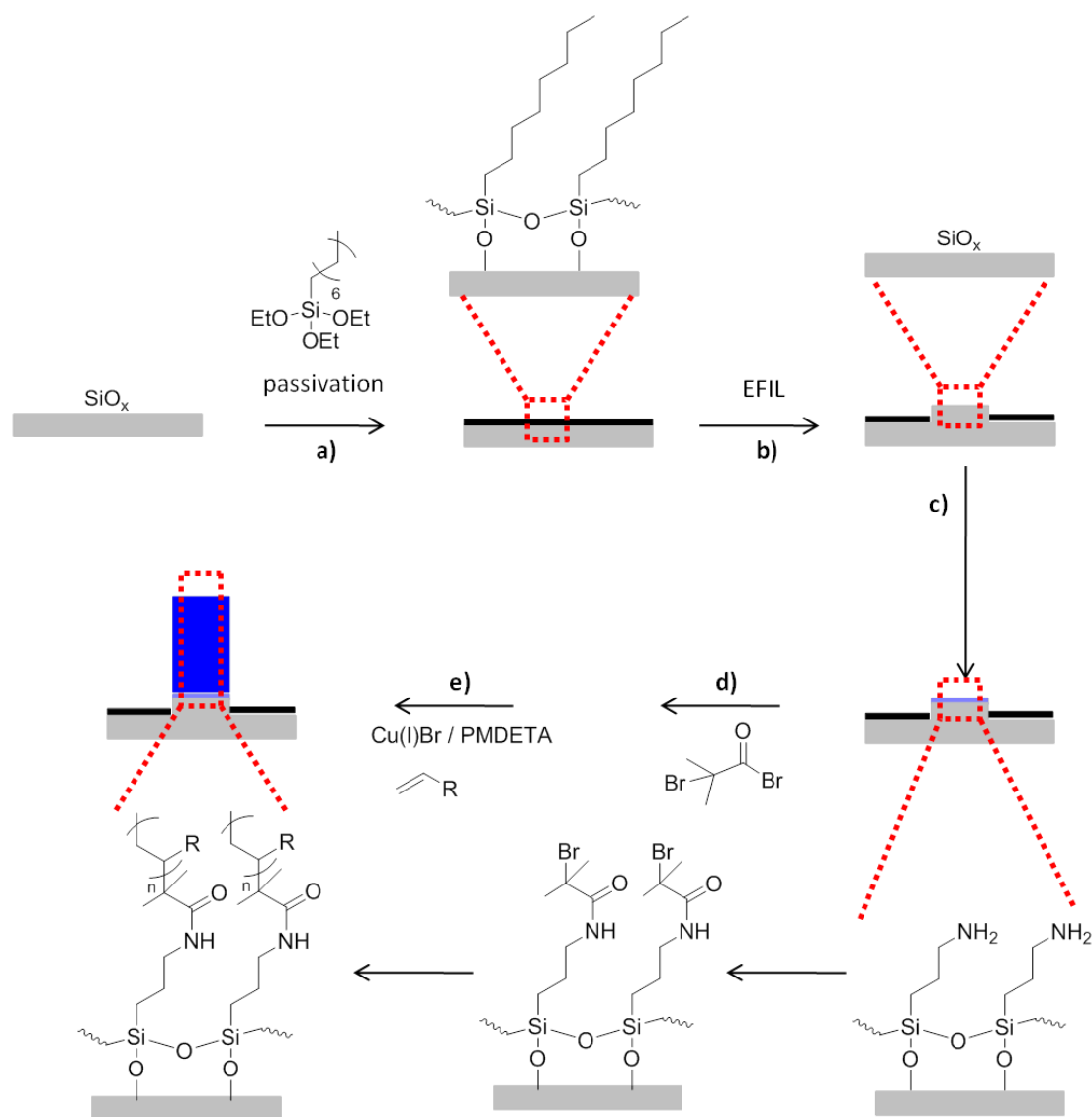


**Figure 45:** Preparation of structured PMAEMA brushes by EFIL and subsequent ATRP. a) passivation of the  $\text{SiO}_x$  surface with OTES; b) formation of an oxide layer by EFIL; c) backfill of the formed oxide areas by silanization with functional APTES; d) conversion of the terminal amine function into an SI-ATRP initiator with bromoisobutyryl bromide; e) ATRP of MAEMA resulting in PMAEMA brushes on the EFIL-treated surface areas.

A freshly cleaned p-type hydroxyl-terminated  $\text{SiO}_x$  surface was passivated in a solution of octyltriethoxysilane (OTES) in dry toluene. After thorough ultrasonication, the APTES-functionalized sample was locally oxidized in an Asylum AFM by applying a bias of -10 V between the tip and the surface while scanning in contact mode with a scan rate of 500 nm/sec. The freshly formed patterns of  $\text{SiO}_x$  were subsequently functionalized with 3-aminopropyltriethoxysilane (APTES) in dry ethanol and converted to an SI-ATRP initiator with bromo-*isobutyryl* bromide. *N,N*-dimethylaminoethyl methacrylate (MAEMA) was used as model monomer and converted into PMAEMA brushes with Cu(I)Br and pentamethyldiethylenetriamine as ligand (PMDETA) in a well-degassed aqueous solution at room temperature. In order to estimate the polymer brush growth rate on  $\text{SiO}_x$  via ATRP, the polymerization of MAEMA was performed under different reaction times. The polymer layer thickness on non-structured samples was determined by AFM measurements on a surface scratch. The resulting linear dependence between polymerization time and polymer layer thickness indicates that early termination due to oxygen contamination in the reaction vial is not an issue under the applied experimental setup (Figure 46) and that the SIP most probably follows a controlled radical polymerization mechanism. While a detailed description of the ATRP process would go far beyond the scope of this study, it is known that for the steady-state of the catalytic cycle of Cu(I) to Cu(II) the right balance of oxygen content is crucial. Therefore, a blue coloring of the reaction solution implying the formation of ligand-coordinated Cu(II) would signify the stop of the ATRP reaction.

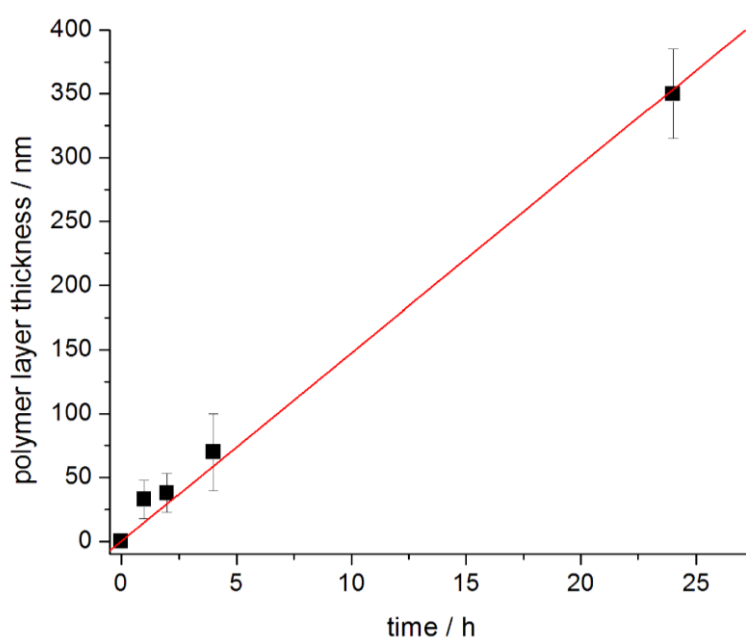
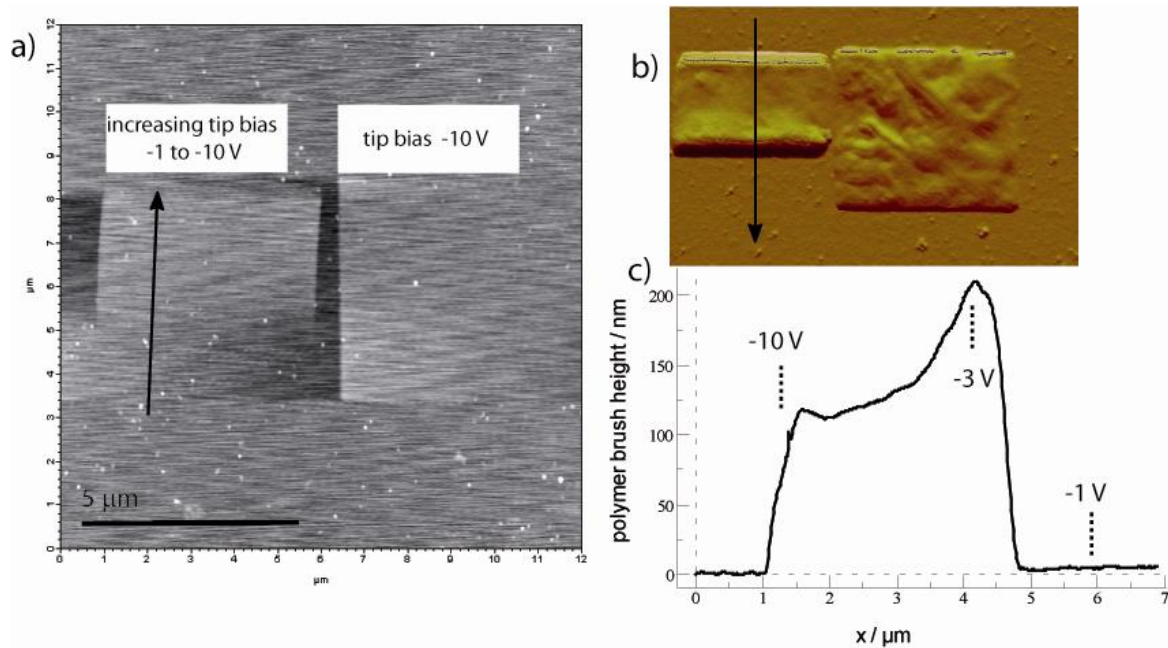


Figure 46: Resulting polymer brush heights determined by AFM after different ATRP reaction times.

In the first experiments,  $5 \times 5 \mu\text{m}^2$  boxes were oxidized with a tip bias of  $-10 \text{ V}$ . The resulting oxide layers can be resolved in AFM with an average thickness of  $2.5 \pm 0.5 \text{ nm}$ . Amplification by ATRP of MAEMA for 20 hours led to the formation of approximately  $200 \text{ nm}$  thick, homogeneous polymer brushes exclusively at the surface areas processed with EFIL. The resulting layer thickness lies in good agreement with the value expected from the preliminary kinetic studies. Despite harsh reaction conditions for the formation of the ATRP initiator, the OTES passivation layer undoubtedly remained intact. In a next step, the influence of the applied tip potential on the resulting polymer brush height was investigated. Therefore, both a  $5 \times 5 \mu\text{m}^2$  box with a tip voltage of  $-10 \text{ V}$  - serving as point of recognition - and a  $5 \times 5 \mu\text{m}^2$  box, processed by increasing the absolute value of the applied tip voltage from  $-1 \text{ V}$  to  $-10 \text{ V}$ , were written on an OTES passivated  $\text{SiO}_x$  surface. Figure 47 presents the AFM scan over the freshly prepared oxide layer (a) and over the PMAEMA polymer layer after ATRP over night (b).



**Figure 47:** EFIL and subsequent ATRP on  $\text{SiO}_x$ ; a) AFM (Asylum) scan over the freshly generated oxide layers immediately after EFIL; b) AFM (DI) scan over the PMAEMA brushes after ATRP; c) AFM section analysis measured at the indicated area with indication of the corresponding potential applied between tip and surface during previous EFIL.

In contrary to expectations arising from the results from CT, the AFM section profile over the PMAEMA brushes (c) does not reveal the same shape as the oxide layer profile. At areas written with  $-10 \text{ V}$ , thus providing the thickest and densest oxide layer, the polymer brush height is around  $120 \pm 10 \text{ nm}$ . A maximum can be observed for a bias of  $-3 \text{ V}$ . Apparently, weaker tip voltage ( $< |-3 \text{ V}|$ ) does not provide a platform for amplification *via* ATRP,

probably because the oxidative energy is not sufficient to penetrate the silane passivation layer or to convert Si into  $\text{SiO}_x$ . The behavior found between -3 and -10 V is still not fully understood. Influencing factors are the grafting density of the passivation layer, the density and homogeneity of the oxide after EFIL, the formation of local surface charges and the quality of the backfilled APTES, but their exact interaction remains unknown. Pretests for the combination of preparing polymer brush structured by SIPGP and ATRP on the same samples were carried out during the research stay. Further optimization and detailed analysis are currently under investigation.

#### 4.1.4 Thermal structuring of poly(1-ethoxyethyl methacrylate) brushes

Inspired by work of Du Prez *et al.* [319] who prepared homogeneous bulk poly(methacrylic acid), P(MA), or poly(acrylic acid), P(AA), by thermal deprotection of poly(1-ethoxyethyl methacrylate), it was investigated whether this approach could as well be applied for the functionalization of  $\text{SiO}_x$  surfaces. Moreover, the completely chemical-free thermolysis strategy to obtain P(MA) brushes might be used for the locally selective conversion of poly(methacrylic ester)s to yield patterned P(MA) brushes. The two-step approaches based on protected acrylic or methacrylic esters are favored over the direct polymerization of acrylic or methacrylic acid because SIPGP does not yield in homogeneous polymer brushes and ATRP is impossible due to interactions of the copper catalyst with the monomer. [320]

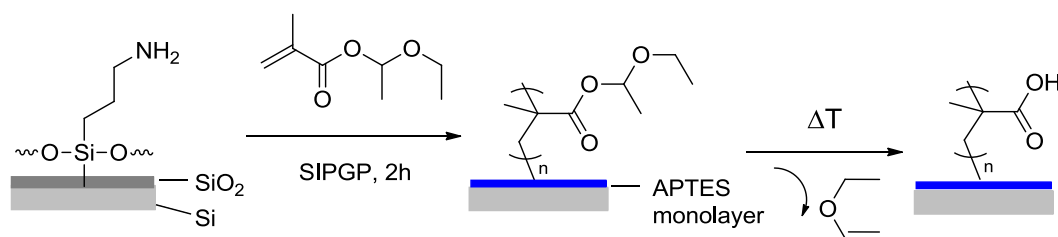


**Figure 48: Thermolytic deprotection of poly(1-ethoxyethyl methacrylate) brushes.**

The synthesis of 1-ethoxyethyl methacrylate (EEMA) was carried out according to literature. [319] Freshly cleaned  $\text{SiO}_x$  samples were functionalized with 3-3-aminopropyltriethoxy silane (APTES) to provide reactive terminal groups (contact angle =  $43 \pm 2^\circ$ ). After thorough ultrasonication, the surface was irradiated in bulk 1-ethoxyethyl methacrylate for 2 hours under UV light for the SIPGP (Figure 48). An  $120 \pm 30$  nm thick P(EEMA) layer was formed which showed a contact angle of  $89 \pm 5^\circ$  and the characteristic acetal band at  $1033 \text{ cm}^{-1}$  in FT-IR.

First, the thermolysis was carried out by exposing the P(EEMA)-functionalized surface in a drying oven to 150°C for 2 hours. A lower contact angle of  $73 \pm 3^\circ$  and a shift in the carbonyl C=O area in FT-IR indicate a chemical conversion of the P(EEMA) layer. The acetal band is reduced but still clearly visible which signifies an incomplete deprotection. In order to obtain quantitative thermolysis and to use this surface chemistry for the preparation of structured P(MA) brushes, the deprotection step was carried out in a YAG laser set-up. Since the ideal parameters were unknown and hard to predict, the P(EEMA) layer was locally exposed to the laser beam at different powers and different applied pulses per area. The analysis of the obtained structured surface revealed that the energy of the laser beam results in heat-induced irregular buckling of the polymer layer or even complete elimination. Lower laser power in combination with only a few pulses, however, did not provide promising results, either: coupling of a fluorescent marker to the thermally generated P(MA) areas did not reveal a chemical contrast between laser-treated and untreated surface areas. Thus, the thermal deprotection approach does not provide a reasonable alternative to surface chemical conversion processes yielding in P(MA) brushes. As outlook for future work, one might consider the local heating by an AFM tip, instead of laser irradiation. The acidic hydrolysis of protected poly(methacrylic acid) derivatives will be presented in chapter 4.2.2.2

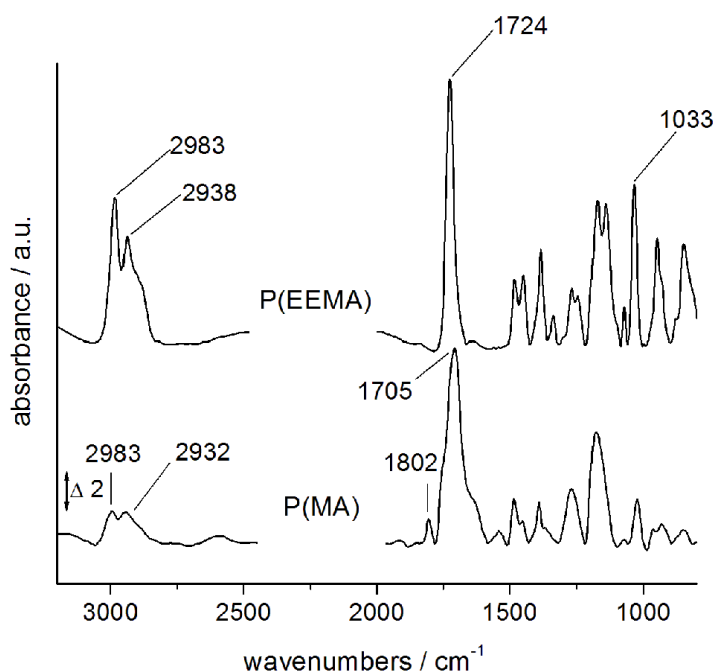


**Figure 49:** FT-IR spectrum of P(EEMA) and P(MA) brushes after thermolysis at 150°C on SiO<sub>x</sub>.

## 4.2 Biofunctionalized polymer brushes

In the following chapters, a substance class will play a key role which is *per se* usually not compatible with metals and semiconductors found in electronic devices: proteins and enzymes. In order to provide a suitable basis for the results on polymer-bound biomolecules, their main features and characteristics will be summarized within the next paragraph.

### 4.2.1 Background on proteins and enzymes

Proteins are biomacromolecules consisting of amino acids which are connected via peptide bonds between the  $\alpha$ -carboxyl group of one amino acid and the  $\alpha$ -amino group of another. Their molecule geometry is defined through their primary (the sequence of aligned amino acids), secondary (local three-dimensional structure elements, e.g.  $\alpha$ -helices), tertiary (all three-dimensional aspects of the folded polypeptide) and their quaternary structure (the arrangement of, if existent, different polypeptide subunits). The interaction between amino acid side chains induces folding and eventual formation of a complex 3D entity and leads to the very unique properties of these biomolecules as well as their very specific biological functions. Enzymes are proteins but with the ability to catalyze chemical reactions. While some can perform without additional components, other enzymes require the incorporation of special chemical groups into the apoenzyme, referred to as a cofactor (inorganic ions, e.g.  $\text{Fe}^{2+}$ ,  $\text{Mg}^{2+}$ ,  $\text{Zn}^{2+}$  or a more complex metalorganic molecule). The major feature of enzyme-mediated reactions is that the reaction takes place in the active site of the enzyme, a specific environment, designed for the respective reaction. The reaction rate of the enzyme-catalyzed transformation is increased as the enzyme lowers the activation energy of the conversion (Figure 50).<sup>[194],[321]</sup> The catalytic potential of enzymes is considerable. Rate enhancements of 5 to 17 orders of magnitude were reported.<sup>[321]</sup> Since the geometry and reactivity of an enzyme are perfectly well-defined, the catalyzed reaction is restricted to a small substance class or even one specific substrate.

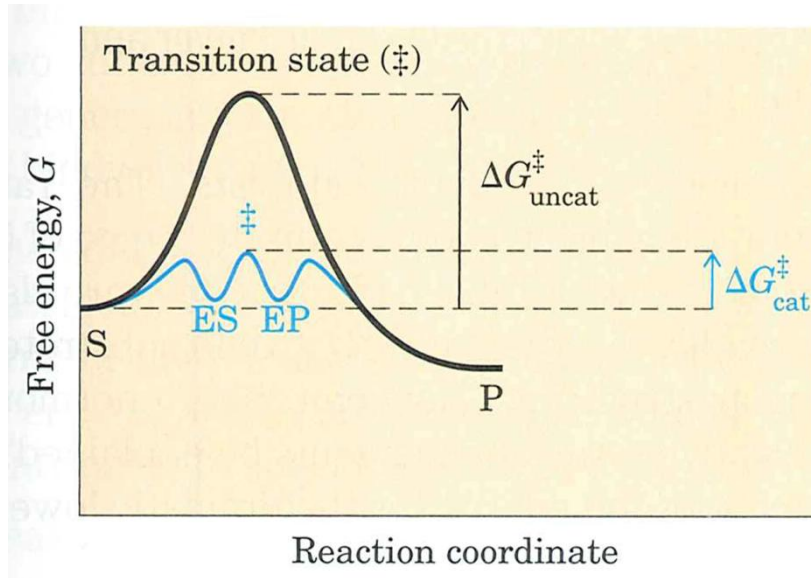
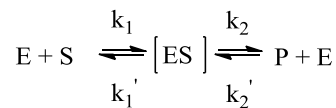
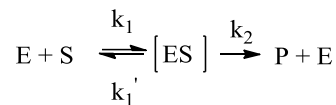


Figure 50: Reaction coordinate diagram of an enzyme-catalyzed reaction under the formation of an enzyme-substrate (ES) and enzyme-product (EP) complex (blue) compared to an uncatalyzed reaction (black). From <sup>[321]</sup>

Kinetic investigations have disclosed a so-called Michaelis Menten dependence for a typical enzyme-catalyzed reaction. The essential of the theory is the formation of an enzyme-substrate complex ES.



Two assumptions have to be made. First, under enzymatic reaction conditions, there is no back reaction of P with E, simplifying the reaction pathway to:



Second, most enzymes can balance unsteady substrate concentrations and therefore, the concentrations of [ES] remains constant:  $\frac{d[ES]}{dt} = 0$

The concentration of [ES] can be expressed by:

$$[ES] = \frac{k_1}{k_1'k_2} [E][S]$$

Eq. 5

And with the introduction of the Michaelis-Menten constant  $K_M = \frac{k_1'k_2}{k_1}$  by:

$$[ES] = \frac{[E][S]}{K_M}$$

**Eq. 6**

Since  $[E]$  is not necessarily known, it can be expressed by  $[E] = [E_0] - [ES]$  and replaced in Eq. 6, giving:

$$[ES] = [E_0] \frac{[S]}{K_M + [S]}$$

**Eq. 7**

The enzymatic reaction rate is

$$v = \frac{dP}{dt} = k_2[ES] = k_2[E_0] \frac{[S]}{K_M + [S]}$$

**Eq. 8**

When the reactive site of the enzyme is saturated with substrate ( $[ES] = [E_0]$ ), the maximum reaction rate is defined as:

$$v_{max} = k_2[E_0]$$

**Eq. 9**

Therefore, the final reaction rate can be expressed by:<sup>[194]</sup>

$$v = \frac{dP}{dt} = v_{max} \frac{[S]}{K_M + [S]}$$

**Eq. 10**

A general test for a Michaelis-Menten behavior is to plot the reaction rate versus the substrate concentration. At high  $[S]$ , the observed curve should reach a saturation giving the value for  $V_{max}$ .

However, all theoretical mechanistic descriptions risk to become obsolete when the enzyme is exposed to changes of the external conditions, which might only alter slightly from their native environments, leading to the loss of their function. This induced damage is called denaturation and is usually the result of structural changes in the folding conformation. Due to their sensitivity, suitable immobilization techniques and environments need to be minded. The strategies used in the course of this project will be addressed in the following chapters.

## 4.2.2 Coupling strategies for biomolecules

### 4.2.2.1 Preparation of biofunctionalized poly(2-oxazoline)e bottle-brush brushes

Bottle-brush molecular structures have gained interest in the design of functional polymers with tailor-made architectures. As they are related to the structure of glycosylated macromolecules located on nearly every living cell,<sup>[230],[231]</sup> bottle-brush polymers have biocompatible and biomimetic potential. Since it has been shown that poly(2-oxazoline)s are non-toxic and that proteins as well as drugs can be coupled to the polymer without losing their activity<sup>[214],[212]</sup> POx-based BBBs appear to be an expedient choice as a matrix for biomolecule immobilization on surfaces. Here, proteins and enzymes were attached to functional groups in the BBB chain ends as displayed schematically in Figure 51.

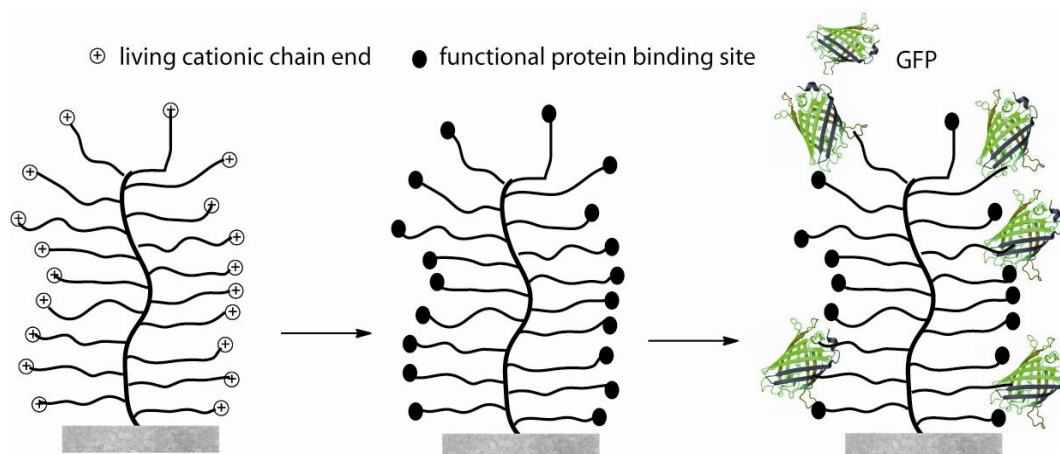


**Figure 51:** Schematic pathway towards biofunctionalized bottle-brush brushes; selective termination of the cationic chain ends with a bifunctional terminating agent and subsequent coupling of the green fluorescent protein (GFP) into poly(2-oxazoline) bottle-brush brushes (BBBs).

Poly(2-oxazoline) based bottle-brush brushes (BBBs) were prepared analogue to chapter 4.1.1.2 and 2-ethyl-2-oxazoline (EtOx) was used as the monomer for the side chain polymerization. LCROP reaction time was reduced to 4 hours at 80°C in an oil bath or 20 minutes at 70°C in the microwave to minimize high side-chain crowding and early uncontrolled termination. The reason for choosing EtOx from all available oxazoline monomers is the right balance between well-controllable reaction rate during LCROP, hydrophilicity and low non-specific protein adsorption investigated by Dr. Ning Zhang.<sup>[232]</sup> The LCROP grafting was terminated with bifunctional terminating agents (Figure 52). The possibility of systematically introducing functional end groups to surface grafted POx bottle-

brushes has previously been demonstrated by reacting amine end groups with rhodamineB *isothiocyanate* and by analyzing the resulting fluorescence.<sup>[308]</sup> Here, an amine moiety (primary or secondary) served to react with the living side chain ends whereas a protected carboxylic acid function was scheduled for proximate coupling reactions. This implies reagents such as 1-boc-piperazine and methyl-*isonipectoate*, but also substances derived from natural amino acids such as 1-boc-piperazine and L-prolin-*tert*butyl ester. The latter two compounds will be the ones addressed in this chapter. The protection served to avoid side reactions with the reactive oxazolinium species during termination, like the coupling of two adjacent brushes or termination with the non-preferred moiety.

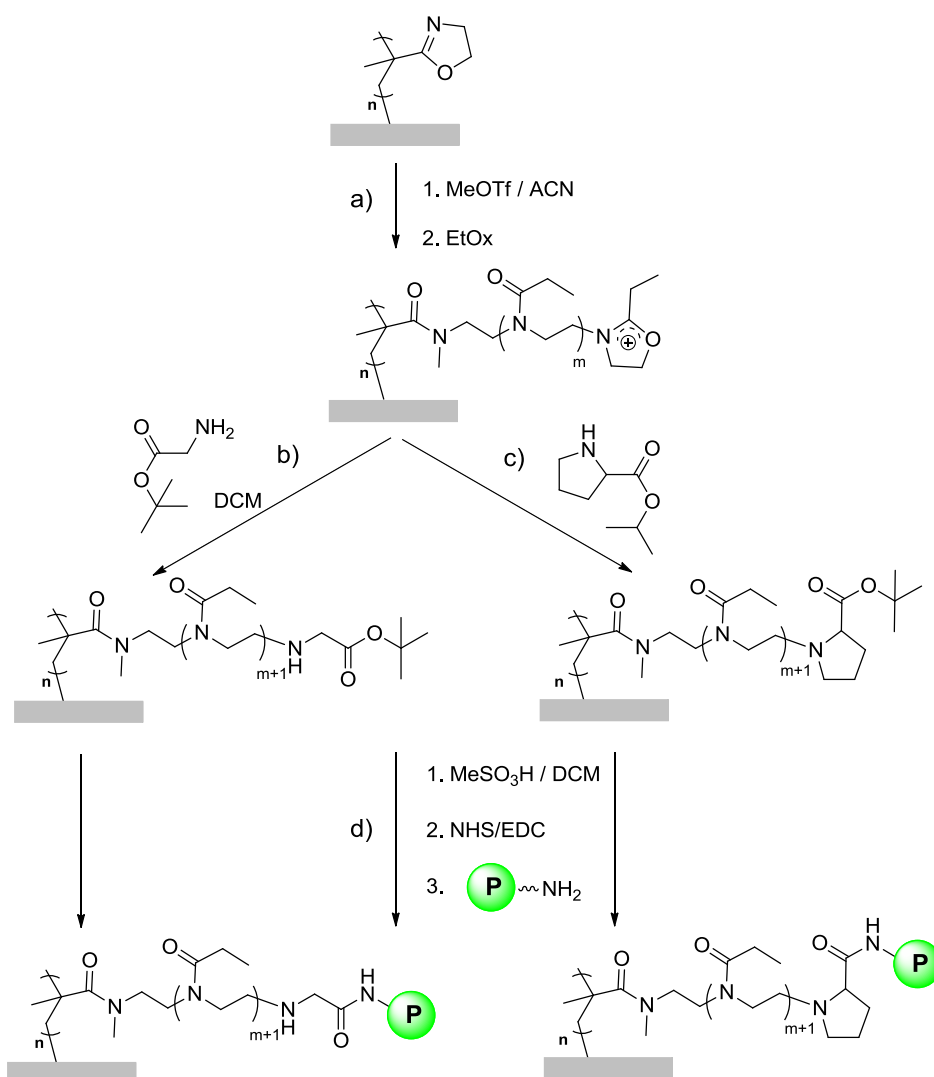


**Figure 52:** Formation of biofunctionalized BBBs on NCD or SiO<sub>x</sub>. a) conversion of P(IPOx) brushes with 2-ethy-2-oxazoline in a LCROP reaction; termination of the living cationic side chain ends with the bifunctional terminating agent b) glycine-*tert*butyl ester or c) prolin-*tert*butyl ester; d) saponification of the protected chain ends to form free carboxyl moieties; subsequent activation of the carboxyl groups with EDC and NHS and subsequent formation of an amide bond between BBB and enzyme.

After deprotection with methylsulfonic acid in DCM and thorough cleaning by ultrasonication, the free carboxylic moieties were activated in *N*-hydroxysuccinimide/1-ethyl-3-(3-dimethylaminopropyl)carbodiimide (NHS/EDC) and reacted with an enzyme in buffer solution overnight. Since harsh ultrasonication can influence the sensitive conformation of the biomolecule potentially causing denaturation, the samples were cleaned by thorough rinsing with buffer and were kept in a shaker for one hour in order to remove physisorbed enzyme. The biofunctionalized diamond surfaces were stored in buffer for at least three days before further investigation. This, in addition to the results on low non-specific adsorption into P(EtOx) BBBs by Dr. Ning Zhang, strengthens the assumption that the enzymes are coupled covalently.

For all experiments, the results on structured surfaces are demonstrated for polymer brushes on carbon templates of a  $10 \times 50 \mu\text{m}^2$  gradient which was prepared by running a focused electron beam at increasing electron doses from 0 to  $50 \text{ mC/cm}^2$  on  $\text{SiO}_x$  and from 0 to  $100 \text{ mC/cm}^2$  on freshly hydrogenated NCD. A polymer brush gradient is a convenient approach to analyze in a single experiment the conjugation of bulky biomolecules within polymer brushes of different grafting densities and thicknesses. Initially, the green fluorescent protein (GFP) was chosen as a test protein (fluorescence analysis is presented in chapter 4.2.3.1) and the different reaction stages were followed by AFM and respective section analysis over a CT gradient. In Figure 53 the resulting gradient profiles of PIPOx, glycine-*tert*butylester terminated P(IPOx-g-EtOx) and P(IPOX-g-EtOx)-GFP are presented.

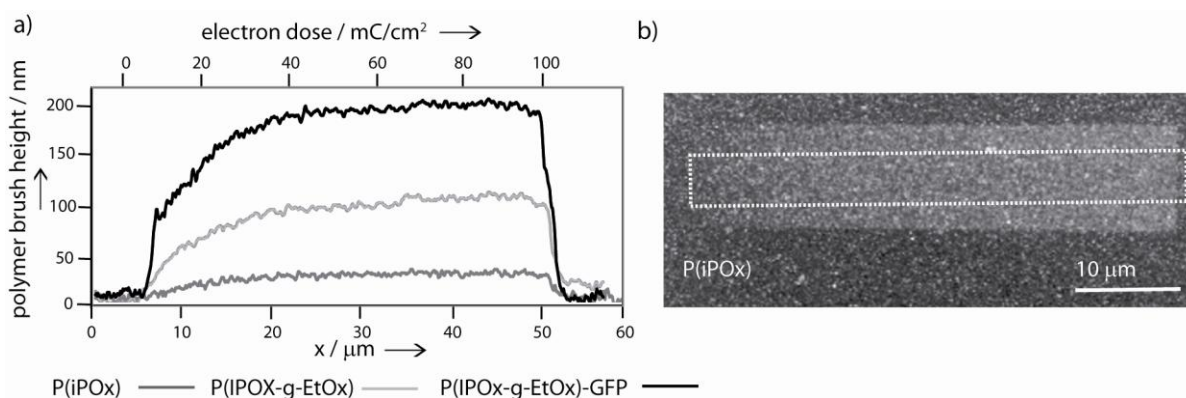


**Figure 53:** a) AFM section analysis at different reaction stages and b) AFM image of P(IPOx) brushes on a  $10 \times 50 \mu\text{m}^2$  CT gradient on NCD; polymer brush height of P(IPOx) (dark grey), P(IPOx-g-EtOx) (pale grey) and GFP-functionalized BBBs (black) versus applied electron dose. Section analysis was performed using height data of the gradient section indicated in b).

After the LCROP, an increase of the polymer layer thickness of around 100 % from  $44 \pm 10 \text{ nm}$  (at maximum layer thickness) to  $90 \pm 8 \text{ nm}$  can be observed which signifies a successful

grafting polymerization of EtOx which is in good agreement with recent results.<sup>[322]</sup> Subsequent to end group hydrolysis and GFP coupling, the gradient profile again drastically increases in thickness by about 100% to  $230 \pm 20$  nm (at maximum layer thickness). This is a good indication for high GFP loading into the polymer brushes.

In order to give an additional proof of principle for the reliability of the termination reaction, X-ray photoelectron spectroscopy (XPS) of differently terminated BBBs on NCD were performed (Figure 55 and Figure 56). In one case, the living  $P(\text{IPOx-g-EtOx})^+ \text{OTf}$  BBB species were terminated with proline-*tert*butylester (Figure 54) and in the other case with fluorophenyl piperazine (Figure 56) which offers the good reactivity of piperazine compounds and the distinctively detectable halogen functionality. Since the discrimination between different compositions which are exclusively composed of N/C/O is very difficult, we used fluorophenyl piperazine as terminating agent (with the characteristic F 1s signal of the fluorine atom) as proof of principle.

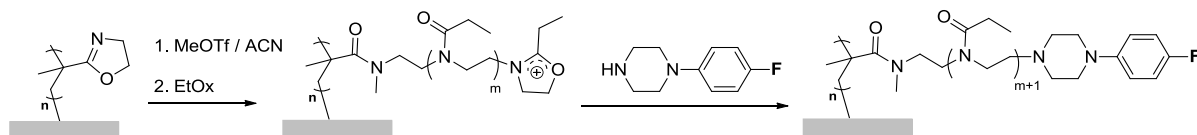


**Figure 54: Conversion of P(IPOx) brushes with 2-ethyl-2-oxaoline in a LCROP reaction and termination of the LCROP with fluorophenyl piperazine.**

Thorough ultrasonication ensured the removal of all physisorbed residues. No F 1s peak can be observed for the termination with the amino acid, thus, all traces of former methyltriflate treatment had been eliminated by the cleaning procedure. Therefore, the fluor response after fluorophenyl piperazine termination can unambiguously be attributed to the side chain end groups of the BBBs. Since the X-ray penetration depth is only around 2 nm, a quantitative analysis to give a representative picture of the N, C, O and F composition was not possible.

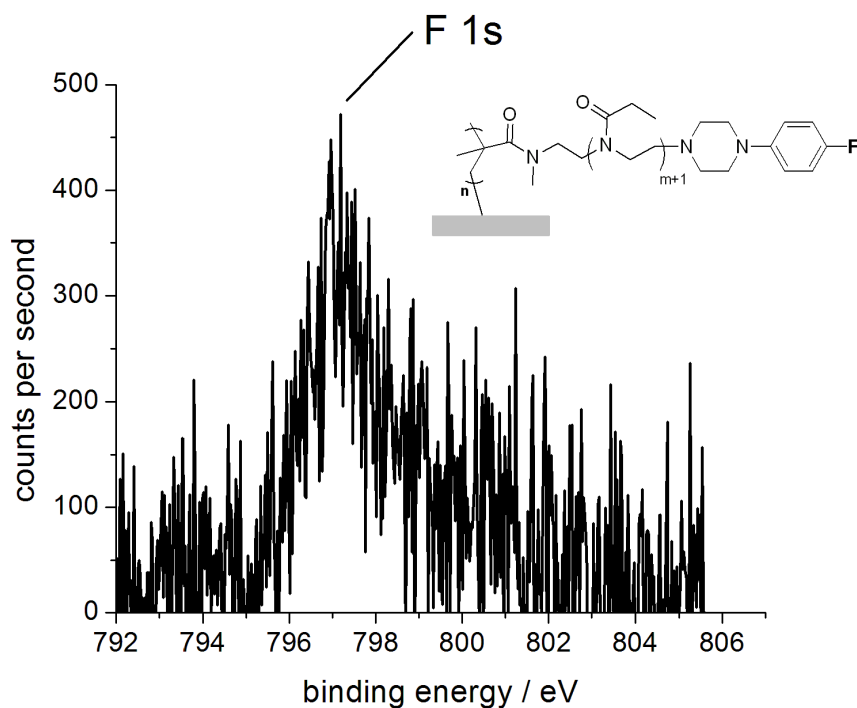


Figure 55: Detail of the XPS spectra for P(IPOx-g-EtOx) BBBs terminated with fluorophenyl piperazine around the F 1s signal.

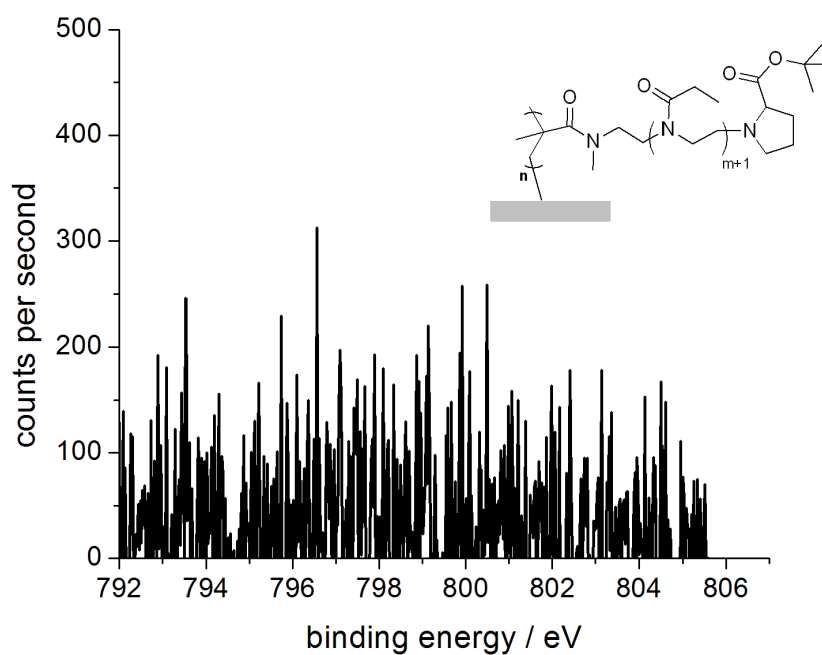
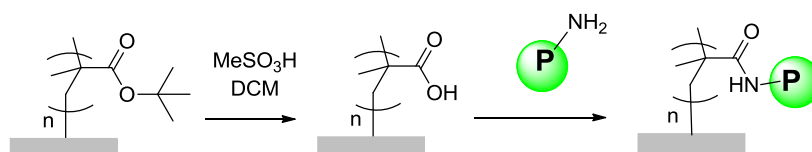


Figure 56: Detail of the XPS spectra for P(IPOx-g-EtOx) BBBs terminated with proline-tertbutylester around the F 1s signal.

#### 4.2.2.2 Biomolecule coupling to poly(methacrylic acid) brushes



**Figure 57: Preparation of biofunctionalized P(MA) brushes.**

Compared to the poly(2-oxazoline)-based multistep approach addressed in the previous chapter, poly(methacrylic acid) brushes (P(MA)) present a straightforward alternative. It is a well-studied and widely used approach for both ionic and covalent attachment for numerous classes of biomolecules.<sup>[204]</sup> A  $10 \times 50 \mu\text{m}^2$  brush gradient of poly(*tert*butyl methacrylate) (P(*t*BuMA)) was prepared by CT and SIPGP (6 hours irradiation time) of *t*BuMA. Hydrolysis was performed with methylsulfonic acid in DCM to yield P(MA) brushes. After NHS/EDC activation, GFP was coupled into the P(MA) brushes to result in polymer brush protein conjugates (Figure 57).

The brush gradient profiles as measured by AFM as well as the thickness decrease of 57% after hydrolysis are in good agreement with results obtained previously on Si surfaces and can be explained by both the removal of bulky *tert*-butyl groups and branched material (Figure 58).<sup>[278],[179]</sup> According to estimations in literature a complete hydrolysis should result in a 52% decrease of the P(*t*BuMA) film thickness.<sup>[175]</sup> After GFP coupling, AFM height profile analysis reveals a thickness increase of the gradient at  $100 \text{ mC/cm}^2$  from  $150 \pm 10 \text{ nm}$  to  $420 \pm 30 \text{ nm}$  after the protein immobilization step (Figure 4c). Although the exact quantity of the protein loading cannot be determined based on these measurements, the remarkable thickness increase can only be explained by multiple protein conjugation to the surface bonded P(MA). By rough estimation, a loading capacity of 45-70 monolayers of absorbed GFP can be found which is in good agreement with similar magnitudes (80 monolayers) reported by Dai *et al.*<sup>[205]</sup>

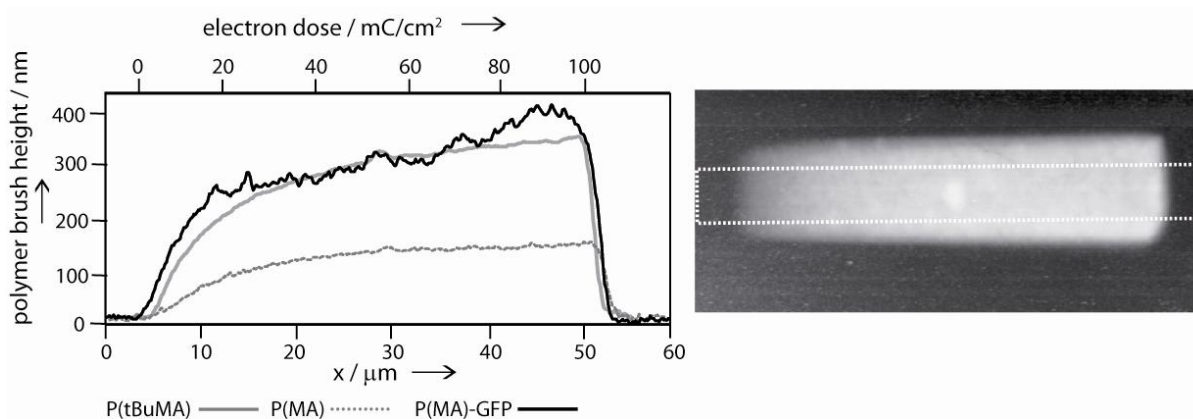


**Figure 58:** AFM section analysis at different reaction stages and AFM image of P(tBuMA) brushes on a  $10 \times 50 \mu\text{m}^2$  CT gradient on NCD; polymer brush height of P(tBuMA) (grey), P(MA) (grey dashed) and P(MA)-GFP (black) versus applied electron dose.

Since the isoelectric point of GFP and the  $pK_a$  value for P(MA) are both around 5, it can be excluded that the protein immobilization at pH 7.5 is due to ionic interactions.<sup>[323]</sup> However, to verify this point, ion exchange experiments with different electrolyte solutions were performed and the functionalized substrate was exposed to different pH and salt concentrations. AFM analysis of the biofunctionalized NCD after exposure to pH 2 and 500 mM NaCl solution did not reveal a significant thickness decrease corroborating a covalent coupling between GFP and P(MA) (Figure 59). Only intensive contact to NaOH solution (1M, over night) in the course of a fluorescence stability experiment (see chapter 4.2.3.1) caused a loss in polymer brush height of around 100 nm.

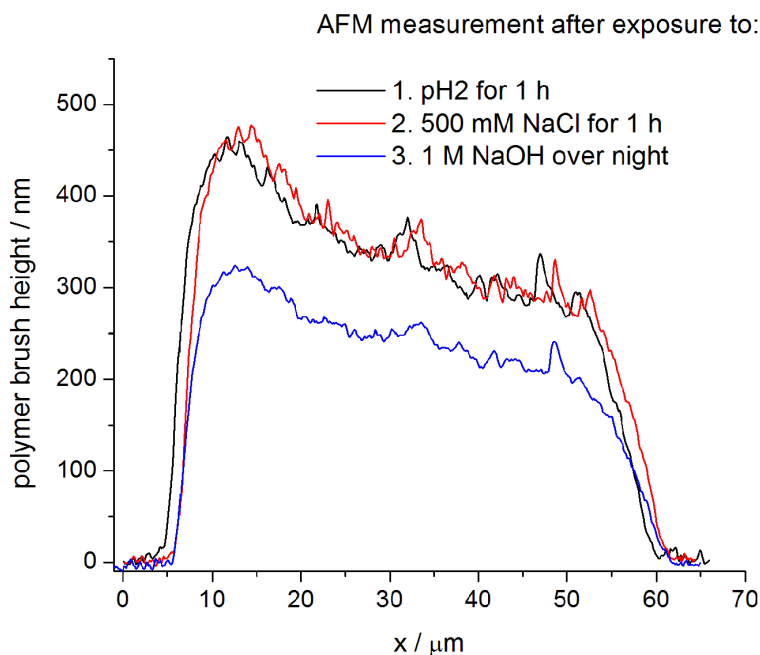


**Figure 59:** AFM section analysis of the P(MA)-GFP gradient after exposure to different aqueous solutions; after 1 h in pH 2 (black), after 1 h in 500 mM NaCl (red), after one night in 1 M NaOH (blue).

A comparable approach based on the direct SIPGP of the NHS-ester of methacrylic acid to create instant protein coupling sites did not provide a useful alternative. Although SIPGP lead to the formation of thick polymer brush layers, they were not reactive for subsequent coupling of biomolecules. This observation is probably due to early loss and inactivation of the reactive NHS leaving group.

The different reaction steps for the preparation of biofunctional P(MA) brushes from P(tBuMA) were also followed by FT-IR spectroscopy (Figure 60) and contact angle measurements (Table 8). It has to be noted that the IR spectra was obtained on a glassy carbon surface which showed the best reflectance performance, while horseradish peroxidase (HRP) was used as model enzyme. In the case of P(tBuMA), the band at  $1720\text{ cm}^{-1}$  can be assigned to the carbonyle ester group and the bands at  $1123\text{ cm}^{-1}$  and  $1236\text{ cm}^{-1}$  to C-O. The band at  $2971\text{ cm}^{-1}$  are only found for P(tBuMA) and belong to the *tert*-butyl group.<sup>[175]</sup> After hydrolysis to P(MA), these signals completely disappear and the spectrum corresponds well to literature reports.<sup>[188]</sup> Subsequent coupling of HRP leads to the appearance of bands in the typical range of amide bonds ( $1800\text{ cm}^{-1}$  -  $1500\text{ cm}^{-1}$ ) and a signal in the aromatic region at  $3011\text{ cm}^{-1}$  which can be assigned to the aromatic amino acids of HRP.

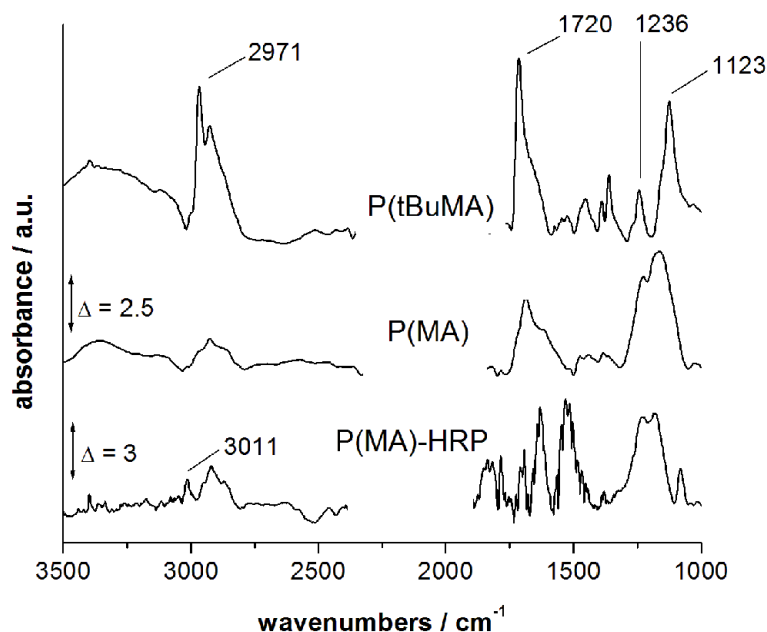


**Figure 60:** FT-IR spectra of P(tBuMA), P(MA) and P(MA)-HRP polymer brushes on a glassy carbon surface.

The relatively high contact angles for protein modified surfaces can be explained by both, the hydrophobic protective domains that serve as protein shell and the slightly increased roughness of the resulting polymer layer.

**Table 8: Contact angles for different NCD surface modifications.**

Sample form	Contact angle $\Theta$ /°
NCD pure	$52 \pm 2$
P(tBuMA)	$80 \pm 4$
P(MA)	$32 \pm 2$
P(MA)-HRP	$50 \pm 3$
P(IPOx)	$60 \pm 4$
P(IPOx-g-EtOx)	$42 \pm 2$
P(IPOx-g-EtOx)-HRP	$52 \pm 1$
P(IPOx-g-CarboxyOx)-HRP <sup>2</sup>	$53 \pm 2$

---

<sup>2</sup> HRP coupled to carboxyl groups in the BBB side chains; details will be disclosed in the following chapter

### 4.2.3 Activity and stability of polymer brush protein conjugates

#### 4.2.3.1 Detection of the green fluorescent protein in fluorescence microscopy

In order to visualize the introduction of a biomolecule into the BBBs, the use of the green fluorescent protein (GFP) is a very effective approach. This protein, acknowledged with the Chemistry Nobel Prize 2008 to Osamu Shimomura, Martin Chalfie as well as Roger Y. Tsien, is characterized by a native fluorescence for excitation wavelengths at both 395 and 475 nm with a major emission peak at 505 nm and an emission shoulder at around 540 nm.<sup>[324],[325],[326],[327]</sup> Among numerous fields of application, GFP was used to monitor selective protein repellent or attracting qualities of polymer brush layers.<sup>[328]</sup> Conveniently, the photophysical properties on GFP correlate with its nativeness, so that the fluorescence spectra of the protein allows to determine that no protein denaturation occurred.<sup>[329],[330]</sup> Inverted fluorescence microscopy measurements of the intensively cleaned biofunctionalized polymer brush gradients showed the selective covalent immobilization of GFP into P(MA) and end-group functionalized P(IPOx-g-EtOx) brushes (Figure 61). Since partially denaturated GFP loses its characteristic photophysical properties, the detection of fluorescence is a clear indication for the presence of native GFP coupled to the polymer brush.<sup>[328],[329]</sup>

Figure 61 displays the height profiles and fluorescence intensities obtained by AFM and fluorescence microscopy (FM) of both the biofunctionalized P(MA) gradient and the P(IPOx-g-EtOx) gradient in a normalized plot. The similarity of the height profile and the fluorescence intensity indicates that the proteins were immobilized throughout the entire polymer brush layer, even in the case of the sterically crowded BBBs.<sup>[278]</sup> If GFP were only coupled within upper interfacial regions of the brush, the resulting fluorescence intensity would be independent of the polymer layer thickness. Moreover, the gradual increase of the fluorescence intensity correlates with the polymer thickness and shows that the amount of immobilized GFP follows the locally applied electron dose used for the CT step. In other words, CT can be used as a direct tool for the preparation of complex biomolecule density gradients which are relevant for the development of functional responsive surfaces for sensing.

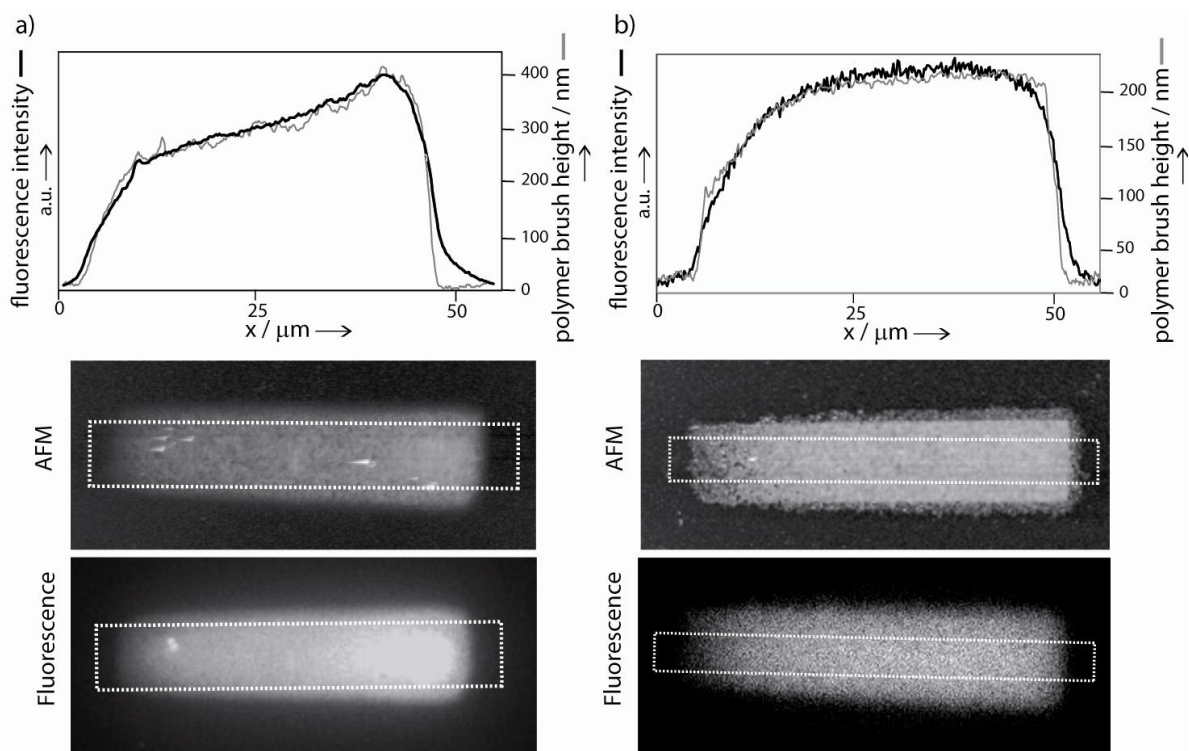


**Figure 61: Analysis of  $10 \times 50 \mu\text{m}^2$  gradients of P(MA)-GFP and P(IPOx-g-EtOx)-GFP on NCD; a) AFM scan and fluorescence image of P(MA)-GFP. Normalized profile plot of the fluorescence intensity and the polymer brush height of the P(MA)-GFP gradient obtained from AFM and FM section analysis (averaged at the indicated area); b) AFM scan and fluorescence image of P(IPOx-g-EtOx)-GFP. Normalized profile plot of the fluorescence intensity and the polymer brush height of the P(IPOx-g-EtOx)-GFP gradient obtained from AFM and FM section analysis.**

The resilience of the polymer brush biomolecules conjugates was tested by exposing the GFP-functionalized samples to harsh external conditions. The freshly biofunctionalized P(MA) brush gradient on NCD revealed a strong fluorescence as shown in Figure 61. Oversaturation occurs because all the fluorescence pictures were taken with the highest excitation intensity (intensity three out of three) to obtain comparable results. After treatment with 0.1 M NaOH over night (16 h), the fluorescence signal drastically decreases, although a clear contrast between the non-modified and the GFP-functionalized NCD persists. Even after treatment of the PMA-GFP brush with 1 M NaOH over night (16 h), fluorescence remains detectable (Figure 62). Despite the treatment under basic conditions which cause denaturation of free GFP<sup>[330]</sup> and loss of fluorescence, the brush conjugated GFP still shows significant fluorescence, indicating an improved stability of polymer-bonded GFP. Experiments carried out by colleagues from the Walter Schottky Institute on GFP coupled to NCD via short linker molecules (decenylamine) have shown that protein monolayers cannot be detected in fluorescence microscopy, so far, as drastic bleaching occurs the very moment of exposure to excitation light.

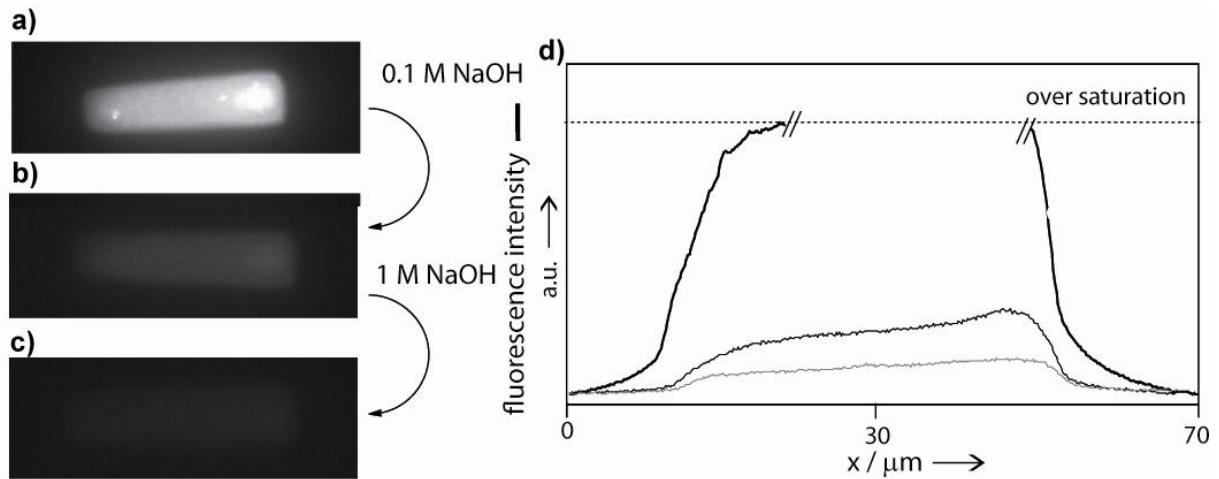
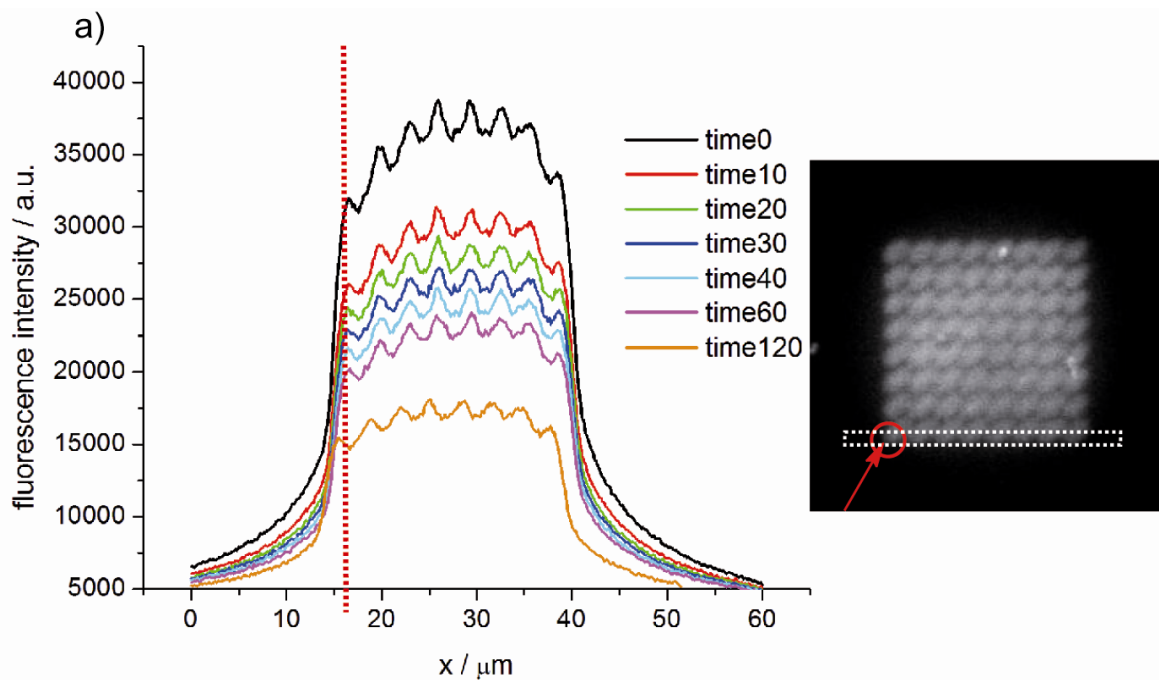
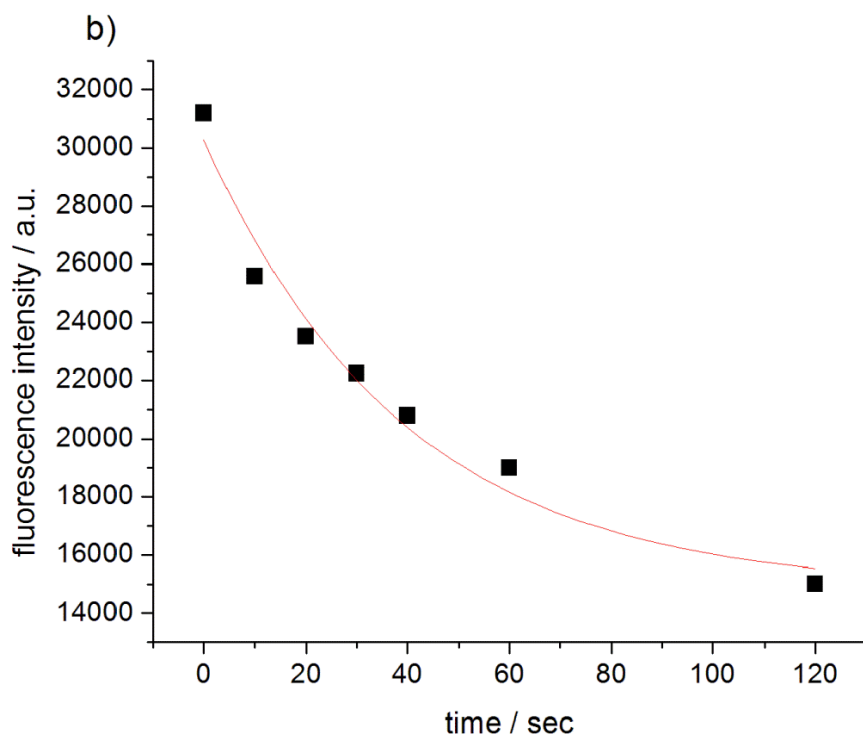


Figure 62: Comparison of the fluorescence of P(MA) bound GFP before and after treatment with NaOH; a) non-treated surface; b) after treatment with 0.1M NaOH over night; c) after treatment with 1 M NaOH over night; d) profile plot of the fluorescence intensity.

Due to the high stability and loading density of GFP in P(MA), it was possible to observe the bleaching behaviour of the protein under constant excitation. A  $8 \times 8$  matrix of P(MA)-GFP patterned in  $2 \times 2 \mu\text{m}^2$  sized squares on NCD was used as the test sample. After two minutes, the fluorescence intensity decreased to 50% but a clear contrast was still visible (Figure 63). The mathematical fit of the bleaching curve indicates a first order exponential decay for the values obtained in the time span of this experiment. This improved stabilization of proteins by polymer brush conjugation is an interesting property for the development of stable biosensors, especially for the use *in vivo*.





**Figure 63:** Fluorescence intensity measured during constant exposure to excitation wavelength; above: section analysis of the fluorescence intensity of eight  $2 \times 2 \mu\text{m}^2$  sized P(MA)-GFP structures measured over 2 minutes at the indicated area; below: fluorescence intensity measured at the left feature indicated by the red circle versus time of exposure to excitation wavelength.

Since the coupling of sterically demanding biomolecules has successfully been performed into P(IPOx-g-EtOx) BBBs with a high chain crowding relative to P(MA), a successive idea was to enhance the protein loading by replacing the non-reactive poly(2-ethyl-2-oxazoline) side chains with functional poly(2-carboxyethyl-2-oxazoline) (Figure 64). A carbon template gradient with increasing electron doses from 0 to  $100 \text{ mC/cm}^2$  on NCD was used as a platform for the SIPGP of IPOx. The pendant side chains were functionalized in a subsequent LCROP by initiation with MeOTf and polymerization with methyl-3-(oxazol-2-yl)propionate at  $70^\circ\text{C}$  and 150W for 30 min. in the microwave. The saponification of the ester into carboxyl moieties was carried out under mild basic conditions with NaOH in methanol at  $50^\circ\text{C}$  according to work from Dr. Robert Luxenhofer.<sup>[331]</sup> Under these conditions, no hydrolysis of the poly(ethyleneimine) backbone of the side chains is expected. IR spectroscopy confirmed the presence of the typical carbonyl bands of poly(2-oxazoline) at  $1647 \text{ cm}^{-1}$  and of the pendant carboxylic acid groups at  $1725 \text{ cm}^{-1}$ . Subsequent coupling of GFP was performed with NHS/EDC activation. The resulting P(IPOx-g-CarboxyOx)-GFP BBBs were analyzed by fluorescence microscopy to determine the presence and activity of GFP. Native GFP could be

unambiguously identified and the possibility of obtaining strong fluorescence response, even after several seconds of exposure, indicates an enhanced stability and/or loading compared to monolayer coupling. However, AFM height profile measurements did not reveal a significant increase of the layer thickness after GFP coupling. Therefore, no high protein ligation was obtained despite using multifunctional side chains in contrast to end-group functionalized P(IPOx-g-EtOx) BBBs.

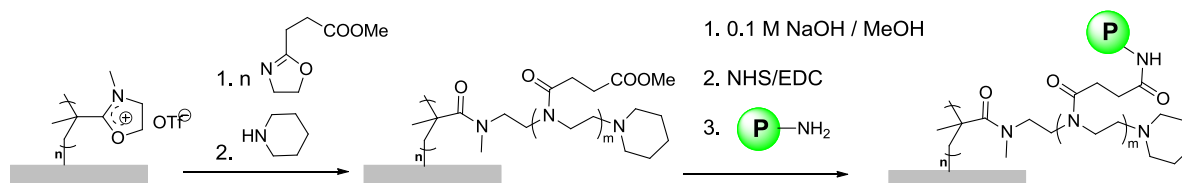


**Figure 64:** Preparation of functional P(IPOx-g-CarboxyOx) BBBs on NCD and subsequent coupling of GFP.

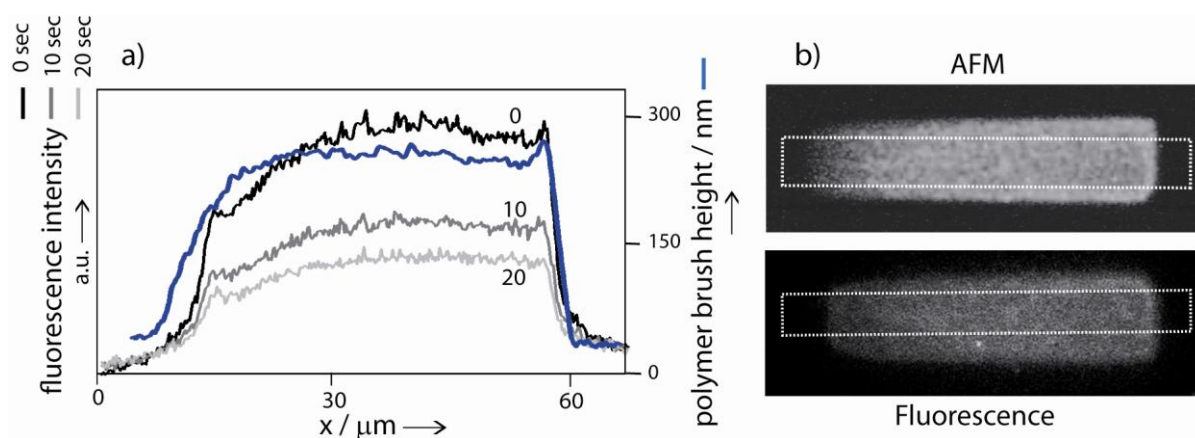


**Figure 65:** Analysis of  $10 \times 50 \mu\text{m}^2$  gradient of P(IPOx-g-CarboxyOx) on NCD; left: normalized profile plot of the fluorescence intensity at  $t=0$ ,  $t=10$  sec and  $t=20$  sec and of the polymer brush height (blue curve) of the P(IPOx-g-CarboxyOx)-GFP gradient obtained from AFM and FM section analysis (averaged at the indicated area); right: AFM and FM image of P(IPOx-g-CarboxyOx)-GFP.

#### 4.2.3.2 Colorimetric essays for the determination of enzymatic reaction kinetics

A great number of very specific colorimetric protein assays have been developed to determine the presence and the activity of biomolecules in solution or other biological environments. While these assays are usually designed as ready-made kits and used for solute proteins, only very few reports are found on the application of colorimetric assays for surface-immobilized proteins. Nevertheless, two well-established colorimetric methods were used for surface-attached proteins in the course of this project. Colorimetry was used as a fast method to determine the presence of native horseradish peroxidase (HRP) <sup>[332]</sup> and glucose oxidase (GlucOx) <sup>[333]</sup> in NCD-grafted polymer brushes. However, due to potential reactivity differences between free and immobilized enzymes, exact quantifications cannot be expected. However, besides AFM measurements and fluorescence, these assays provide an additional proof for a successful coupling and allow an insight into the reaction kinetics of polymer brush conjugated enzymes.

**Horseradish peroxidase:** In a usual setup for the determination of HRP, the biofunctionalized NCD sample was immersed in a photocuvette containing the substrate ( $H_2O_2$ ) and the dye 2,2',5,5'- tetramethylbenzidine (TMB) in buffer. The reaction scheme for the formation of the diimine causing the characteristic color is presented in Figure 66. The change of absorbance ( $A = \log(I_T/I_0)$ ) over time is recorded in a UV-Vis photometer at a wavelength of 655 nm while using different TMB concentrations per run.

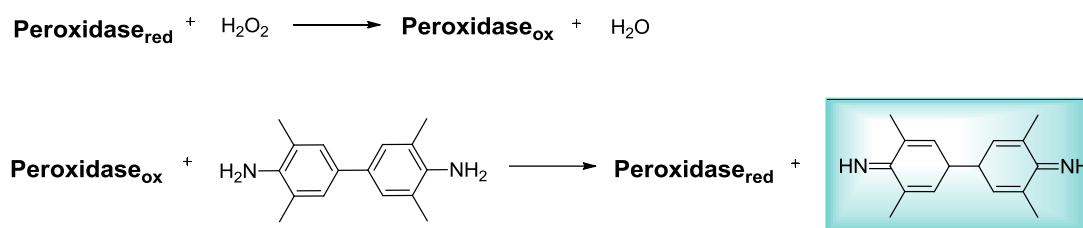


**Figure 66: Conversion of TMB into a dye catalyzed by a peroxidase enzyme.**

Ideally, the absorbance increases linearly over time due to constant enzymatically induced dye formation when there is an excess of substrate which cannot be consumed in the given time span. An example is given in Figure 67, for P(IPOx-g-EtOx) BBBs terminated with proline and functionalized with HRP. From the slope of the curve  $dA/dt$ , a concentration specific conversion rate, i.e. reaction rate, can be calculated. However, the exact substrate concentration remains unknown because the exact composition of the assay kit is not provided by the supplier. Therefore, the TMB concentration is given in volume percent of kit in buffer.

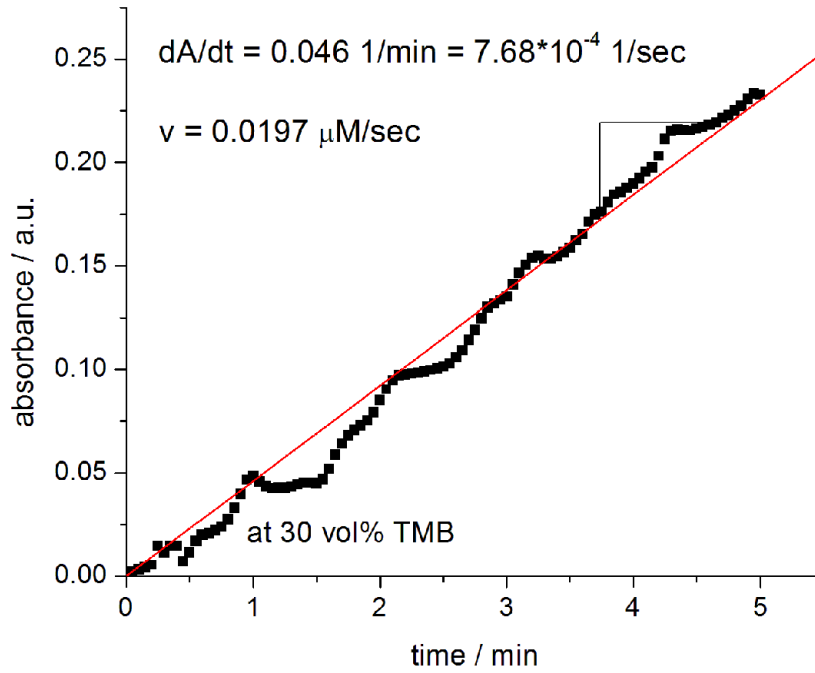


**Figure 67:** Exemplary curve of the conversion of TMB by HRP coupled to P(IPOx-g-EtOx) BBBs determined by measuring the absorbance of the colored product formed during 5 minutes; the slope of the linear fit provides the reaction rate at the respective substrate concentration.

According to the Lambert Beer Law,  $dA/dt$  can be transformed into a reaction rate  $v$  by combining

$$\frac{dA_{TMB}}{dt} = l \cdot \alpha_{TMB} \cdot \frac{dc_{TMB}}{dt}$$

**Eq. 11** with  $l$ : path length through the analyte solution;  $\alpha$ : extinction coefficient of TMB =  $3.9 \times 10^4$  (Mcm)<sup>-1</sup>

and

$$v = \frac{dc_{product}}{dt} = \left( \frac{dc_{H_2O_2}}{dt} \right) = \frac{dc_{TMB}}{dt}$$

**Eq. 12**

to give

$$v = \frac{dc_{TMB}}{dt} = \frac{dA_{TMB}}{dt} \cdot \frac{1}{l \cdot \alpha_{TMB}}$$

**Eq. 13**

Subsequent plotting of the reaction rate versus substrate concentration provides information about the Michaelis Menten kinetics. In the case of HRP coupled to BBBs, no significant

curves could be obtained. This might be due to diffusion limitation of TMB and dye into and out of the brushes caused by the difficult realization of constant stirring. Low enzyme loading is unlikely since AFM measurements could confirm a successful coupling in high yields (see chapter 4.2.2.1).

A typical Michealis Menten behavior, i.e. linear diffusion-limited dependence for low substrate concentrations followed by a regime of saturation, was observed in case of  $60 \pm 5$  nm thick P(MA)-HRP on NCD (Figure 68). A  $v_{\max}$  of approximately  $0.028 \mu\text{M}/\text{sec}$  was found. From the derivation of the Michaelis Menten equation presented in chapter 4.2.1,  $K_M$  can be graphically extracted from the plot of substrate concentration versus reaction rate since  $K_M$  equals  $[S]$  at  $v = \frac{1}{2} v_{\max}$  (compare Eq. 8). Therefore,  $K_M$  is  $0.4$  (divided by the unknown concentration  $c_{\text{H}_2\text{O}_2}$ ) for that specific example.

For all colorimetric assays performed in this thesis, the polymer brush-bound biocatalysts are not free in solution with a defined concentration. Therefore the exact enzyme surface coverage is unknown and an estimation of the kinetic constant is not possible. However, when ideally assuming similar kinetic constants  $k_2$  (with  $v_{\max} = k_2 \times [E]$ ) for polymer brush conjugated HRP and free HRP, the activity obtained on the biofunctionalized NCD samples can be compared to reference measurements on free HRP with a known concentration. For a concentration of  $2.5 \times 10^{-5} \mu\text{M}$  HRP ( $7.5 \times 10^{-14}$  mol in the cuvette),  $v_{\max} = 2.0 \mu\text{M}/\text{sec}$  and  $K_M = 0.49/c_{\text{H}_2\text{O}_2}$  was found.<sup>[334]</sup> By comparing the ratios of the respective  $v_{\max}$ , a theoretical total enzyme loading can be derived and a HRP concentration of  $1.05 \times 10^{-15}$  mol HRP<sup>3</sup> in the P(MA) brushes can be calculated with the parameters given in the footnote.<sup>[335]</sup>

$$\frac{[E_{\text{free}}]}{[E_{\text{bound}}]} = \frac{v_{\max\text{free}}}{v_{\max\text{bound}}} \rightarrow [E_{\text{bound}}] = \frac{7.5 \cdot 10^{-14} \text{ mol} \cdot 0.028 \frac{\mu\text{M}}{\text{sec}}}{2.0 \frac{\mu\text{M}}{\text{sec}}}$$

For a projective area of around  $7 \text{ nm}^2$  per enzyme, the number of theoretically calculated HRP molecules would not even correspond to a monolayer coverage. Repeated reference measurements for  $3.1 \times 10^{-5} \mu\text{M}$  of free HRP in another photometer gave similar results ( $v_{\max} = 5.0 \mu\text{M}/\text{sec}$ ,  $3.49 \times 10^{-15}$  mol HRP).

---

<sup>3</sup> Calculations are based on the following parameter for HRP: molecular weight = 44000 g/mol, projective area =  $7 \text{ nm}^2$

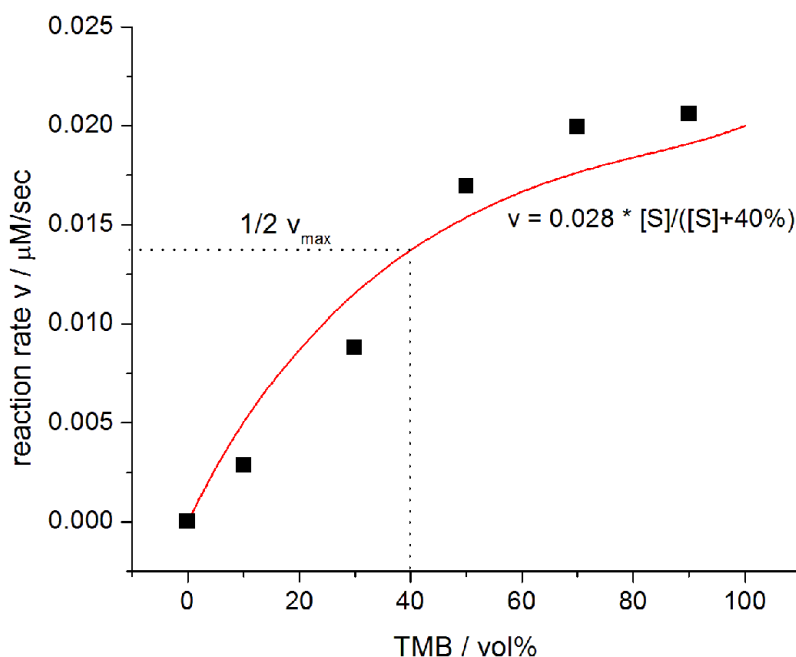


**Figure 68: Colorimetric assay for P(MA)-HRP on diamond; the reaction rate is plotted against the relative substrate concentration.**

Evidently, the obtained activity values for polymer brush conjugated HRP, based on these measurements and calculations are orders of magnitude too low. Although it is still unclear why the absorbance in the photometric setups was so low, parallel investigation on another device in the Walter Schottky Institute provided higher but still unlikely results. The conversion rates were found two orders of magnitude higher on a comparable substrate ( $h_{\text{P(MA)-HRP}} = 62 \pm 15 \text{ nm}$  and identical functionalization chemistry). We eventually obtained a  $v_{\text{max}} = 1.69 \mu\text{M}/\text{sec}$  and thus a  $6.34 \times 10^{-14} \text{ mol HRP}$ .

In order to investigate the stability of the polymer brush - HRP conjugates, the reaction of the P(MA)-HRP sample with TMB/H<sub>2</sub>O<sub>2</sub> was measured once again after 8, 22 and 34 days and the respective colorimetric assays are plotted in Figure 69. After a month, the activity had decreased to one fourth of the original value but the conversion was still unambiguously detectable in the UV-Vis spectrometer. In the first week,  $v_{\text{max}}$  remained nearly constant at  $0.028 \mu\text{M}/\text{sec}$ . After 22 days the activity decreased to  $0.023 \mu\text{M}/\text{sec}$  and even after more than a month nearly one fourth of the original value could be detected.

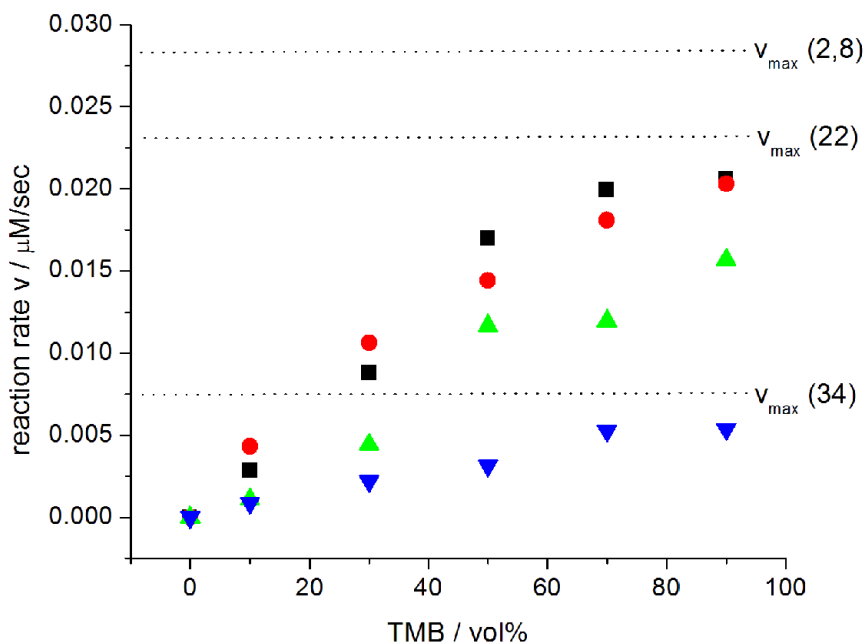


**Figure 69:** Colorimetric assay for P(MA)-HRP on diamond; measurement after 2 (black), 8 (red), 22 (green) and 34 (blue) days after sample preparation.

**Glucose oxidase:** The biomolecule is a dimeric protein including one tightly but non-covalently bound flavine adenin dinucleotide (FAD) cofactor per monomer which is surrounded by a glycoprotein shell.<sup>[336]</sup> Polymer-brush bound glucose oxidase (GlucOx) was analyzed in a multi-step reaction pathway according to the well-established homovanillic acid assay. The simplified net reaction shown in Figure 70 combines the generation of gluconolactone and  $H_2O_2$  by GlucOx in one reaction step. In fact, the enzymatical conversion implies two partial reactions at the cofactor unit<sup>[35]</sup>:

1.  $glucose + GlucOx(FAD) \rightarrow gluconolactone + GlucOx(FADH_2)$
2.  $FADH_2 + O_2 \rightarrow FAD + H_2O_2$

The usual application of a commercially available kit is designed for the detection of glucose. In order to test the activity of GlucOx with a known substrate concentration, the assay was adjusted by emerging the GlucOx-modified NCD samples in a mixture of a defined concentration of glucose, homovanillic acid (HVA) and HRP in buffer. The intensity of the fluorescence was measured over 5 minutes, respectively, while the solution was stirred manually between each data point. Since the extinction coefficient of the oxidized product of HVA is unknown and since the fluorescence intensity depends on the emission filters, the conversion rate is given in arbitrary units per second.

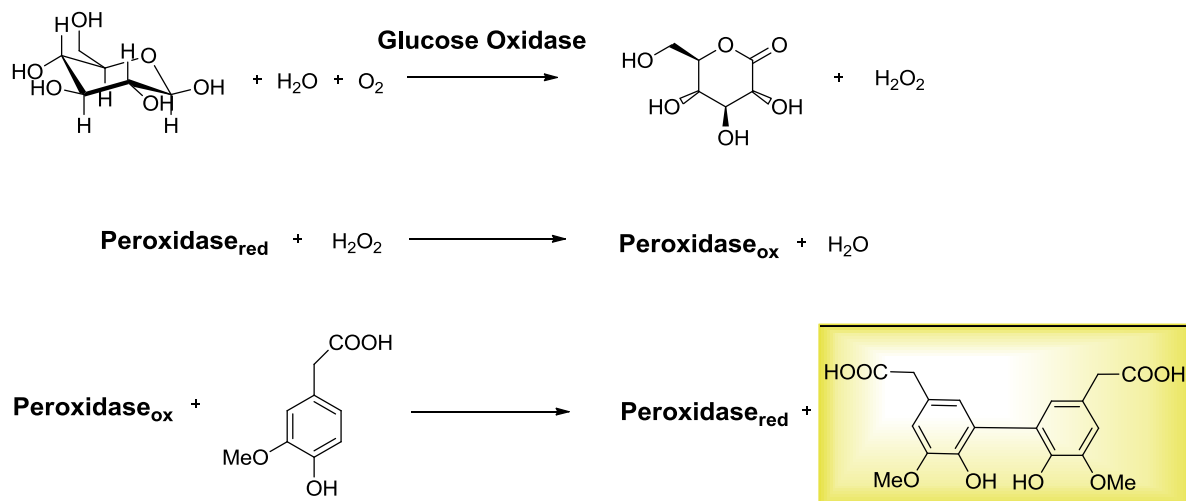


**Figure 70:** Formation of the oxidized fluorescent form of HVA triggered by GlucOx; first: enzymatic reaction of GlucOx with glucose under the formation of hydrogen peroxide; second: reaction of a peroxidase (here: horseradish peroxidase) with hydrogen peroxide; third: recovery of the reduced peroxidase by the oxidation of HVA yielding a fluorescent product.

Fitting the obtained colorimetric data to a Michaelis Menten curve gives a  $v_{\max} = 0.4 \text{ sec}^{-1}$  and  $K_M = 0.35 \text{ M}$  (Figure 71). In order to obtain any quantitative information, the activity of free GlucOx was tested under identical conditions. A highly diluted solution of the enzyme with a concentration of 3.1 nM (corresponding to  $6.2 \times 10^{-4} \text{ nmol}$  in the cuvette<sup>4</sup>) was prepared in order to avoid oversaturation in the fluorescence photometer and to assure comparable values to surface-bound GlucOx under the same photometer settings (intensity filter: medium). Assuming the same  $K_M$  for the free enzyme and identical reaction behavior, a  $v_{\max} = 1.3 \text{ sec}^{-1}$  is calculated (Figure 72). The relation between  $v_{\max}$  at the respective enzyme concentration helps to evaluate the amount of immobilized GlucOx in the P(MA) brushes analogue to the example presented for P(MA)-HRP.

$$[E_{\text{bound}}] = \frac{0.4 \frac{1}{\text{s}}}{1.3 \frac{1}{\text{s}}} \cdot 6.2 \cdot 10^{-4} \text{ nmol}$$

The estimation results in  $1.92 \times 10^{-4} \text{ nmol}$  GlucOx on the surface, i.e.  $1.16 \times 10^{11}$  molecules per  $\text{cm}^2$ . A densely packed monolayer of GlucOx with a footprint area of  $72.6 \text{ nm}^2$ <sup>[337]</sup> would thus consist of around  $8.4 \times 10^{12}$  molecules. The amount for the P(MA)-GlucOx NCD surface obtained by theoretical calculations would then only correspond to merely 8% of a monolayer.

<sup>4</sup> Calculations are based on the following parameters for GlucOx: molecular weight = 160000 g/mol, footprint area =  $72.6 \text{ nm}^2$

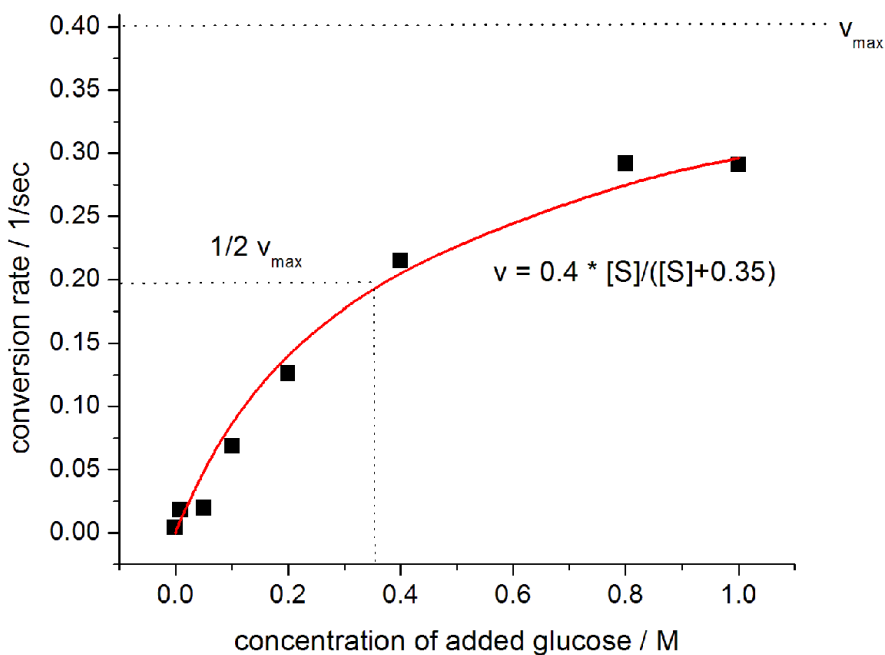


**Figure 71: Colorimetric assay of P(MA)-GlucOx on NCD; Dependence of the reaction rate, i.e. the formation of the fluorescent HVA derivative, on the glucose concentration and respective Michaelis Menten fit.**

However, the presented calculations are based on assumptions and approximations which potentially distort the results and which are briefly summarized here:

- Kinetic constants (free enzyme) = kinetic constants (bound enzyme)
- Identical reactivity of HRP either bound at the polymer-brush interface or inside the polymer brushes
- Equal mobility of substrate or chromatic product (no retention inside the polymer brushes)
- The same molecular diameter or footprint area for free and immobilized enzymes

Moreover, a major error for the calculation might be the exact mass of free enzyme and the assumption that all net weight really corresponds 100% to enzyme.

Therefore, it is likely - especially considering the results for enzyme loading obtained by AFM - that the amount of attached enzyme exceeds the theoretically evaluated amount and that other magnitudes for the activity of immobilized GlucOx might represent a more accurate basis for the calculations. Another influencing factor might be the unspecific coupling of the biomolecules to a random, easily accessible amine bond which can cause a decrease in

activity. Then, it is consequential that a strong increase in polymer brush height due to enzyme loading is not necessarily attended by a high enzyme activity.

The herein obtained results are difficult to compare with other findings in literature, since the few reports on colorimetric assays with surface-bound GlucOx either lack kinetic calculations or are based on the enzymatic conversion of compounds other than homovanillic acid.<sup>[338],[339],[340]</sup> In order to assess the obtained results nevertheless, the presented colorimetric method was also used for the determination of GlucOx bound to monolayer-functionalized diamond. A comparison in terms of enzyme activity between biomolecules attached to polymer brushes and monolayers will be addressed in chapter 4.4.4.

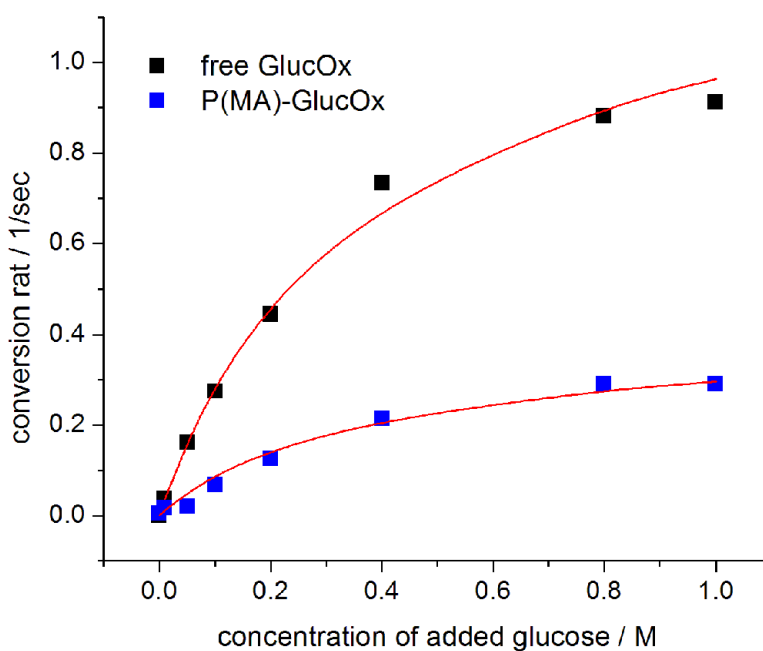


**Figure 72: Colorimetric assay of free GlucOx compared to P(MA)-bound GlucOx; Dependence of the reaction rate, i.e. the formation of the fluorescent HVA derivative, on the glucose concentration and respective Michaelis Menten fit.**

### 4.3 Polymer brushes as polymeric mediators

Fluorescence activity and colorimetric assays of polymer-bound proteins presented in the previous chapter do not rely on the electrical properties of the interlayer. For electrochemical sensing applications of enzyme-electrodes however, an unimpeded charge transport throughout the entire polymer brush matrix is crucial in order to detect all recognition reactions including those occurring in the upper layers (Figure 73).



**Figure 73: challenge of ensuring a charge transfer along the polymer brushes in a schematic illustration.**

The following chapter addresses methods to bind mediators, i.e. charge transfer molecules, to polymer brushes. Although such mediators can in principle be added to the analyte solution, there is a potential risk of leaching out of the sensor interface which renders this approach unfeasible for usage *in vivo*. However, by means of covalent coupling of the mediator species, this drawback can be overcome.<sup>[86]</sup> All herein presented experiments were carried out with conductive boron-doped diamond.

#### 4.3.1 Theoretical insight into voltammetric and amperometric techniques

First, a brief general introduction to the electrochemical methods cyclic voltammetry and chronoamperometry will be given in this chapter. Electrochemistry has been essentially beneficial to biochemistry since it allows a close insight into numerous important biological processes.<sup>[79]</sup> The various techniques are mostly based on phenomena in which chemical reactions are a) either triggered by electrical energy or b) in which chemical changes induce the production of an electric current. Per definition, the cell in which the experiment is carried

out is named “electrolytic cell” for case a) and “galvanic cell for case b).<sup>[341]</sup> The *Faraday* laws<sup>[79]</sup> form the theoretical basis for a quantitative connection between the measurable so-called faradaic current in a cell with the concentration of the active species. The corresponding equation is founded on the two assumptions made by Faraday:

1. “In electrolysis, the quantities of substances involved in the chemical change are proportional to the quantity of electricity which passes through the electrolyte”.<sup>[79]</sup>
2. “The masses of different substances set free or dissolved by a given amount of electricity are proportional to their chemical equivalents”.<sup>[79]</sup>

$$1. \Delta n = \frac{v_j Q}{nF} \quad 2. v_j = \frac{1}{S} \frac{dn_j}{dt} = v_j \frac{i}{nF}$$

**Eq. 14** with  $\Delta n$ : moles of converted substance;  $Q$ : amount of charge;  $F$ : Faradays constant,  $v_j/n$ : chemical equivalent of the substance;  $v_j$ : specific reaction rate;  $i$ : current density

#### A) Cyclic voltammetry (CV):

A typical experimental cell for cyclic voltammetry consists of a three-electrode arrangement:

1. The **working electrode** is the “electrode of interest”, at which the respective relevant reaction occurs (in this thesis: the functionalized doped diamond sample).
2. The **counter electrode**, also referred to as auxiliary electrode, together with the working electrode closes a circuit in which the specific current can flow (in this thesis: a platinum wire).
3. The potential of the working electrode is usually not measured directly through the counter electrode, but instead, against a **reference electrode**. The reference electrode does not form part of the essential circuit and therefore maintains a stable reference potential (in this thesis: a Ag/AgCl standard reference electrode, commercially available).

Additionally, a potentiostat forms an important part in the experimental setup by controlling the voltage across the working electrode – counter electrode pair. During cyclic voltammetry, a linear potential sweep in alternating onward and reverse scan directions is applied to the electrolyte solution. Assuming that a faradaic reaction occurs at the working electrode somewhere in the range of the chosen potential sweep, an exemplary CV curve would look as depicted in Figure 74. In the beginning of the scan, only non faradaic current flows and its value is nearly zero. When the applied potential approaches the formal potential  $E_0$ , the reduction of the species starts and a faradaic current begins to flow. Since the species is

consumed at the electrode surface, the flux from bulk solution towards the electrode increases which results in an increased current until the reduction peak is reached. Eventually, the electrode vicinity becomes depleted from redox active molecules and the current decreases. When the potential scan is reversed, a large concentration of oxidizable species is present and reoxidation starts in the range of the standard potential of the redox couple  $E_0$ . The reverse current shows a similar shape for the same reasons. It is noteworthy that  $E_0$  cannot be read out directly from the graph but needs to be derived from Eq. 15, because the redox peaks  $E_a$  and  $E_c$  do not exactly correspond to  $E_0$ . Instead, at  $E_0$ , the main faradaic reaction just initiates but the potential value still allows non-reacted species to outlast in the electrode vicinity. Therefore, the flux of species (which affects the current signal) induced by the concentration gradient is relatively low. At higher potentials however, all reactive molecules will immediately be converted, inducing an increased flux.<sup>[341],[79]</sup>

$$E^0 = E_{1/2} = \frac{(E_a + E_c)}{2}$$

**Eq. 15** with  $E_a$ : anodic (oxidative) potential;  $E_c$ : cathodic (reductive) potential.

Apart from  $E_0$ , further typical characteristics which can be evaluated from a CV curve are the ratio of the peak current integrals  $i_c/i_a$  and the separation of the peak potentials  $E_c/E_a$ . The significance of these values will be discussed for the respective results in chapter 4.3 and 4.4.

The reaction rate at the electrode depends on the following factors:

- Mass transfer from bulk solution to the electrode
- Surface reactions such as adsorption, desorption or crystallization
- Electron transfer during the electrode reaction
- Chemical reactions proceeding or following the electron transfer (e.g. protonation, dimerization, decomposition)

To evaluate the rate limiting step of the reaction the Cottrell equation<sup>[341]</sup> can be used to describe the current as a function of time assuming diffusion limitation. In this regime, the current depends on  $t^{-1/2}$  and consequently in a simplified description on the square root of the scan rate.

$$i = \frac{nFAc_j^0 \sqrt{D_j}}{\sqrt{\pi t}} = \frac{k}{\sqrt{t}} = k' \sqrt{v}$$

**Eq. 16** with  $i$ : current;  $A$ : area of the electrode;  $c_j^0$ : initial concentration of the analyte,  $D_j$ : diffusion coefficient;  $t$ : time

### B) (Chrono)amperometry:

Generally, the experimental setup for amperometry equals that of cyclic voltammetry. But in this case, instead of deliberately sweeping a potential range, the potentiostat provides a constant potential at a suitable value. Since the cell current is measured as a function of time (and not as a function of the potential as in cyclic voltammetry), the method is termed chronoamperometry. During the experimental time span, the chemical environment of the electrochemical cell is subjected to external changes; In the course of these studies, different substrate concentrations were added stepwise to the electrochemical cell. When the substrate undergoes a redox reaction in the cell, current will flow and an exemplary chronoamperometric curve would look according to Figure 74.

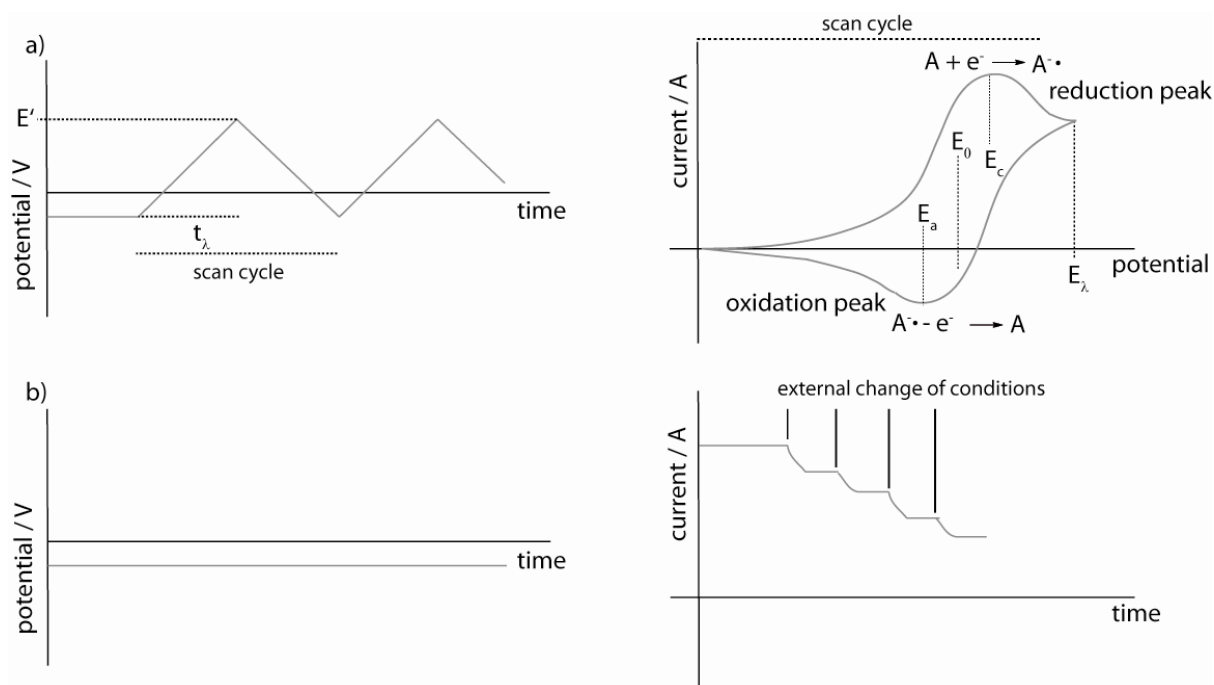


**Figure 74: Schematic illustration of the applied electrochemical methods; adjustment of the potential and exemplary resulting current-potential dependence for a) cyclic voltammetry and b) chronoamperometry; with  $E_0$ : formal potential of the redox couple;  $E_a$ : anodic potential;  $E_c$ : cathodic potential;  $E_\lambda$ : switching potential.**

However, despite all theoretical considerations, the detection of redox processes does not always proceed as desired. Difficulties arise when the reaction which generates or consumes electrons does not occur in the closest vicinity to the electrode. This is the case when redox active moieties or biomolecules are attached to the working electrode via a linker. The probability of electron tunneling is given by

$$P \sim e^{-\frac{4\pi\sqrt{2m\phi}}{h}x} \sim e^{-\beta x}$$

Eq. 17

where  $x$  is the distance over which the tunneling occurs while the factor  $\beta$  combines characteristics of the nature of the media and the energy barrier for the tunneling process.<sup>[341]</sup>

In order to avoid losing electrical information somewhere else than at the electrode, the redox active centers can be connected using two main strategies:

1. Addition of free mediator to the electrolyte solution. The choice of the mediator is limited by water-solubility and redox potential.

or

2. Using a conductive interface between the redox center and the electrode, e.g. electrically conductive polymer brushes

**Table 9: Different well-proven mediators and their redox potentials relative to a reference saturated calomel electrode (SCE).**

Mediator <sup>[28]</sup>	Redox potential versus SCE
Ferrocene carboxylic acid	275
[Ru(CN) <sub>6</sub> ] <sup>4-</sup>	685
Benzoquinone	39
[Fe(CN) <sub>6</sub> ]	180
Hydroxymethyl ferrocene	190

Apart from the electron transfer limitation through the linker, large biomolecules themselves are often electrically insulating or their redox active centers are shielded from the surrounding media by dense non-conductive peptide chains.<sup>[33]</sup> This phenomenon has to be considered for electrochemical experiments with enzymes. Some groups have overcome this problem by chemically modifying the enzyme with mediator molecules.<sup>[33]</sup> Although a higher loading of electron shuttles increases the electric contact, this technique is limited since it simultaneously may cause enzyme deactivation.<sup>[47]</sup>

### 4.3.2 Carbazole as hole conducting moiety in poly(2-oxazoline) bottle-brush brushes

Due to their hole-transporting and electroluminescent properties polymers containing carbazole side chains are investigated for applications such as photovoltaic cells or organic light emitting diodes.<sup>[342],[343]</sup> The charge carrier transport proceeds via a hopping mechanism between the carbazole units.<sup>[343-344]</sup> For the fabrication of semiconductive, hydrophilic, and biocompatible polymer brushes on diamond, the carbazole moieties were integrated as 2-(carbazolyl)ethyl-2-oxazoline (CarbOx) monomer in poly(2-oxazoline) BBBs. The synthesis of CarbOx was carried out according to Litt *et al.*<sup>[345]</sup> (Figure 75) via a 9-(3-cyanoethyl)carbazole intermediate which was further reacted with ethanolamine by catalytical amounts of cadmium acetate dehydrate to yield the oxazoline ring.

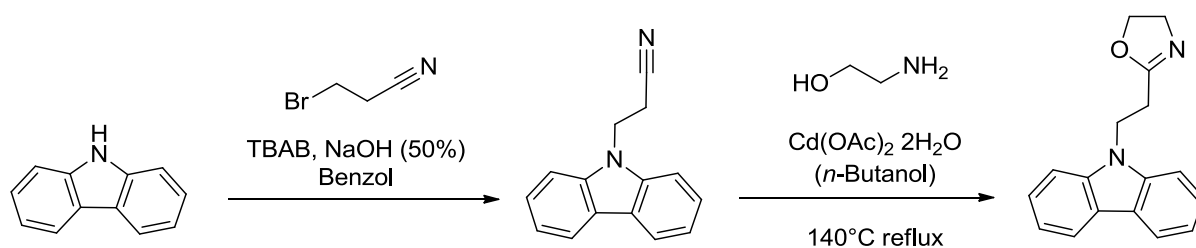


**Figure 75: Synthesis of 2-(carbazolyl)ethyl-2-oxazoline (CarbOx).**

Analogue to chapter 4.1.1.2 PIPOx brushes were prepared on OH/H-patterned diamond (10  $\mu\text{m}$  dots) or by CT on SiO<sub>x</sub> (gradient). The conversion of the neutral PIPOx brushes into the cationic macroinitiator P(IPOx<sup>+</sup>OTf) was achieved by submerging the structured NCD or SiO<sub>x</sub> substrate in a solution of methyl triflate in acetonitrile for 5 h at rt. For the investigation of the macroinitiator, a sample was isolated from the reaction solution and rinsed with dry acetonitrile. The P(IPOx<sup>+</sup>OTf) brush layer was characterized by FT-IR (Figure 77). A strong C-F stretching band at 1268 cm<sup>-1</sup> as well as a S=O stretching band at 1025 cm<sup>-1</sup> are clearly visible and prove the existence of the triflate counter ion of the initiator species. Successively, the side chain LCROP was performed with CarbOx for 16 hours at 80°C to obtain BBBs (Figure 76). The polymerization was terminated with piperidine. It is noteworthy that for the LCROP, the monomer was directly added to the reaction mixture without further cleaning of the macroinitiator substrate (contrary to the above described IR characterization) in order to avoid side reactions of the reactive oxazolinium initiator moieties.

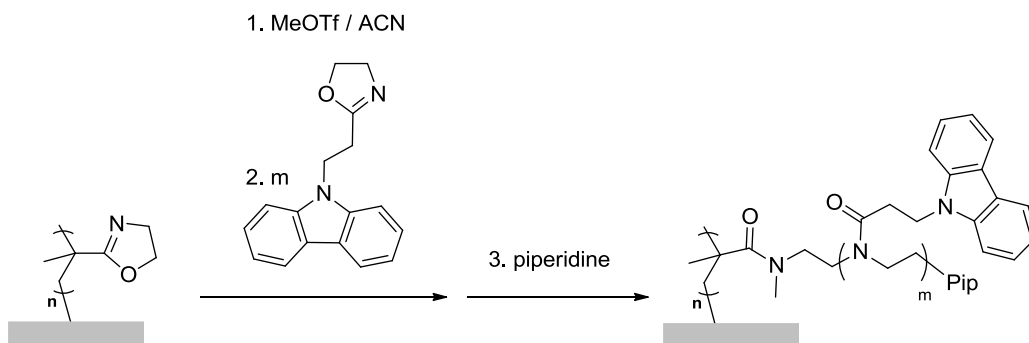


**Figure 76: Preparation of P(IPOx-g-CarbOx) BBBs on NCD and SiO<sub>x</sub>; Formation of the macroinitiator by reacting P(IPOx) brushes with methyltriflate in ACN; subsequent LCROP with 2-(carbazolyl)ethyl-2-oxazoline and termination with piperidine.**

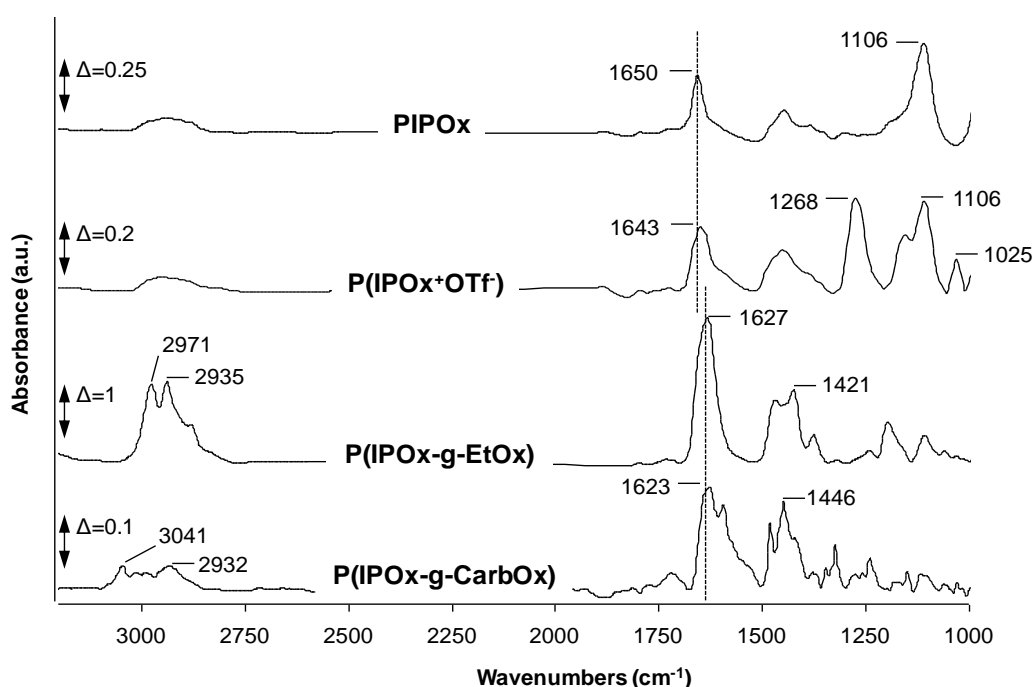


**Figure 77: FT-IR spectra of PIPOx, P(IPOx<sup>+</sup>OTf) brushes as well as P(IPOx-g-EtOx) and P(IPOx-g-CarbOx) BBBs on NCD.**

FT-IR spectroscopy indicates full conversion of PIPOx brushes into P(IPOx-g-CarbOx). The C=N ( $1650\text{ cm}^{-1}$ ) and C-O ( $1106\text{ cm}^{-1}$ ) stretching bands, characteristic for the pendant oxazoline moiety, disappear completely after the side chain polymerization. Figure 77 shows the typical carbonyl stretching band at  $1627\text{ cm}^{-1}$  for P(IPOx-g-EtOx) and  $1623\text{ cm}^{-1}$  for P(IPOx-g-CarbOx) and the strong CH<sub>x</sub> deformation mode at around  $1450\text{ cm}^{-1}$ . Moreover, an increasing intensity of the aliphatic C-H stretching band between  $2850$  and  $3000\text{ cm}^{-1}$  indicates the additional alkyl groups in the BBB side chains. The aromatic C-H stretching

band of P(IPOx-g-CarbOx) can be observed at  $3041\text{ cm}^{-1}$ . The contact angle was found to increase from  $60^\circ$  (PIOx) to  $72^\circ$  after LCROP with CarbOx, compared to  $42^\circ$  with EtOx.

The conversion of PIOx into P(IPOx-g-CarbOx) was also monitored by AFM (Figure 78). PIOx brushes on  $\text{SiO}_x$  with a maximum height of the CT gradient of  $13 \pm 1\text{ nm}$  (a) and  $56 \pm 10\text{ nm}$  thick PIOx brushes on diamond (b) nm resulted in respectively  $17 \pm 1\text{ nm}$  (a) and  $110 \pm 15\text{ nm}$  (b) thick P(IPOx-g-CarbOx) BBB structures after the side chain LCROP. These experiments show that even sterically demanding monomers can be applied for the side chain LCROP on polymer brushes.

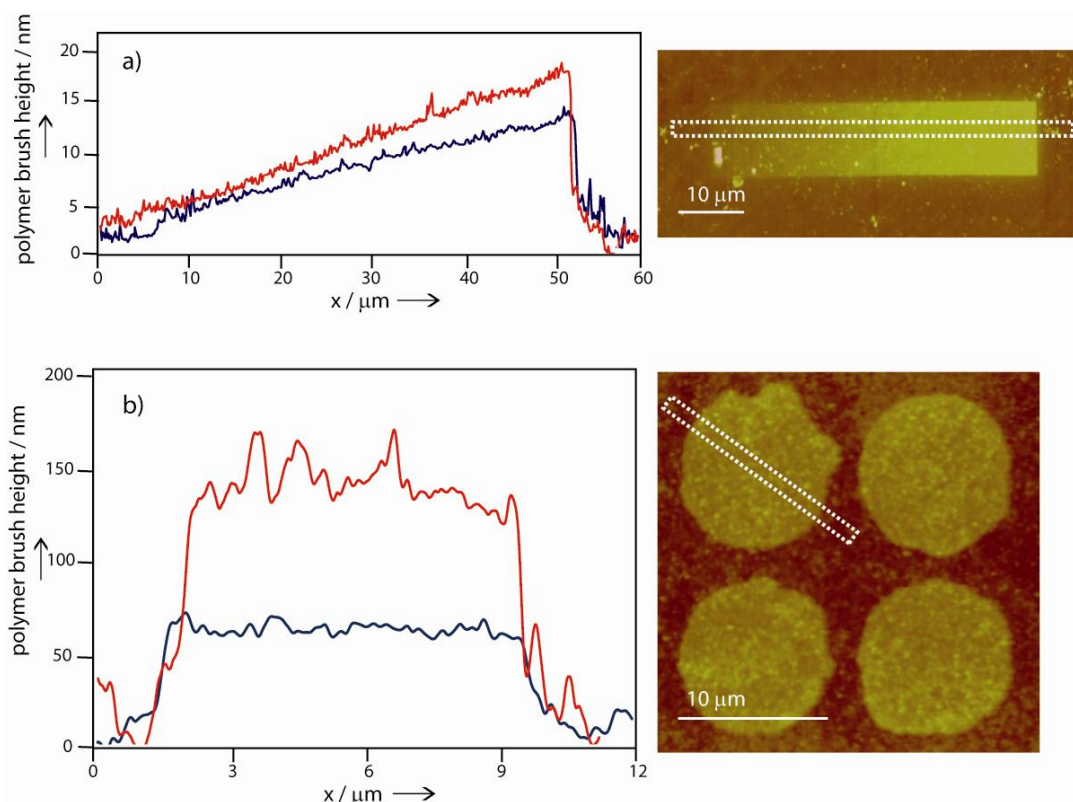


**Figure 78:** AFM section analysis and image of P(IPOx) brushes (blue) and P(IPOx-g-CarbOx) BBBs (red); a)  $10 \times 50\ \mu\text{m}^2$  gradient prepared by CT on  $\text{SiO}_x$ ; b) dots with a diameter of  $10\ \mu\text{m}$  prepared by common photolithography on NCD.

Since the carbazole function is fluorescent with an excitation maximum at 400 nm, fluorescence microscopy (FM) analysis of the P(IPOx-g-CarbOx) functionalized diamond samples was carried out. The successful incorporation of carbazole moieties could be demonstrated by a clear fluorescence emission at  $\lambda > 550$  (Figure 79).<sup>[346]</sup> Furthermore, the area selective grafting reaction of P(IPOx-g-CarbOx) is shown by strong and selective fluorescence only at the polymer-modified and initially oxidized NCD areas. No fluorescence

could be observed on H-terminated NCD areas. The strong contrast also indicates the incorporation of a significant amount of bulky carbazole moieties into the BBB side chains.

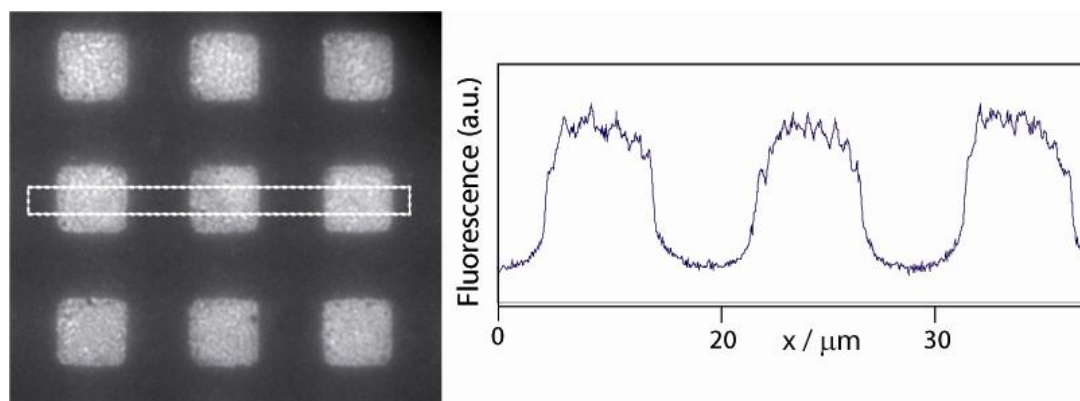


**Figure 79:** Fluorescence microscopy with an emission filter opened for  $\lambda \geq 550$  nm and average section analysis at the indicated area of a patterned NCD surface, functionalized with P(IPOx-g-CarbOx) BBBs. The bright regions correspond to the regions of oxidized surface areas.

P(IPOx-g-CarbOx) BBB modified diamond electrodes have been characterized by CV in an aqueous electrolyte. The CV scans indicated the presence of redox active species on the surface. One exemplary scan for a P(IPOx-g-CarbOx) modified NCD is given in Figure 80. Compared to findings in literature, the peaks of the current response reveal different positions. This is due to the fact that unlike previous reports in acetonitrile or dichloromethane <sup>[347],[348]</sup>, the measurements were performed in aqueous solution for direct comparison to results with biofunctionalized samples.

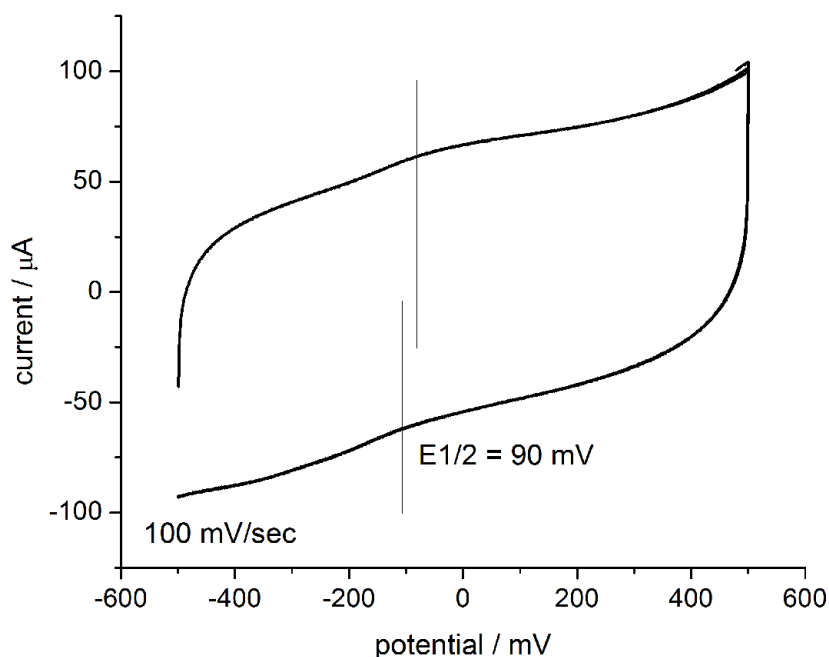


**Figure 80:** CV scan at a scan rate of 100 mV/sec of P(IPOx-g-CarbOx) BBBs on NCD.

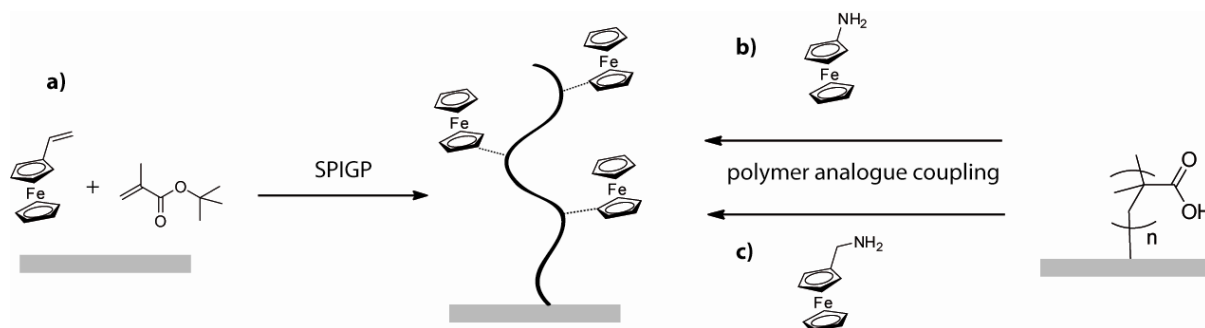
Although stable coupling of carbazole could be demonstrated by CV, it was not possible to evaluate reliable surface coverage data from the relatively small redox peaks. The approach using carbazole as mediator was found not to be suitable for amperometric detection of biomolecules. Experiments on carbazole containing BBBs with cytochrome c attached to the side chain end groups did not succeed in detecting the biomolecule and its typical redox-reaction. However, cytochrome c turned out to be essentially complex to measure due to its sensible reactivity behavior upon different immobilization geometries. This was found in later experiments with cytochrome c attached to other polymer brushes and to monolayers, or when it was directly physisorbed onto the electrode. Hence, cytochrome c was replaced by other enzymes in later experiments.

The successful incorporation of carbazole moieties into poly(2-oxazoline) BBBs was shown. But due to the hydrophobicity and high chain crowding of the resulting polymeric interlayer another mediator, namely ferrocene, was envisaged for the future course of the project.

#### 4.3.3 Ferrocene as redox mediator

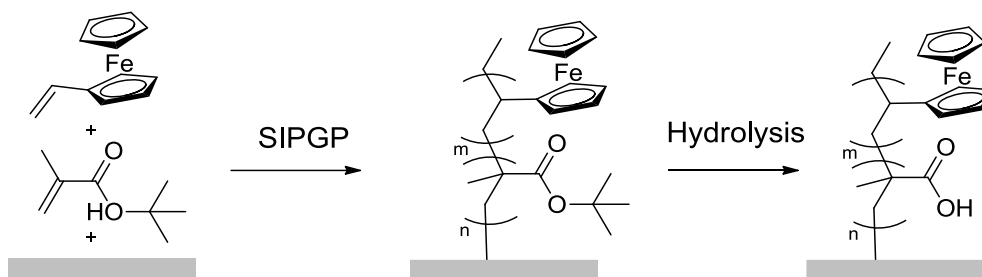
Ferrocene, including its oxidized ferricinium derivative, is one of the most widely used mediators for charge transport in enzyme electrodes and offers a broad application window since the cyclopentadienyl ring can be chemically modified and linked to polymers.<sup>[349],[350],[33]</sup> Important properties, such as high electron density, aromaticity and redox reversibility characterize this organometallic compound.<sup>[351]</sup>

Figure 81 provides a schematic presentation of the three approaches for the introduction of ferrocene moieties into polymer brushes, used in the course of this project.



**Figure 81:** Synthetic strategies towards ferrocene-containing polymer brushes; a) co-SIPGP of vinylferrocene and tBuMA; b) polymer analogue coupling of aminoferrocene into P(MA) brushes; c) polymer analogue coupling of aminomethylferrocene into P(MA) brushes.

#### 4.3.3.1 Incorporation of ferrocene using vinylferrocene as co-monomer in SIPGP



**Figure 82: Preparation of Poly(methacrylic acid - co - vinylferrocene) polymer brushes (P(MA)-co-VFc).**

In a first approach, ferrocene-containing polymer brushes were prepared by using vinylferrocene as co-monomer during the SIPGP of tBuMA (Figure 81 a, Figure 82). Since vinylferrocene is a solid, it needed to be dissolved in order to perform the SIPGP. Moreover, poly(vinylferrocene) (P(VFc)) homopolymer brushes alone are not a suitable platform for the coupling of biomolecules. Therefore, vinylferrocene was copolymerized with tBuMA which simultaneously served as solvent and provides chemical functionality for protein coupling reactions. The NCD sample was irradiated with UV light ( $\lambda_{\text{max}} = 350 \text{ nm}$ ) in the dark red solution of vinylferrocene in tBuMA (1:9 eq.) for 2 days. After thorough cleaning of the sample by ultrasonication, ellipsometry measurements only revealed a polymer brush thickness of  $21 \pm 4 \text{ nm}$  despite the long irradiation time. The absorbance of the vinyl ferrocene solution was analyzed by UV-vis spectroscopy and two absorbance maxima of the Cp rings were found at 290 and 450 nm. Thus, in contrast to transparent bulk monomer, the light intensity at the NCD surface is attenuated in the VFc solution which hinders the formation of thick polymer layers. However, it has to be noted that ellipsometry measurements provide a rather rough estimation, since the refractive index of P(tBuMA-co-VFc) is unknown. Therefore, calculations were performed with reference values of PMMA from literature.<sup>5</sup>

CV of (P(MA)-co-VFc) functionalized NCD samples were performed in an aqueous polyelectrolyte solution and show redox peaks in the microampere range with an  $E_{1/2}$  of 307 mV.  $E_{1/2}$  is obtained by taking the mean of  $E_c$  and  $E_a$  and corresponds in very good approximation to the formal potential  $E_0$  (Eq. 15, chapter 4.3.1). The magnitude of the current response indicates multiple loading of ferrocene groups on the surface. The ferrocene loading on the NCD electrode can be estimated from the integral over the oxidation (or the reduction)

<sup>5</sup> n and k values are obtained from the database Luxpop <http://www.luxpop.com/>

peak which represents the overall charge produced in the redox reaction. The area beneath the peak was approximated by calculating the peak width  $\Delta E$  times the current at half height relative to the background (Figure 83).

$$\int \text{redox peak} \approx \frac{\Delta i_{1/2}}{A} \cdot \Delta E$$

Eq. 18 considers the applied scan rate and provides information on charge or charge density which can be transformed into molecules per surface area.

$$\frac{Q}{A} = \frac{\frac{\Delta i_{1/2}}{A} \cdot \Delta E}{\nu}$$

**Eq. 18** with  $Q/A$ : charge density;  $\Delta i_{1/2}/A \cdot \Delta E$ : approximated integral over the peak area;  $\nu$ : scan rate

For a  $24 \pm 2$  nm thick P(tBuMA-co-VFc) brush layer on NCD, a charge density of  $65 \mu\text{C}/\text{cm}^2$  was evaluated from CV according to Eq. 18. With a charge of  $1.6 \times 10^{-19}$  Coulomb per electron,  $4.07 \times 10^{14}$  electrons are involved per  $\text{cm}^2$  which equals the number of converted ferrocene molecules. Assuming a molecular size of  $1 \text{ nm}^2$  and reliable detection plus full conversion of ferrocene, a density of approximately 4 molecules per  $\text{nm}^2$ , i.e. 4 monolayers, is obtained (see exemplary calculation).

$$\frac{Q}{A} = \frac{\frac{12 \cdot 10^{-6} \text{ A}}{\text{cm}^2} \cdot 0.543 \text{ V}}{0.1 \frac{\text{V}}{\text{sec}}} = 65.2 \frac{\mu\text{C}}{\text{cm}^2}$$

$$\frac{65.2 \cdot 10^{-6} \frac{\text{C}}{\text{cm}^2}}{1.6 \cdot 10^{-19} \text{ C}} = 4.1 \cdot 10^{14} \frac{\text{electrons}}{\text{cm}^2} = 4 \frac{\text{ferrocene}}{\text{nm}^2}$$

This calculative approach was verified by performing a second exemplary calculation; this time based on the automated calculation of the peak integral by software. Here, for the same integral beneath the peak current (as presented in Figure 83, black curve), a charge density of  $59 \mu\text{C}/\text{cm}^2$  was obtained which is in good agreement with the result demonstrated above. It has to be noted that for both calculations the major error occurs by defining the background curve relative to the peak current.

In a second step, the P(tBuMA-co-VFc) brushes were hydrolyzed in methane sulfonic acid in DCM to generate carboxylic acid moieties for further functionalization with biomolecules. After hydrolysis, the peak intensity drops into the nanoampere range (Figure 83). This can be explained by the loss of material which can also be observed by the four- to fivefold decrease of polymer brush height from P(tBuMA) to P(MA) measured by AFM. The quantity of

electrode-bound ferrocene was considered to be insufficient for a subsequent use as polymeric mediator for enzymatic sensing applications.

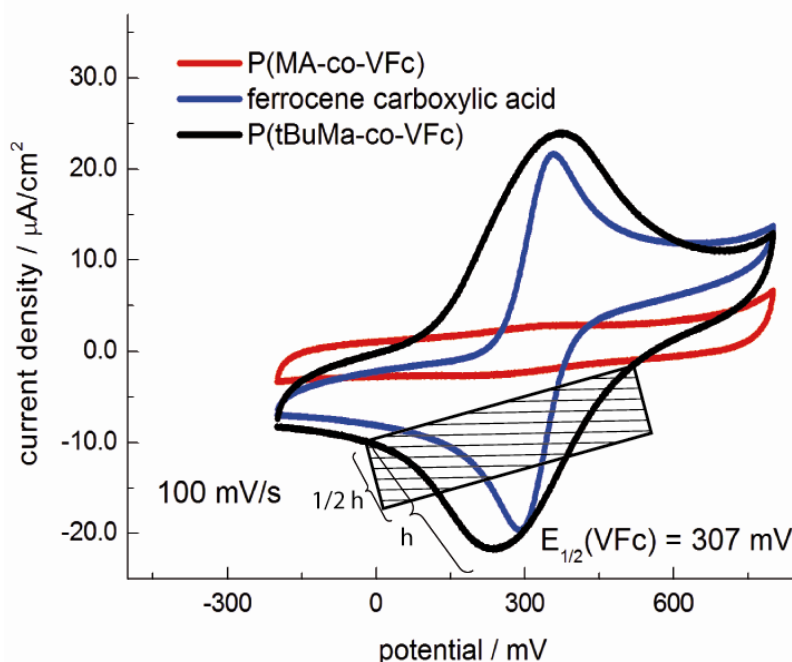


**Figure 83:** CV with a scan rate of 100 mV/sec of ferrocene carboxylic acid in solution (blue), NCD electrodes functionalized with P(tBuMA-co-VFc) (black) and P(MA-co-VFc) (red); determination of the peak integral by using the area of current at half height  $\Delta i_{1/2}$  times potential peak width.

After numerous scan cycles or several days after preparation, the intensity of the redox peaks of the P(tBuMA-co-VFc)-modified NCD electrodes decreased clearly (Figure 84). CV scans were performed two days after the first measurement (b) and revealed an integrated charge density of  $25.9 \mu\text{C}/\text{cm}^2$  and a resulting ferrocene loading of 1.6 monolayers assuming the same conditions as presented before. After constant scanning for another 4.5 hours (c) the charge density dropped further down to  $14.0 \mu\text{C}/\text{cm}^2$  and the ferrocene loading to 0.9 monolayers. Since thorough ultrasonic cleaning had been performed preliminary to the measurement, a loss of material cannot be entirely excluded but is unlikely to be the major cause. A possible explanation is the formation of “irreversible” ferrocene Fe(III) species which gradually deprive the electrode from the Fe(II) species. The process becomes irreversible when in the weaker state of Fe(III)-Cp coordination (in contrast to strong ligand coordination in case of Fe(II)), a Cp is for example exchanged by an aqua ligand. Then, the entire complex can be separated from the polymer brush or it is trapped in an energetic minimum from which, under the applied potential, no back-reduction is possible.

It was shown that the copolymerization of vinyl ferrocene dissolved in *tert*-butyl methacrylate is feasible by SIPGP on oxidized NCD. The generation of free carboxylic functionalities by hydrolysis of P(tBuMA), however, involves a significant loss of ferrocene moieties. Consequently, the incorporation of mediator molecules by the use of a polymer analogue reaction was considered for the following investigations.

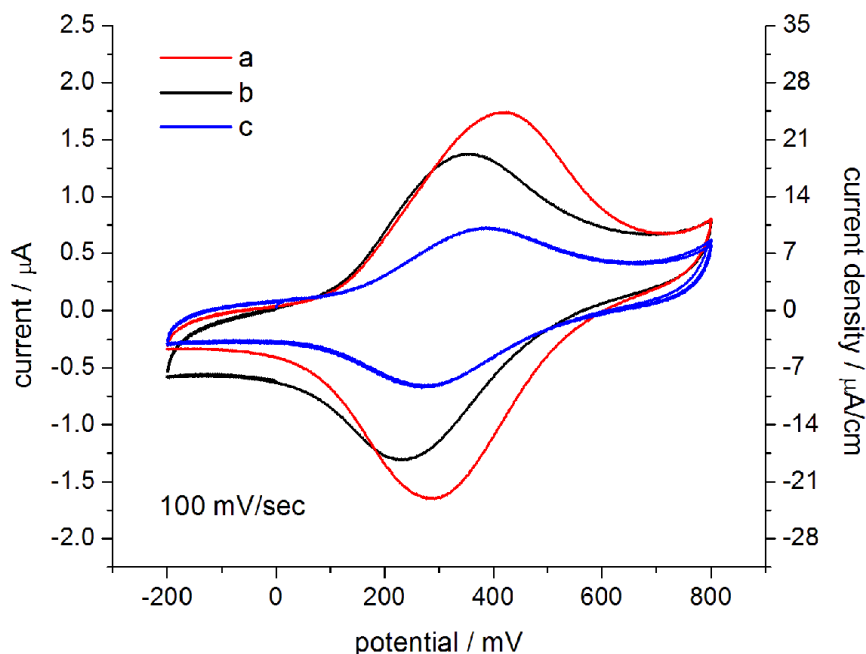


**Figure 84:** CV scan of P(tBuMA-co-VFc); freshly prepared sample (a); measurements after two days stored under air at rt (b); 4.5 hours after b) subsequent to constant measuring in the electrochemical cell (c).

#### 4.3.3.2 Polymer analogue coupling of aminoferrocene to P(MA) brushes

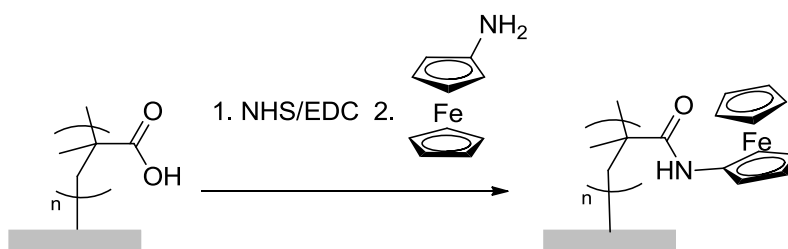


**Figure 85:** Preparation of P(MA)-AmFc under the formation of an amide bond between carboxylic acid moieties and aminoferrocene.

Since the hydrolysis of P(tBuMA-co-VFc) leads to a significant loss of mediator functionalities, a second strategy to incorporate ferrocene into polymer brushes was investigated, namely the polymer-analogue coupling of aminoferrocene into P(MA) brushes (Figure 81, b and Figure 85). Aminoferrocene coupled to a carboxy-terminus of a peptide has

already been used as a mediator in bioconjugates.<sup>[352]</sup> First, P(MA) brushes on NCD were prepared by the SIPGP of tBuMA for 6 hours and subsequent hydrolysis of the P(tBuMA) brushes with methanesulfonic acid in DCM at rt. The resulting layer thicknesses were determined by ellipsometry. In a next step, the carboxylic acid groups were activated in NHS/EDC and aminoferrocene was coupled into the P(MA) brushes in buffer at rt. Although water does not present an ideal solvent for aminoferrocene, the aqueous solution was chosen in order to conduct the reaction in enzyme-friendly conditions. The resulting P(MA)-AmFc brushes were thoroughly cleaned in ultrasonication and characterized by AFM, contact angle and CV. The CV peaks show the presence of ferrocene at the electrode, but reveal a shoulder which indicates that the ferrocene is not homogeneously attached to the brushes (Figure 86). Furthermore, the redox current peak lies at approximately 500 nA which is four times less than in copolymerized P(tBuMA-co-VFc). The dependence of different polymer brush thicknesses on the resulting CV peaks was investigated. Expectedly, the sample with 120 nm polymer brush height shows the largest peak integral with a charge density of  $15.9 \mu\text{C}/\text{cm}^2$  (Figure 86, black curve). However, an unclear dependence was found for 60 and 20 nm P(MA)-AmFc brushes which both show particularly small response in CV.

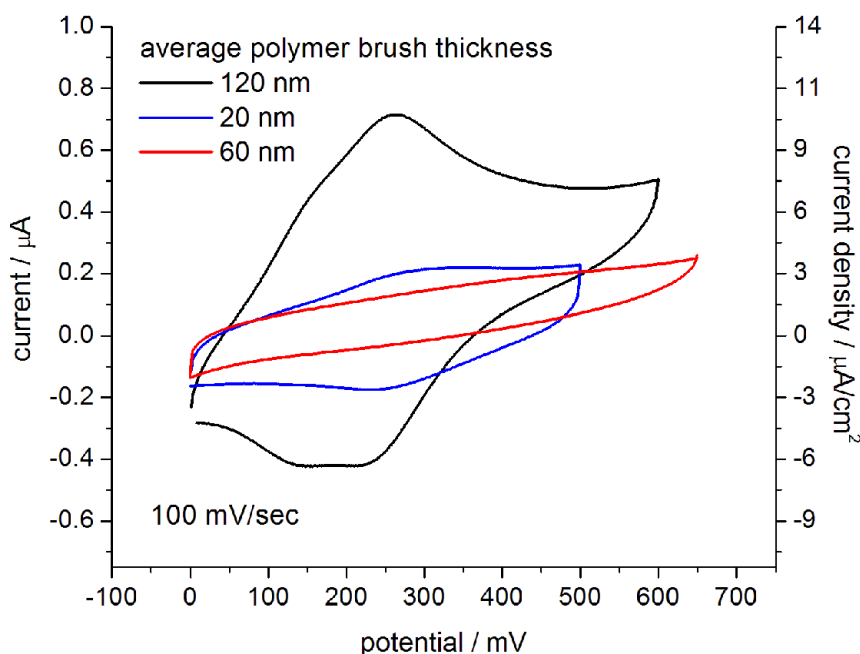


**Figure 86:** CV of P(MA)-AmFc at a scan rate of 100 mV/sec; measurement of samples with different polymer brush height determined by ellipsometry.

AFM measurements on structured P(MA)-AmFc brushes did not reveal a significant height difference between P(MA) and P(MA)-AmFc which indicates, corroborating the CV experiments, that only little amounts of ferrocene was coupled into the brushes. On another set of NCD samples, the polymer analogue reaction of aminoferrocene was carried out in acetonitrile representing a better solvent than water. However, no significant enhancement of coupling performance could be observed. The results are in agreement with the work of Gerhard Richter from our group, who observed a low reactivity of amine groups directly substituted at an aromatic ring. Therefore, a small spacer between the mine moiety and the Cp ring is expected to drastically increase the reactivity of the ferrocene derivative.

#### 4.3.3.3 Polymer analogue coupling of aminomethylferrocene in P(MA) brushes

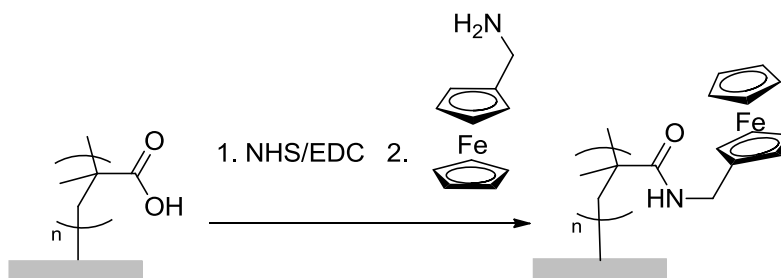


**Figure 87: Preparation of P(MA)-AmMeFc under the formation of an amide bond between carboxylic acid moieties and aminomethylferrocene**

Aminomethylferrocene (AmMeFc) was synthesized from ferrocene-carbaldehyde according to Beer *et al.* [353] via ferrocenecarbaldehyde oxime (Figure 88). Aminomethylferrocene was identified by FT-IR and NMR but traces of LiOH generated during work-up were difficult to remove from the resulting oily product.

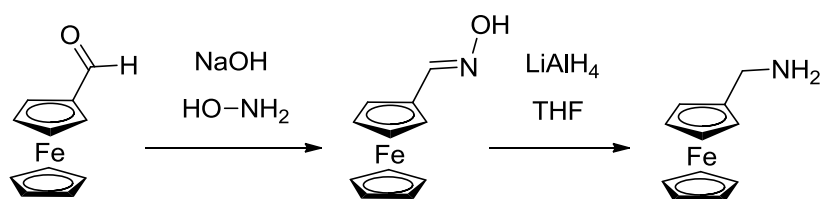


**Figure 88: Synthesis of aminomethylferrocene; formation of an oxime intermediate starting from ferrocenecarbaldehyde and reduction to aminomethylferrocene with lithiumaluminiumhydride.**

The incorporation into P(MA) brushes was performed analogue to chapter 4.3.3.2 (Figure 81 c). First, P(MA) brushes on NCD were prepared by the SIPGP of tBuMA for 6 hours and subsequent hydrolysis of the P(tBuMA) brushes with methanesulfonic acid in DCM at rt. In a next step, the carboxylic acid groups were activated in NHS/EDC and aminoferrocene was

coupled into the P(MA) brushes either in buffer or in acetonitrile at rt (Figure 87). Further analysis of the functionalized NCD samples was provided by cyclic voltammetry, AFM measurements of structured surfaces, contact angle and XPS.

CV measurements of P(MA)-AmMeFc revealed well-defined redox peaks with an  $E_{1/2}$  of 278 mV. Evaluation of the peak integral analogue to chapter 4.3.3.1 results in a charge density of  $238.4 \mu\text{C}/\text{cm}^2$  which corresponds to approximately 15 units of ferrocene per  $\text{nm}^2$ . Thus, the mediator loading is around one order of magnitude higher than in case of P(MA)-AmFc. Figure 89 clearly illustrates the difference in redox responsiveness between aminoferrocene and aminomethylferrocene functionalized P(MA) brushes on NCD.

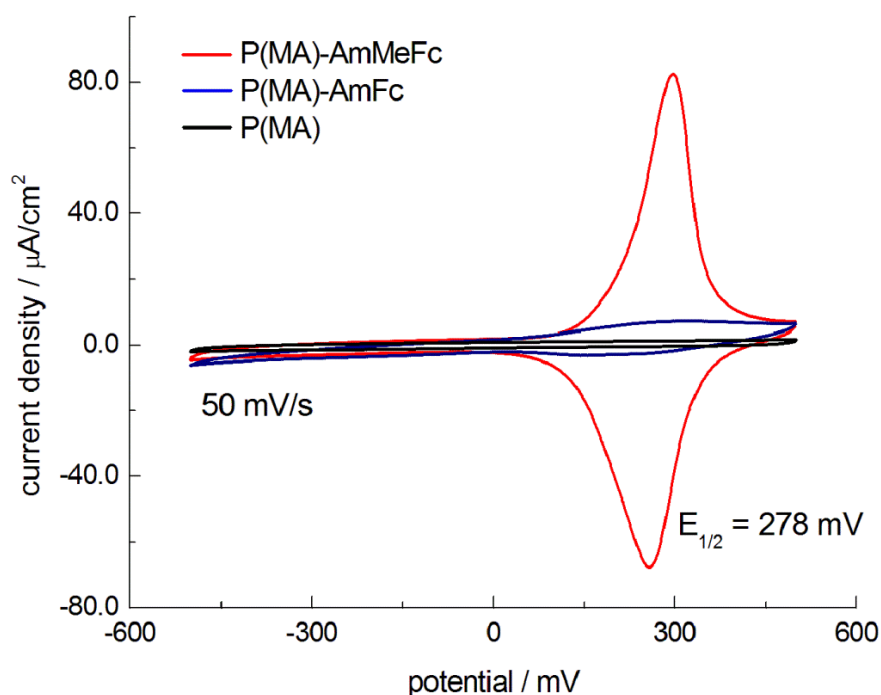


**Figure 89:** CV scan at 50 mV/sec of a P(MA)-AmMeFc modified NCD electrode in comparison to a P(MA) reference and a P(MA)-AmFc modified sample;  $h_{\text{P(MA)-AmMeFc}} = 32 \pm 2 \text{ nm}$ ,  $h_{\text{P(MA)-AmFc}} = 100 \pm 20 \text{ nm}$ ,  $h_{\text{P(MA)}} = 18 \pm 2 \text{ nm}$ .

NCD samples patterned by photolithography were functionalized with P(tBuMA), P(MA) and P(MA)-AmMeFc, successively, in order to follow the surface chemical modification in terms of polymer brush height. Figure 90 depicts the AFM image and the section analysis of the respective reaction steps towards P(MA)-AmMeFc brushes. A thickness increase from around  $160 \pm 10 \text{ nm}$  at the highest point before to  $300 \pm 20 \text{ nm}$  after ferrocene modification could be observed. In addition to the results obtained by CV, the increase in polymer layer thickness is an additional indication for high mediator loading. Although an exact quantification cannot be performed based on these AFM measurements, the aminomethylferrocene loading appears higher when investigated by AFM in comparison to the results from CV. This gives rise to the

assumption that either not all ferrocene species are converted during the potential sweep or that the charge transfer from distant ferrocene moieties to the electrode surface is hindered.

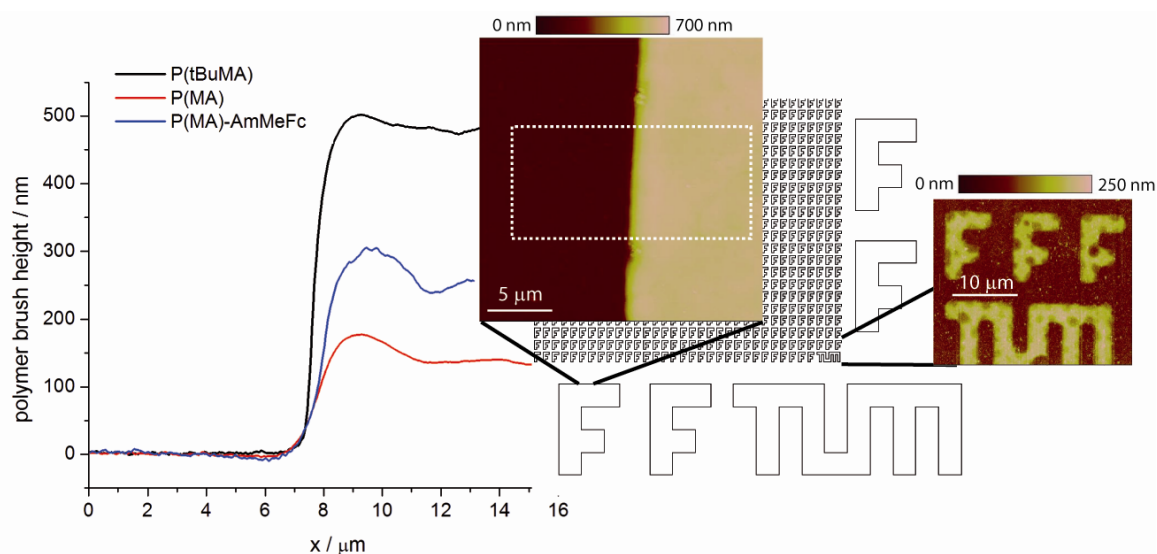


**Figure 90:** AFM section analysis and image measured over the indicated area of F-patterned features prepared by common photolithography and amplified by the SPIGP of tBuMA; resulting P(tBuMA) (black), P(MA) (red) and P(MA)-AmMeFc brush heights.

Furthermore, contact angle measurements of ferrocene-modified polymer brushes on NCD were carried out (Table 10). According to the results obtained by AFM and CV, most quantitative introduction of ferrocene is achieved by polymer analogue coupling of aminomethylferrocene resulting in a contact angle close to 90°.

**Table 10:** Results of contact angle measurements on differently functionalized NCD surfaces.

Sample form	Contact angle $\Theta$ /°
NCD pure	$52 \pm 2$
P(tBuMA)	$80 \pm 4$
P(MA)	$32 \pm 2$
P(MA-co-VFc)	$56 \pm 3$
P(MA)-MeFc	$54 \pm 2$
P(MA)-AmMeFc	$89 \pm 7$

Functionalized NCD samples were characterized by X-ray photoelectron spectroscopy (XPS) to complete the investigation on ferrocene-modified polymer brushes. Figure 91 provides a comparison between P(MA) and ferrocene-modified P(MA)-AmMeFc brushes prepared in acetonitrile. The silicon response at 103 eV and 153 eV on the P(MA) sample is caused by

scratches in the thin diamond surface exposing the underlying  $\text{SiO}_x$  substrate. The coupling of aminomethylferrocene results in a nitrogen peak at 399 eV from the amide bond and the very characteristic 2p peaks for iron, split into the two spin-orbit components at 708 eV for  $2p_{3/2}$  and 720 eV for  $2p_{1/2}$ . A normalized atomic ratio of approximately 1.5 was found for Fe(II)/Fe(III). The three additional iron peaks result from Auger electrons and do not provide further valuable information. The magnification into the area between 700 and 735 eV and respective deconvolution fitting allows an insight into the Fe 2p region showing distinct peaks for Fe(III) and Fe(II) species (Figure 92). Traces of lithium are found at 45 eV because the last synthetic step towards aminomethylferrocene includes  $\text{LiAlH}_4$  and consequently  $\text{Li(OH)}$  which persists in small amounts during the polymer analogue reaction.

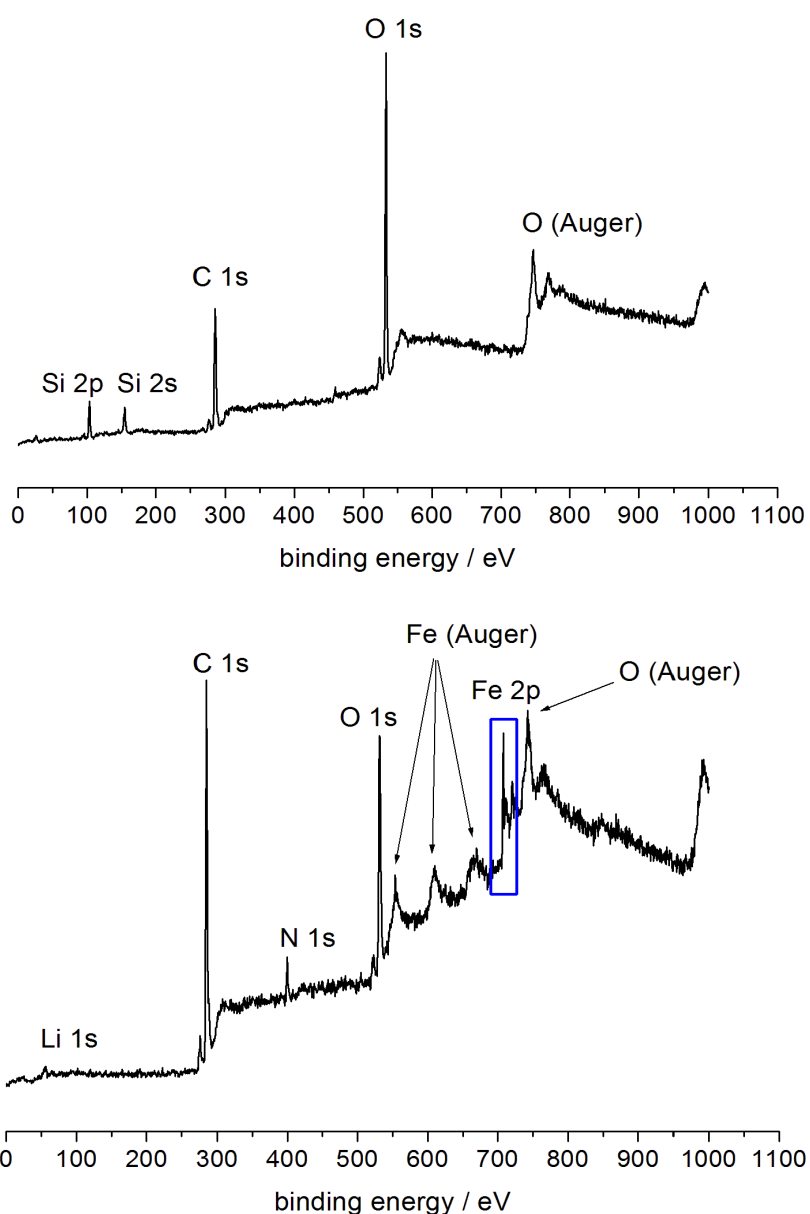
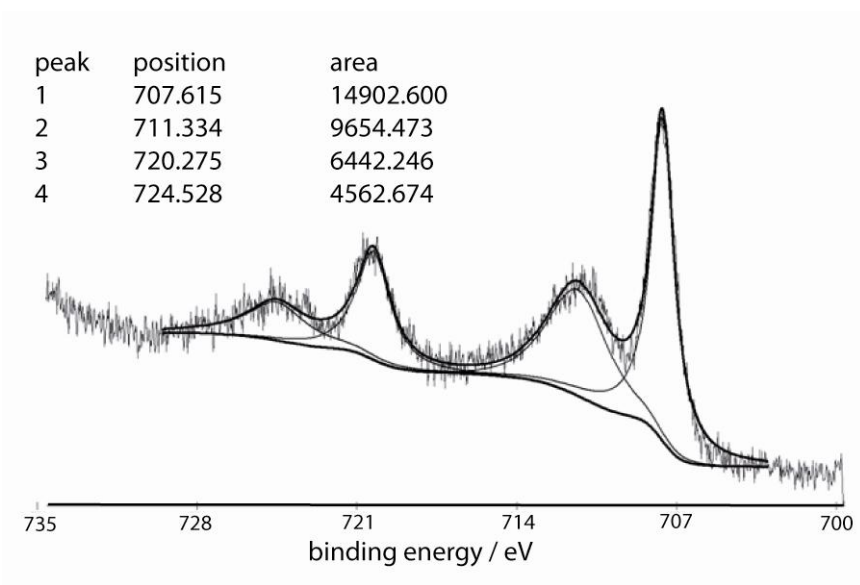


Figure 91: XPS analysis of a P(MA) reference sample and P(MA)-AmMeFc.



**Figure 92: Magnified section of the area for Fe 2p with respective deconvolution fits of the Fe(II) and Fe(III) species.**

Polymer analogue coupling of aminoferrocene and aminomethylferrocene into P(MA) brushes grafted on NCD was investigated and presented in this chapter. In terms of the reactivity of the pendant amine, aminomethylferrocene providing a C1-spacer at the Cp ring was found to be more qualified than aminoferrocene. A high and stable loading of ferrocene moieties was determined by CV and AFM measurements. Consequently, using P(MA)-AmMeFc polymeric mediators is a promising approach for ensuing amperometric sensing experiments involving redox enzymes.

## 4.4 Electrochemical analysis of biofunctionalized polymer brushes on diamond electrodes

### 4.4.1 Electrochemical enzyme detection without mediator

Horseradish peroxidase (HRP)-based enzyme electrodes were prepared according to chapter 4.2.2.2 by NHS/EDC activation and subsequent coupling to P(MA) brushes on boron-doped NCD. Initially, the CV experiments were carried out without the addition of a charge carrier to obtain a reference spectrum. The Fe(II)/Fe(III) containing heme prosthetic group shows minor redox response (Figure 93). Because of insufficient electron transport, only HRP located at the very vicinity of the electrode could be detected. From the integration of the HRP redox peaks, a number of  $2 \times 10^{12} \text{ cm}^{-2}$  (detected) enzymes on the surface could be determined. This corresponds to a theoretical surface coverage of 14 % assuming an enzymatic diameter of 3 nm.<sup>[335]</sup> However, this number does not represent the real quantity on the NCD surface because low charge transfer between the prosthetic group and the electrode inhibits a proper determination. Therefore, chronoamperometric measurements are meaningless without the presence of a mediator.

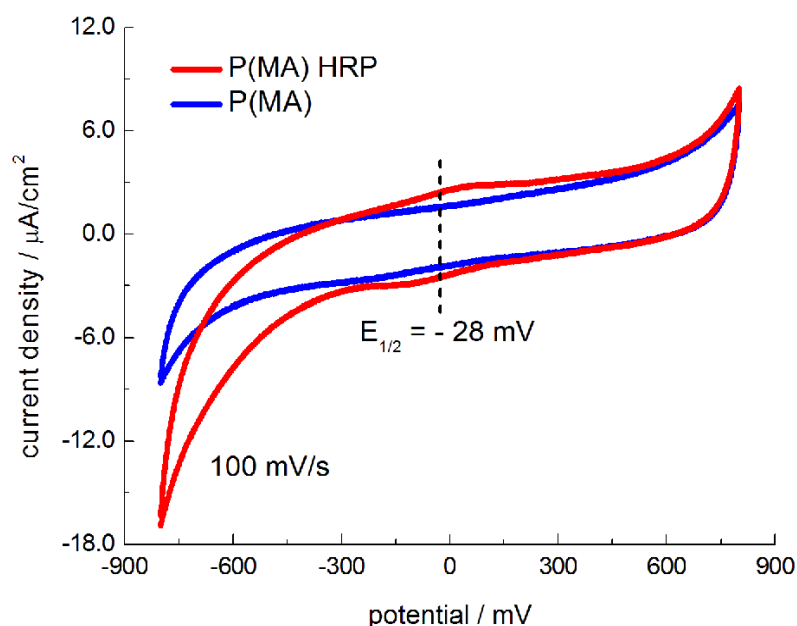


**Figure 93:** CV scan of a P(MA)-HRP functionalized NCD electrode and a P(MA) reference at a scan rate of 100 mV/sec without the addition of a mediator.

#### 4.4.2 Application of free mediator in solution

To provide electron transfer in the biomolecule-polymer brush-electrode system is an essential challenge in the design of amperometric biosensors. Two strategies for the introduction of charge mediators into the biofunctionalized diamond electrodes were applied in the course of this thesis. A widely used approach, which is discussed in this chapter, is the addition of a free mediator to the electrolyte; the second one is the integration of charge carrier molecules as polymeric mediators (Figure 94).

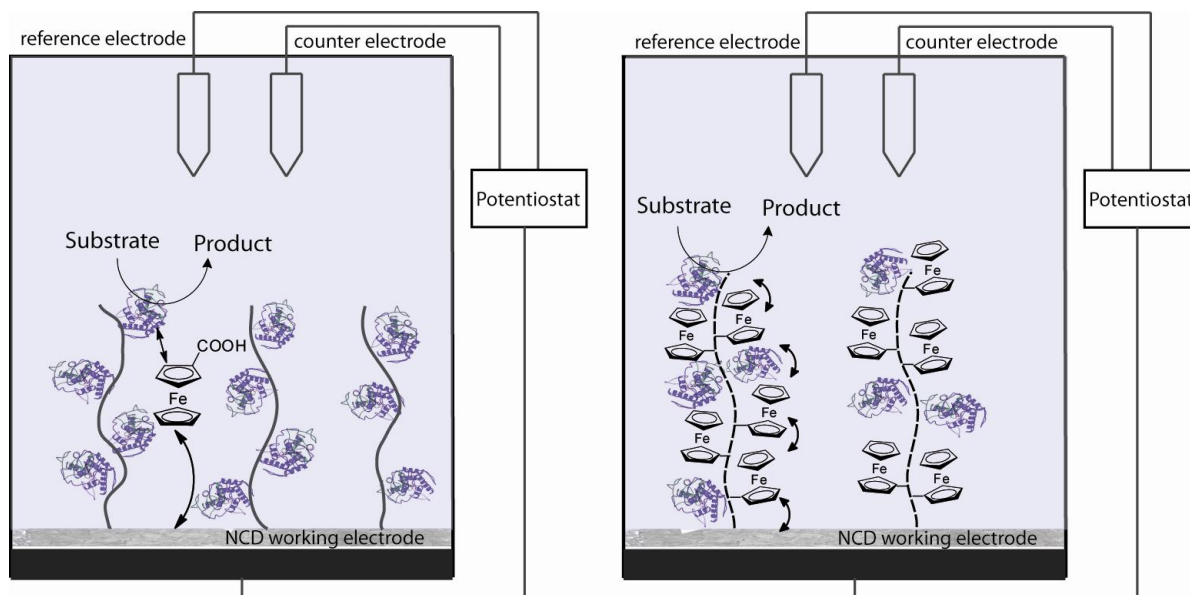
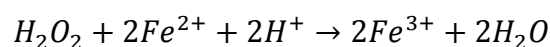


**Figure 94:** Scheme of an experimental set-up for amperometric measurements on biofunctionalized NCD electrodes; left: addition of the mediator as free ferrocene carboxylic acid in solution; right: mediator as AmFc or AmMeFc attached onto polymer brushes.

The considered enzyme electrode system was P(MA) brushes on NCD, biofunctionalized with HRP. To the buffer solution in the electrochemical cell, 0.1 mM of ferrocene carboxylic acid was added prior to the measurement. Thus, this experimental set-up would correspond to a 2<sup>nd</sup> generation biosensor. Naturally, clear ferrocene peaks were obtained during CV. However, when switching to chronoamperometric mode, the current response upon external addition of up to 100 mM H<sub>2</sub>O<sub>2</sub> of pure P(MA) functionalized samples equaled those of P(MA)-HRP. So, the enzymatic conversion of the substrate is found to be dominated by an electrode side reaction in which H<sub>2</sub>O<sub>2</sub> is directly converted by the ferrocene carboxylic acid as in:



Obviously, this reaction is not unknown and has even been used - without enzyme - for sensing applications <sup>[354]</sup> but surprisingly, some research groups do not report difficulties in HRP-H<sub>2</sub>O<sub>2</sub>-ferrocene systems. <sup>[355]</sup>

The interference caused by the high excess of mediator compared to HRP was expected to diminish in case of the polymeric mediator system P(MA)-AmMeFc. In addition to that, it is hard to argue for potential biosensor applications, especially working *in vivo*, when a free compound without detailed toxicological profile needs to be added.

#### 4.4.3 Enzymatic reactions in polymeric mediators

A very straightforward method for the parallel coupling of both enzymes and ferrocene was developed. The carboxylic moieties of P(MA) brushes on diamond were activated in NHS/EDC and subsequently reacted with a buffer solution of horseradish peroxidase (HRP) for one hour. Then, after short rinsing, the sample was emerged in a buffer solution of aminomethylferrocene in order to saturate the remaining NHS-esters (Figure 95). The bulky enzyme conformation gives rise to the assumption that the enzyme does certainly not take up all active coupling sites during the first hour. Aminomethylferrocene on the other hand, was found to be very reactive and to yield in a high loading after merely ten minutes (chapter 4.3.3.3). By using such a polymeric mediator approach, a 3<sup>rd</sup> generation type biosensor is created.

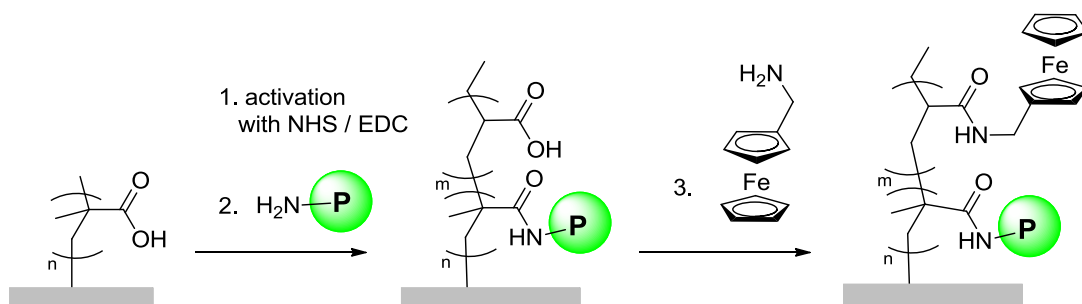


**Figure 95: Preparation of P(MA)-enzyme-AmMeFc by coupling of the biomolecule to P(MA) and subsequent reaction with AmMeFc; with protein P = horseradish peroxidase or glucose oxidase.**

The CV scans of P(MA)-HRP-AmMeFc were hard to interpret since the redox peaks showed irregular peak shoulders (Figure 96). Hence, amperometric scans did not give reliable current responses. Presumably, the side reaction of ferrocene with H<sub>2</sub>O<sub>2</sub> discussed in chapter 4.4.2 leads to very complex electrochemical activities at the electrode interface. Moreover, it can be observed that the measured current is considerably smaller than in the case of enzyme free

P(MA)-AmMeFc (Figure 89). One explanation might be the hindered accessibility of the reactive NHS-ester sites during aminomethylferrocene coupling due to the pendant HRP molecules. Another reason is certainly a lower conversion for the mediator coupling reaction in buffer (for P(MA)-HRP-AmMeFc) instead of ACN (for enzyme-free P(MA)-AmMeFc).

In order to overcome the disturbing side reaction of ferrocene with  $H_2O_2$ , the surface electrochemistry had to be reconsidered. Adhering to the very promising polymeric mediator system P(MA)-AmMeFc the enzyme-substrate pair was replaced by glucose oxidase (GlucOx) and glucose - a well-established recognition reaction which does not run the risk of interfering with ferrocene.<sup>[33-34]</sup> The preparation protocol was maintained, except for the coupling of GlucOx instead of HRP.

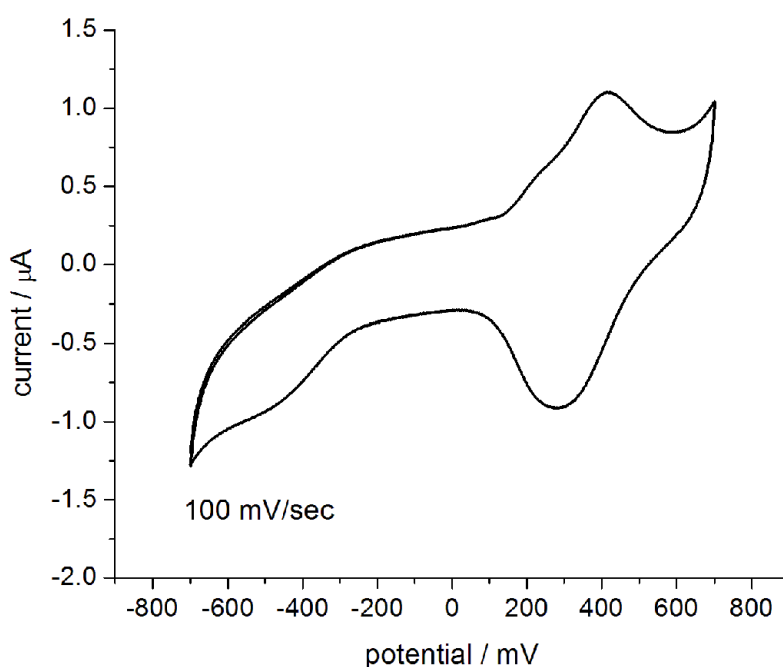


**Figure 96:** CV scan of P(MA)-HRP-AmMeFc at a scan rate of 100 mV/sec.

The coexistence of GlucOx and ferrocene in the P(MA) brushes on NCD was proven by determining the enzymatic activity in a colorimetric assay (Figure 97) and by visualizing the presence of the mediator in CV, respectively (Figure 98). The enzymatic assay with homovanillic acid (see chapter 4.2.3.2) displayed accurate increase of the fluorescence intensity over time. Moreover, a clear dependence of the reaction rate with the glucose concentration was observed. The reaction rates are lower than in the case of ferrocene-free P(MA)-GlucOx because the coupling of GlucOx to P(MA) was only allowed one hour instead of 20 hours.

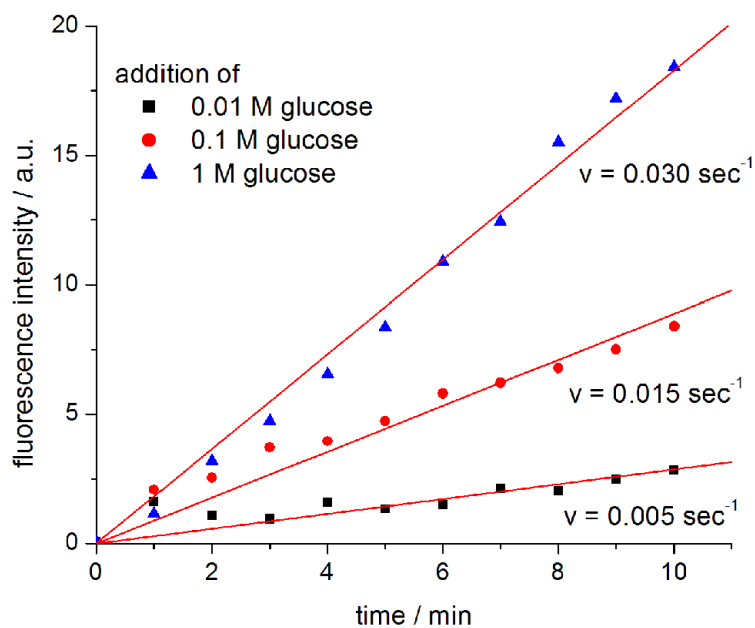


**Figure 97:** Colorimetric assay with HVA to determine the presence of active GlucOx on a P(MA)-GlucOx-AmMeFc functionalized NCD surface.

The potential  $E_{1/2}$ , taking the mean of  $E_a$  and  $E_c$ , for P(MA)-GlucOx-AmMeFc was found at 255 mV which is in good agreement with the values obtained for aminomethylferrocene in P(MA)-AmMeFc brushes (278 mV, Figure 89). Upon variation of the scan rate from 10 to 1000 mV/sec, an increasing overpotential can be observed which is expressed by an increased peak-to-peak separation and which is due to a delayed response time of the system at high sweep rates. Moreover, the peak integrals become larger. The integration of the redox peaks, e.g. for  $v = 1000$  mV/sec, yields a charge density of  $157 \mu\text{C}/\text{cm}^2$  which corresponds to a density of  $9.8 \times 10^{14}$  ferrocene moieties per  $\text{cm}^2$ . This calculates to thus at least a 10-times multilayer (assuming a projected area  $A_{\text{fc}} = 1 \text{ nm}^2$ ). It is noteworthy that the charge density found for each respective scan rate is approximately constant because at higher scan rates, the same amount of charge is converted in a shorter period of time which necessarily leads to a higher current. This dependence can be found in Eq. 18 presented in chapter 4.3.3.1. The observed current as a function of the scan rate is given in Figure 99.

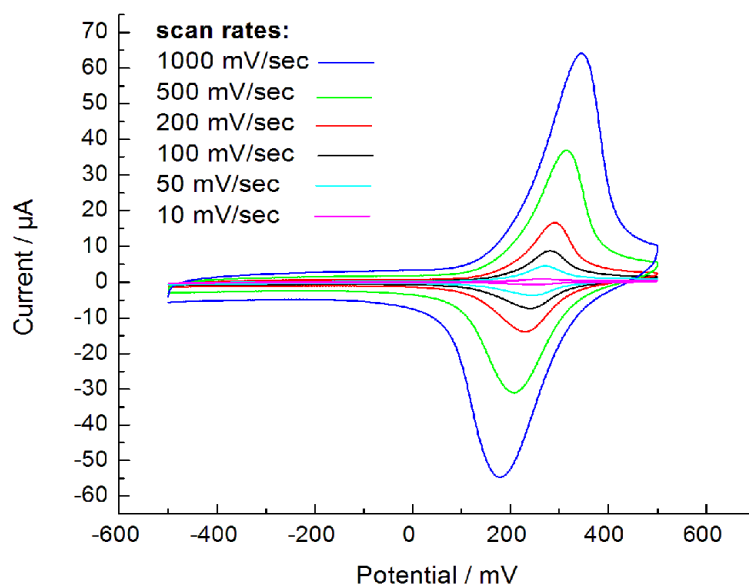


Figure 98: CV scan of a P(MA)-GlucOx-AmMeFc functionalized NCD electrode at various scan rates.

When the maximum oxidative current as a function of the scan rate for the P(MA)-GlucOx-AmMeFc functionalized samples (Figure 99) is compared to a system with free ferrocene-carboxylic acid (Figure 100), there is an indication that the electron transport kinetics differ. However, the exact mechanism of electron transport in the polymeric mediator system is not fully understood, yet, and will be a focused in more detail in proceeding work by Andreas Reitingner, WSI.

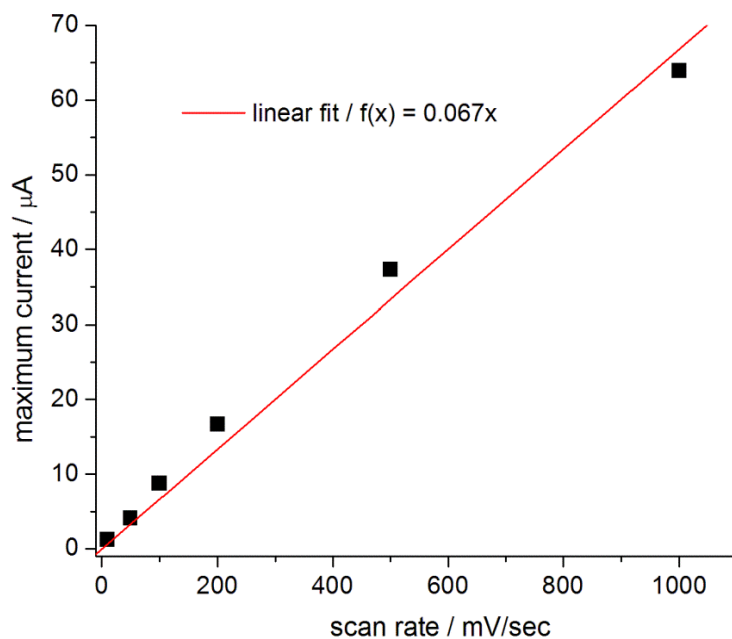
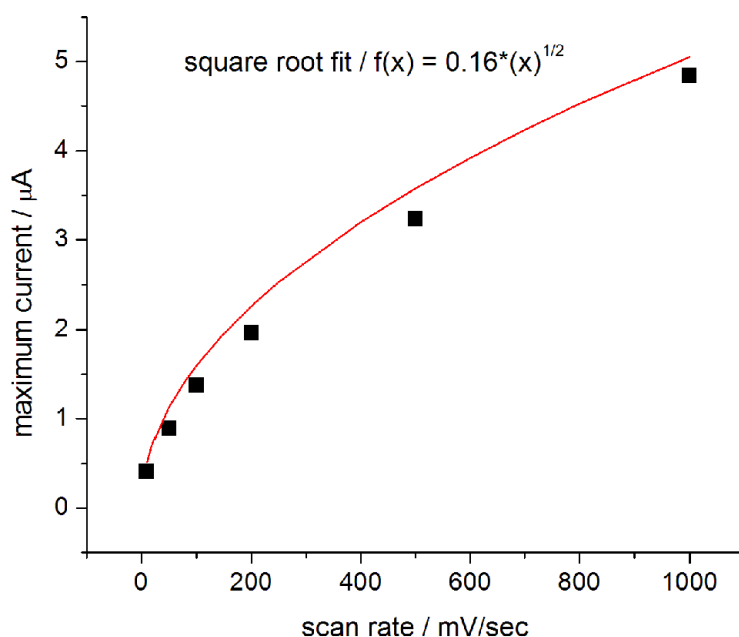


Figure 99: Dependence between the maximum peak current and the scan rate during CV of P(MA)-GlucOx-AmMeFc and linear fit.



**Figure 100: Dependence between the maximum peak current and the scan rate during CV of free ferrocene carboxylic acid (0.1 mM) and fit in square root dependence.**

For chronoamperometry, a steady potential of 400 mV was applied between the NCD working functionalized with P(MA)-GlucOx-AmMeFc and the counter electrode. In the beginning, a steep current drop from  $10^{-7}$  to  $10^{-8}$  A is observed upon applying a potential and the system is kept under constant conditions for one hour in order to reach equilibrium. (This first period of time of the chronoamperometric scan is not displayed in the following figures.) Then, the external conditions are changed by the step-wise addition of glucose and the resulting current is measured. The obtained spectra exclusively show the experimental results after a one-hour period of pre-stirring.

A comparison of the results on a P(MA)-AmMeFc reference sample compared to enzyme-functionalized P(MA)-GlucOx-AmMeFc is given in Figure 101. A spontaneous, shortly persisting drop of the current at the very moment of substrate addition is attributed to the stirring method and does not serve further electrochemical interpretation. No activity upon addition of glucose was found for the enzyme-free P(MA)-AmMeFc sample. Thus, by changing the biomolecule-substrate system unwanted side-effects from a possible reaction of ferrocene with the substrate could be avoided.

- RESULTS AND DISCUSSION -

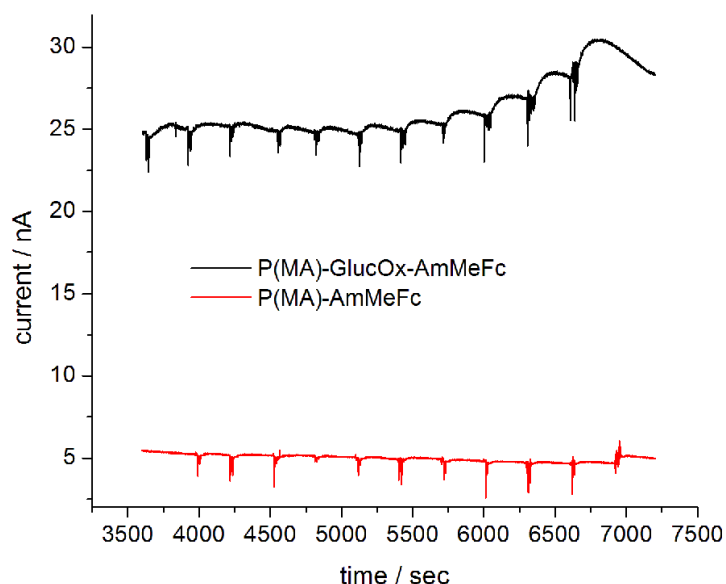


**Figure 101: Chronoamperometric measurement of a P(MA)-GlucOx-AmMeFc functionalized NCD sample upon addition of different concentrations of glucose (black); reference measurement of a P(MA)-AmMeFc modified sample (red).**

The addition of glucose (0.001 to 100 mM) to the P(MA)-GlucOx-AmMeFc modified NCD electrode leads to a current increase in the range above the redox potential of ferrocene, attributed to the mediated enzymatic oxidation of glucose (Figure 102). Diffusion of glucose to the polymer brush-bound enzymes plays an important role in the performance of the current signal and is probably causing the fact that the current plateaus drop to a certain extent.

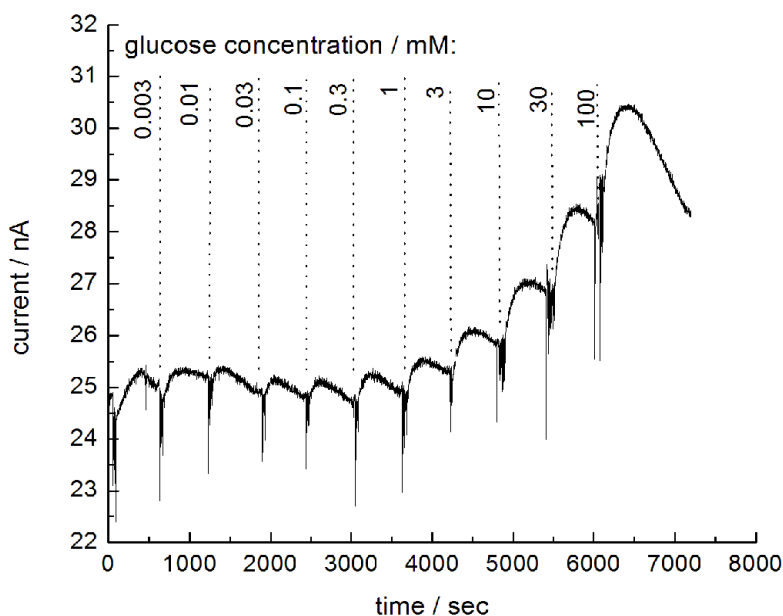


**Figure 102: Magnification of the plot presented in Figure 101; Chronoamperometric measurement of a P(MA)-GlucOx-AmMeFc functionalized NCD sample upon addition of different concentrations of glucose; the total glucose concentration in the electrochemical cell is varied between 0.003 mM and 100 mM.**

The current values at the maxima were used to plot the current response over glucose concentration (Figure 103) and thus giving the actual result for the sensing performance. Since it was operated under very low currents, it is crucial to subtract the reference measurement for reliable interpretation. At a concentration of 100 mM glucose in the cell volume ( $2 \times 10^{-3}$  mol), a current of 23.5 nA ( $= 2.35 \times 10^{-8}$  C/sec) was observed. Reverse calculations produce a corresponding flux of electrons of  $1.47 \times 10^{11}$  electrons/sec and consequently  $7.33 \times 10^{10}$  molecules of converted glucose/sec ( $= 1.22 \times 10^{-13}$  mol/sec). Assuming that the observed current represents the full enzymatic reaction without loss during electron transfer, the complete consumption of the present glucose would take over 500 years. However, this calculation is based on a small surface area of only  $7.07 \text{ mm}^2$ . When the surface is theoretically expanded to a still practicable size of  $7.07 \text{ dm}^2$ , full conversion could be reached after 19 days (disregarding diffusion limitations). Moreover, the current response can certainly be enhanced by optimizing the charge transfer.

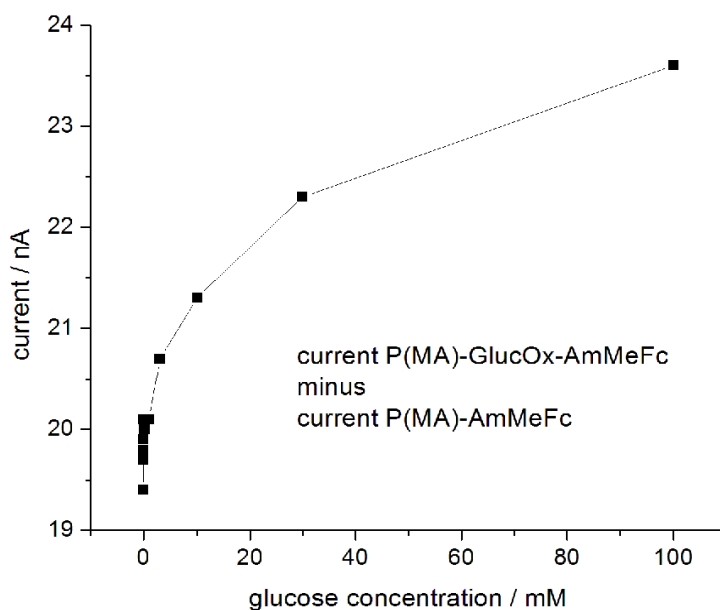


**Figure 103: Normalized plot of the current maxima determined by chronoamperometry versus the respective concentration of glucose; the background current obtained from the P(MA)-AmMeFc reference experiment is subtracted from the original plot presented in Figure 102.**

The detection of the glucose concentrations is carried out indirectly via the measurement of the current produced due to the re-oxidation of the ferrocene mediator (Figure 104).<sup>[34]</sup> Similarly to the colorimetric assay, the detailed biochemical pathway is again based on the reaction of the cofactor flavine adenine dinucleotide (FAD).<sup>[35]</sup>

1.  $glucose + GlucOx(FAD) \rightarrow gluconolactone + GlucOx(FADH_2)$
2.  $GlucOx(FADH_2) + 2Fc(III) \rightarrow GlucOx(FAD) + 2Fc(II) + 2H^+$
3.  $2Fc(II) \rightarrow 2Fc(III) + 2e^-$

It is noteworthy, that the reaction scheme presented in Figure 104 only takes half of the cell process into account. The electric circuit is closed by the reaction occurring at the distant platinum counter electrode where presumably protons are reduced to hydrogen gas.

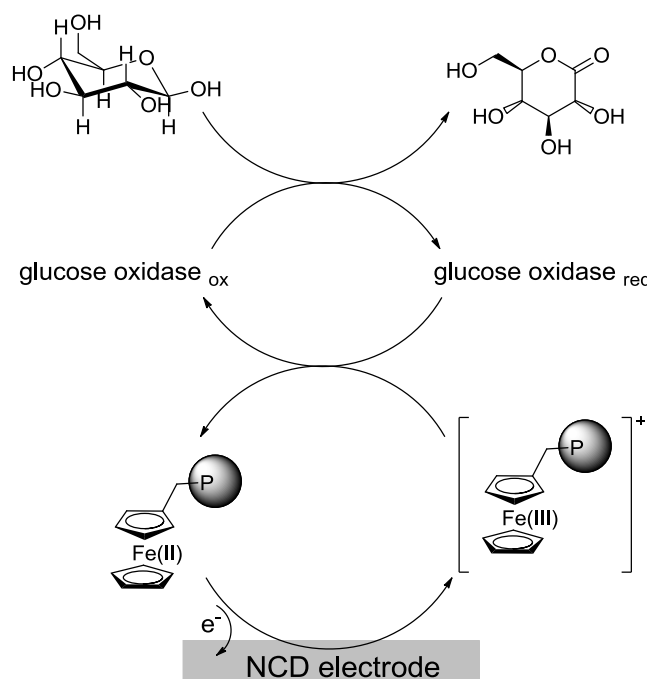


**Figure 104:** Reaction cycle occurring during the amperometric detection of glucose with biofunctionalized NCD electrode; first: specific recognition reaction between glucose and  $GlucOx_{ox}$ ; recovery of the initial oxidation state of the enzyme by polymer brush-bound ferrocene; eventual re-oxidation of the ferrocene to ferrocinium moieties under the generation of a current at the NCD electrode.

In comparison to results presented by other research groups, relatively low values for the current were obtained. Some current values obtained for the same enzymatic reaction with 30 mM glucose on graphite electrodes (covalently immobilized glucose oxidase)<sup>[34]</sup> and on gold electrodes (physisorbed glucose oxidase)<sup>[32]</sup> are 20  $\mu$ A and 85 nA (Figure 12), respectively. Still, the presented concept of a NCD-based enzyme electrode provides a sufficient sensitivity despite the initially high background current. The obtained results have shown that the P(MA)-AmMeFc-GlucOx functional interface can be used for biosensing

applications. Some optimization measures can help to improve the performance in future experiments: One parameter which could be taken into account for optimization is the pH value operated in. So far, at pH 7, the functionalized P(MA) brushes with a  $pK_a$  of around 5 are expected to be strongly stretched. According to Kilbey *et al.* <sup>[323]</sup>, the thickness increase in swollen P(MA) layers occurs primarily at around pH 5 and the P(MA) chains are fully deprotonated above pH 6. However, electron transport could be enhanced by working in more collapsed state of the brushes where the contact between the ferrocene units is stronger (below pH 5). This dependency has been described by Kim *et al.* <sup>[349]</sup> who compared the electron transfer rates for ferrocene-containing brushes in different solvents. It was found that electron transfer is likely to be higher when the collapse of the film enables closer Fc-Fc contacts. <sup>[349]</sup>

So far, without further modification of the setup, the presented enzyme electrode would not be efficient as an energy source. In common fuel cells, a second cell reaction, separated via a membrane, would need to be coupled to the GlucOx/glucose reaction in order to dissipate reaction products and in order to ensure charge neutrality in the course of a long-term chronoamperometric run.

#### 4.4.4 Comparison between monolayer- and polymer brush bound enzymes

At first glance, enzyme electrodes on a monolayer platform seem to be an easier approach than using polymer brushes, because charge transfer is less challenging and the surface architecture is usually well known. Yet, 3 D interlayers bearing multiple functional groups are reported to enhance the long-term performance, i.e. the stability of the biomolecule and the matrix, and the signal intensity. This chapter gives a short summary of three different fields, in which the polymer brush method indeed implicates optimization, namely in enzyme activity measured by colorimetry, in fluorescence microscopy and in the electrochemical detection.

##### 4.4.4.1 Colorimetric assays

P(MA)-HRP and P(MA)-AmFc-HRP brushes were synthesized as described in chapter 4.2.2.2 and 4.4.3. The monolayer functionalized NCD was prepared in the Walter Schottky Institute according to a non-published protocol: Aminocaproic acid (ACA) was photochemically absorbed or grafted onto hydrogenated diamond. The exact mechanism and kind of surface link is not yet clear. Presumably, the interaction proceeds via the amine group as covalent bond or in ionic interactions. The resulting terminal carboxyl moiety was activated by NHS/EDC and reacted with HRP (Figure 105).

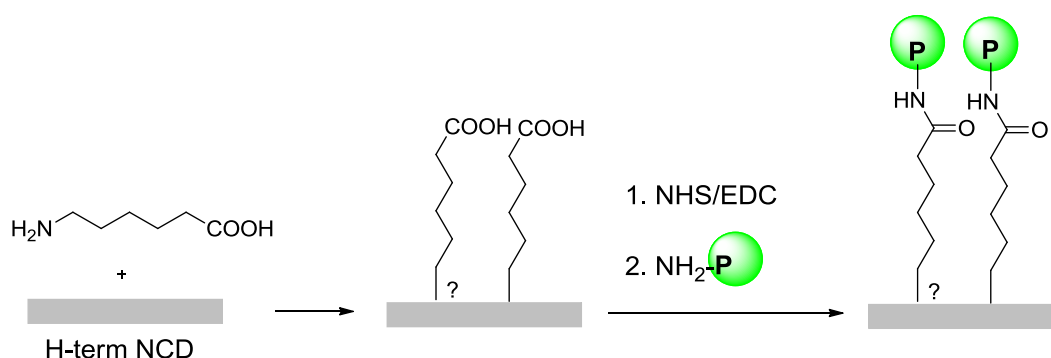


**Figure 105: Functionalization of hydrogenated NCD surfaces with aminocaproic acid and subsequent coupling of HRP.**

In a colorimetric assay with tetramethylbenzidine (TMB), performed three days after the sample preparation (described in chapter 4.2.3.2), the substrate conversion of three different samples was compared: The HRP-functionalized polymer brushes, with and without ferrocene, and the ACA-HRP surface (Figure 106). In all cases, the conversion rate as a function of TMB concentration show the characteristic Michaelis Menten behavior which

indicates a native enzymatic behavior. The reaction rates and Michaelis Menten constants are summarized in Table 11.

**Table 11: Kinetic parameters for enzymatic reactions on differently biofunctionalized NCD surfaces.**

Sample form	$v_{\max}$	$K_M$
P(MA)-AmFe-HRP	1.39	0.74
P(MA)-HRP	1.69	0.48
ACA-HRP	0.43	0.47

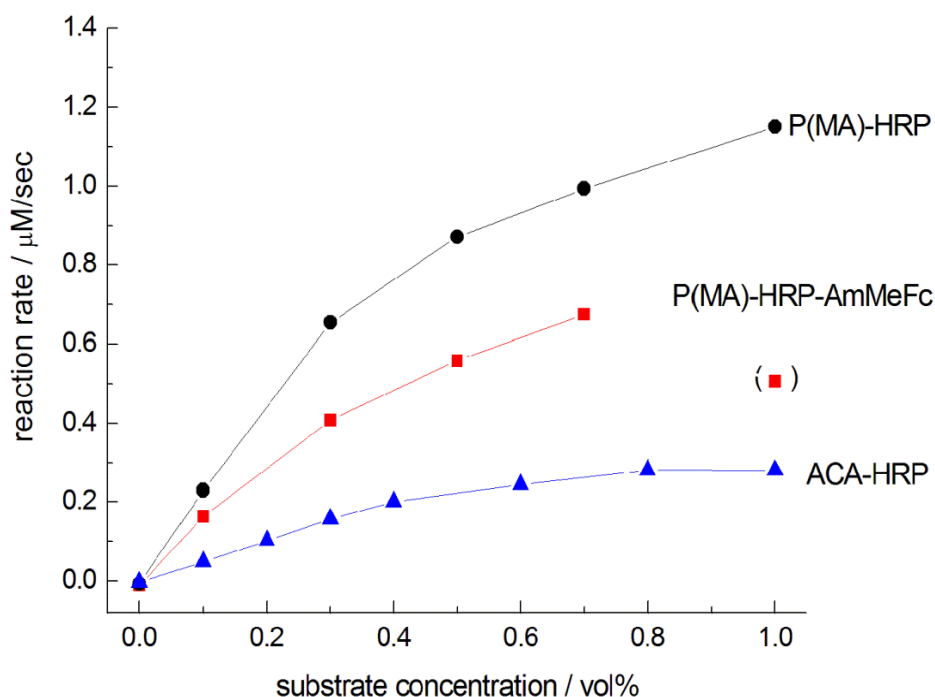


**Figure 106: Reaction rate versus TMB concentration from colorimetric TMB assays of HRP coupled to NCD surfaces; monolayer approach: ACA-HRP on NCD (blue); polymer brush-biomolecule conjugate: P(MA)-HRP (black); HRP on a polymeric mediator: P(MA)-HRP-AmMeFc (red).**

Higher  $v_{\max}$  for P(MA)-HRP compared to ACA-HRP can be ascribed to a higher surface concentration of the enzyme. The ferrocene-containing P(MA) sample yields less formation of dye because for the dual functionalized samples, less time was allowed for HRP coupling (1 hour instead of 16 hours) presumably causing incomplete immobilization. However, the activity might be underestimated in the experimental set-up as it could be observed that, even under thorough stirring, the blue compound adhered strongly to the polymer brushes and did not diffuse homogeneously to the optical path.

The enzyme loading was estimated by measuring the P(MA) layer thickness before and after biofunctionalization by ellipsometry (Table 12).

**Table 12: Polymer layer thickness determined by ellipsometry and approximated HRP loading.**

Sample form	thickness / nm as P(MA) precursor	thickness / nm as P(MA)-mod	approximated HRP loading
P(MA)-AmFe-HRP	11 ± 2	25 ± 5	not calculable
P(MA)-HRP	18 ± 4	28 ± 6	only ~ 3 layers of HRP <sup>6</sup>

The P(MA)-HRP sample reveals approximately three layers of HRP compared to an ideally assumed full monolayer coverage in case of ACA-HRP. This factor of three can be correspondingly found in the obtained conversion rates (Table 11) which display a  $v_{\max\text{-P(MA)-HRP}}$  around three times higher than  $v_{\max\text{-ACA-HRP}}$ .

The amount of loaded enzyme in P(MA)-AmFe-HRP cannot be calculated because both the coupled aminoferrocene and HRP are responsible for the thickness increase of the polymer brush layer, but their ratio of immobilization is unknown. Also, it has to be noted that ellipsometry results are not fully reliable because the  $n$  and  $k$  values of the respective surface intermediates are not defined and instead, as approximation, P(MMA) standard values were used for the thickness estimation which leads to considerable errors.

Different glucose oxidase functionalized samples were also compared regarding immobilization into polymer brushes or monolayers. The SAM was prepared by silanization reaction of aminopropyltriethoxysilane (APTES) on oxidized NCD. Coupling of GlucOx was carried out by means of glutaric dialdehyde as bifunctional linker as reported by our group.<sup>[356]</sup> By fluorescence photospectroscopy an approximately two orders of magnitude lower conversion of glucose was found in case of the monolayer-linked enzyme compared to a sample functionalized with P(MA)-GlucOx (Figure 107).

<sup>6</sup> assuming an average diameter of HRP of 4.5 nm

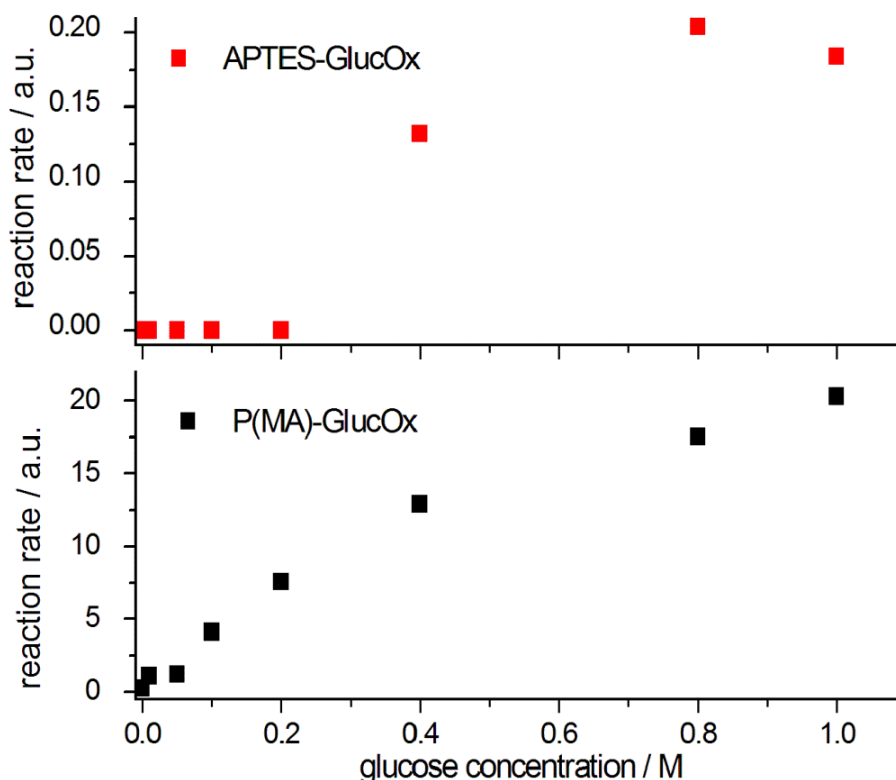


**Figure 107:** Colorimetric assay with HVA for the determination of glucose with GlucOx coupled to a NCD surface; APTES-GlucOx (red); P(MA)-GlucOx (black).

#### 4.4.4.2. Fluorescence bleaching

Originally, the idea was to compare the remarkable stability - even under drastically basic conditions - of P(MA)-bound GFP (presented in chapter 4.2.3.1) with monolayer-bound GFP. As demonstrated in Figure 108, a P(MA)-GFP polymer brush gradient prepared by carbon templating on NCD was exposed to light with a suitable excitation wavelength (395 nm) and the emission was measured over time. Using a medium intensity filter (level 2 out of 3), the emitted light is even oversaturated at  $t=0$ . After two minutes of constant exposure, the fluorescence still values over 50% of the original intensity. However, when performing a similar experiment on SAM-linked GFP, for example with aminocaproic acid, no fluorescence could be detected. Whether this is due to deficient surface chemistry during the preparation, or due to an instant bleaching upon exposure, remains uncertain.

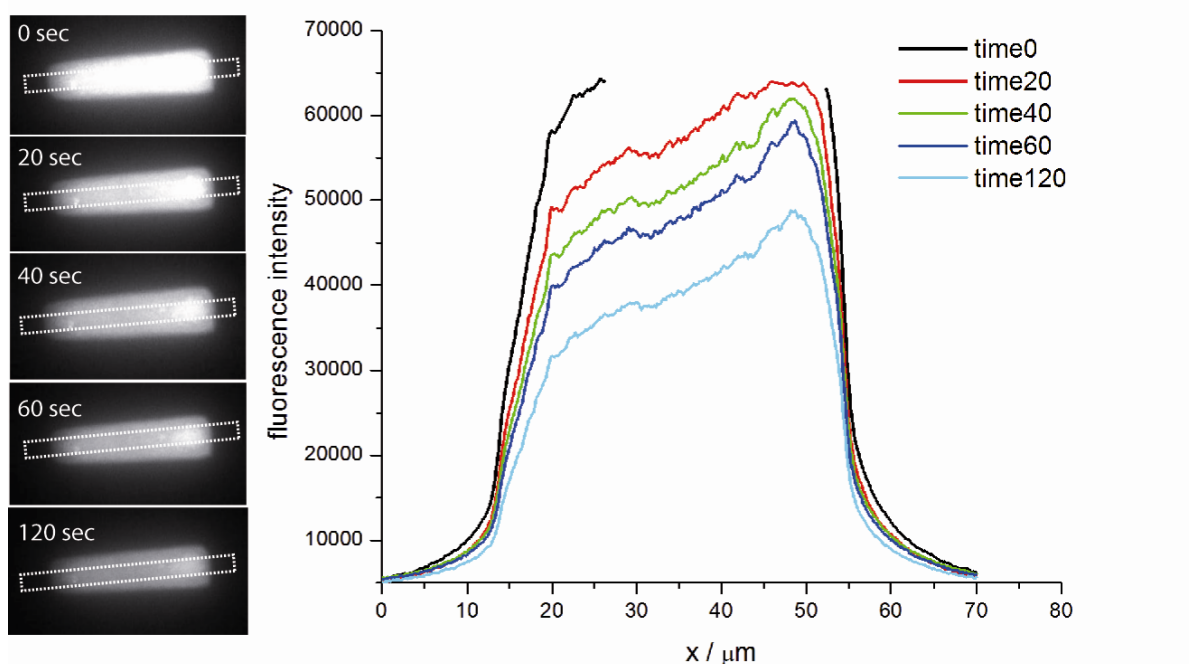


**Figure 108:** Section analysis measured over the indicated areas of fluorescence microscopy images of a P(MA)-GFP gradient ( $10 \times 50 \mu\text{m}^2$ ) on NCD prepared by CT; fluorescence intensity after different times of exposure to excitation wavelength.

#### 4.4.4.3 Amperometric detection of glucose

Stutzmann and coworkers have reported on the successful detection of HRP coupled to NCD electrodes via an APTES monolayer.<sup>[290]</sup> The obtained current change upon the addition of  $\text{H}_2\text{O}_2$  lies in the range of 20 nA. In order to compare the results from chronoamperometry of P(MA)-GlucOx-AmMeFc modified samples (chapter 4.4.3) with a monolayer approach, an oxidized NCD sample was first functionalized with APTES and subsequently reacted with glutardialdehyde and GlucOx (Figure 109).<sup>[356]</sup>

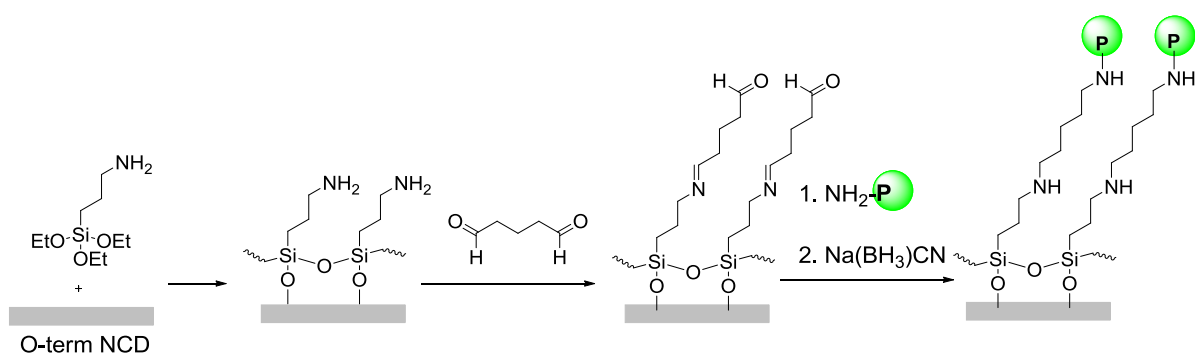


**Figure 109:** Preparation of a biofunctionalized NCD surface with APTES as cross-linker; silanization of the NCD surface, subsequent reaction with the bifunctional coupling agent glutardialdehyde and coupling of the enzyme; reduction of the imines in order to obtain a stable monolayer.

The bio-electrode surface was analyzed at a potential of 400 mV with regard to different glucose concentrations. At high amounts of substrate (100 mM), a faint current response can be observed, though reference measurements with non-biofunctionalized samples showed similar dependences. Unlike P(MA)-coupled GlucOx, the APTES-GlucOx electrodes prepared in the course of these studies were not sufficiently sensitive for unambiguous detection of glucose.

## 5. SUMMARY

“An additional project was to couple biological systems (enzyme, cells, etc.) to electric conductive synthetic diamond in order to use this material in amperometric biosensor implants. (...) Also here, different synthetic routes have been investigated for the functionalization of polymer grafts, in order to prepare polymer coatings with various chemical functions. The functionalization of these polymer grafts with enzymes is currently under investigation.”<sup>[311]</sup> This statement represented the state of the art before the beginning of this PhD project and, based on this excellent preliminary work by Dr. Marin Steenackers, provided the initial point to the preparation of biofunctionalized polymer brushes on nanocrystalline diamond (NCD) for biosensor applications. The three major challenges for paving the way towards amperometric sensors based on diamond-enzyme-electrodes were:

- a) The preparation of polymer brush - biomolecule conjugates on NCD
- b) To create micro- and nanopatterned polymer brushes on the surface
- c) Electrochemical analysis of the modified NCD surfaces and first sensing experiments in a chronoamperometric measuring setup.

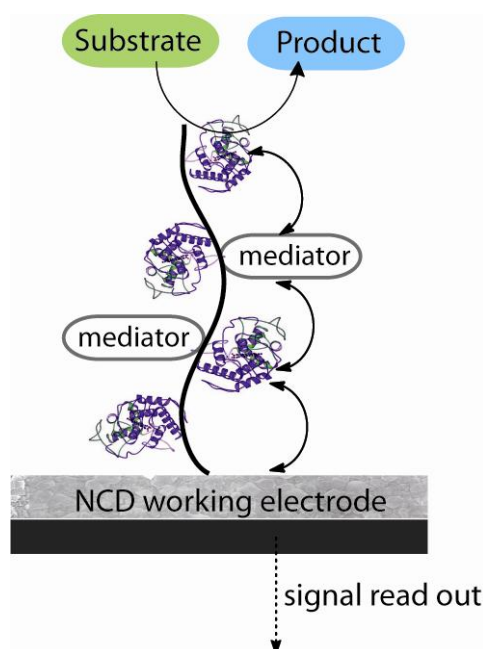


**Figure 110: Conceptual design of an amperometric biosensor based on polymer brush-modified diamond electrodes; the signal transduction from a biochemical recognition reaction proceeds via mediator molecules.**

**Preparation of polymer brush - biomolecule conjugates on NCD.** Fulfilling the requirements of being hydrophilic, having been successfully tested for biomedical applications and providing reactive functional groups for the coupling of biomolecules, the two major polymer classes used in the course of this project were poly(2-oxazoline)s including their more complex bottle-brush derivatives and poly(methacrylic acid) brushes (P(MA)). An overview on the chemical strategies is presented in Figure 111. The common feature was the presence of carboxylic moieties as reactive functional group for covalent protein immobilization.

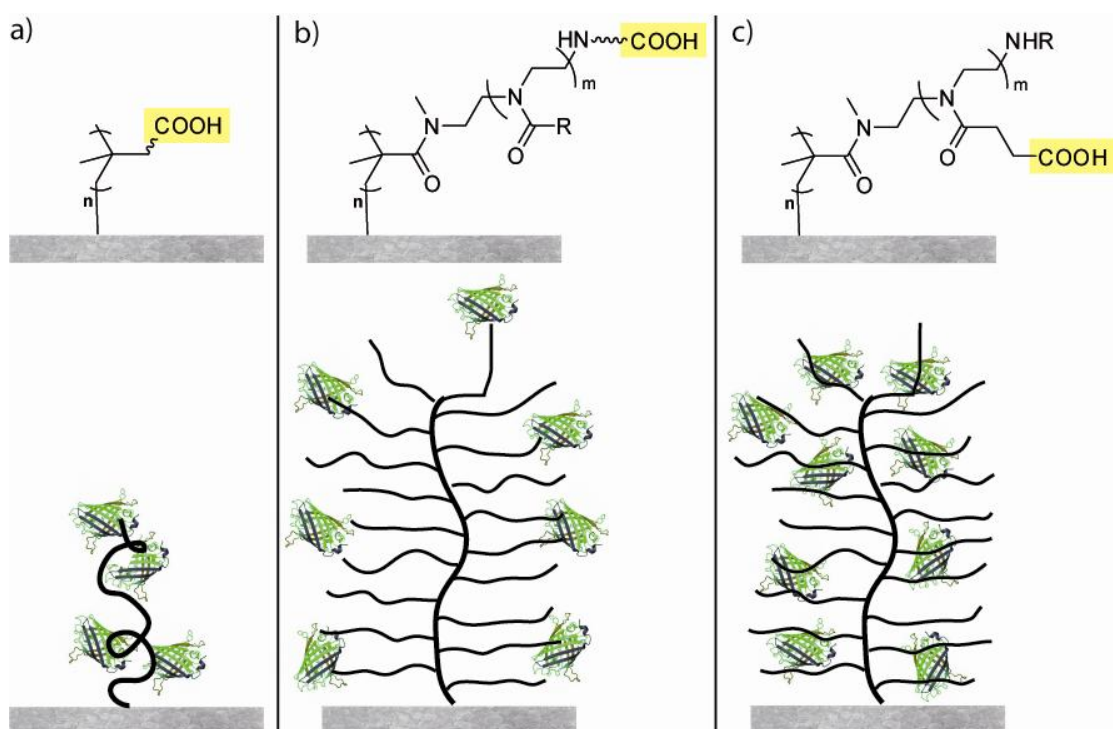


**Figure 111: Strategies for the preparation of polymer brush - biomolecule conjugates on NCD (chemical structure above, schematic illustration above); introduction of carboxylic moieties by a) using poly(methacrylic acid) brushes, b) the synthesis of P(IPOx-g-EtOx) BBBs with functional terminating end groups, c) the synthesis of P(IPOx-g-CarboxyOx) BBBs with functional poly((oxazol-2-yl)propionat) side chains.**

Stable and homogenous microstructured poly(2-isopropenyl-2-oxazoline) (PIPOx) brushes were obtained by the self-initiated photografting and photopolymerization (SIPGP) of IPOx directly onto oxidized NCD. Subsequently, the pendant oxazoline functionalities were converted into reactive initiator species for the side chain living cationic ring opening polymerization (LCROP) of 2-ethyl-2-oxazoline (EtOx). The highly reactive macroinitiator intermediate  $\text{P(IPOx}^+\text{OTf)}$  brushes could be isolated and were characterized by FT-IR

measurements. Due to a living polymerization mechanism, it was possible to selectively terminate the side chains with a bifunctional terminating agent, such as prolin-*tert*butyl ester or glycine-*tert*butyl ester. Alternatively, functional moieties could be introduced by using methyl-3-(oxazol-2-yl)propionate as monomer for the side chain LCROP. Subsequent saponification leads to the formation of multiple carboxyl moieties in the BBB side chains. The formation of bottle-brush brushes (BBBs) resulted in a significant increase of the polymer layer thickness indicating a strong stretching of the PIPOx backbone because of high side chain crowding. The poly(2-oxazoline) based SIPGP-LCROP approach gives access to the design of complex polymer brush architectures on diamond electrodes that allows the incorporation of a broad variety of chemical functionalities.

Alternatively, P(MA) brushes were synthesized by the SIPGP of *tert*butyl-methacrylate (tBuMA) resulting in P(tBuMA) brushes and subsequent hydrolysis under acidic conditions.

The coupling of biomolecules was performed by activating the polymer-pendant carboxylic group with a carbodiimide (EDC) and *N*-hydroxysuccinimide (NHS) and by subsequent reaction with a well-accessible amine group of the biomolecule under the formation of an amide bond. The successful coupling of biomolecules could be demonstrated by IR and contact angle measurements and the investigation of the polymer brush heights after the respective functionalization steps. Beyond that, it could be demonstrated by both fluorescence microscopy (in the case of GFP) and colorimetric assays (in the case of horseradish peroxidase and glucose oxidase) that the coupled proteins maintained their native activity after immobilization in the polymer.

Colorimetric assays for horseradish peroxidase (HRP) and glucose oxidase (GlucOx) revealed a characteristic Michaelis-Menten behavior when plotting the measured conversion rate during dye formation against the substrate concentration. In fluorescence microscopy experiments, an increased stability of the GFP - polymer brush conjugates was found which resulted in a strong fluorescence response even after long exposure to excitation light or after treatment in harsh chemical conditions.

**Micro- and nanopatterned polymer brushes.** In order to both provide a platform for a better insight into the coupling of biomolecules to polymer brushes and with regard to potential micro-array applications, the preparation of stable nanostructured polymer brushes on NCD by the carbon templating (CT) technique was presented. The CT technique, involving the

exposure of the surface to a focussed electron beam, allows the design of array systems on the micro- and nanometer range with a free choice of possible patterns without the need of a specific surface chemistry, mask, resist or other primary coating. Monomers, such as styrene, methyl methacrylate, *tert*-butyl methacrylate, *N,N*-dimethyl-aminoethyl methacrylate, 4-vinyl pyridine and 2-*iso*-propenyl-2-oxazoline were successfully grafted onto various CT features. Carbon templates prepared by electron beam-induced carbon deposition (EBCD) with dimensions down to 5 nm could be selectively amplified into larger polymer structures by SIPGP of IPOx and subsequent LCROP to form BBBs.

Protein density gradients could readily be realized, adding a third tunable variable to the biofunctionalization process of surfaces (Figure 112). Therefore, a  $10 \times 50 \mu\text{m}^2$  CT gradient was prepared by linearly increasing the electron dose during the electron-beam carbon deposition. The functionalization of structured P(MA) layers with GFP showed that direct immobilization of biomolecules could be achieved on NCD using the CT approach and high biomolecule loading can be realized. Multiple coupling of GFP onto polymer brushes of complex bottle-brush brush (BBB) architectures was successfully demonstrated by preparing end group functionalized poly(2-oxazoline) based BBBs as soft interlayer on the NCD. BBB architectures are common features in living organisms and therefore have biomimetic potential.

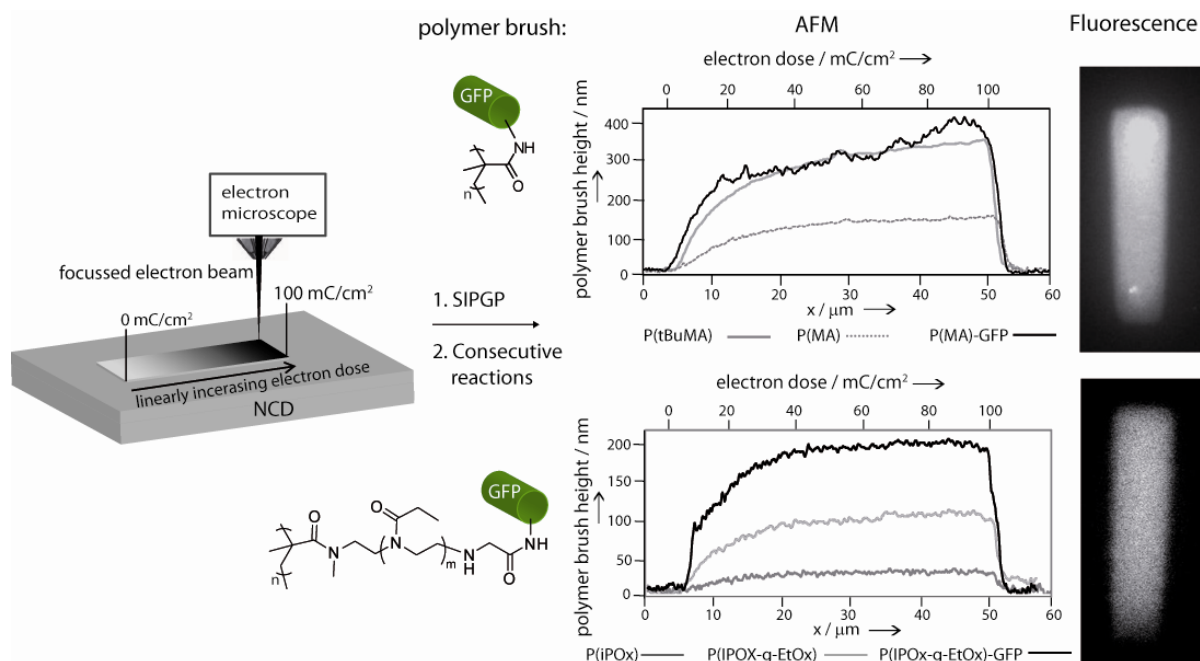


**Figure 112: CT technique for the preparation of polymer brush gradients on NCD; demonstration of P(MA)-GFP or P(IPOx-g-EtOx)-GFP protein density gradients by AFM section analysis and fluorescence microscopy.**

Having gained a closer insight into the formation structured functional polymer brushes on diamond and proven the feasibility of covalently attaching active proteins and enzymes into the polymeric interlayer, the next consequent step was the tuning of the polymer brush - biomolecule systems towards amperometric sensing applications.

**Electrochemical analysis of the modified NCD surfaces and first sensing experiments in a chronoamperometric measuring setup.** In order to ensure a charge transfer through the polymer brush layer to the NCD electrode, so-called mediators (charge carrier molecules) were combined with the polymer-functionalized NCD system. The approach was varied in terms of:

- Choice of mediator
- Choice of polymer class
- Integration of the mediator to the polymer brush - electrode system
- Choice of enzyme

The following ideas were realized and investigated for their applicability as amperometric sensing electrodes for enzymatic reaction:

1) Carbazole as hole-conducting moiety was successfully introduced into poly(2-oxazoline) based BBBs by using 2-(Carbazolyl)ethyl-2-oxazoline (CarbOx) as monomer for the LCROP. The formation of BBBs from the sterically demanding CarbOx monomer resulted in a significant increase of the polymer layer thickness indicating a strong stretching of the PIPOx backbone because of high side chain crowding. FT-IR spectroscopy and fluorescence microscopy confirmed the area selective consecutive grafting reactions.

Major drawback: Hydrophobicity of the polymer brushes, hindered immobilization of enzymes due to high chain crowding. Solution: change of mediator and polymer system

2) Instead of carbazole, ferrocene carboxylic acid was used as mediator by adding it to the electrolyte solution. The system of horseradish peroxidase (HRP) in poly(methacrylic acid) brushes (P(MA)) was investigated upon the addition of hydrogen peroxide as substrate.

Major drawback: significantly high side reaction of ferrocene with  $H_2O_2$ . Solution: use of polymeric mediators instead of unbound mediator

- 3) Ferrocene was covalently bonded to P(MA) brushes by copolymerizing tBuMA and vinylferrocene during SIPGP. The presence of ferrocene on the NCD surface could unambiguously be identified by cyclic voltammetry. However, after hydrolysis of the P(tBuMA) sites to P(MA), the ferrocene loading decreased strongly.

Major drawback: significant loss of ferrocene groups during saponification of P(tBuMA-co-VFc). Solution: polymer analogue coupling of ferrocene

- 4) Polymer analogue coupling of ferrocene to the polymer brushes was carried out by reacting P(MA) with aminoferrocene or - which turned out to be the more reactive compound - aminomethylferrocene under the formation of an amide bond. The redox behavior of the polymeric mediator was investigated by cyclic voltammetry. X-ray photoelectron spectroscopy (XPS) studies gave further confirmation of the presence of ferrocene. In order to simultaneously couple an enzyme and the mediator, the NHS/EDC activated P(MA) brushes were first reacted with HRP and the remaining NHS-ester functionalities were saturated with amino(methyl)ferrocene. The activity of HRP could be shown by colorimetric assays, but the above named side reaction of  $H_2O_2$  with ferrocene in electrochemical experiments could not be entirely suppressed.

Major drawback: significantly high side reaction of ferrocene with  $H_2O_2$ . Solution: change of the enzyme/substrate system

Eventually, the combination of P(MA) brushes as polymeric matrix, polymer analogue coupling of aminomethylferrocene and glucose oxidase (GlucOx)/glucose as enzyme/substrate system were found to be most promising for sensing applications (Figure 113).

- 5) P(MA) brushes on NCD were functionalized with first GlucOx and subsequently aminomethylferrocene to yield P(MA)-GlucOx-AmMeFc brushes. Apart from colorimetric analysis (proving the presence of native GlucOx) and cyclic voltammetry (proving the presence of ferrocene), chronoamperometry was performed with this type of enzyme electrode. Upon addition of glucose, a current could be determined which undoubtedly originated from the reaction of GlucOx with the substrate and the consequent redox cycle of the ferrocene/ferrocenium mediator.

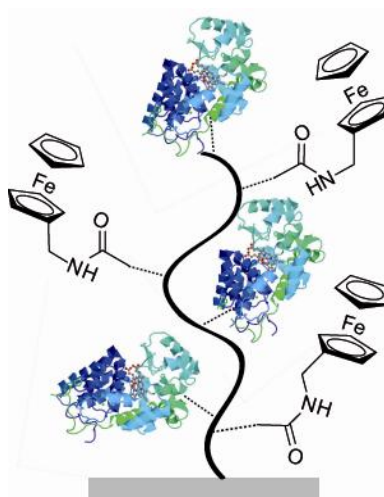


**Figure 113: Schematic illustration of the ideal polymer brush - mediator - enzyme system for amperometric sensing applications: P(MA)-GlucOx-AmMeFc on NCD.**

The combination of the presented route for the (bio)functionalization of diamond and a broad variety of possible 2D and 3D designs will enable the study of cell surface interaction with the precise variation of the surface topography, polymer layer mechanics and local biomolecule concentration. These factors are crucial for the realization of complex biosensor arrays for high-throughput screening. Also, a completely new strategy for the preparation of enzyme electrodes has been presented. By covalently binding both the enzyme and the mediator into polymer brushes on boron-doped NCD, reliable electrochemical detection of small substrate concentrations is possible and opens the way towards a novel class of amperometric biosensors. The complex role of the polymeric mediator during charge transfer will be further investigated in the ongoing course of this project by Dipl. Phys. Andreas Reitingner (WSI).

## 6. ZUSAMMENFASSUNG

„Ein weiteres Projekt war die Anbindung biologischer Systeme (Enzyme, Zellen, etc.) an elektrisch leitfähigen Bor-dotierten Diamant, um dieses Material in amperometrischen Biosensorimplantaten zu verwenden. (...) Hierfür wurden ebenfalls neue Syntheserouten für die Funktionalisierung von Polymerbürsten untersucht, um Polymerschichten mit verschiedenen chemischen Funktionalitäten herzustellen<sup>7</sup>.“ [311] Dieses Zitat spiegelt den wissenschaftlichen Stand der Dinge vor Beginn dieses Promotionsprojektes wider und bildet, basierend auf der exzellenten Vorarbeit von Dr. Marin Steenackers, den Ausgangspunkt für die Herstellung biofunktionalisierter Polymerbürsten auf nanokristallinem Diamant (NCD) für Biosensoranwendungen.

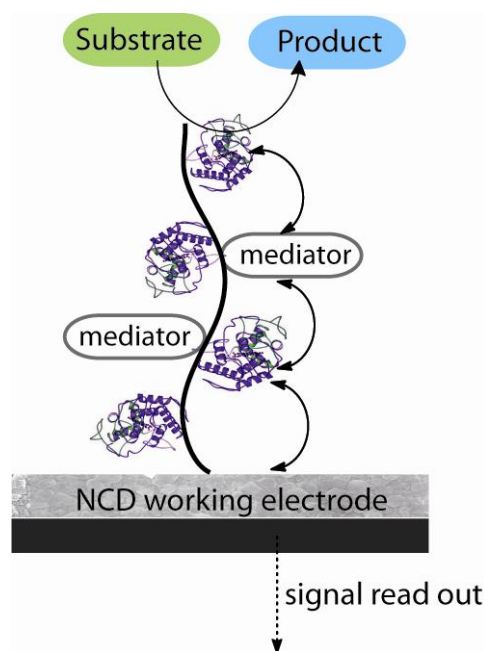


**Abbildung 114: Konzept eines amperometrischen Biosensors auf der Basis von Polymerbürsten-modifizierten Diamantelektroden; Die Signalübertragung nach einer biochemischen Substratreaktion erfolgt mittels Ladungsträgermolekülen (Mediatoren).**

Die drei größten Themengebiete und Herausforderungen zur Realisierung von amperometrischen Biosensoren auf Basis von Diamantelektroden waren:

<sup>7</sup> übersetzt aus dem Originaldokument / translated from the master document

- a) Die Herstellung von kombinierten Polymer-Biomolekül Systemen auf NCD
- b) Die Mikro- und Nanostrukturierung von Polymerbürsten auf der Oberfläche
- c) Elektrochemische Analyse der modifizierten NCD Oberflächen und erste Sensorik-Experimente in chronoamperometrischen Messaufbauten.

**Herstellung von kombinierten Polymer-Biomolekül Systemen.** Zwei Polymerklassen, die im Zuge dieses Projektes untersucht wurden und die mit ihren Eigenschaften Hydrophilie, Anwendbarkeit für biomedizinische Aufgaben und Besitz funktioneller Gruppen für die Proteinanbindung ideale Voraussetzungen erfüllen, sind Poly(2-oxazolin)e mitsamt ihren komplexen *bottle-brush* Derivaten sowie Poly(methacrylsäure) (P(MA)). Abbildung 115 bietet einen Überblick über die verwendeten Synthesestrategien. Sie haben als gemeinsames Merkmal, dass oberflächen-gebundene Carboxygruppen generiert werden, die als reaktive funktionelle Gruppe zur Immobilisierung von Proteinen genutzt werden können.

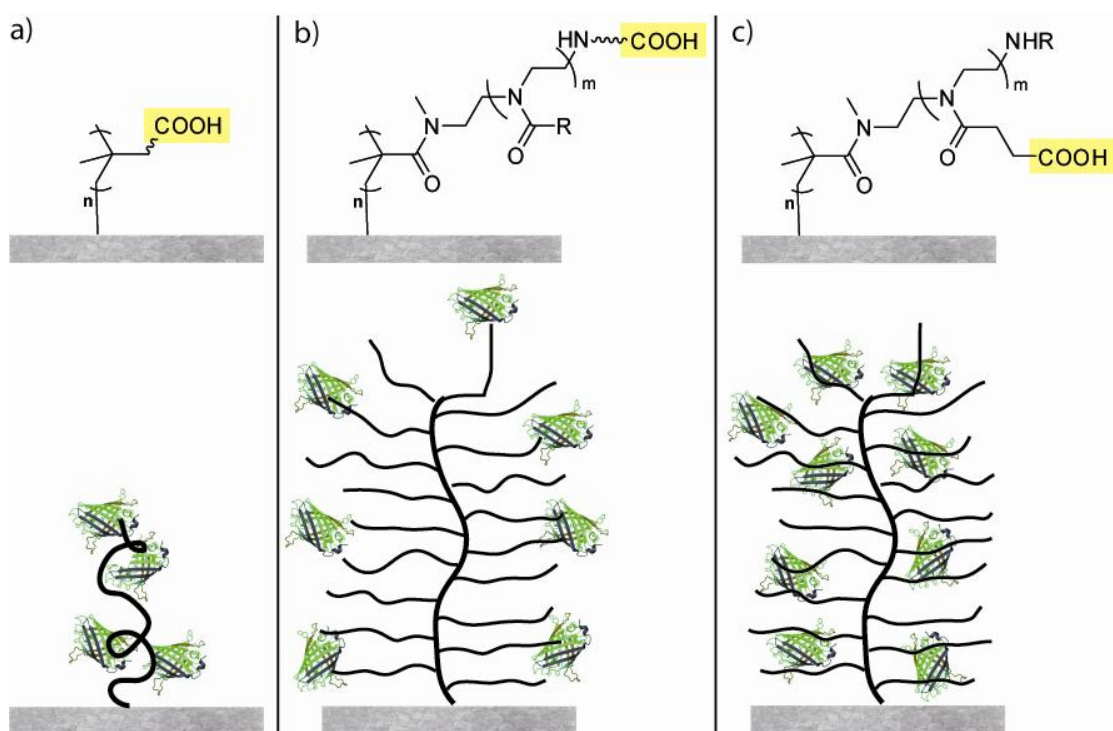


**Abbildung 115: Strategien für die Herstellung von Polymerbürsten-Biomolekül-Systemen auf NCD (oben: chemische Strukturen der Polymerbürsten, unten: schematische Darstellung der biofunktionalisierten Polymerbürsten); Einführung einer Carboxygruppe durch: a) Verwendung von Poly(methacrylsäure) Bürsten; b) Synthese von P(IPOx-g-EtOx) BBBs mit funktionellen Endgruppen in den Seitenketten; c) Synthese von P(IPOx-g-CarboxyOx) BBBs mit funktionellen Poly((oxazol-2-yl)propionat) Seitenketten.**

Stabile und homogene, mikrostrukturierte Poly(2-isopropenyl-2-oxazolin) (PIPOx) Bürsten wurden durch die *self-initiated photografting and photopolymerization* (SIPGP) von IPOx direkt auf oxidiertem NCD hergestellt. Anschließend wurden die Oxazolin-Einheiten in reaktive Initiatorspezies überführt, um die lebende kationische Ringöffnungspolymerisation (LCROP) mit 2-Ethyl-2-oxazolin (EtOx) zum Aufbau von Polymerseitenketten zu starten. Das hochreaktive Makroinitiator-Intermediat  $P(\text{IPOx}^+\text{OTf})$  konnte isoliert und mittels FT-IR analysiert werden. Aufgrund des lebenden Polymerisationsmechanismus war es möglich die Seitenketten selektiv mit einem bifunktionellen Terminationsreagenz, wie Prolin-*tert*-butylester oder Glycin-*tert*-butylester, abubrechen. Alternativ zu dieser Methode konnten funktionelle Gruppen auch über das Seitenkettenmonomer eingebracht werden, indem Methyl-3-(oxazol-2-yl)propionat für die LCROP verwendet wurde. Durch anschließende Verseifung wurden freie Carboxygruppen in den BBB Seitenketten generiert. Die Synthese von BBBs führte zu einem deutlichen Anstieg der Polymerschichtdicke, die auf eine starke Streckung des P(IPOx) Rückgrates aufgrund hoher sterischer Ansprüche der Seitenketten zurückzuführen ist. Der SIPGP-LCROP Ansatz basierend auf Poly(2-oxazolin)en ermöglicht den Zugang zu einer Vielzahl an funktionellen Gruppen und zu komplexen Polymerarchitekturen auf Diamantelektroden.

Ein weiterer Ansatz war die Synthese von P(MA) Bürsten mittels SIPGP von *tert*-Butylmethacrylat (tBuMA) und anschließender Hydrolyse der P(tBuMA) Bürsten unter sauren Bedingungen.

Die kovalente Anbindung von Biomolekülen gelang durch Aktivierung der Carboxygruppe am Polymer mithilfe eines Carbodiimides (EDC) und *N*-Hydroxysuccinimid (NHS), gefolgt von der Reaktion mit leicht zugänglichen Aminogruppen des Biomoleküls unter Ausbildung einer Amidbindung. Die erfolgreiche Anbindung konnte durch IR, Kontaktwinkelmessungen, sowie der Untersuchung der Polymerschichtdicke nach den jeweiligen Reaktionsschritten bestätigt werden. Darüber hinaus wurde mittels Fluoreszenzmikroskopie (im Falle von GFP) oder kolorimetrische Enzymassays (im Falle von Meerrettichperoxidase und Glucose-Oxidase) gezeigt, dass die gebundenen Proteine ihre natürliche Aktivität auch nach der Immobilisierung in das Polymer behielten.

In kolorimetrischen Enzymassays für Meerrettichperoxidase (engl. *horseradish peroxidase*, HRP) und Glucose-Oxidase (GlucOx) konnte durch die Auftragung der ermittelten Umsatzrate zur Farbstoffbildung gegen die Substratkonzentration ein charakteristisches Verhalten nach Michaelis Menten nachgewiesen werden. Untersuchungen mittels

Fluoreszenzmikroskopie ergaben eine erhöhte Stabilität der GFP-funktionalisierten Polymerbürsten, die selbst nach langer Zeit unter der Anregungswellenlänge oder unter harten chemischen Bedingungen ein starkes Fluoreszenzsignal zeigten.

**Mikro- und Nanostrukturierung von Polymerbürsten.** Mikro- und nanostrukturierte Polymerbürsten auf NCD wurden mittels der *carbon templating* (CT) Methode hergestellt, um zum einen einen besseren Einblick in die Anbindung von Biomolekülen in Polymerbürsten zu bekommen, und um diese Strukturierungsmethode zum anderen im Hinblick auf mögliche Mikroarrayanwendungen zu untersuchen. Die CT Methode, basierend auf der Bestrahlung der Oberfläche mit einem fokussierten Elektronenstrahl, ermöglicht den Aufbau von Arraysstrukturen im Mikro- und Nanometerbereich mit einer freien Auswahl an verschiedensten Formen und ohne eine spezielle Vorbehandlung der Oberfläche, einer Photomaske oder eines Photolacks. Monomere, wie Styrol, Methylmethacrylat, *tert*-Butylmethacrylat, *N,N*-Dimethyl-aminoethylmethacrylat, 4-Vinylpyridin und 2-*iso*-Propenyl-2-oxazolin wurden erfolgreich auf verschiedene CT Strukturen gepfropft. *Carbon templates* bis in den 5 nm - Bereich konnten gezielt mittels SIPGP von IPOx und anschließender LCROP in größere Polymerstrukturen und schließlich in BBBs umgewandelt werden.

Gradientenstrukturen mit ansteigender Proteindichte konnten erfolgreich hergestellt werden und lieferten somit eine dritte variable Prozessgröße für die Biofunktionalisierung der Oberfläche (Abbildung 116). Hierbei wurde ein  $10 \times 50 \mu\text{m}^2$  CT Gradient hergestellt, indem während der Elektronenbestrahlung die Elektronendosis kontinuierlich linear erhöht wurde. Durch die Funktionalisierung der strukturierten P(MA) Schichten mit GFP zeigte sich, dass die direkte Immobilisierung von Biomolekülen auf NCD mittels der CT Methode in hohen Beladungsdichten resultiert. Vielfache Anbindung von GFP in komplexe BBB Strukturen als funktionelle Grenzschicht auf NCD wurde durch die Herstellung von Poly(2-oxazolin)-basierten BBBs mit funktionellen Endgruppen realisiert. BBB Architekturen sind bekannte Strukturmerkmale in lebenden Organismen und haben daher biomimetisches Potential.

Nachdem ein detaillierterer Einblick in die Herstellung von strukturierten funktionellen Polymerbürsten auf Diamant gegeben und die Durchführbarkeit einer kovalenten Anbindung von Biomolekülen demonstriert werden konnte, wurden die Polymerbürsten-Biomolekül-Systeme im Weiteren entsprechend für ihre Anwendbarkeit in amperometrischen Biosensoren modifiziert.

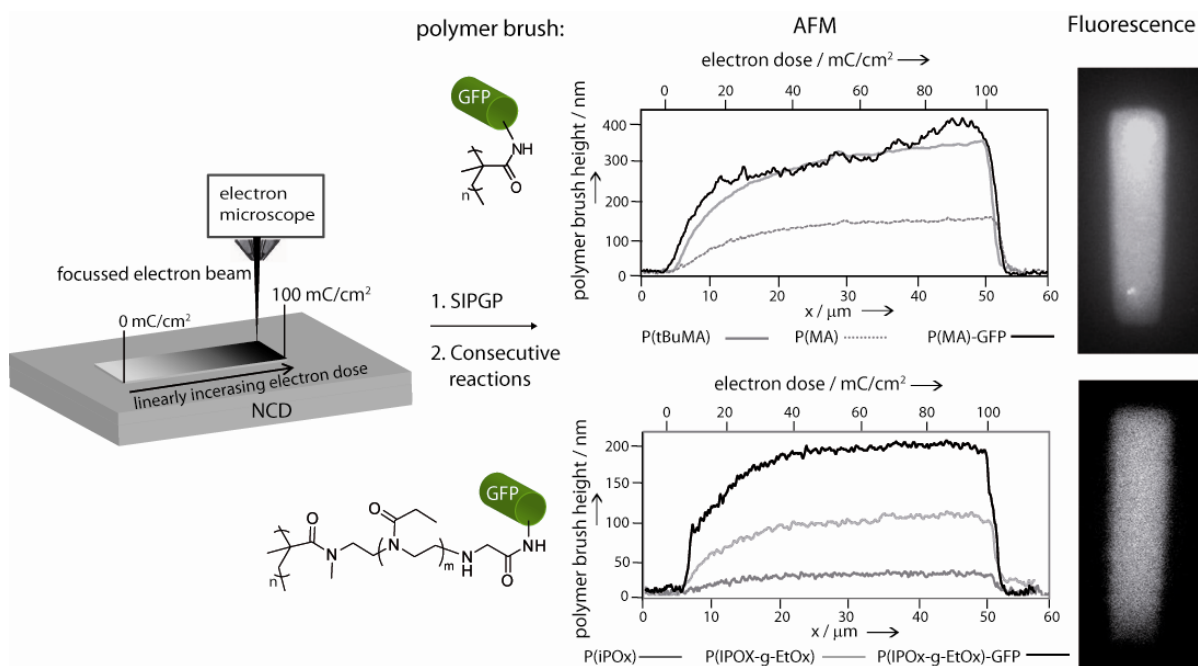


**Abbildung 116: CT Methode zur Herstellung von Polymerbürstengradienten auf NCD; Darstellung von P(MA)-GFP und P(IPOx-g-EtOx)-GFP Gradienten mit ansteigender Proteindichte als AFM Profil und in Fluoreszenzmikroskopie.**

**Elektrochemische Analyse der modifizierten NCD Oberflächen und Untersuchung als Biosensoren.** Um einen Ladungstransfer durch die Schicht aus Polymerbürsten bis hin zu der NCD Elektrode sicherzustellen, wurden die Polymer-funktionalisierten NCDs mit sogenannten Mediatoren (Ladungsüberträger) kombiniert. Es gab hierzu verschiedene Ansätze je nach:

- Wahl des Mediators
- Wahl der Polymerklasse
- Einbindung des Mediators in das System aus Polymerbürsten-Elektrode
- Wahl des Enzyms

Im Folgenden werden diejenigen Ansätze zusammengefasst, die in die Tat umgesetzt und hinsichtlich ihrer Anwendbarkeit als amperometrische Sensoren für Enzymreaktionen untersucht wurden.

- 1) Carbazolgruppen besitzen lochleitende Eigenschaften und wurden erfolgreich in Poly(2-oxazolin)-basierte BBBs durch den Einsatz von 2-(Carbazolyl)ethyl-2-oxazolin (CarbOx) als Monomer für die LCROP integriert. Der Aufbau von BBBs aus sterisch

anspruchsvollen CarbOx Monomeren führte zu einem deutlichen Anstieg der Polymerschichtdicke, was auf eine starke Streckung des PIPOx Rückgrates aufgrund hoher räumlicher Beanspruchung der Seitenketten hinweist. FT-IR Spektroskopie, sowie Fluoreszenzmikroskopie bestätigten die auf PIPOx aufbauende, ortsspezifische Seitenkettenreaktion.

Nachteil: Hydrophobizität der Polymerbürsten, erschwerte Immobilisierung von Enzymen aufgrund der sterisch anspruchsvollen Seitenketten. Lösungsansatz: Wechsel des Mediator- und Polymersystems.

- 2) Anstelle des Carbazols wurde Carboxyferrocen als Mediator der Elektrolytlösung zugegeben. Die Kombination aus Meerrettichperoxidase (HRP) in Poly(methacrylsäure) Bürsten (P(MA)) wurde auf die Reaktion mit Wasserstoffperoxid als Substrat untersucht.

Nachteil: erhebliche Nebenreaktion des Ferrocens mit  $H_2O_2$ . Lösungsansatz: Verwendung eines polymeren Mediators anstatt eines ungebundenen.

- 3) Die kovalente Anbindung von Ferrocen an P(MA) Bürsten erfolgte über die Copolymerisation von tBuMA und Vinylferrocen während der SIPGP. Durch cyclische Voltammetrie konnte die Anwesenheit der Ferrocengruppen auf der Oberfläche eindeutig nachgewiesen werden. Allerdings nahm die Oberflächenbeladung mit Ferrocen nach der Hydrolyse der P(tBuMA) Bürsten zu P(MA) stark ab.

Nachteil: signifikanter Verlust an Ferroceneinheiten während der Verseifung von P(tBuMA-co-VFc). Lösungsansatz: Polymeranaloge Anbindung von Ferrocen.

- 4) Die polymeranaloge Anbindung von Ferrocen in die Polymerbürsten erfolgte durch die Reaktion von P(MA) mit Aminoferrocen oder - was sich schließlich als reaktiveres Reagenz herausstellte - mit Aminomethylferrocen unter Ausbildung von Amidbindungen. Das Redoxverhalten wurde mittels cyclischer Voltammetrie untersucht. Die Existenz der Ferrocengruppen wurde zusätzlich mit Röntgenphotoelektronenspektroskopie (engl. XPS) bestätigt. Um in einem weiteren Schritt gleichzeitig den Mediator und das Enzym an die Polymerbürsten zu binden, wurden NHS/EDC aktivierte P(MA) Bürsten erst mit HRP umgesetzt und die verbleibenden NHS-Ester anschließend mit Amino(methyl)ferrocen abgesättigt. Die Aktivität der immobilisierten HRP konnte in kolorimetrischen Assays gezeigt werden, aber die bereits beschriebene Nebenreaktion von Ferrocen mit  $H_2O_2$  in elektrochemischen Experimenten ließ sich nicht vollständig verhindern.

Nachteil: erhebliche Nebenreaktion des Ferrocens mit  $H_2O_2$ . Lösungsansatz: Wechsel zu einem anderen Enzym/Substrat System.

Letztendlich stellte sich die Kombination aus P(MA) als Polymermatrix, einer polymeranalogen Anbindung von Aminomethylferrocen und Glucoseoxidase (GlucOx)/Glucose als Enzym/Substrat System als am vielversprechendsten für Biosensoranwendungen heraus (Abbildung 117).

5) P(MA) Bürsten auf NCD wurden zuerst mit GlucOx und anschließend mit Aminomethylferrocen funktionalisiert, um P(MA)-GlucOx-AmMeFc Bürsten zu bekommen. Neben kolorimetrischer Analytik (zur Bestätigung der Enzymaktivität) und cyclischer Voltammertrie (zur Bestätigung des Vorhandenseins von Ferrocen), wurden chronoamperometrische Messungen mit dieser speziellen Enzymelektrode durchgeführt. Durch die gezielte Zugabe von Glucose konnte ein Ladungsfluss detektiert werden, der zweifelsfrei von der Reaktion von GlucOx mit dem Substrat und der daraus resultierenden Redoxzyklen des Ferrocen/Ferrocenium Mediators verursacht wurde.

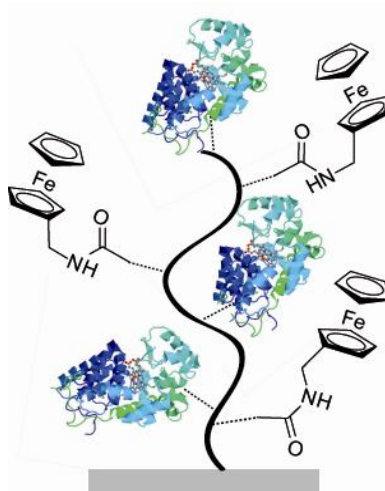


**Abbildung 117: Schematische Darstellung des idealen Systems aus Polymerbürste-Mediator-Enzym für amperometrische Biosensoranwendungen: P(MA)-GlucOx-AmMeFc Bürsten auf NCD.**

Die Kombination aus der beschriebenen Strategie für die (Bio)Funktionalisierung von Diamant und eine weite Auswahl an 2D und 3D Designs ermöglicht die Erforschung von Wechselwirkungen zwischen Zellen und Oberflächen durch präzise Einstellung der Oberflächentopographie, Beschaffenheit der Polymerschicht und lokale Biomoleküldichte. Diese Faktoren spielen eine entscheidende Rolle bei der Entwicklung komplexer

Biosensorarrays für Screening Anwendungen mit hohem Durchsatz. Außerdem wurde eine neuartige Strategie zur Herstellung von Enzymelektroden präsentiert. Durch die kovalente Anbindung sowohl des Enzym als auch des Mediators in Polymerbürsten auf Bor-dotiertem Diamant konnte die elektrochemische Detektion von sehr geringen Substratkonzentrationen realisiert werden und ebnet somit den Weg für die Entwicklung neuartiger amperometrischer Biosensoren. Die komplexe Rolle des polymeren Mediators während des Ladungstransportes wird im Detail im weiteren Verlauf des Projektes von Dipl. Phys. Andreas Reitingner (WSI) untersucht werden.

## 7. EXPERIMENTAL PART

### 7.1 Instruments and methods

#### **Atomic force microscopy (AFM):**

##### Standard Topographic scans:

Instrument: Nanoscope IIIa MultiMode<sup>TM</sup> scanning probe microscope from Veeco Instruments

Scanner: 5298 J and 5308 E

AFM tips: Veeco, Model: RTESP, phosphorus doped Si

All AFM measurements were performed in tapping mode. The AFM measurements were analyzed and visualized using the Nanoscope III-software (version 5.12r3, Digital Instruments). Roughness values were calculated from 1  $\mu\text{m}^2$  areas if not otherwise stated.

##### Wet-cell measurements and electric-field induced lithography:

Instrument: MFP3D-SA from Asylum Research

AFM tips: DCP 11 Golden Silicon cantilevers, tip side diamond (N-doped) coated

The swelling behavior of the polymer brushes and their behavior under a certain applied potential were determined in cooperation with the research group of Prof. Thorsten Hugel from the physics department of the TU Munich. Electric-field induced lithography was performed in the research group of Prof. Stefan Zauscher from the department of biomechanical engineering of the Duke University (US). The silicon surface was fixed to the sample holder by a sticking copper stripe and electrical contact was further ensured by sealing one edge of the silicon surface with silver glue. During lithography, the applied tip potential was set at -10 V and a scan rate of 500 nm/sec was maintained. For gradient structures, a 5  $\mu\text{m}$  box was designed with linearly increasing potentials from 0 to -10 V.

#### **Infrared spectroscopy:**

Instrument: Bruker, Vertex 70 with a nitrogen cooled MCT-detector.

Spectral resolution:  $6 \text{ cm}^{-1}$

The infrared measurements of the polymer grafts were recorded using a diffusion reflectance Fourier transformed (DRIFT) setup from Spectra Tech. 550 scans were accumulated.

Organic compounds were measured as KBr moldings in transmission mode.

#### **Nuclear magnetic resonance (NMR) spectroscopy:**

NMR Spectra were recorded on a Bruker ARX 300 (1H, 300.13 MHz and 13C, 75.48 MHz).  
Standard: solvent signal as internal standard.

Acetonitrile:  $^1\text{H-NMR}$ :  $\delta = 1.93 \text{ ppm}$ ,  $^{13}\text{C-NMR}$ :  $\delta = 118.2 \text{ ppm}$

DMSO:  $^1\text{H-NMR}$ :  $\delta = 2.49 \text{ ppm}$ ,  $^{13}\text{C-NMR}$ :  $\delta = 39.5 \text{ ppm}$

Chloroform:  $^1\text{H-NMR}$ :  $\delta = 7.26 \text{ ppm}$ ,  $^{13}\text{C-NMR}$ :  $\delta = 77.4 \text{ ppm}$

#### **Fluorescence microscopy (FM):**

FM images were obtained with a Leica DMI 6000 B microscope equipped with a Hamamatsu C4742 camera. The samples were irradiated using a Leica Fluo A filter cube (BP340-380 nm). The cross section analysis of the grey scale fluorescence intensity was performed by pixel analysis of the 256 bit black and white fluorescence image using the public domain *Image J* software package.

#### **Water contact angle measurements:**

The water contact angles were determined with a fully automated Krüss DSA 10 Mk2 contact angle goniometer. The data were obtained with the aid of the Krüss Drop Shape Analysis v3 software package.

#### **UV-vis measurements for colorimetric assays:**

Colorimetric assays were carried out in a Cary 500 Scan UV-vis spectrophotometer from Varian equipped with a single cell Peltier accessory. The biofunctionalized surface was glued to a stamp pointing into the cuvette above the light path using sticky tape. The cuvette solution contained buffer, the colorimetric substrate and a stir bar and was kept at  $22^\circ\text{C}$ . In order to determine the enzyme activity, light absorption curves were measured over 10 minutes time at different substrate concentrations.

enzyme	substrate	description
Horse radish peroxidase	3,3',5,5'-Tetramethylbenzidine	preparation of different TMB solutions (vol% in buffer pH 6.2): 0, 10, 30, 50, 70, 90

#### **UV-Fluorescence spectrophotometer for fluorescence assays:**

Fluorescence assays were carried out in a Cary Eclipse fluorescence spectrophotometer from Varian. The rate of change in fluorescence with time is recorded at an excitation wavelength  $\lambda_{\text{ex}}$  of 315 nm and  $\lambda_{\text{em}}$  of 425 nm. For the determination of glucose oxidase activity, the GlucOx functionalized NCD sample was emerged in a solution of 2.7 mL of buffer containing 0.1 mL homovanillic acid in water (2.5 mg/mL), 0.1 mL horse radish peroxidase in buffer (0.75 mg/mL) and 0.1 mL of different glucose solutions (0.01 M to 1 M). Emission data was obtained every minute over 10 minutes of time after thorough stirring in between the measurements cycles.

#### **Electrochemical measurements:**

Cyclic voltammetry and chronoamperometry were conducted in a three electrode configuration of an electrochemical cell in cooperation with the Walter Schottky Institute. From above, the counter (Pt-wire) and the reference electrode (Ag/AgCl reference electrode with 197 mV vs NHE) were dipped into a glass cylinder (20 mL volume) with an opening at the bottom onto which the working electrode (=NCD sample) was pressed against with a rubber ring. The cylinder is surrounded by a teflon ground and lid. Before measurement, the cell was flushed with nitrogen in order to avoid disturbing background currents caused by electrode reactions of dissolved oxygen. As buffer, a phosphate buffer (PBS) of pH 7 was used.

#### **Ex situ x-ray photoelectron spectroscopy (XPS) measurements:**

XPS measurements were performed in the Walter Schottky Institute (Physics department of the TU Munich) lab source operated at  $10^{-10}$  mbar and using an aluminum source with  $K_{\alpha}(\text{Al}) = 1468.6$  eV.

Alternatively, XPS measurements were carried out at the Université Libre de Bruxelles (Chemical Physics of Materials - Catalysis and Tribology).

### **Carbon Templating in a scanning electron microscope (SEM):**

Electron beam induced carbon deposition (EBCD) was performed on freshly hydrogenated NCD or on SiO<sub>x</sub> surfaces with a focused electron beam in a Zeiss E-Line scanning electron microscope (vacuum pressure around  $2 \times 10^{-5}$  mbar). The electron beam was run at 20 keV with a beam current of around 300 pA. All structures, except gradients or if otherwise stated, were irradiated with an electron dose of 50 mC/cm<sup>2</sup>. The gradients were prepared with an electron dose linearly increasing from 0 to 50 mC/cm<sup>2</sup> in the case of SiO<sub>x</sub> and from 0 to 100 mC/cm<sup>2</sup> in the case of NCD.

### **Ultrapure water:**

Ultrapure water was tapped from a Millipore Direct Q facility.

## **7.2 Solvents, Chemicals, Substrates**

### **General remarks:**

In order to ensure particularly clean working conditions for surface modification or characterization, the used glassware was first cleaned in an isopropyl/KOH bath, an HCl bath and with distilled water and then dried at 130°C. Before every application, the tweezers were rinsed with acetone.

All chemicals were purchased from Aldrich, ABCR or Acros. All solvents were used in HPLC grade purity or higher. Solvents of lower grade were purified and dried prior to use.

All monomers (styrene, MMA, tBuMA, IPO<sub>x</sub>, dMAEMA) were passed through a basic Al<sub>3</sub>O<sub>2</sub> column (Aldrich) to remove the inhibitor. The monomers for the living cationic ring-opening polymerization were dried with CaH<sub>2</sub> and purified by fractionation distillation at reduced pressure and stored at -4 °C. Delicate reactions were carried out in a UNILab glovebox from MBraun under argon atmosphere (O<sub>2</sub> content < 0.1 ppm, water content < 0.1 ppm).

### **Biomolecules:**

His-tagged Green fluorescent protein (GFP) was synthesized as described below and kindly provided by Dr. Martin Haslbeck from the chair of biotechnology at the TU Munich. The GFP gene was amplified by PCR from genomic DNA, previously obtained with an established protocol<sup>[357]</sup> and cloned into an expression vector. This construct was electrotransformed into

*E.coli* and selected for on Luria-Bertani (LB) agar plates containing ampicillin (150mg/l). A single colony was cultured at 37°C to an OD of ~0.6 in 1 L of LB containing ampicillin, 1 mM isopropyl  $\beta$ -D-1-thiogalactopyranoside was added to induce expression and the culture was incubated at 37°C for 4 hours. Cells were harvested by centrifugation. Recombinant GFP proteins were purified by His Trap HP column/ Ni<sup>2+</sup>-affinity chromatography. The protein was eluted using linear gradient from 0 to 500 mM imidazole.

Peroxidase Type II from horse radish, Cytochrome c from horse heart, Acetylcholinesterase from *electrophorus electricus* and glucose oxidase from *aspergillus niger* were purchased from Sigma Aldrich. The purity of the enzymes was determined by gel electrophoresis.

### **Nanocrystalline diamond (NCD):**

Nanocrystalline diamond wafers were kindly provided by Oliver Williams from the group of Prof. Christoph Nebel at the Fraunhofer Institut für angewandte Festkörperphysik. In brief, NCD was grown by microwave plasma enhanced chemical vapor deposition. Prior to growth, prime grade 100 silicon wafers were cleaned with standard SC1 solution and seeded with a colloid of monodisperse diamond nanoparticles known to realize nucleation densities in excess of  $10^{11} \text{cm}^{-2}$ .<sup>[284]</sup> The growth conditions were 3% CH<sub>4</sub> diluted in hydrogen at a pressure of 50 mbar. The microwave power was 3500 W and the film was grown to 150 nm thickness in around 25 min at a temperature of 700°C. The resulting diamond phase grains are in the order of 10-100 nm.

## **7.3 Surface functionalization procedures**

### **7.3.1 Treatment of surfaces**

#### **Structured H- and OH-terminated NCD:**

Clean NCD surfaces were hydrogenated in a commercial microwave plasma reactor (AX5010) using a hydrogen flow 100 sccm, hydrogen pressure 50 mbar and microwave power of 750 W during 15 min. The structuring was performed using a Shipley S1818 photoresist that was spin-coated at 6000 rpm with a MicroTec MJB 3 mask aligner (Süss, Garching, Germany). After exposure (Mercury i-line) and development, the samples were oxidized in a Technics Plasma 100-E plasma system (oxygen pressure 1.4 mbar, microwave

power 200 W, 5 min). The photoresist was removed by ultrasonication in acetone and 2-propanol.

Freshly structured or H-terminated samples were never exposed to air longer than 1 h but either reacted immediately or stored under argon atmosphere.

**Silicon substrates:**

Prior to use, the samples were sonicated for 5 minutes in ethyl acetate and ethanol, cleaned in a piranha solution, sonicated in water and dried under nitrogen.

7.3.2 Formation of SAMs and polymer brushes

**Self-initiated photografting and photopolymerization (SIPGP):**

Freshly prepared substrates were submerged in approximately 2 mL of distilled and degassed monomer in a photoreaction tube under dry argon atmosphere. Polymerization was carried out under constant irradiation with UV light (300-400 nm;  $\lambda_{\text{max}} = 350$  nm) at RT or different times indicated in the table. After SIPGP, the samples were immediately cleaned by sequential ultrasonication in different solvents (all HPLC grade) for 5 minutes each.

The intensity of the UV light source was  $8.9 \pm 0.2$  mW/cm<sup>2</sup> measured at direct contact to the lamp,  $3.9 \pm 0.5$  mW/cm<sup>2</sup> at a distance to the lamp corresponding to the thickness of the glass slide and  $3.6 \pm 0.5$  mW/cm<sup>2</sup> measured through the glass slide of an empty reaction tube.

Monomer	polymerization time (h)	subsequent cleaning
styrene	24	toluene, ethyl acetate, ethanol
sulfonated styrene in water	2	water, ethyl acetate, ethanol
methyl methacrylate	6	chloroform, ethyl acetate, ethanol
<i>tert</i> -butyl methacrylate	8	dichloromethane, ethyl acetate, ethanol
dimethyl-aminoethyl methacrylate	2	water, ethanol, ethyl acetate
4-vinyl pyridine	24	ethanol, acetonitrile, ethyl acetate
2- <i>iso</i> -propenyl-2-oxazoline	24	chloroform, acetonitrile, ethanol

### Silanization of silicon surfaces:

Prior to surface silanization, freshly cleaned  $\text{SiO}_x$  surfaces were immersed in 0.1 M aqueous NaOH solution for 2 min and subsequently 0.1 M aqueous  $\text{HNO}_3$  for 10 min to generate terminal hydroxyl groups. The samples were rinsed with water and blown dry in a stream of nitrogen.

a) Aminopropyl-triethoxysilane (APTES) functionalization: The surfaces were incubated in a 5 v% solution of APTES in acetone under nitrogen atmosphere and sonicated for 1 h. Afterwards, they were sonicated in acetone and ethanol and blown dry.

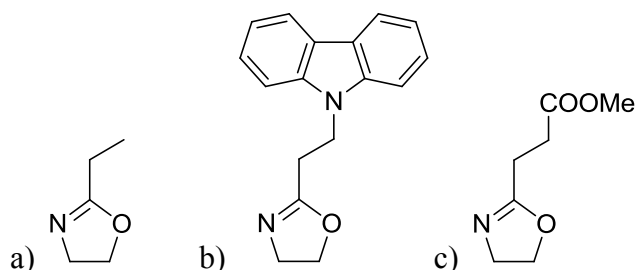
b) Octyl-triethoxysilane (OTES) functionalization: The surfaces were reacted in a 5 v% solution of OTES in hexane under nitrogen atmosphere at  $90^\circ\text{C}$  for 24 h. Afterwards, they were sonicated in hexane and ethanol and blown dry.

### Atom-transfer radical polymerization (ATRP) on silicon surfaces:

The APTES monolayer on a  $\text{SiO}_x$  substrate was converted into the ATRP initiator by emerging the freshly cleaned sample into a solution of 0.03 mL bromo-*isobutyryl* bromide and 0.03 mL triethylamine in 3 mL DCM for 30 minutes. Afterwards, the sample was rinsed with DCM and emerged in 2 mL of ultrapure water. After degassing under constant nitrogen stream, 4 mL of thoroughly degassed water containing MAEMA (2 mL, 1 eq.) and  $\text{Cu(I)Br}$  (0.01 eq.), prepared prior to the initiator formation, was added *via* a syringe. Subsequently, pentamethyldiethylenetriamine (0.033 eq.) as ligand was added and the ATRP solution was kept at room temperature for 20 h (or for various amounts of time in case of kinetic studies).

### 7.3.3 Polymer analogue reactions

#### LCROP:



The poly(2-isopropenyl-2-oxazoline) (PIPOx) functionalized surface was submerged in a solution of 2 mL dry and freshly distilled acetonitrile (ACN) with an excess amount of methyl trifluoromethane sulfonate (MeOTf) at approximately -35 °C under a dry argon atmosphere. After stirring for 3 h at 0 °C, the mixture was allowed to equilibrate to RT and was stirred for 60 min before monomer a), b) or c) was added under an argon atmosphere. In case of b) 2 mL of dry ACN were added at this point. The reaction solution was stirred at 80°C for 16 h. Finally, an excess of terminating agent was added to terminate the LCROP. After 60 min, the sample was removed from the reaction solution and thoroughly washed with a saturated solution of potassium carbonate in deionized water (Millipore). Final cleaning was performed by sequential ultrasonication in deionized water, ethanol, ACN and ethyl acetate for 5 min each.

Terminating agent for LCROP	solvent
Piperidine	ACN
Glycine- <i>tert</i> -butyl ester	ACN + Chloroform anhydrous
L-Prolin- <i>tert</i> -butyl ester	ACN

#### **Hydrolysis of *tert*.butyl ester moieties:**

Both poly(*tert*-butyl methacrylate) brushes and glycine-*tert*-butylester or L-prolin-*tert*-butyl ester terminated (IPOx-g-EtOx) bottle-brush brushes were hydrolyzed in a solution of methanesulfonic acid in dichloromethane (1:100) at RT for 30 minutes. The surfaces were successively cleaned by ultrasonication in DCM, water and ethanol.

#### **Biomolecule coupling to polymer brushes (GFP, HRP, acetylcholinesterase, cytochrome c, glucose oxidase)**

The pendant carboxylic acid functional groups of the polymer brushes were activated in an aqueous solution of 400 mM 1-ethyl-3-(3-dimethylaminopropyl)carbodiimid (EDC) and 100 mM *N*-hydroxysuccinimide (NHS) for 1 hour. After cleaning with a buffer solution, the sample was covered with a solution of the biomolecules in buffer (1.5 mg/mL<sup>\*</sup>) for 24 hours, rinsed thoroughly and stored at 4°C in buffer solution. <sup>\*</sup> Since the net weight of commercially available enzyme containing solid does not necessarily correspond to the net weight of pure

enzyme, the exact concentration of biomolecule in buffer was determined by photometric measurements:

$$c = \frac{\bar{E}}{\epsilon \cdot d} \cdot M$$

with E = average extinction;  $\epsilon$  = extinction coefficient according to ExPASy database; d = sample thickness; M = molar mass of the biomolecule

biomolecule	buffer pH	* concentration evaluated by photometry
GFP	6.2	/
HRP	6.2	0.37 mg protein/mL in 1.5 mg substance/mL
Acetylcholinesterase	8.0	/
Cytochrome c	7.0	/
Glucose oxidase	7.0	1.0 mg protein/mL in 1.5 mg substance/mL

### **Ferrocene functionalized polymer brushes**

#### **a) SIPGP of vinylferrocene:**

100 mg (or 50 mg) of vinylferrocene were dissolved in 0.7 mL of inhibitor-free *tert*-butyl methacrylate. After five freeze-thaw cycles, the oxygen terminated diamond sample was added and the solution was irradiated under UV according to SIPGP conditions. After 4 days of irradiation, the sample was cleaned by ultrasonication in chloroform, ethyl acetate and ethanol.

#### **b) Polymer analogue coupling of ferroceneamines into poly(methacrylic acid) brushes:**

For experiments excluding further coupling and measurements of enzymes, aminoferrocene or aminomethylferrocene were dissolved in acetonitrile to obtain a 1 mg/mL solution. However, in order to test the applicability of ferrocene coupling in enzyme-compatible conditions, the ferroceneamines were dispersed in buffer and dissolved by ultrasonication.

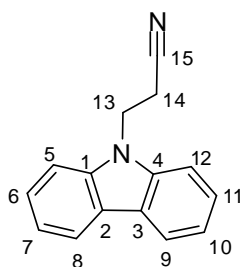
P(MA) modified diamond samples were first activated in a solution of NHS (100 mM) and EDC (400 mM) for an hour, rinsed with water and emerged in the freshly prepared ferroceneamine solution. The coupling was allowed to complete over night if not otherwise stated in the results. Finally, the samples were cleaned by ultrasonication in acetonitrile, ethyl acetate and ethanol.

### Parallel coupling of enzymes and aminomethylferrocenes into poly(methacrylic acid) brushes:

Freshly NHS/EDC- activated P(MA) modified diamond samples were emerged in a 1 mg/mL solution of enzyme in its appropriate buffer. After one hour of enzyme coupling, the samples were taken out of the solution and without further rinsing emerged in a 1 mg/mL solution of aminomethylferrocene in order to saturate the remaining NHS-ester moieties with the ferrocene compound. After 3.5 hours, the samples were thoroughly rinsed with buffer and further cleaned by shaking in buffer for 2 hours.

## 7.4 Synthesis of organic molecules

### *N*-Propionitril-carbazol:

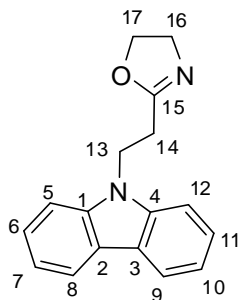


According to a synthetic route described by Litt *et al.* [358] bromopropionitrile was added drop wise to a suspension of carbazole (1eq), *tert*-butylammoniumbromide (0.03 eq) in NaOH (50%) and benzene at rt. After two hours the reaction was quenched with hot water and the resulting yellow precipitate was filtered and washed with hot water. After recrystallization in ethanol, the obtained *N*-propionitril-carbazol was dissolved in aminoethanol (1.4 eq) and *n*-butanol. Cadmiumacetat dihydrate (0,03 eq) was added and the reaction mixture was stirred under reflux for 24 h at 140°C. After evaporating the solvent the residue was purified by recrystallization in hexane yielding 2-(ethylcarbazol)-2-oxazoline as a white solid (yield: 85%)

$^1\text{H}$  NMR  $\delta$  ppm 7.86 (m, 2H, *aromat.*), 7.32 (m, 2H, *aromat.*), 7.22 (m, 2H, *aromat.*), 6.97 (m, 2H, *aromat.*), 4.41 (t,  $J = 6.60$  Hz, 2H,  $H^{13}$ ), 2.68 (t,  $J = 6.61$  Hz, 2H,  $H^{14}$ ).

IR: 3049 (m), 2949 (m), 2245 (s), 752 (s).

### 2-(Carbazolyl)ethyl-2-oxazoline (CarbOx):



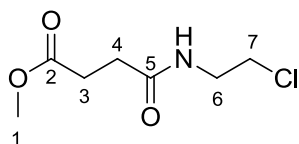
*N*-propionitril-carbazol was dissolved in aminoethanol (1.4 eq) and *n*-butanol. Cadmiumacetate dihydrate (0.03 eq) was added and the reaction mixture stirred under reflux for 24 h at 140°C. After evaporation of the solvent the residue was purified by recrystallization in hexane to yield CarbOx as a colorless solid (yield 70%).

<sup>1</sup>H NMR δ ppm 8.10 (m, 2H, *aromat.*), 7.45 (m, 4H, *aromat.*), 7.24 (m, 2H, *aromat.*), 4.65 (t, 1H, *H*<sup>13</sup>), 4.18 (t, *J* = 9.43, 9.43 Hz, 2H, *H*<sup>17</sup>), 3.80 (t, *J* = 9.85, 9.85 Hz, 2H, *H*<sup>16</sup>), 2.81 (t, 2H, *H*<sup>14</sup>).

<sup>13</sup>C NMR δ ppm 27.32 (*C*<sup>13</sup>), 39.70 (*C*<sup>14</sup>), 54.41 (*C*<sup>16</sup>), 67.36 (*C*<sup>17</sup>), 108.45 (*C*<sup>5,12</sup>), 119.10, 120.42, 123.01, 125.71 (*C*<sup>2,3,6,7,8,9,10,11</sup>), 139.95 (*C*<sup>1,4</sup>), 165.68 (*C*<sup>15</sup>).

IR: 3047 (m), 2952 (m), 1669 (s).

### Methyl-7-chloro-4-oxo-5-azaheptanoat:<sup>[359]</sup>

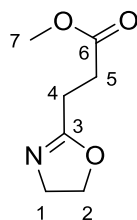


Succinic acid monomethylester chloride (1 eq.) and 2-chloroethylamine hydrochloride (1 eq.) were dissolved in dry dichloromethane under nitrogen atmosphere. At 0°C triethylamine (2.25 eq.) was added drop wise within 60 min. under the formation of a white precipitate. After stirring over night at rt, 50 mL of water were added. The organic phase was extracted with brine and the aqueous phase with dichloromethane. The joined organic solution was concentrated by evaporation and the product was obtained as orange oil.

$^1\text{H}$  NMR  $\delta$  ppm 3.62 – 3.65 (m, 4H,  $H^{6/7}$ ), 3.56 (s, 3H,  $H^1$ ), 2.62 (t, 2H,  $H^4$ ), 2.48 (t, 2H,  $H^3$ )

$^{13}\text{C}$  NMR  $\delta$  ppm 173.3 ( $C^5$ ), 171.6 ( $C^2$ ), 51.8 ( $C^1$ ), 43.8 ( $C^7$ ), 41.2 ( $C^6$ ), 30.8 ( $C^4$ ), 29.2 ( $C^3$ )

**Methyl-3-(oxazol-2-yl)propionate:**<sup>[359]</sup>

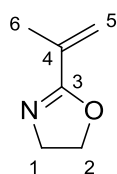


Anhydrous sodium carbonate (1.3 eq.) was added to methyl-7-chloro-4-oxo-5-azaheptanoate (1 eq.). At 40 °C the mixture was carefully evacuated at the vacuum line until formation of gas was completed. Afterwards, the mixture was heated up to 140 °C and the product was obtained by distillation (1.6 mbar, 80°C) but forms a white solid after cooling to rt (yield: 20%).

$^1\text{H}$  NMR  $\delta$  ppm 4.19 (t, 2H,  $H^1$ ), 3.79 (t, 2H,  $H^2$ ), 3.64 (s, 3H,  $H^7$ ), 2.53-2.62 (m, 4H,  $H^{5,6}$ )

$^{13}\text{C}$  NMR  $\delta$  ppm 172.2 ( $C^6$ ), 168.0 ( $C^3$ ), 67.5 ( $C^2$ ), 54.8 ( $C^1$ ), 51.5 ( $C^5$ ), 30.3 ( $C^4$ ), 23.0 ( $C^7$ )

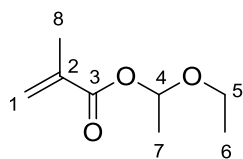
**2-Isopropenyl-2-oxazoline (IPOx):**



IPOx was synthesized according to literature.<sup>[227]</sup> 2-Ethyl-2-oxazoline (1 eq.) was reacted with paraformaldehyde (1 eq.) in the presence of catalytic amounts of triethylamine to form the hydroxyethyl derivative 2-(hydroxy-2-propyl)-2-oxazoline. IPOx was obtained by water elimination with a Dean-Stark apparatus at 85°C and 70-80 mbar with sodium hydroxide and small amounts of radical inhibitor. The product was dried and cleaned by vacuum distillation over calcium hydride (42 mbar, 62°C).

$^1\text{H}$  NMR  $\delta$  ppm 5.78 (s, 1H,  $H^5$ ), 5.41 (s, 1H,  $H^6$ ), 4.28 (t, 2H,  $H^1$ ), 3.93 (t, 2H,  $H^2$ ), 2.00 (s, 3H,  $H^3$ )

**1-Ethoxyethyl metacrylate:**<sup>[319]</sup>

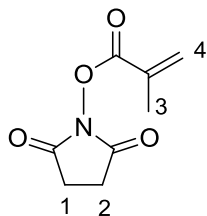


At 0°C, ethylvinyl ether (1.2 eq.) was added dropwise to a solution of methacrylic acid (1.0 eq.) and phosphoric acid (0.002 eq.). The reaction mixture was stirred at rt for 48 h and filtered over aluminum oxide. The residual ether was removed by evaporation and the product was further purified by vacuum distillation (6.5 mbar, 32°C) (yield: 75%).

<sup>1</sup>H NMR  $\delta$  ppm 6.15 (d, 1H,  $H^1$ ), 6.00 (d, 1H,  $H^2$ ), 5.59 (q, 1H,  $H^4$ ), 3.55-3.73 (m, 2H,  $H^5$ ), 1.94 (s, 3H,  $H^8$ ), 1.43 (d, 3H,  $H^7$ ), 1.21 (t, 3H,  $H^6$ )

<sup>13</sup>C NMR  $\delta$  ppm 167.0 ( $C^3$ ), 136.2 ( $C^2$ ), 125.9 ( $C^1$ ), 96.6 ( $C^4$ ), 64.6 ( $C^5$ ), 20.9 ( $C^7$ ), 18.2 ( $C^8$ ), 15.0 ( $C^6$ )

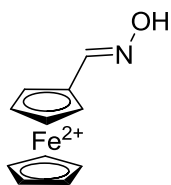
***N*-methacryloxysuccinimide:**



The synthesis of *N*-methacryloxysuccinimide was performed according to a synthesis procedure for *N*-acryloxysuccinimide:<sup>[360]</sup> A solution of *N*-hydroxysuccinimide (1 eq.) and triethylamine (1 eq.) in 65 mL chloroform was cooled to 0°C and methacryloyl chloride (1.1 eq.) was added drop wise with a dropping funnel within 20 min. The solution was stirred for 45 min. at 0°C and then washed with ice-cold water and ice-cold brine. The organic phase was dried over MgSO<sub>4</sub>, evaporated and dissolved in hexane. After several hours at 0°C, the formed colorless crystals were separated by filtration (yield: 68%).

<sup>1</sup>H NMR  $\delta$  ppm 6.41-6.42 (m, 1H,  $H^4$ ), 5.88-5.89 (m, 1H,  $H^3$ ), 2.83-2.86 (m, 4H,  $H^2$ ), 2.05-2.06 (m, 3H,  $H^1$ ).

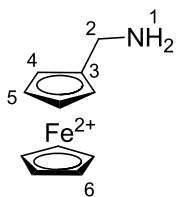
**Aminomethyl-ferrocene via ferrocenecarbaldehyde oxime:**<sup>[353],[361]</sup>



Ferrocenecarbaldehyde (1 eq., 4.7 mmol) was dissolved in 15 mL ethanol under argon atmosphere. First, hydroxylamine (2 eq.) in 5mL water followed by sodiumacetate (3 eq.) in water/ethanol (1/1) was added to the solution. The reaction mixture was stirred under reflux for 3.5 h and after cooling concentrated under vacuum. The residue was extracted in water and chloroform and the organic phase was evaporated to dryness, yielding in an orange-brown solid (ferrocenecarbaldehyde oxime).

<sup>1</sup>H NMR  $\delta$  ppm 7.90 (s, 1H, Fc-CH-N), 4.14-4.52 (m, 9H, Fc-H).

IR: 3252 (br), 3090 (m), 1656 (m), 1631 (m).



After confirmation of the intermediate product in NMR and IR, ferrocenecarbaldehyde oxime (1 eq.) was dissolved in dry THF under argon and cooled to 0°C, before lithium aluminium hydride (4.5 eq.) was added drop wise with care. The mixture was stirred at rt over night. Benzene and ethyl acetate were consecutively added and the solution was eventually carefully quenched with drops of 5M NaOH until gas formation was over. Inorganic precipitations were removed by filtration and the filtrate was evaporated in vacuum. The residue was freeze-dried from benzene yielding in aminomethyl ferrocene (yield: n/a).

<sup>1</sup>H NMR  $\delta$  ppm 4.07 (m, 9H,  $H^{4,5,6}$ ), 3.47 (s, 2H,  $H^2$ ), 1.56 (br, 2H,  $H^1$ ).

<sup>13</sup>C NMR  $\delta$  ppm 91.0 ( $C^3$ ), 68.3, 67.7, 67.1 ( $C^{4,5,6}$ ), 41.3 ( $C^2$ )

## 8. REFERENCES

- [1] S. H. Richardson, H. J. Erlank, J. W. Harris, S. R. Hart, *Nature* **1990**, *346*, 54-56.
- [2] U. Schwarz, *Chemie in unserer Zeit* **2000**, *34*, 212-222.
- [3] C. L. Mantell, in *Carbon and Graphite Handbook*, Interscience Publisher, **1968**.
- [4] H. Moissan, *Annales De Chimie Et De Physique* **1905**, *5*, 174-208.
- [5] C. Donnet, *Surf. Coat. Technol.* **1998**, *100*, 180-186.
- [6] F. Z. Cui, D. J. Li, *Surf. Coat. Technol.* **2000**, *131*, 481-487.
- [7] M. K. Singh, E. Titus, M. G. Willinger, J. Gracio, *J. Nanosci. Nanotechnol.* **2010**, *10*, 2422-2433.
- [8] A. Aleksov, M. Kubovic, N. Kaeb, U. Spitzberg, A. Bergmaier, G. Dollinger, T. Bauer, M. Schreck, B. Stritzker, E. Kohn, *Diam. Relat. Mat.* **2003**, *12*, 391-398.
- [9] M. V. Hauf, L. H. Hess, J. Howgate, M. Dankerl, M. Stutzmann, J. A. Garrido, *Appl. Phys. Lett.* **2010**, *97*, 093504-093507.
- [10] H. Y. Chan, D. M. Aslam, J. A. Wiler, B. Casey, *J. Microelectromech. Syst.* **2009**, *18*, 511-521.
- [11] G. M. Swain, R. Ramesham, *Anal. Chem.* **1993**, *65*, 345-351.
- [12] T. Yano, D. A. Tryk, K. Hashimoto, A. Fujishima, *J. Electrochem. Soc.* **1998**, *145*, 1870-1876.
- [13] A. Härtl, E. Schmich, J. A. Garrido, J. Hernando, S. C. R. Catharino, S. Walter, P. Feulner, A. Kromka, D. Steinmuller, M. Stutzmann, *Nat. Mater.* **2004**, *3*, 736-742.
- [14] R. J. Hamers, J. E. Butler, T. Lasseter, B. M. Nichols, J. N. Russell, K. Y. Tse, W. S. Yang, *Diam. Relat. Mat.* **2005**, *14*, 661-668.
- [15] L. Marcon, M. Wang, Y. Coffinier, F. Le Normand, O. Melnyk, R. Boukherroub, S. Szunerits, *Langmuir* **2010**, *26*, 1075-1080.
- [16] E. Colombo, Y. Men, J. Scharpf, C. Pietzka, M. Dipalo, P. Herfurth, Z. Gao, M. Schneider, V. Carabelli, E. Carbone, E. Kohn, A. Pasquarelli, *Diam. Relat. Mat.* **2011**, *20*, 793-797.
- [17] M. Montagnana, M. Caputo, D. Giavarina, G. Lippi, *Clin. Chim. Acta* **2009**, *402*, 7-13.
- [18] D. F. Williams, *Biomaterials* **2008**, *29*, 2941-2953.
- [19] S. F. Bent, *Surf. Sci.* **2002**, *500*, 879-903.
- [20] J. M. Berg, J. L. Tymoczko, L. Stryer, *Biochemistry*, 5 ed., W.H. Freeman and Company.
- [21] B. Eggins, *Biosensors*, 1 ed., Wiley / Teubner, **1996**.
- [22] X. Chen, Z. P. Yang, S. H. Si, *J. Electroanal. Chem.* **2009**, *635*, 1-6.
- [23] I. C. Stancu, A. Fernandez-Gonzalez, L. M. Butac, R. Salzer, *J. Optoelectron. Adv. Mater.* **2007**, *9*, 2696-2702.
- [24] M. Sugawara, K. Kojima, H. Sazawa, Y. Umezawa, *Anal. Chem.* **1987**, *59*, 2842-2846.
- [25] C. H. Nielsen, *Anal. Bioanal. Chem.* **2009**, *395*, 697-718.
- [26] L. C. Clark, R. Wolf, D. Granger, Z. Taylor, *J. Appl. Physiol.* **1953**, *6*, 189-193.

- [27] L. C. Clark, C. Lyons, *Ann. N. Y. Acad. Sci.* **1962**, *102*, 29-&.
- [28] A. Chaubey, B. D. Malhotra, *Biosens. Bioelectron.* **2002**, *17*, 441-456.
- [29] M. Mehrvar, M. Abdi, *Anal. Sci.* **2004**, *20*, 1113-1126.
- [30] A. K. Ajay, D. N. Srivastava, *Biosens. Bioelectron.* **2007**, *23*, 281-284.
- [31] T. L. Delaney, D. Zimin, M. Rahm, D. Weiss, O. S. Wolfbeis, V. M. Mirsky, *Anal. Chem.* **2007**, *79*, 3220-3225.
- [32] C. Padeste, B. Steiger, A. Grubelnik, L. Tiefenauer, *Biosens. Bioelectron.* **2003**, *19*, 239-247.
- [33] W. Schuhmann, T. J. Ohara, H. L. Schmidt, A. Heller, *J. Am. Chem. Soc.* **1991**, *113*, 1394-1397.
- [34] A. E. G. Cass, G. Davis, G. D. Francis, H. A. O. Hill, W. J. Aston, I. J. Higgins, E. V. Plotkin, L. D. L. Scott, A. P. F. Turner, *Anal. Chem.* **1984**, *56*, 667-671.
- [35] A. Heller, *J. Phys. Chem.* **1992**, *96*, 3579-3587.
- [36] A. Heller, *Annu. Rev. Biomed. Eng.* **1999**, *1*, 153-175.
- [37] T. Ruzgas, E. Csoregi, J. Emneus, L. Gorton, G. MarkoVarga, *Anal. Chim. Acta* **1996**, *330*, 123-138.
- [38] J. Kulys, R. D. Schmid, *Bioelectrochem. Bioenerg* **1990**, *24*, 305-311.
- [39] T. Tatsuma, Y. Okawa, T. Watanabe, *Anal. Chem.* **1989**, *61*, 2352-2355.
- [40] J. C. Vidal, M. A. Yague, J. R. Castillo, *Sens. Actuators, B* **1994**, *21*, 135-141.
- [41] M. Vreeke, R. Maidan, A. Heller, *Anal. Chem.* **1992**, *64*, 3084-3090.
- [42] T. Tatsuma, M. Gondaira, T. Watanabe, *Anal. Chem.* **1992**, *64*, 1183-1187.
- [43] Q. Deng, S. J. Dong, *J. Electroanal. Chem.* **1994**, *377*, 191-195.
- [44] Zulfikar, D. B. Hibbert, P. W. Alexander, *Electroanalysis* **1995**, *7*, 722-725.
- [45] M. Senel, E. Cevik, M. F. Abasiyanik, *Sens. Actuators, B* **2010**, *145*, 444-450.
- [46] A. E. G. Cass, *Biosensors - A Practical Approach*, 1 ed., IRL Press, **1990**.
- [47] I. Willner, E. Katz, *Angew. Chem.* **2000**, *112*, 1230-1269.
- [48] J. C. W. Kuan, H. K. Y. Lau, G. G. Guilbault, *Clin. Chem.* **1975**, *21*, 67-70.
- [49] R. Koncki, A. Radomska, S. Glab, *Talanta* **2000**, *52*, 13-17.
- [50] D. S. Papastathopoulos, G. A. Rechnitz, *Anal. Chem.* **1975**, *47*, 1792-1796.
- [51] H. Klauk, *Organic Electronics*, 1 ed., Wiley VCH, **2006**.
- [52] F. Buth, D. Kumar, M. Stutzmann, J. A. Garrido, *Appl. Phys. Lett.* **2011**, *98*, 1533021-1533023.
- [53] N. Chaniotakis, N. Sofikiti, *Anal. Chim. Acta* **2008**, *615*, 1-9.
- [54] J. Munoz, C. Jimenez, A. Bratov, J. Bartroli, S. Alegret, C. Dominguez, *Biosens. Bioelectron.* **1997**, *12*, 577-585.
- [55] R. J. W. Lugtenberg, R. J. M. Egberink, A. van den Berg, J. F. J. Engbersen, D. N. Reinhoudt, *J. Electroanal. Chem.* **1998**, *452*, 69-86.
- [56] M. Dankerl, M. V. Hauf, A. Lippert, L. H. Hess, S. Birner, I. D. Sharp, A. Mahmood, P. Mallet, J.-Y. Veuillen, M. Stutzmann, J. A. Garrido, *Adv. Funct. Mater.* **2010**, *20*, 3117-3124.
- [57] A. Sibbald, A. K. Covington, R. F. Carter, *Clin. Chem.* **1984**, *30*, 135-137.
- [58] K. Ataka, J. Heberle, *Anal. Bioanal. Chem.* **2007**, *388*, 47-54.

- [59] K. E. Sapsford, Y. S. Shubin, J. B. Delehanty, J. P. Golden, C. R. Taitt, L. C. Shriver-Lake, F. S. Ligler, *J. Appl. Microbiol.* **2004**, *96*, 47-58.
- [60] J. Homola, *Anal. Bioanal. Chem.* **2003**, *377*, 528-539.
- [61] C. L. Baird, D. G. Myszka, *J. Mol. Recognit.* **2001**, *14*, 261-268.
- [62] R. D. Harris, B. J. Luff, J. S. Wilkinson, J. Piehler, A. Brecht, G. Gauglitz, R. A. Abuknesha, *Biosens. Bioelectron.* **1999**, *14*, 377-386.
- [63] P. M. Fratamico, T. P. Strobaugh, M. B. Medina, A. G. Gehring, *Biotechnol. Tech.* **1998**, *12*, 571-576.
- [64] J. Curie, P. Curie, *Comput. Rend. Acad. Sci. Paris* **1880**, *91*, 294-297.
- [65] K. A. Marx, *Biomacromolecules* **2003**, *4*, 1099-1120.
- [66] M. A. Cooper, V. T. Singleton, *J. Mol. Recognit.* **2007**, *20*, 154-184.
- [67] Y. M. Long, Y. J. Liu, L. H. Lei, L. H. Nie, S. Z. Yao, *Analyst* **2001**, *126*, 1090-1094.
- [68] A. Shons, J. Najarian, F. Dorman, *J. Biomed. Mater. Res.* **1972**, *6*, 565-&.
- [69] S. H. Si, L. Si, F. L. Ren, D. R. Zhu, Y. S. Fung, *J. Colloid Interface Sci.* **2002**, *253*, 47-52.
- [70] Q. Chen, W. Tang, D. Z. Wang, X. J. Wu, N. Li, F. Liu, *Biosens. Bioelectron.* **2010**, *26*, 575-579.
- [71] J. Halamek, J. Pribyl, A. Makower, P. Skladal, F. W. Scheller, *Anal. Bioanal. Chem.* **2005**, *382*, 1904-1911.
- [72] G. F. Li, S. Morita, S. Ye, M. Tanaka, M. Osawa, *Anal. Chem.* **2004**, *76*, 788-795.
- [73] I. S. Park, D. K. Kim, N. Adanyi, M. Varadi, N. Kim, *Biosens. Bioelectron.* **2004**, *19*, 667-674.
- [74] J. Halamek, A. Makower, K. Knosche, P. Skladal, F. W. Scheller, *Talanta* **2005**, *65*, 337-342.
- [75] C. J. Percival, S. Stanley, A. Braithwaite, M. I. Newton, G. McHale, *Analyst* **2002**, *127*, 1024-1026.
- [76] J. Wannlund, M. Deluca, *Anal. Biochem.* **1982**, *122*, 385-393.
- [77] C. Spink, I. Wadsö, *Methods Biochem. Anal.* **1976**, *23*, 1.
- [78] K. Ramanathan, B. Danielsson, *Biosens. Bioelectron.* **2001**, *16*, 417-423.
- [79] V. S. Bagotsky, *Fundamentals of Electrochemistry*, 2 ed., Wiley, **2006**.
- [80] L. Husaru, R. Schulze, G. Steiner, T. Wolff, W. D. Habicher, R. Salzer, *Anal. Bioanal. Chem.* **2005**, *382*, 1882-1888.
- [81] G. Woodhouse, L. King, L. Wiczorek, P. Osman, B. Cornell, *J. Mol. Recognit.* **1999**, *12*, 328-334.
- [82] S. W. Lucas, M. M. Harding, *Anal. Biochem.* **2000**, *282*, 70-79.
- [83] S. Y. Oh, B. Cornell, D. Smith, G. Higgins, C. J. Buffell, T. W. Kok, *Biosens. Bioelectron.* **2008**, *23*, 1161-1165.
- [84] D. Gan, *Diabetes atlas*, 3 ed., World Diabetes Foundation, Brussels, **2006**.
- [85] P. Zhang, X. Zhang, J. B. Brown, D. Vistisen, R. A. Sicree, J. Shaw, G. A. Nichols, in *Diabetes Atlas*, 4 ed., World Diabetes Foundation, Brussels, **2009**.
- [86] S. Vaddiraju, I. Tomazos, D. J. Burgess, F. C. Jain, F. Papadimitrakopoulos, *Biosens. Bioelectron.* **2010**, *25*, 1553-1565.
- [87] A. Chaubey, K. K. Pande, V. S. Singh, B. D. Malhotra, *Anal. Chim. Acta* **2000**, *407*, 97-103.

- [88] I. Karube, S. Mitsuda, S. Suzuki, *Eur. J. Appl. Microbiol.* **1979**, *7*, 343-350.
- [89] R. N. Adams, *Anal. Chem.* **1958**, *30*, 1576-1576.
- [90] F. N. Comba, M. D. Rubianes, P. Herrasti, G. A. Rivas, *Sens. Actuators, B* **2010**, *149*, 306-309.
- [91] R. Ojani, J. B. Raoof, S. Fathi, *Electroanalysis* **2008**, *20*, 1825-1830.
- [92] X. Cheng, S. Zhang, H. Y. Zhang, Q. J. Wang, P. G. He, Y. Z. Fang, *Food Chem.* **2008**, *106*, 830-835.
- [93] A. B. Kharitonov, M. Zayats, A. Lichtenstein, E. Katz, I. Willner, *Sens. Actuators, B* **2000**, *70*, 222-231.
- [94] B. G. Healey, L. Li, D. R. Walt, *Biosens. Bioelectron.* **1997**, *12*, 521-529.
- [95] K. S. Carmon, R. E. Baltus, L. A. Luck, *Biochemistry* **2004**, *43*, 14249-14256.
- [96] G. S. Wilson, R. Gifford, *Biosens. Bioelectron.* **2005**, *20*, 2388-2403.
- [97] B. J. Gilligan, M. C. Shults, R. K. Rhodes, S. J. Uppdike, *Diabetes Care* **1994**, *17*, 882-887.
- [98] Y. Moskovitz, S. Srebnik, *Biophys. J.* **2005**, *89*, 22-31.
- [99] J. F. Kang, A. Ulman, S. Liao, R. Jordan, G. H. Yang, G. Y. Liu, *Langmuir* **2001**, *17*, 95-106.
- [100] A. Ulman, *Chem. Rev.* **1996**, *96*, 1533.
- [101] F. Davis, S. P. J. Higson, *Biosens. Bioelectron.* **2005**, *21*, 1-20.
- [102] F. Schreiber, *Prog. Surf. Sci.* **2000**, *65*, 151-256.
- [103] S. Frey, V. Stadler, K. Heister, W. Eck, M. Zharnikov, M. Grunze, B. Zeysing, A. Terfort, *Langmuir* **2001**, *17*, 2408-2415.
- [104] P. E. Laibinis, G. M. Whitesides, *J. Am. Chem. Soc.* **1992**, *114*, 9022-9028.
- [105] M. A. Bryant, S. L. Joa, J. E. Pemberton, *Langmuir* **1992**, *8*, 753-756.
- [106] O. M. Magnussen, B. M. Ocko, M. Deutsch, M. J. Regan, P. S. Pershan, D. Abernathy, G. Grubel, J. F. Legrand, *Nature* **1996**, *384*, 250-252.
- [107] C. L. McGuinness, A. Shaporenko, C. K. Mars, S. Uppili, M. Zharnikov, D. L. Allara, *J. Am. Chem. Soc.* **2006**, *128*, 5231-5243.
- [108] J. F. Kang, S. Liao, R. Jordan, A. Ulman, *J. Am. Chem. Soc.* **1998**, *120*, 9662-9667.
- [109] M. Frasconi, F. Mazzei, T. Ferri, *Trends Biochem. Sci.* **2010**, *398*, 1545-1564.
- [110] J. Li, G. Cheng, S. Dong, *J. Electroanal. Chem.* **1996**, *416*, 97-104.
- [111] M. Schaeferling, S. Schiller, H. Paul, M. Kruschina, P. Pavlickova, M. Meerkamp, C. Giammasi, D. Kambhampati, *Electrophoresis* **2002**, *23*, 3097-3105.
- [112] S. Flink, F. van Veggel, D. N. Reinhoudt, *Adv. Mater.* **2000**, *12*, 1315-1328.
- [113] J. Spinke, M. Liley, F. J. Schmitt, H. J. Guder, L. Angermaier, W. Knoll, *J. Chem. Phys.* **1993**, *99*, 7012-7019.
- [114] R. Bhure, A. Mahapatro, *Silicon* **2010**, *2*, 117-151.
- [115] J. Sagiv, *J. Am. Chem. Soc.* **1980**, *102*, 92-98.
- [116] P. Silberzan, L. Léger, D. Ausserré, J. J. Benattar, *Langmuir* **1991**, *7*, 1647-1651.
- [117] Y. Wang, M. Liebermann, *Langmuir* **2003**, *19*, 1159-1167.
- [118] S. J. Schoell, M. Hoeb, I. D. Sharp, W. Steins, M. Eickhoff, M. Stutzmann, M. S. Brandt, *Appl. Phys. Lett.* **2008**, *92*, 153301.
- [119] F. Vianello, L. Zennaro, M. L. Di Paolo, A. Rigo, C. Malaranre, M. Scarpa, *Biotechnol. Bioeng.* **2000**, *68*, 488-495.

- [120] G. Urban, G. Jobst, F. Kohl, A. Jachimowicz, F. Olcaytug, O. Tilado, P. Goiser, G. Nauer, F. Pittner, T. Schalkhammer, E. Mannbuxbaum, *Biosens. Bioelectron.* **1991**, *6*, 555-562.
- [121] S. Yoshida, H. Kanno, T. Watanabe, *Anal. Sci.* **1995**, *11*, 251-256.
- [122] S. K. Bhatia, M. J. Cooney, L. C. Shriverlake, T. L. Fare, F. S. Ligler, *Sens. Actuators, B* **1991**, *3*, 311-317.
- [123] P. Allongue, C. Henry de Villeneuve, G. Cherouvier, R. Cortès, M.-C. Bernard, *J. Electroanal. Chem.* **2003**, *550-551*, 161-174.
- [124] S. Boland, F. Barrière, D. Leech, *Langmuir* **2008**, *24*, 6351-6358.
- [125] M. P. Stewart, F. Maya, D. V. Kosynkin, S. M. Dirk, J. J. Stapleton, C. L. McGuinness, D. L. Allara, J. M. Tour, *J. Am. Chem. Soc.* **2004**, *126*, 370.
- [126] S. Q. Lud, M. Steenackers, R. Jordan, P. Bruno, D. M. Gruen, P. Feulner, J. A. Garrido, M. Stutzmann, *J. Am. Chem. Soc.* **2006**, *128*, 16884-16891.
- [127] A. Adenier, E. Cabet-Deliry, A. Chausse, S. Griveau, F. Mercier, J. Pinson, C. Vautrin-UI, *Chem. Mater.* **2005**, *17*, 491-501.
- [128] B. Chen, A. K. Flatt, H. Jian, J. L. Hudson, J. M. Tour, *Chem. Mater.* **2005**, *17*, 4832.
- [129] G. Richter, in *PhD Thesis*, TU München, **2011**.
- [130] S. Q. Lud, S. Neppel, G. Richter, P. Bruno, D. M. Gruen, R. Jordan, P. Feulner, M. Stutzmann, J. A. Garrido, *Langmuir* **2010**, *26*, 15895-15900.
- [131] D. Evrard, F. Lambert, C. Policar, V. Balland, B. Limoges, *Chem. Eur. J.* **2008**, *14*, 9286-9291.
- [132] J. M. Buriak, *Chem. Rev.* **2002**, *102*, 1271-1308.
- [133] J. M. Buriak, *Adv. Mater.* **1999**, *11*, 265-+.
- [134] A. B. Sieval, A. L. Demirel, J. W. Nissink, M. R. Linford, J. H. van der Maas, W. H. de Jeu, H. Zuilhof, E. J. R. Suhhölter, *Langmuir* **1998**, *14*, 1759.
- [135] A. B. Sieval, R. Opitz, H. P. A. Maas, M. G. Schoeman, G. Meijer, F. J. Vergeldt, H. Zuilhof, E. J. R. Sudholter, *Langmuir* **2000**, *16*, 10359-10368.
- [136] M. R. Linford, C. E. D. Chidsey, *J. Am. Chem. Soc.* **1993**, *115*, 12631.
- [137] M. M. Sung, J. Lkluth, O. W. Yauw, R. Maboudian, *Langmuir* **1997**, *13*, 6164.
- [138] R. L. Cicero, M. R. Linford, C. E. D. Chidsey, *Langmuir* **2000**, *16*, 5688.
- [139] J. M. Buriak, M. J. Allen, *J. Am. Chem. Soc.* **1998**, *120*, 1339.
- [140] M. P. Stewart, J. M. Buriak, *Angew. Chem. Int. Ed.* **1998**, *37*, 3257.
- [141] C. Dahmen, A. Janotta, D. Dimova-Malinovska, S. Marx, B. Jeschke, B. Nies, H. Kessler, M. Stutzmann, *Thin Solid Films* **2003**, *427*, 201-207.
- [142] C. E. Nebel, D. Shin, D. Takeuchi, T. Yamamoto, H. Watanabe, T. Nakamura, *Elsevier Science Sa*, **2006**, 1107-1112.
- [143] T. Strother, T. Knickerbocker, J. N. J. Russell, J. E. Butler, L. M. Smith, R. J. Hamers, *Langmuir* **2002**, *18*, 968.
- [144] B. M. Nichols, J. E. Butler, J. N. J. Russel, R. J. Hamers, *J. Phys. Chem. B* **2005**, *109*, 20938-20947.
- [145] V. J. Razumas, J. J. Jasaitis, J. J. Kulys, *Bioelectrochem. Bioenerg.* **1984**, *12*, 297-322.
- [146] S. P. Cullen, I. C. Mandel, P. Gopalan, *Langmuir* **2008**, *24*, 13701-13709.
- [147] Y. Nakabayashi, H. Yoshikawa, *Anal. Sci.* **2000**, *16*, 609-613.

- [148] E. J. Calvo, C. Danilowicz, C. M. Lagier, J. Manrique, M. Otero, *Biosens. Bioelectron.* **2004**, *19*, 1219-1228.
- [149] V. Coman, T. Gustavsson, A. Finkelsteinas, C. von Wachenfeldt, C. Hagerhall, L. Gorton, *J. Am. Chem. Soc.* **2009**, *131*, 16171-16176.
- [150] S. A. Merchant, T. O. Tran, M. T. Meredith, T. C. Cline, D. T. Glatzhofer, D. W. Schmidtke, *Langmuir* **2009**, *25*, 7736-7742.
- [151] S. A. Merchant, D. T. Glatzhofer, D. W. Schmidtke, *Langmuir* **2007**, *23*, 11295-11302.
- [152] A. Lueking, M. Horn, H. Eickhoff, K. Buessow, H. Lehrach, G. Walter, *Anal. Biochem.* **1999**, *270*, 103.
- [153] B. A. Stillmann, J. L. Tonkinson, *BioTechniques* **2000**, *29*, 630.
- [154] P. Arenkov, A. Kukhtin, A. Gemmell, S. Voloshchuk, V. Chupeeva, A. Mirzabekov, *Anal. Biochem.* **2000**, *278*, 123.
- [155] J. Trmcic-Cvitas, E. Hasan, M. Ramstedt, X. Li, M. A. Cooper, C. Abell, W. T. S. Huck, J. E. Gautrot, *Biomacromolecules* **2009**, *10*, 2885-2894.
- [156] S. J. Sofia, V. Premnath, E. W. Merrill, *Macromolecules* **1998**, *31*, 5059-5070.
- [157] A. Hucknall, S. Rangarajan, A. Chilkoti, *Adv. Mater.* **2009**, *21*, 2441-2446.
- [158] L. Ionov, M. Stamm, S. Diez, *Nano Lett.* **2006**, *6*, 1982-1987.
- [159] L. Ionov, A. Synytska, S. Diez, *Adv. Funct. Mater.* **2008**, *18*, 1501-1508.
- [160] W. Senaratne, L. Andruzzi, C. K. Ober, *Biomacromolecules* **2005**, *6*, 2427-2448.
- [161] J. E. Raynor, T. A. Petrie, K. P. Fears, R. A. Latour, A. J. Garcia, D. M. Collard, *Biomacromolecules* **2009**, *10*, 748-755.
- [162] M. Chiari, M. Cretich, F. Damin, G. Di Carlo, C. Oldani, *J. Chromatogr. B* **2008**, *866*, 89-103.
- [163] S. Diamanti, S. Arifuzzaman, A. Elsen, J. Genzer, R. A. Vaia, *Polymer* **2008**, *49*, 3770-3779.
- [164] S. Tugulu, A. Arnold, I. Sielaff, K. Johnsson, H. A. Klok, *Biomacromolecules* **2005**, *6*, 1602-1607.
- [165] T. K. Tam, M. Ornatska, M. Pita, S. Minko, E. Katz, *J. Phys. Chem. C* **2008**, *112*, 8438-8445.
- [166] T. Matrab, M. M. Chehimi, J. P. Boudou, F. Benedic, J. Wang, N. N. Naguib, J. A. Carlisle, *Diam. Relat. Mater.* **2006**, *15*, 639-644.
- [167] S. Zauscher, A. Chilkoti, *BioInterphases* **2009**, *4*, 1-2.
- [168] P. Jain, G. L. Baker, M. L. Bruening, *Annu. Rev. Anal. Chem.* **2009**, *2*, 387-408.
- [169] B. A. Kuznetsov, G. P. Shumakovich, O. V. Koroleva, A. I. Yaropolov, *Biosens. Bioelectron.* **2001**, *16*, 73-84.
- [170] J. Hrabakova, K. Ataka, J. Heberle, P. Hildebrandt, D. H. Murgida, *Phys. Chem. Chem. Phys.* **2006**, *8*, 759-766.
- [171] D. Grieshaber, R. MacKenzie, J. Voros, E. Reimhult, *Sensors* **2008**, *8*, 1400-1458.
- [172] D. A. Paggi, D. F. Martin, A. Kranich, P. Hildebrandt, M. A. Marti, D. H. Murgida, *Electrochim. Acta* **2009**, *54*, 4963-4970.
- [173] A. Avila, B. W. Gregory, K. Niki, T. M. Cotton, *J. Phys. Chem. B* **2000**, *104*, 2759-2766.
- [174] S. T. Milner, *Science* **1991**, *251*, 905-914.

- [175] R. C. Advincula, W. J. Brittain, K. C. Caster, J. R uhe, *Polymer Brushes*, 1 ed., Wiley-VCH, Weinheim, **2004**.
- [176] S. T. Milner, T. A. Witten, M. E. Cates, *Macromolecules* **1988**, *21*, 2610-2619.
- [177] S. T. Milner, T. A. Witten, M. E. Cates, *Macromolecules* **1989**, *22*, 853-861.
- [178] P. Auroy, L. Auvray, L. Leger, *Phys. Rev. Lett.* **1991**, *66*, 719-722.
- [179] M. Steenackers, A. K uller, S. Stoycheva, M. Grunze, J. R., *Langmuir* **2009**, *25*, 2225.
- [180] B. Zhao, W. J. Brittain, *Prog. Poly. Sci.* **2000**, *25*, 677-710.
- [181] G. Boven, R. Folkersma, G. Challa, A. J. Schouten, *Polym. Commun.* **1991**, *32*, 50-53.
- [182] D. M. Jones, A. A. Brown, W. T. S. Huck, *Langmuir* **2002**, *18*, 1265-1269.
- [183] R. Jordan, A. Ulman, *J. Am. Chem. Soc.* **1998**, *120*, 243-247.
- [184] M. Husseman, E. E. Malmstrom, M. McNamara, M. Mate, D. Mecerreyes, D. G. Benoit, J. L. Hedrick, P. Mansky, E. Huang, T. P. Russell, C. J. Hawker, *Macromolecules* **1999**, *32*, 1424-1431.
- [185] W. K. Lee, K. C. Caster, J. Kim, S. Zauscher, *Small* **2006**, *2*, 848-853.
- [186] M. Biesalski, D. Johannsmann, J. Ruhe, *J. Chem. Phys.* **2004**, *120*, 8807-8814.
- [187] J. Ruehe, M. Ballauff, M. Biesalski, P. Dziezok, F. Grohn, D. Johannsmann, N. Houbenov, N. Hugenberg, R. Konradi, S. Minko, M. Motornov, R. R. Netz, M. Schmidt, C. Seidel, M. Stamm, T. Stephan, D. Usov, H. N. Zhang, in *Polyelectrolytes with Defined Molecular Architecture I, Vol. 165*, **2004**, pp. 79-150.
- [188] B. Lego, W. G. Skene, S. Giasson, *Macromolecules* **2010**, *43*, 4384-4393.
- [189] C. Reichhart, C. Czeslik, *Colloid Surf. B-Biointerfaces* **2010**, *75*, 612-616.
- [190] M. Ulbricht, H. Yang, *Chem. Mater.* **2005**, *17*, 2622-2631.
- [191] F. Evers, C. Reichhart, R. Steitz, M. Tolan, C. Czeslik, *Phys. Chem. Chem. Phys.* **2010**, *12*, 4375-4382.
- [192] L. da Silva, F. E. da Silva, C. V. Franco, R. B. Nuernberg, T. Gomes, R. Miranda, M. M. D. Paula, *Mat. Sci. Eng. C-Bio. S* **2009**, *29*, 599-601.
- [193] K. Ainikin, C. R ocker, A. Wittemann, J. Wiedemann, M. Ballauff, G. U. Nienhaus, *J. Phys. Chem. B* **2005**, *109*, 5418-5420.
- [194] T. Ekbad, O. Andersson, F. I. Tai, T. Ederth, B. Liedberg, *Langmuir* **2009**, *25*, 3755-3762.
- [195] E. S. Forzani, V. M. Solis, E. J. Calvo, *Anal. Chem.* **2000**, *72*, 5300-5307.
- [196] I. Tokarev, M. Orlov, E. Katz, S. Minko, *J. Phys. Chem. B.* **2007**, *111*, 12141.
- [197] T. K. Tam, J. Zhou, M. Pita, M. Ornatska, S. Minko, E. Katz, *J. Am. Chem. Soc.* **2008**, *130*, 10888.
- [198] M. L. Bruening, D. M. Dotzauer, P. Jain, L. Ouyang, G. L. Baker, *Langmuir* **2008**, *24*, 7663-7673.
- [199] C. Gergely, S. Bahi, B. Szalontai, H. Flores, P. Schaaf, J.-C. Voegel, F. J. G. Cuisinier, *Langmuir* **2004**, *20*, 5575-5582.
- [200] R. Janzen, K. K. Unger, *J. Chromatogr.* **1990**, *522*, 77-93.
- [201] W. M uller, *J. Chromatogr.* **1990**, *510*, 133-140.
- [202] R. Barbey, E. Kauffmann, M. Ehrat, H. A. Klok, *Biomacromolecules* **2010**, *11*, 3467-3479.
- [203] P. Jain, J. H. Dai, G. L. Baker, M. L. Bruening, *Macromolecules* **2008**, *41*, 8413-8417.

- [204] S. P. Cullen, X. Liu, I. C. Mandel, F. J. Himpfel, P. Gopalan, *Langmuir* **2008**, *24*, 913-920.
- [205] J. H. Dai, Z. Y. Bao, L. Sun, S. U. Hong, G. L. Baker, M. L. Bruening, *Langmuir* **2006**, *22*, 4274-4281.
- [206] R. Dong, S. Krishnan, B. A. Baird, M. Lindau, C. K. Ober, *Biomacromolecules* **2007**, *8*, 3082-3092.
- [207] J. H. Dai, G. L. Baker, M. L. Bruening, *Anal. Chem.* **2006**, *78*, 135-140.
- [208] S. Huber, N. Hutter, R. Jordan, *Colloid Polym. Sci.* **2008**, *286*, 1653-1661.
- [209] S. Huber, R. Jordan, *Colloid Polym. Sci.* **2008**, *286*, 395-402.
- [210] C. Diehl, H. Schlaad, *Macromol. Biosci.* **2009**, *9*, 157-161.
- [211] N. Adams, U. S. Schubert, *Adv. Drug Deliv. Rev.* **2007**, *59*, 1504-1520.
- [212] A. Mero, G. Pasut, L. D. Via, M. W. M. Fijten, U. S. Schubert, R. Hoogenboom, F. M. Veronese, *J. Controlled Release* **2008**, *125*, 87-95.
- [213] R. Konradi, B. Pidhatika, A. Muhlebach, M. Textort, *Langmuir* **2008**, *24*, 613-616.
- [214] F. C. Gaertner, R. Luxenhofer, B. Blechert, R. Jordan, M. Essler, *J. of Controlled Release* **2007**, *119*, 291-300.
- [215] H. V. William, D. M. Rapti, S. Anuradha, K. Guneet, S. Gurudas, S. R. Judy, *Biotech. and Bioengi.* **1992**, *39*, 1024-1030.
- [216] M. A. Deverall, S. Garg, K. Ludtke, R. Jordan, J. Ruhe, C. A. Naumann, *Soft Matter* **2008**, *4*, 1899-1908.
- [217] A. Fortig, R. Jordan, K. Graf, G. Schiavon, O. Purruicker, M. Tanaka, *Macromol. Symposia* **2004**, *210*, 329-338.
- [218] K. Ludtke, R. Jordan, N. Furr, S. Garg, K. Forsythe, C. A. Naumann, *Langmuir* **2008**, *24*, 5580-5584.
- [219] K. Ludtke, R. Jordan, P. Hommes, O. Nuyken, C. A. Naumann, *Macromol. Biosci.* **2005**, *5*, 384-393.
- [220] C. J. Waschinski, V. Herdes, F. Schueler, J. C. Tiller, *Macromol. Biosci.* **2005**, *5*, 149-156.
- [221] C. J. Waschinski, J. C. Tiller, *Biomacromolecules* **2005**, *6*, 235-243.
- [222] R. Luxenhofer, A. Schulz, C. Roques, S. Li, T. K. Bronich, E. V. Batrakova, R. Jordan, A. V. Kabanov, *Biomaterials* **2010**, *31*, 4972-4979.
- [223] A. M. Ansari, P. V. Scaria, C. Martin, M. C. Woodle, *Patent Application PCT* **2003**, *WO 03/066069*.
- [224] J. Tong, R. Luxenhofer, X. A. Yi, R. Jordan, A. V. Kabanov, *Mol. Pharm.* **2010**, *7*, 984-992.
- [225] T. G. Bassiri, A. Levy, M. Litt, *Polym. Lett.* **1967**, *5*, 871-879.
- [226] T. Kagiya, S. Narisawa, T. Maeda, K. Fukui, *Polym. Lett.* **1966**, *4*, 441-445.
- [227] W. Seeliger, E. Aufderha, W. Diepers, R. Feinauer, R. Nehring, W. Thier, H. Hellmann, *Angew. Chem., Int. Ed. Engl.* **1966**, *5*, 875-&.
- [228] S. Cesana, J. Auernheimer, R. Jordan, H. Kessler, O. Nuyken, *Macromol. Chem. Phys.* **2006**, *207*, 183-192.
- [229] N. Zhang, M. Steenackers, R. Luxenhofer, R. Jordan, *Macromolecules* **2009**, *42*, 5345-5351.
- [230] N. B. Holland, Y. X. Qiu, M. Ruegsegger, R. E. Marchant, *Nature* **1998**, *392*, 799-801.

- [231] R. A. Dwek, *Chem. Rev.* **1996**, *96*, 683-720.
- [232] N. Zhang, R. Luxenhofer, T. Pompe, C. Werner, R. Jordan, **2011**, *in preparation*.
- [233] S. Yamamoto, J. Pietrasik, K. Matyjaszewski, *Macromolecules* **2008**, *41*, 7013-7020.
- [234] A. Naderi, J. Iruthayaraj, A. Vareikis, R. Makuska, P. M. Claesson, *Langmuir* **2007**, *23*, 12222-12232.
- [235] N. P. Huang, R. Michel, J. Voros, M. Textor, R. Hofer, A. Rossi, D. L. Elbert, J. A. Hubbell, N. D. Spencer, *Langmuir* **2001**, *17*, 489-498.
- [236] X. P. Yan, S. S. Perry, N. D. Spencer, S. Pasche, S. M. De Paul, M. Textor, M. S. Lim, *Langmuir* **2004**, *20*, 423-428.
- [237] T. Pettersson, A. Naderi, R. Makuska, P. M. Claesson, *Langmuir* **2008**, *24*, 3336-3347.
- [238] N. Zhang, S. Huber, A. Schulz, R. Luxenhofer, R. Jordan, *Macromolecules* **2009**, *42*, 2215-2221.
- [239] R. Luttge, *J. Phys. D-Appl. Phys.* **2009**, *42*, 18.
- [240] B. D. Gates, Q. B. Xu, M. Stewart, D. Ryan, C. G. Willson, G. M. Whitesides, *Chem. Rev.* **2005**, *105*, 1171-1196.
- [241] R. Ducker, A. Garcia, J. M. Zhang, T. Chen, S. Zauscher, *Soft Matter* **2008**, *4*, 1774-1786.
- [242] T. M. Bloomstein, M. F. Marchant, S. Deneault, D. E. Hardy, M. Rothschild, *Optics Express* **2006**, *14*, 6434-6443.
- [243] Z. Nie, E. Kumacheva, *Nat. Mater.* **2008**, *7*, 277-290.
- [244] D. Petrini, K. Larsson, *J. Phys. Chem. C* **2007**, *111*, 795-801.
- [245] A. Kumar, G. M. Whitesides, *Appl. Phys. Lett.* **1993**, *63*, 2002-2004.
- [246] R. K. Smith, P. A. Lewis, P. S. Weiss, *Prog. Surf. Sci.* **2004**, *75*, 1-68.
- [247] H. Tu, C. E. Heitzman, P. V. Braun, *Langmuir* **2004**, *20*, 8313-8320.
- [248] D. J. Dyer, *Adv. Funct. Mater.* **2003**, *13*, 667-670.
- [249] M. Husemann, D. Mecerreyes, C. J. Hawker, J. L. Hedrick, R. Shah, N. L. Abbott, *Angew. Chem.-Int. Edit.* **1999**, *38*, 647-649.
- [250] M. Husemann, M. Morrison, D. Benoit, K. J. Frommer, C. M. Mate, W. D. Hinsberg, J. L. Hedrick, C. J. Hawker, *J. Am. Chem. Soc.* **2000**, *122*, 1844-1845.
- [251] T. Chen, R. Jordan, S. Zauscher, *Polymer* **2011**, *52*, 2461-2467.
- [252] L. J. Guo, *J. Phys. D-Appl. Phys.* **2004**, *37*, R123-R141.
- [253] M. D. Austin, H. X. Ge, W. Wu, M. T. Li, Z. N. Yu, D. Wasserman, S. A. Lyon, S. Y. Chou, *Appl. Phys. Lett.* **2004**, *84*, 5299-5301.
- [254] H. Cao, Z. N. Yu, J. Wang, J. O. Tegenfeldt, R. H. Austin, E. Chen, W. Wu, S. Y. Chou, *Appl. Phys. Lett.* **2002**, *81*, 174-176.
- [255] S. B. Jhaveri, M. Beinhoff, C. J. Hawker, K. R. Carter, D. Y. Sogah, *ACS Nano* **2008**, *2*, 719-727.
- [256] A. Genua, J. A. Alduncin, J. A. Pomposo, H. Grande, N. Kehagias, V. Reboud, C. Sotomayor, I. Mondragon, D. Mecerreyes, *Nanotechnology* **2007**, *18*.
- [257] M. Kaholek, W. K. Lee, B. LaMattina, K. C. Caster, S. Zauscher, *Nano Lett.* **2004**, *4*, 373-376.
- [258] X. G. Liu, S. W. Guo, C. A. Mirkin, *Angew. Chem., Int. Ed.* **2003**, *42*, 4785-4789.
- [259] S. Zapotoczny, E. M. Benetti, G. J. Vancso, *J. Mater. Chem.* **2007**, *17*, 3293-3296.
- [260] H. Jung, R. Kulkarni, C. P. Collier, *J. Am. Chem. Soc.* **2003**, *125*, 12096-12097.

- [261] R. D. Piner, J. Zhu, F. Xu, S. H. Hong, C. A. Mirkin, *Science* **1999**, *283*, 661-663.
- [262] M. Zhang, D. Bullen, S. W. Chung, S. Hong, K. S. Ryu, Z. F. Fan, C. A. Mirkin, C. Liu, *Nanotechnology* **2002**, *13*, 212-217.
- [263] S. H. Hong, J. Zhu, C. A. Mirkin, *Science* **1999**, *286*, 523-525.
- [264] H. Sugimura, N. Nakagiri, *Nanotechnology* **1995**, *6*, 29-33.
- [265] H. Sugimura, T. Uchida, N. Kitamura, H. Masuhara, *J. Phys. Chem.* **1994**, *98*, 4352-4357.
- [266] H. Sugimura, T. Uchida, N. Kitamura, H. Masuhara, *Appl. Phys. Lett.* **1993**, *63*, 1288-1290.
- [267] S. Bae, C. S. Han, M. S. Kim, C. C. Chung, H. Lee, *Nanotechnology* **2005**, *16*, 2082-2085.
- [268] E. S. Snow, P. M. Campbell, *Appl. Phys. Lett.* **1994**, *64*, 1932-1934.
- [269] W. Yang, B. Ranby, *J. Appl. Polym. Sci.* **1996**, *62*, 533.
- [270] S. Hoepfner, U. S. Schubert, *Small* **2005**, *1*, 628-632.
- [271] P. Avouris, T. Hertel, R. Martel, *Appl. Phys. Lett.* **1997**, *71*, 285-287.
- [272] P. Avouris, R. Martel, T. Hertel, R. Sandstrom, *Appl. Phys.-Materials Science & Processing* **1998**, *66*, S659-S667.
- [273] S. Xu, G. Y. Liu, *Langmuir* **1997**, *13*, 127-129.
- [274] T. Djenizian, P. Schmuki, *J. Electroceram.* **2006**, *16*, 9-14.
- [275] O. Guise, H. Marbach, J. Levy, J. Ahner, J. T. Yates, *Surf. Sci.* **2004**, *571*, 128-138.
- [276] U. Schmelmer, A. Paul, A. Küller, M. Steenackers, A. Ulman, M. Grunze, A. Golzhauser, R. Jordan, *Small* **2007**, *3*, 459-465.
- [277] M. Steenackers, A. Küller, N. Ballav, M. Zharnikov, M. Grunze, R. Jordan, *Small* **2007**, *3*, 1764-1773.
- [278] M. Steenackers, M. Jordan, A. Küller, M. Grunze, *Adv. Mater.* **2009**, *21*, 2921.
- [279] M. Steenackers, I. D. Sharp, K. Larsson, N. A. Hutter, M. Stutzmann, R. Jordan, *Chem. Mater.* **2009**, *22*, 272-278.
- [280] T. Djenizian, L. Santinacci, P. Schmuki, *Appl. Phys. Lett.* **2001**, *78*, 2940-2942.
- [281] W. F. van Dorp, C. W. Hagen, *J. Appl. Phys.* **2008**, *104*.
- [282] D. M. Gruen, *Annu. Rev. Mater. Sci.* **1999**, *29*, 211-259.
- [283] B. V. Spitsyn, L. L. Bouilov, B. V. Derjaguin, *J. Cryst. Growth* **1981**, *52*, 219.
- [284] O. A. Williams, O. Douheret, M. Daenen, K. Haenen, E. Osawa, M. Takahashi, *Chem. Phys. Lett.* **2007**, *445*, 255-258.
- [285] J. H. T. Luong, K. B. Male, J. D. Glennon, *Analyst* **2009**, *134*, 1965-1979.
- [286] S. Szunerits, R. Boukherroub, *J. of Solid State Electrochem.* **2008**, *12*, 1205-1218.
- [287] O. A. Williams, M. Nesladek, *Physica Status Solidi a-Applications and Materials Science* **2006**, *203*, 3375-3386.
- [288] V. Vermeeren, S. Wenmackers, P. Wagner, L. Michiels, *Sensors* **2009**, *9*, 5600-5636.
- [289] J. Rubio-Retama, J. Hernando, B. Lopez-Ruiz, A. Hartl, D. Steinmuller, M. Stutzmann, E. Lopez-Cabarcos, J. A. Garrido, *Langmuir* **2006**, *22*, 5837-5842.
- [290] J. Hernando, T. Pourrostami, J. A. Garrido, O. A. Williams, D. M. Gruen, A. Kromka, D. Steinmuller, M. Stutzmann, *Diam. Rel. Mat* **2007**, *16*, 138-143.
- [291] J. Iniesta, P. A. Michaud, M. Panizza, G. Cerisola, A. Aldaz, C. Cominellis, *Electrochim. Acta* **2001**, *46*, 3573-3578.

- [292] Y. Coffinier, S. Szunerits, C. Jama, R. Desmet, O. Melnyk, B. Marcus, L. Gengembre, E. Payen, D. Delabouglise, R. Boukherroub, *Langmuir* **2007**, *23*, 4494-4497.
- [293] K. Takahashi, M. Tanga, O. Takai, H. Okamura, *Diam. Relat. Mat.* **2003**, *12*, 572-576.
- [294] D. Petrini, K. Larsson, *J. Phys. Chem. C* **2007**, *111*, 795-801.
- [295] Y. Coffinier, S. Szunerits, B. Marcus, R. Desmet, O. Melnyk, L. Gengembre, E. Payen, D. Delabouglise, R. Boukherroub, *Diam. Relat. Mat.* **2007**, *16*, 892-898.
- [296] S. Szunerits, N. Shirahata, P. Actis, J. Nakanishi, R. Boukherroub, *Chem. Commun.* **2007**, 2793-2795.
- [297] L. Li, J. L. Davidson, C. M. Lukehart, *Carbon* **2006**, *44*.
- [298] P. Actis, M. Manesse, C. Nunes-Kirchner, G. Wittstock, Y. Coffinier, R. Boukherroub, S. Szunerits, *Phys. Chem. Chem. Phys.* **2006**, *8*, 4924-4931.
- [299] P. Zhang, J. H. Yang, W. C. Li, W. Wang, C. J. Liu, M. Griffith, W. G. Liu, *J. Mater. Chem.* **2011**, *21*, 7755-7764.
- [300] M. Steenackers, S. Q. Lud, M. Niedermeier, P. Bruno, D. M. Gruen, P. Feulner, M. Stutzmann, J. A. Garrido, R. Jordan, *J. Am. Chem. Soc.* **2007**, *129*, 15655-15661.
- [301] C. E. Nebel, B. Rezek, D. Shin, H. Uetsuka, N. Yang, *J. Phys. D-Appl. Phys.* **2007**, *40*, 6443-6466.
- [302] H. J. Mathieu, *Surf. Interface Anal.* **2001**, *32*, 3-9.
- [303] W. S. Yang, O. Auciello, J. E. Butler, W. Cai, J. A. Carlisle, J. Gerbi, D. M. Gruen, T. Knickerbocker, T. L. Lasseter, J. N. Russell, L. M. Smith, R. J. Hamers, *Nat. Mater.* **2002**, *1*, 253-257.
- [304] T. Knickerbocker, T. Strother, M. P. Schwartz, J. N. Russell, J. Butler, L. M. Smith, R. J. Hamers, *Langmuir* **2003**, *19*, 1938-1942.
- [305] C. Padeste, H. H. Solak, H. P. Brack, M. Slaski, S. A. Gursel, G. G. Scherer, *J. Vac. Sci. Technol., B* **2004**, *22*, 3191-3195.
- [306] S. A. Dahoumane, M. N. Nguyen, A. Thorel, J. P. Boudou, M. M. Chehimi, C. Mangeney, *Langmuir* **2009**, *25*, 9633-9638.
- [307] J. P. Deng, W. T. Yang, B. Ranby, *Macromol. Rapid Commun.* **2001**, *22*, 535-538.
- [308] N. Zhang, M. Steenackers, R. Luxenhofer, R. Jordan, *Macromolecules* **2009**, *42*, 5345.
- [309] N. Zhang, S. Huber, A. Schulz, R. Luxenhofer, R. Jordan, *Macromolecules* **2009**, *42*, 2215-2221.
- [310] W. K. Lee, M. Patra, P. Linse, S. Zauscher, *Small* **2007**, *3*, 63-66.
- [311] M. Steenackers, in *PhD Thesis*, TU München, **2007**.
- [312] T. Djenizian, E. Balaur, P. Schmuki, *Nanotechnology* **2006**, *17*, 2004-2007.
- [313] J. Wang, M. A. Firestone, O. Auciello, J. A. Carlisle, *Langmuir* **2004**, *20*, 11450-11456.
- [314] K. May, S. Dapprich, F. Furche, B. V. Unterreiner, R. Ahlrichs, *Phys. Chem. Chem. Phys.* **2000**, *2*, 5084-5088.
- [315] M. Steenackers, R. Jordan, A. Küller, M. Grunze, *Adv. Mater.* **2009**, *21*, 2921-+.
- [316] M. Patra, P. Linse, *Nano Lett.* **2006**, *6*, 133-137.
- [317] R. Ducker, A. Garcia, J. Zhang, T. Chen, S. Zauscher, *Soft Matter* **2008**, *4*, 1774-1786.
- [318] M. Patra, P. Linse, *Macromolecules* **2006**, *39*, 4540-4546.
- [319] W. Van Camp, F. E. Du Prez, *Macromolecules* **2004**, *37*, 6673-6675.

- [320] D. Wouters, W. Van Camp, B. Dervaux, F. E. Du Prez, U. S. Schubert, *Soft Matter* **2007**, *3*, 1537-1541.
- [321] D. L. Nelson, M. M. Cox, *Lehninger Principles of Biochemistry*, 4 ed., W H Freeman, New York, **2008**.
- [322] N. A. Hutter, A. Reitingner, N. Zhang, M. Steenackers, O. A. Williams, J. A. Garrido, R. Jordan, *Phys. Chem. Chem. Phys.* **2010**, *12*, 4360-4366.
- [323] S. B. Rahane, J. A. Floyd, A. T. Metter, S. M. Kilbey, *Adv. Funct. Mater.* **2008**, *18*, 1232-1240.
- [324] M. Chalfie, Y. Tu, G. Euskirchen, W. W. Ward, D. C. Prasher, *Science* **1994**, *263*, 802-805.
- [325] O. Shimomura, F. H. Johnson, Y. Saiga, *J. Cellular and Comparative Physiology* **1962**, *59*, 223-&.
- [326] M. Ormö, A. B. Cubitt, K. Kallio, L. A. Gross, R. Y. Tsien, S. J. Remington, *Science* **1996**, *273*, 1392-1395.
- [327] R. Heim, A. B. Cubitt, R. Y. Tsien, *Nature* **1995**, *373*, 663-664.
- [328] J. E. Gautrot, W. T. S. Huck, M. Welch, M. Ramstedt, *Acs Appl. Mater. & Interfaces* **2009**, *2*, 193-202.
- [329] T. D. Craggs, *Chem. Soc. Rev.* **2009**, *38*, 2865-2875.
- [330] W. W. Ward, S. H. Bokman, *Biochemistry* **1982**, *21*, 4535-4540.
- [331] R. Luxenhofer, TU München, **2004**.
- [332] L. Piras, M. Adami, S. Fenu, M. Dovis, C. Nicolini, *Anal. Chimica Acta* **1996**, *335*, 127-135.
- [333] G. G. Guiltbault, P. Brignac, M. Zimmer, *Anal. Chem.* **1968**, *40*.
- [334] F. Fuchs, in *Diploma Thesis*, TU München, **2011**.
- [335] J. I. Herren, K. S. Kunzelmann, C. Viocelka, C. R. P., B. D. Spiess, *Stroke* **1997**, *28*, 2025-2030.
- [336] G. Wohlfahrt, S. Witt, J. Hendle, D. Schomburg, H. M. Kalisz, H. J. Hecht, *Acta Crystallographica Section D-Biological Crystallography* **1999**, *55*, 969-977.
- [337] F. Vianello, S. Bortoluzzi, L. Zennaro, A. Rigo, *J. Biochem. Biophys. Methods* **2002**, *51*, 263-271.
- [338] K. P. Fears, R. A. Latour, *Langmuir* **2009**, *25*, 13926-13933.
- [339] X. H. Hou, B. L. Liu, X. B. Deng, B. T. Zhang, H. L. Chen, R. Luo, *Anal. Biochem.* **2007**, *368*, 100-110.
- [340] K. Taga, S. Weger, R. Gobel, R. Kellner, *Sensors and Actuators B-Chemical* **1993**, *11*, 553-559.
- [341] A. J. Bard, L. R. Faulkner, *Electrochemical Methods*, 2 ed., Wiley, **2001**.
- [342] S. Dong, Z. Li, J. Qin, *J. Phys. Chem. B* **2009**, *113*, 434-441.
- [343] N. Leclerc, A. Michaud, K. Sirois, J. F. Morin, M. Leclerc, *Adv. Funct. Mat.* **2006**, *16*, 1694-1704.
- [344] X. Z. Jiang, R. A. Register, K. A. Killeen, M. E. Thompson, F. Pschenitzka, J. C. Sturm, *Chem. Mater.* **2000**, *12*, 2542-2549.
- [345] B. R. Hsieh, M. H. Litt, *Macromolecules* **1985**, *18*, 1388-1394.
- [346] X. Liu, Y. M. Sun, Y. H. Zhang, N. Zhao, H. S. Zhao, G. C. Wang, X. Q. Yu, H. Liu, *J. of Fluorescence* **2011**, *21*, 497-506.

- [347] P. Taranekar, C. Huang, T. M. Fulghum, A. Baba, G. Jiang, J. Y. Park, R. C. Advincula, *Adv. Funct. Mater.* **2008**, *18*, 347-354.
- [348] C. Y. Huang, G. Q. Jiang, R. Advincula, *Macromolecules* **2008**, *41*, 4661-4670.
- [349] B. Y. Kim, E. L. Ratcliff, N. R. Armstrong, T. Kowalewski, J. Pyun, *Langmuir* **2010**, *26*, 2083-2092.
- [350] B. Yu, H. Y. Hu, D. A. Wang, W. T. S. Huck, F. Zhou, W. M. Liu, *J. of Mater. Chem.* **2009**, *19*, 8129-8134.
- [351] L. Q. Xu, D. Wan, H. F. Gong, K. G. Neoh, E. T. Kang, G. D. Fu, *Langmuir* **2010**, *26*, 15376-15382.
- [352] J. L. Jios, S. I. Kirin, N. N. Buceta, T. Weyhermüller, C. O. Della Védova, N. Metzler-Nolte, *J. Organometal. Chem.* **2007**, *692*, 4209-4214.
- [353] P. D. Beer, D. K. Smith, *Dalton Trans.* **1998**, 417-423.
- [354] N. Sun, L. Guan, Z. Shi, N. Li, Z. Gu, Z. Zhu, M. Li, Y. Shao, *Anal. Chem.* **2008**, *78*, 6050-6057.
- [355] V. S. Tripathi, V. B. Kandimalla, H. Ju, *Biosens. Bioelectron.* **2006**, *21*, 1529-1535.
- [356] G. T. Hermanson, *Bioconjugate Techniques*, 2 ed., Academic Press, **2008**.
- [357] K. Wilson, *Preparation of genomic DNA from bacteria*, Greene Publishing Associates, New York, **1994**.
- [358] B. R. Hsieh, M. H. Litt, *Macromolecules* **1986**, *19*, 516-520.
- [359] M. T. Zarka, O. Nuyken, R. Weberskirch, *Chem. Eur. J.* **2003**, *9*, 3228-3234.
- [360] Z. Q. Wu, *J. Appl. Polym. Sci.* **2008**, *110*, 777-783.
- [361] S. Huikai, W. Qingmin, R. H. Heng, L. Yonghong, *J. Organometal. Chem.* **2002**, *655*, 182-185.